AD-766 047

FUNDAMENTAL STUDIES IN THE USE OF SONIC POWER FOR ROCK CUTTING

Karl F. Graff

Ohio State University. Research Foundation

Prepared for:

Advanced Research Projects Agency
Bureau of Mines

April 1973

DISTRIBUTED BY:

NTIS
National Technical Information Service
U. S. DEPARTMENT OF COMMERCE
5285 Port Royal Road, Springfield Va. 22151

AD 766047

FUNDAMENTAL STUDIES IN THE USE OF SONIC POWER FOR ROCK CUTTING

Karl F. Graff

The Ohio State University
Research Foundation
Columbus, Ohio 43212

FINAL REPORT

April, 1973

Reproduced by
NATIONAL TECHNICAL
INFORMATION SERVICE
U S Department of Commerce
Springfield VA 22151

Sponsored By
Advanced Research Project Agency
ARPA Order No. 1579 Amend. 3
Program Code 2F10

Monitored By
U.S. Bureau of Mines
Twin Cities Mining Research Center
Twin Cities, Minnesota

DDC
RECEIVED
SEP 10 1973
B

DISTRIBUTION STATEMENT A
Approved for public release;
Distribution Unlimited

203

Security Classification

DOCUMENT CONTROL DATA - R & D

(Security classification of title, body of abstract and indexing annotation must be entered when the overall report is classified)

1. ORIGINATING ACTIVITY (Corporate author)
The Ohio State University Research Foundation
1314 Kinnear Road, Columbus, Ohio 43212

2a. REPORT SECURITY CLASSIFICATION
Unclassified

2b. GROUP
N/A

3. REPORT TITLE
FUNDAMENTAL STUDIES IN THE USE OF SONIC POWER FOR ROCK CUTTING

4. DESCRIPTIVE NOTES (Type of report and inclusive dates)
Final February 23, 1972 through April 22, 1973

5. AUTHOR(S) (First name, middle initial, last name)
Karl F. Graff

6. REPORT DATE
April, 1973

7a. TOTAL NO. OF PAGES
200

7b. NO. OF REFS
48

8a. CONTRACT OR GRANT NO.
H0220037

b. PROJECT NO. ARPA Order 1579
Amendment No. 3

c.

d.

9a. ORIGINATOR'S REPORT NUMBER(S)

9b. OTHER REPORT NO(S) (Any other numbers that may be assigned this report)

10. DISTRIBUTION STATEMENT
Distribution of this document is unlimited.

11. SUPPLEMENTARY NOTES

12. SPONSORING MILITARY ACTIVITY
Defense Advanced Research Projects Agency
1400 Wilson Boulevard
Arlington, VA 22209

13. ABSTRACT

The utilization of high power, high frequency sonic transducers for rock cutting has been in progress at Ohio State University for two years with the second year of work presented in this report. Two modes of rock cutting were investigated; the first, simple drilling and the second, layer cutting. An impact coupling technique, which utilized a small, bouncing cutting tool at the tip of the transducer, was used in both modes of cutting. The overall study was divided into a system development phase, where laboratory cutting apparatus was tested, and a system analysis phase, where basic studies of sonic processes and devices were carried out.

Unclassified
Security Classification

14 KEY WORDS	LINK A		LINK B		LINK C	
	ROLE	WT	ROLE	WT	ROLE	WT
Rock cutting						
Power ultrasonics						
Rock drilling						
Ultrasonic drilling						
Ultrasonic transducers						

FUNDAMENTAL STUDIES IN THE USE OF SONIC POWER FOR ROCK CUTTING

Karl F. Graff
Principal Investigator (614)422-2731

The Ohio State University
Research Foundation
Columbus, Ohio 43212

FINAL REPORT

April, 1973

Contract No. - H0220037
Effective Date of Contract - February 23, 1972
Contract Expiration Date - April 22, 1973
Amount of Contract - $51,735.00
Technical Project Officer - Patrick J. Cain, Twin Cities Mining Research Center, Twin Cities, Minnesota

Period Covered: February 23, 1972 to April 22, 1973

This research was supported by the Advanced Research Projects Agency of the Department of Defense and was monitored by the U.S. Bureau of Mines, under Contract No. H0220037

The views and conclusions contained in this document are those of the authors and should not be interpreted as necessarily representing the official policies, either expressed or implied, of the Advanced Research Projects Agency or the U.S. Government.

ib

PREFACE

This project on sonic rock cutting was sponsored by the Advanced Research Projects Agency and was monitored by the U. S. Bureau of Mines, Twin Cities, Minnesota under Contract No. H0220037. James T. Olson of the Twin Cities Mining Research Center was the ARPA Program Coordinator, with Dr. Patrick J. Cain of the Twin Cities organization acting as Project Officer. The work was an extension of earlier work under Contract No. H0210010 and was initiated on February 23, 1972 and completed on April 22, 1973.

The work was performed in the Engineering Mechanics Department and Sonic Power Laboratory of The Ohio State University under Research Foundation Project RF 3396. Dr. Karl F. Graff, Professor of Engineering Mechanics was project supervisor. Charles C. Libby, Assistant Professor of Welding Engineering, was in charge of the layer cutting phase of work from February 23 through September 30, 1972. Peter Au and Gary Streby worked on the development of layer cutting techniques. Long-chin Shieh carried out experimental work in rock drilling while Ting-yu Lo conducted the analysis of the drilling process. The analysis of sonic transducers was done by Ching-chio Feng, as was the analysis of layer cutting. The report on a pulse-reflector for sonic transducers was prepared by Nelson Ma. Henry A. Bobulski, Sonic Laboratory Manager, carried out instrumentation and assisted in the development phases of all laboratory work.

SUMMARY

The utilization of high power, high frequency sonic transducers for rock cutting has been in progress at Ohio State University for two years with the second year of work presented in this report. Two modes of rock cutting were investigated; the first, simple drilling and the second, layer cutting. An impact coupling technique, which utilized a small, bouncing cutting tool at the tip of the transducer, was used in both modes of cutting. The overall study was divided into a system development phase, where laboratory cutting apparatus was tested, and a system analysis phase, where basic studies of sonic processes and devices were carried out.

Considering first the analysis phase of work, basic studies of the transducer, the drilling process, layer cutting and of a pulse reflector were carried out. In the development phase, the work on drilling was continued from the first year into new tool designs and hard rock cutting. In layer cutting, which was new to the second year, apparatus was constructed, tested on limestone, and then applied to cutting granite.

While drilling and layer cutting in Indiana limestone was successful in the sense of simply being able to remove rock, difficulties were encountered in penetrating hard rock. Numerous variations of cutting parameters were tested, until some success in layer cutting of granite was achieved. Nevertheless, results were marginal. While numerous complex explanations are available regarding the difficulties, it is possible to summarize them quite simply. The impact coupling technique of energy transfer presently represents a poor impedance match between the transducer and the load.

TABLE OF CONTENTS

Page

INTRODUCTION

1 - SONIC LAYER CUTTING OF ROCK 3

- 1-1 Introduction 3
- 1-2 Preliminary Apparatus 5
- 1-3 Layer Cutting Apparatus 8
- 1-4 Layer Cutting in Indiana Limestone 8
- 1-5 Results for Limestone 15
  - (A) Results from preliminary apparatus 15
  - (B) Results from large cutting apparatus 15
- 1-6 Layer Cutting in Granite 22
  - (A) Difficulties encountered 26
  - (B) Attack angle 26
  - (C) Tool design 27
  - (D) Spring-return system 32
  - (E) Transmission line optimization 33
- 1-7 Results for Granite 33

2 - TECHNICAL LITERATURE APPLICABLE TO ANALYSIS OF LAYER CUTTING 41

- 2-1 Introduction 41
- 2-2 Failure Theories of Rock 41
  - (A) The empirical critieria 41
  - (B) Phenomenalogical failure theories 45
  - (C) Statistical failure theories 48
- 2-3 Literature Applicable to Layer Cutting 48
- 2-4 References 62

3 - SONIC ROCK DRILLING 65

- 3-1 Apparatus 65
- 3-2 Tool Design 67
- 3-3 Drilling Results in Limestone 67
- 3-4 Drilling Tests in Granite 73

TABLE OF CONTENTS (continued)

Page

4 - ANALYSIS OF ROCK DRILLING 79

4-1 Tool Impact on Rock--Specific Energy 81
4-2 Tool Impact on a Vibrating Transmission Line 82
4-3 Transducer Vibration 86

(A) Forced vibration of a cylindrical sandwich type resonator 88
(B) Transducer vibration and recovery of transducer tip amplitude 93
(C) Internal energy and tip amplitude 95

4-4 Drilling Analysis 96

(A) Internal energy during steady state operation 99
(B) Impact coupling 101
(C) Power transmission 106
(D) Drilling rate of a sonic transducer 109
(E) Numerical example 109

4-5 References 113

5 - TRANSDUCER ANALYSIS 115

5-1 Sonic Resonators 116

(A) The symmetrical simple resonator 116
(B) The asymmetric simple resonator 124
(C) The P-7 resonator 131

5-2 The P-7 Transducer 132
5-3 Static Bias and Temperature Effects on Transducer Resonant Frequencies 136

(A) Summary of prestress, temperature and voltage on PZT-4 properties 137
(B) Effects of prestress, temperature and voltage on resonant frequencies 140
(C) Effect of prestress on resonant frequency, based on the spring model 147
(D) Resonant frequency experiments 154

5-4 Summary 165
5-5 References 167

TABLE OF CONTENTS (continued)

Page

6 - DEVELOPMENT OF A PULSE REFLECTOR FOR SONIC TRANSDUCERS 169

6-1 Reflector Design 170

(A) Theoretical analysis of reflection characteristics 170
(B) Analysis of resonance characteristics of reflectors 172

6-2 Measurement of Resonance and Reflection Characteristics 178

(A) Measurement of resonance characteristics 178
(B) Measurement of reflection characteristics 179
(C) Measurements of pulse reflector efficiency 180

6-3 Summary 180

6-4 References 186

LIST OF FIGURES

Fig. No.		Page
1-1	Early configuration of P-7 transducer used for kerf cutting	4
1-2	Early layer cutting configuration using the P-11 transducer	6
1-3	View of the transmission line tip and the pivoted cutting tool of the early layer cutting apparatus	7
1-4	Apparatus for sonic layer cutting of rock	9
1-5	Welded steel frame and drive screw for large cutting apparatus	10
1-6	Electric motor and chain drive for layer cutting apparatus	11
1-7	Traverse speed versus motor and gear setting	12
1-8	Flat-faced cutting tool	16
1-9	Plow-shaped cutting tool	16
1-10	Rate of rock removal for early apparatus	17
1-11	Specific energy of rock removal versus depth of cut for early apparatus	18
1-12	Layer cutting action on large apparatus	19
1-13	Volume of rock removal versus cutting speed for a 0.5 inch depth of cut	20
1-14	Volume of rock removal versus cutting speed for a 0.25 inch depth of cut	21
1-15	Specific energy of rock removal versus cutting speed for 0.5 inch cutting depth	23
1-16	Specific energy of rock removal versus cutting speed for 0.25 inch cutting depth	24
1-17	Specific energy of removal versus cutting speed for two depths of cut (attack angle at 10°)	25
1-18	Heavy plow tool	28

Fig. No.		Page
1-19	Stepped cutting tool	28
1-20	Chisel-type tool	29
1-21	Two-piece impact tool	30
1-22	Various layer cutting tools	31
1-23	Spring assisted tool return assembly	32
1-24	No-load, low-voltage resonant frequency change with change in line length	34
1-25	Input power versus line length under cutting conditions	35
1-26	Layer cutting action in granite	36
1-27	Typical cuts in granite	37
1-28	Volume of rock removal versus speed of cutting	38
1-29	Specific energy of rock removal versus cutting speed	39
2-1	A two-dimensional stress state	42
2-2	The σ_1-σ_3 failure boundary	44
2-3	Mohr envelope of failure	45
2-4	Griffith Theory (G.T.) and Modified Griffith Theory (M.G.T.)	47
2-5	Merchants' metal cutting model	49
2-6	Merchants' shear failure model	49
2-7	Merchants' force components on a chip	50
2-8	Cutting force P versus rake angle α relations from Merchants' theory	51
2-9	Chip formation zone	52
2-10	Lines of slip in the chip formation zone	53
2-11	Evan's plowing problem	53

Fig. No.		Page
2-12	The horizontal thrust force P versus the half-wedge angle α	55
2-13	Evans' blunt wedge plowing model	56
2-14	Comparison between experimental and theoretical results, continuous cutting with blunted picks	56
2-15	Failure process of rock cutting	57
2-16	Stress distribution and cutting forces for orthogonal rock cutting	57
2-17	The angle of friction of rock cutting	59
2-18	Garners possible fractures for crater indexing	61
2-19	Cheathams possible slip lines for indexing in a plastic rock	61
3-1	Drilling apparatus	66
3-2	Schematic of depth-time measuring system	68
3-3	Tool designs used in limestone drilling	69
3-4	Second series of tool designs	70
3-5	Tool design for granite cutting	71
3-6	Effects of static force on drilling for various tools	72
3-7	Penetration rate with and without the air-vacuum system	74
3-8	Depth of penetration versus time for fixed and variable frequency operation	75
3-9	Depth of penetration versus time for (a) tool # 3 and (b) tool # 7	76
3-10	Depth of penetration versus time for tools # 8 (upper trace) and # 6 (lower trace)	77
4-1	Sonic rock drilling system	80
4-2	Variations of specific energy and volume removal (m_e = 1.08 inch)	83

Fig. No.		Page
4-3	Incident-rebound velocity relationship ($R = 10''$ and $m_e = 0.5''$)	84
4-4	Variation of incident-rebound velocity relationship with respect to equivalent length $m_e(R = 5'')$	87
4-5	Transducer tip vibration under impact	89
4-6	Recovery of tip vibration amplitude	89
4-7	Cylindrical sandwich type resonator	90
4-8	Simplified model of cylindrical sandwich type resonator	90
4-9	Amplitude-voltage relationship (transducer temperature = 75°F)	97
4-10	Variations of amplitude and input power as a function of driving frequency	97
4-11	Effect of transducer temperature on amplitude, resonant frequency and power	98
4-12	Variation of tip vibration amplitude	100
4-13	Variation of internal energy	100
4-14	Steady-state velocities for $c_i = 1.0$ mil, $m_e - 0.5$ inch and $R = 10''$	102
4-15	Transducer acted upon by static force F_s and impact force $f(t)$	104
4-16	Rigid body motion of a transducer acted upon by static force and impact	105
4-17	Velocity difference for various values of equivalent length of the tool	108
4-18	Solution of c_i (graphical method)	111
5-1	The symmetrical simple resonator	117
5-2	Equivalent circuit for the symmetrical simple resonator--thickness plate model	117
5-3	Simplified equivalent circuits	118

Fig. No.		Page
5-4	Equivalent circuit for the symmetrical simple resonator-longitudinal rod model	121
5-5	The spring model for the symmetrical simple resonator	124
5-6	The natural frequency versus the spring constant K	125
5-7	The asymmetric simple resonator	126
5-8	The spring model for the asymmetric simple resonator	131
5-9	The P-7 resonator	132
5-10	The P-7 transducer	133
5-11	The resonant frequency versus the length of horn of a P-7 transducer	134
5-12	The spring model for the P-7 transducer	135
5-13	The detuning effect on a transducer	137
5-14	The d_{33} and ϵ_{33}^{T} versus the parallel stress (from [3] and [14])	139
5-15	The Youngs' modulus versus the parallel stress	139
5-16	S_{33}^{D} and S_{33}^{E} versus prestress as calculated from Fig. 5-14	140
5-17	The prestress effect on the resonant frequency of a simple resonator	142
5-18	The prestress effect on the resonant frequency of a P-7 resonator	142
5-19	The prestress effect on the resonant frequency of a P-7 transducer	143
5-20	The prestressed ceramic and center bolt	143
5-21	Prestress release versus temperature change on a simple resonator	144
5-22	Theoretical-experimental temperature effects on the resonant frequency of a simple resonator	145

Fig. No.		Page
5-23	The prestressed ceramic, center bolt and metal sleeve	145
5-24	Theoretical-experimental temperature-prestress release effects on a P-7 resonator	146
5-25	Theoretical-experimental temperature-prestress release effects on a P-7 transducer	146
5-26	The experimental K versus prestress relation obtained from the symmetric simple resonator	148
5-27	The resonant frequency of the P-7 resonator versus the spring constant K	149
5-28	Resonant frequencies of P-7 transducers with horns of different lengths versus K	150
5-29	The second, third and fourth modes of a P-7 resonator with a 35-inch horn versus K	151
5-30	The theoretical prestress effect on resonant frequency of the P-7 resonator, the spring model	152
5-31	The theoretical prestress effect on the resonant frequency of the P-7 transducer, the spring model	153
5-32	Experimental setup for resonant frequencies of resonators and transducers	155
5-33	Calibration and empirical curves for the torque versus prestress relation of a P-7 transducer	156
5-34	The resonant frequency versus the prestress for a symmetric simple resonator	157
5-35	The resonant frequency versus the prestress relations for a P-7 resonator	158
5-36	Resonant frequency versus prestress for a P-7 transducer with 4.75 inch horn	159
5-37	Resonant frequency versus temperature for the symmetric simple resonator	161
5-38	Resonant frequency versus temperature for the P-7 resonator	162

Fig. No.		Page
5-39	Resonant frequency versus temperature for a P-7 transducer with a 4.75 inch horn	163
5-40	Experimental resonant frequency versus voltage for the symmetric simple resonator	164
5-41	Experimental resonant frequency versus voltage for the P-7 resonator	164
5-42	Experimental resonant frequency versus voltage for the P-7 transducer	165
6-1	Waves across a discontinuity	170
6-2	Relations between $2/(1 + A_2/A_1)$, $(A_2/A_1 - 1)/(1 + A_2/A_1)$ versus A_2/A_1	173
6-3	Dimensions and coordinates of Type A pulse reflector	174
6-4	Dimensions and coordinates of the Type B pulse reflector	176
6-5	Schematic diagram of apparatus	178
6-6	Schematic diagram of experimental set-up	179
6-7	Typical stress pulse output observed for Type A reflector with interpretation of the waveform	181
6-8	Typical stress pulse output for Type B reflector with interpretation of the waveform	182
6-9	Stress pulse output for P-11 horn with interpretation of the waveform	183
6-10	Typical stress pulse and voltage output for P-11 transducer, without a pulse reflector	184
6-11	Typical stress pulse and voltage output for P-11 transducer with the Type A pulse reflector in place	185

LIST OF TABLES

Table No.		Page
4-1	Sonic drilling of granite	112
5-1	Numerical data for the OSU simple resonator	120
5-2	Dimensions for the P-7 resonator	132
6-1	Resonance frequencies of reflectors and P-11 horn	179

INTRODUCTION

The possibility of using ultrasonics for rock cutting was noted by Mauer [1].* The technique proposed earlier was essentially an extension of the ultrasonic slurry drilling technique that has been successfully used for many years for cutting extremely hard materials, such as tungsten carbide. However, the relative inefficiency and slow cutting rate of the slurry drilling process seemed to preclude use of ultrasonics for cutting rock.

However, as has been noted in an earlier report [2], developments in power sonics at Ohio State University indicated that sonic rock cutting on a large scale might be feasible. An impact coupling means of energy transfer had been developed that enabled significant amounts of energy to be transferred to a work surface. Large sonic transducers, rated at 10 kilowatts had been developed. Crude experiments on drilling and cutting concrete had been carried out.

Accordingly, a two-year study of sonic rock cutting has been conducted of which this report covers the second year. The work has been divided into systems development and systems analysis phases. In the development aspect, laboratory rock cutting hardware has been constructed and tested. In the analysis aspects, various fundamental characteristics of sonic devices and processes have been investigated, utilizing both theory and experiment.

The work in the second year, reported herein, was aimed at utilizing two modes of cutting to penetrate hard rock. The first mode was the simple drilling of holes of one to one-and-a-quarter inch in diameter. The second mode was layer cutting. In this work, a sonic transducer was traversed across the rock surface. The transducer and impact tool were so arranged as to cut a gouge in the surface of one-quarter to one-half inch in depth. Such an arrangement, it was felt, could be extended to a multiple array of transducers on a tunneling machine.

Fundamental studies that accompanied hardware development included analysis of the transducer, analysis of the drilling process and development of a stress pulse reflector for the transducers. The work on the transducer, which included both theory and experiment, was directed at understanding the influence of prestress, voltage and temperature on transducer frequency. The drilling analysis also comprised theory and experiment and was aimed at predicting drilling rate, with effects of tool, static forces and rock type included in the analysis. The pulse reflector development arose from the need to mitigate the stress pulses transmitted into the transducer during impact coupling.

---

*Numbers in brackets refer to references at the end of this section.

A major objective of the second year of work was cutting of hard rock, and as basalt, quartzite and granite. Previous work had been done mainly on Indiana limestone. In the development of the layer cutting technique, which was completely new in the second year, cutting tests were carried out on limestone until the apparatus was perfected. In terms of simple ability to cut rock, results were acceptable while working in the softer rock. Considerable difficulty was encountered in cutting hard rock, such as granite, however. This also held true in the drilling work. While some success was achieved in cutting hard rock, the results were quite marginal, both in terms of rate of rock removal and in terms of specific energy of removal.

While numerous complex explanations could be put forth as to the difficulty in cutting hard rock in a significant way, it is possible to summarize the problem quite simply. It was one of mechanical (impedance) mismatch between the transducer and the load. The transducer is a powerful motor, known to be capable of transmitting 10 kilowatts of power into a matched load. However, the impact coupling technique is a very poor matching system between the transducer and load. The bouncing tool was found to transmit only a small fraction of the energy in the transducer to the rock in an impact. Further, the rate of tool impact in rock cutting is on the order of hundreds of impacts per second, versus transducer vibration frequencies of 10,000 Hz. Thus, the transducer was operating effectively unloaded most of the time. The energy transfer process was thus found to be both inadequate and inefficient.

References

1. Mauer, W. C., Novel Drilling Techniques, Pergamon Press, 1968, pp. 44-49.

2. Graff, K. F., "Fundamental Studies in the Use of Sonic Power for Rock Cutting." Annual Technical Report, Bureau of Mines Contract No. H0210010, Dec., 1971.

1. SONIC LAYER CUTTING OF ROCK

1-1 INTRODUCTION

The use of sonic energy for cutting layers or kerfs in rock is not new. In earlier work,* the model P-7 transducer was used to cut kerfs in concrete, as shown in Fig. 1-1. In this illustration the transducer delivers reciprocating force to the pivoted blade by means of intermittent or bouncing contact at the upper end of the blade or tool. The lower end of the tool cuts a groove in the limestone rock as the transducer-tool combination is traversed from right to left. In this assembly the traverse is made parallel to the rock face and its velocity is determined by the rate at which a control wheel is rotated manually.

Rock grooving, by this means, requires relatively large amounts of energy per cubic volume removed. This is because the rock is highly pulverized by the particular tool configuration used. Very few chips of any significant size are produced. The groove is, therefore, smooth-sided and sharp-edged. The process thus met the requirements for kerf cutting in highways of minimum chipping and a sharp-edged groove. However, in layer cutting for excavation purposes, maximum volume of rock removal and rapid cutting speed is of greater interest. In particular, it becomes desirable to produce considerable chipping from the region of the cut.

The basic concept of layer cutting in the present work was somewhat different than in Fig. 1-1. Basically, the approach was to traverse a sonic transducer across the face of the rock, using a small impact tool at the tip of the transducer instead of the lengthy, massive tool of Fig. 1-1. By slightly inclining the transducer relative to the rock face, it was possible to apply sonic impact, via the impact tool, directly to the rock, instead of indirectly by the lever action of Fig. 1-1.

The use of a small impact tool and the impact coupling means of energy transfer is common to many sonic processes. Basically, in the intermittent or noncontinuous type of impact mode rock cutting, mechanical energy is withdrawn from the transducer in discrete quantities during the intervals between impacts of the metallic tool by the electrical power supply system. The duration of tool impact is very short, a small percent of the relatively longer time between impacts; impact duration is fairly constant, whereas the duration of the time interval between impacts varies inversely with the amplitude of the externally applied static force. This static force is applied in the direction of the traverse of the rock cutting assembly.

---

*Work sponsored by The Ohio Department of Highways and the Federal Highway Administration under Ohio State Engineering Experiment Station Project EES 22C, "Development of Sonic and Ultrasonic Power Devices for Application in Highway Engineering."

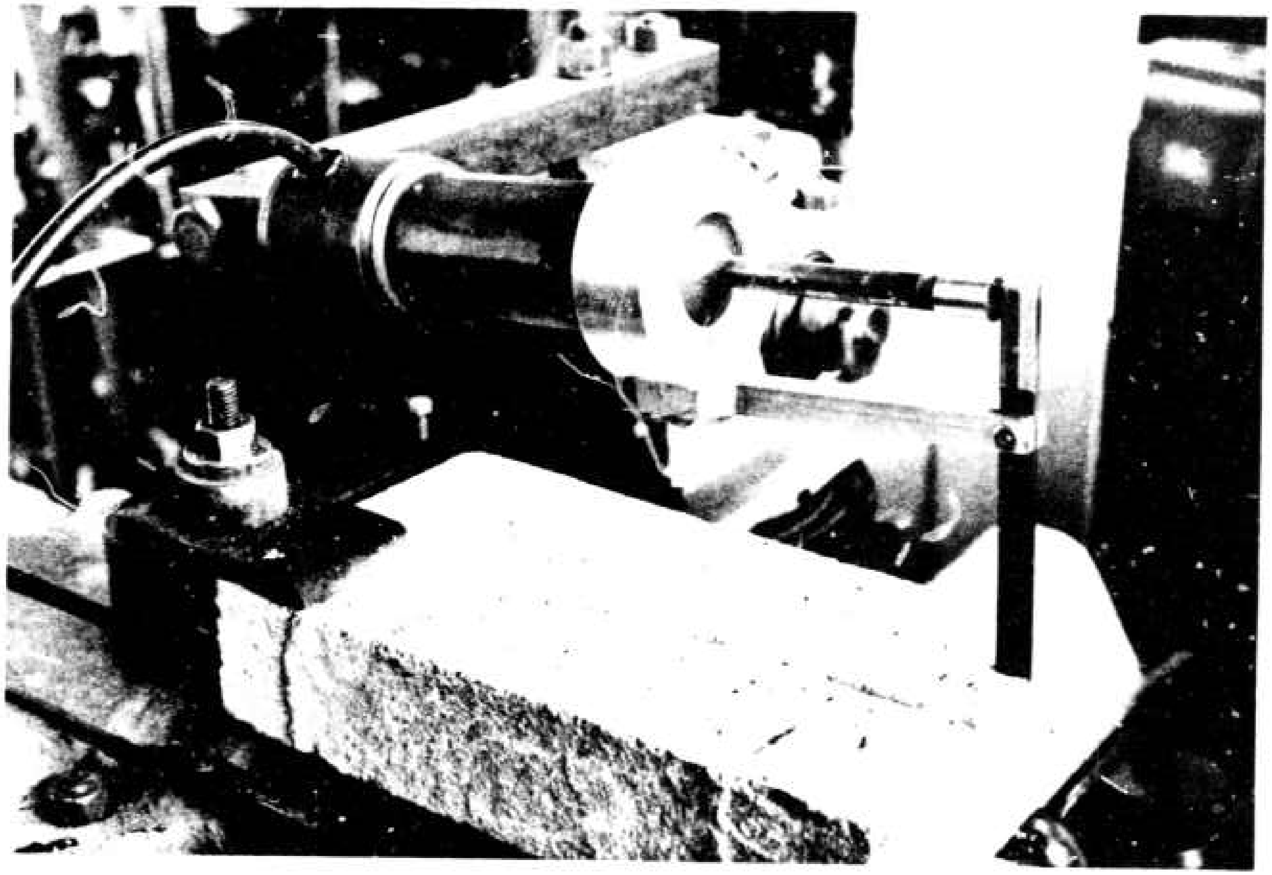

Fig. 1-1 Early configuration of P-7 transducer used for kerf cutting

In the application of sonic energy to layer cutting, three phases of development occurred. In the first, rather crude, manually-operated apparatus was used to study various principles of cutting. In the second phase, a moderately elaborate piece of apparatus was developed to carry out extensive layer cutting tests in Indiana limestone. In the final phase of work, layer cutting of hard rock was studied.

1-2 PRELIMINARY APPARATUS

The preliminary apparatus on which tests were made on the principles of layer cutting of rock by sonic impact means is shown in Fig. 1-2. In this view, a surplus machine shop grinder has been utilized to support and traverse the rock relative to the Model P-11 transducer* and its tool assembly. The block of limestone rock illustrated here is bolted down to the work surface of the grinder. The handwheels shown in the lower portion of the pictures are utilized to raise and lower the transducer assembly, and to traverse the assembly horizontally.

The small impact tool at the tip of the transducer is evident. A second tool configuration, detached from its holding fixture, is also being shown by the researcher in Fig. 1-2. The impact tool is supported by a simple pivot about two inches above the impact point. A cantilever, attached at the nodal location of the transducer, holds the pivot assembly fixed relative to the transducer. A closer view of the cutting apparatus is shown in Fig. 1-3, where a partially completed cut has been made. Note in the figures that the transducer is slightly inclined relative to the rock surface and that the line of transducer action is nearly direct into the cutting surface.

The tool is free to swing in an arc, with its motion limited at one extreme by a flat-faced contact with the transducer tip, and at the other extreme by impact with the rock. As the transducer is moved parallel to the rock face, the tool is pushed against the tip of the then excited transducer. The longitudinal vibration of the transducer tip applies a force-impulse to the rool during a short interval of contact time. This force-impulse sends the tool away from the transducer, moving in an arc about its pivot, and into impact with the rock surface. The kinetic energy of the tool is converted into work, breaking the rock surface. After the tool strikes the rock face, it rebounds toward the transducer tip, which is, of course, also moving slowly toward the tool due to the traverse motion of the assembly. The process of impact with the transducer and the rock is, therefore, repeated rapidly by the tool, and a stable impact-frequency develops.

---

*The P-11 transducer has been described in the final report on Contract H0210010.

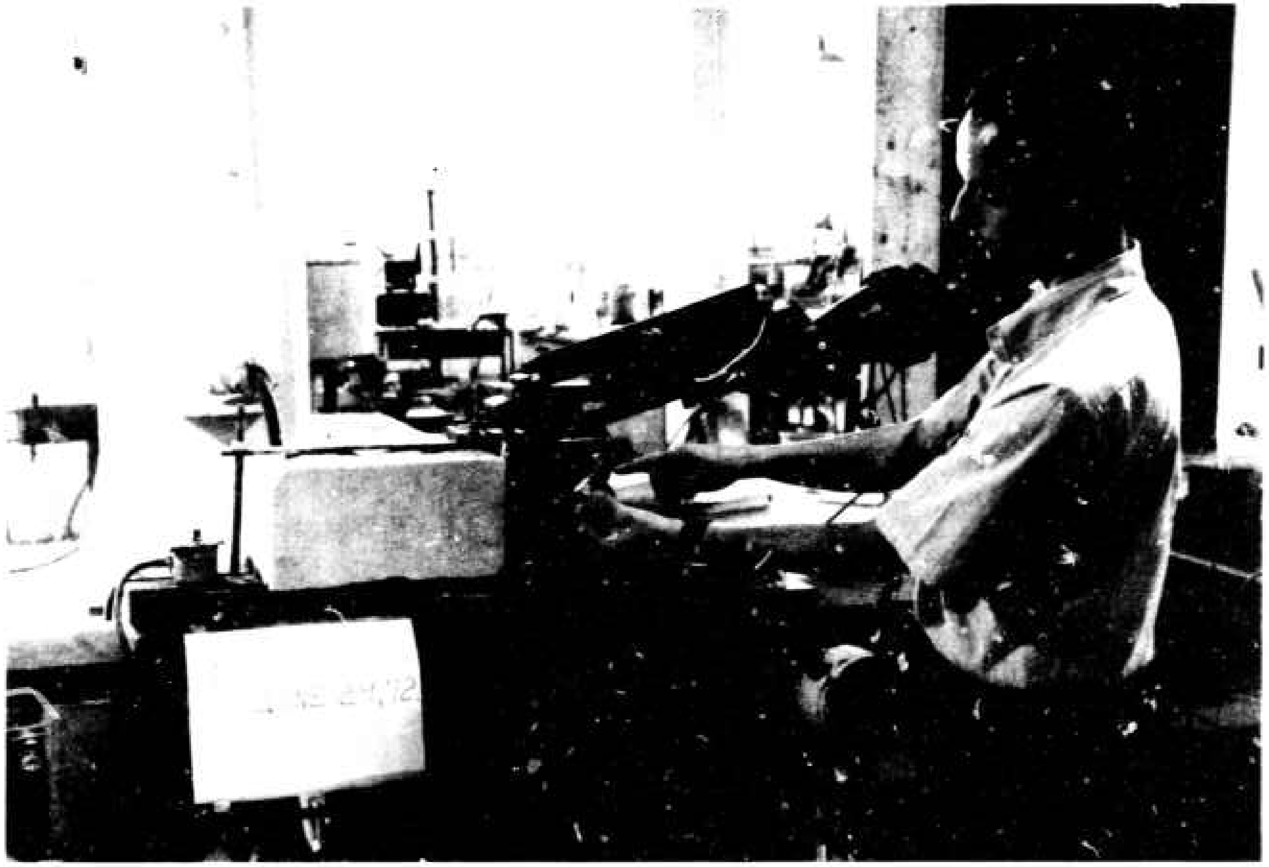

Fig. 1-2 Early layer cutting configuration using the P-11 transducer

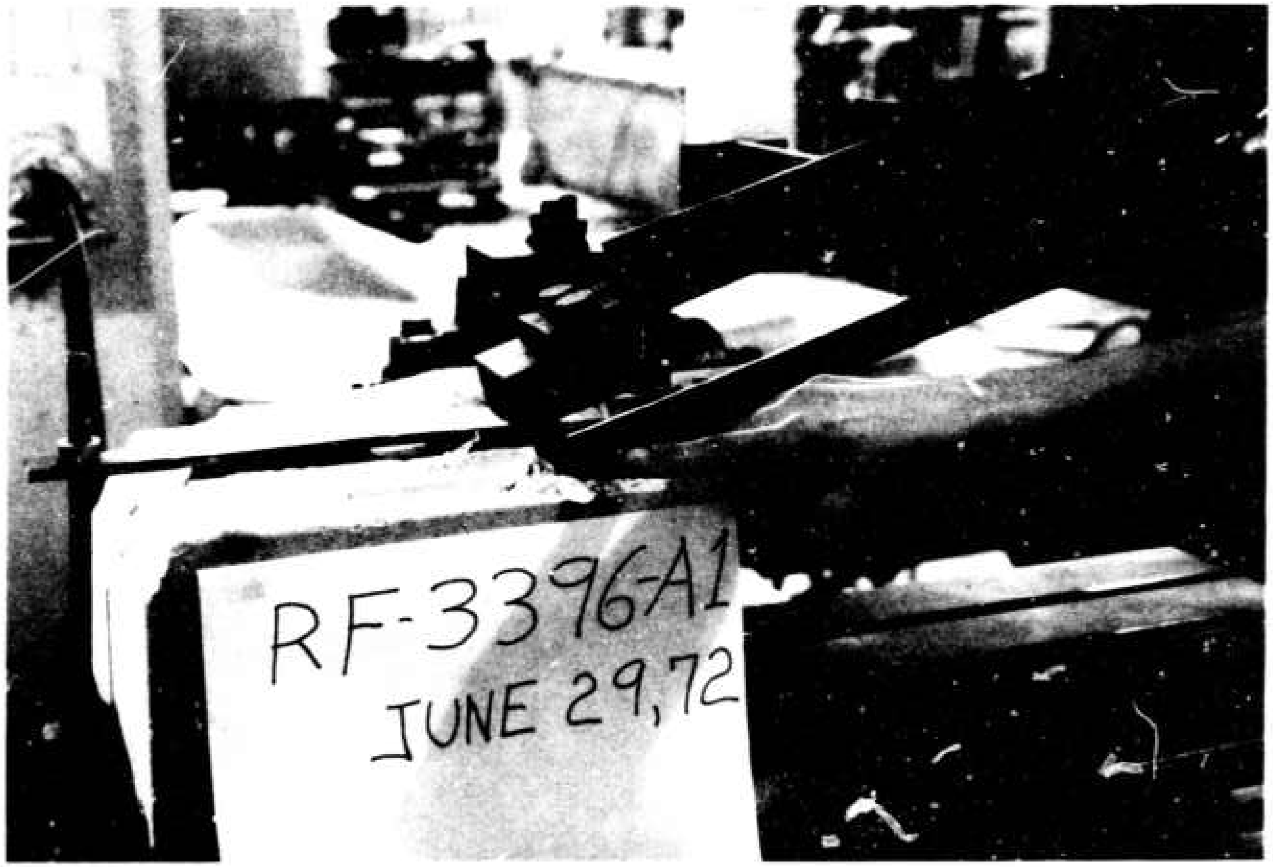
RF-3396-A1
JUNE 29,72

Fig. 1-3 View of the transmission line tip and the pivoted cutting tool of the early layer cutting apparatus

Several basic parameters controlling the layer cutting process were identified during work with the preliminary apparatus. The mass and geometry of the tools were, of course, parameters of the process, as they are for drilling or other impact coupling processes. The depth of cut and speed of traverse were parameters, as was the angle of inclination of the transducer relative to the rock face. The voltage to the transducer was a parameter. Finally, the material properties of the rock directly influenced the cutting process.

1-3 LAYER CUTTING APPARATUS

The design and assembly of a larger device for layer cutting of rock proceeded immediately after tests in the preliminary apparatus were completed. The resulting apparatus consists essentially of a large, welded, steel frame with a track of approximately eight feet in length, along which a carriage may be traversed. The carriage, on which is mounted the sonic transducer and cutting tool, is driven by a lead screw which is in turn chain driven by an adjustable-speed gear motor.

Figure 1-4 shows an overall view of the equipment, with frame, carriage, transducer, screw-drive and motor all shown. Means for supporting and clamping rock specimens also is shown. The welded steel frame is shown schematically in Fig. 1-5. A detail of the electric motor and chain drive is shown in Fig. 1-6. By varying the speed setting of the motor, as well as by interchanging gears, carriage traverse speeds from 0.25 to 4.75 inches per second could be attained. The speed calibration chart for the system is given in Fig. 1-7.

The mounting that holds the transducer at the nodal point and in turn attaches to the carriage is designed to allow the transducer to be aligned in any position from vertical to horizontal, in 10° increments. The angle adjustment points show on the carriage in Fig. 1-4 as the series of holes along a circular arc. Provisions for load cells were also incorporated in the carriage and show as the four short, vertical elements between the wheeled portion and transducer holding portion of the carriage in Fig. 1-4. However, actual force readings were not done during the project.

1-4 LAYER CUTTING IN INDIANA LIMESTONE

In carrying out tests of layer cutting in Indiana limestone, the previously mentioned parameters of tool mass and geometry, depth of cut, speed of traverse and transducer voltage and angle of attack were varied. Some of the dependent variables of the process included power input to the transducer and volume of rock removed, as well as such items as frequency of tool impact and forces developed in the supporting structure.

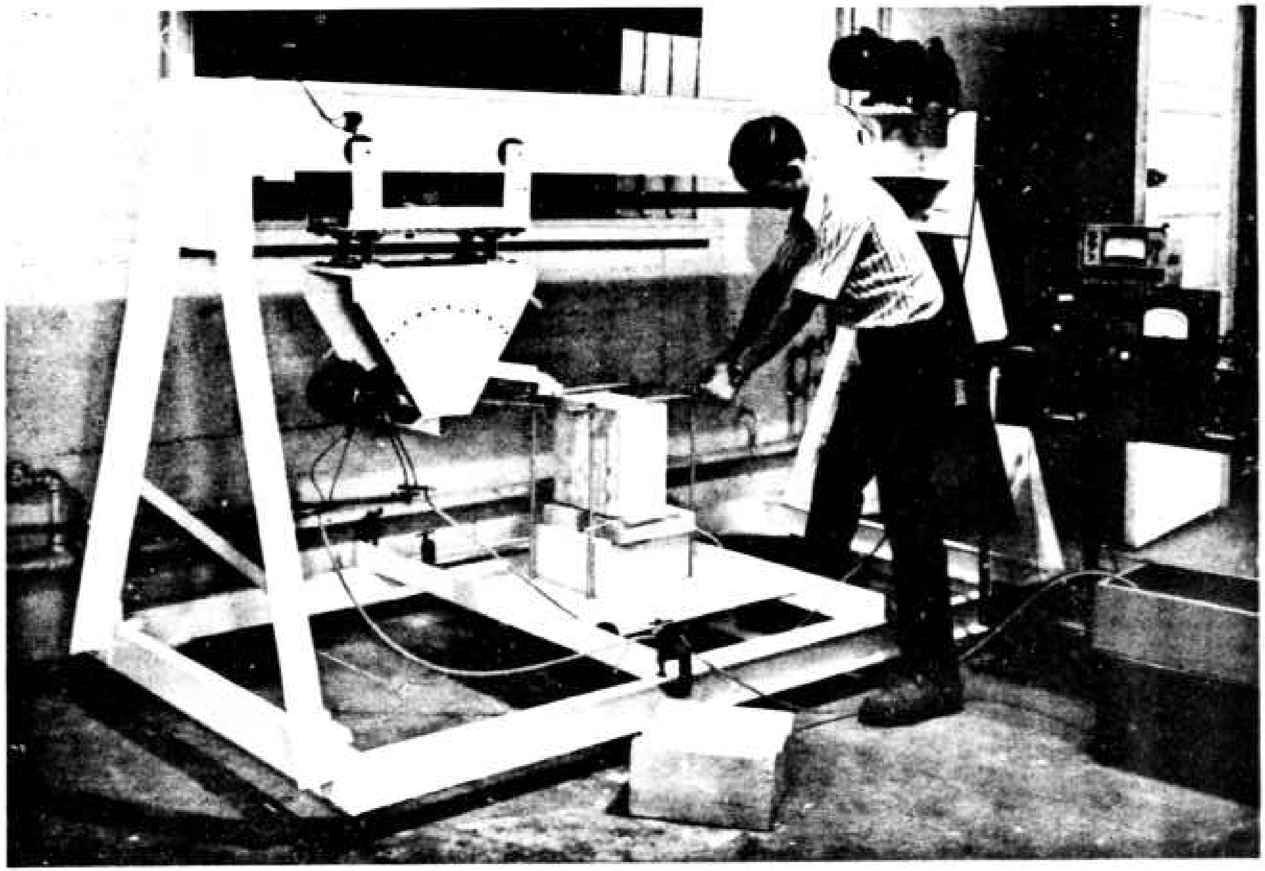

Fig. 1-4 Apparatus for sonic layer cutting of rock

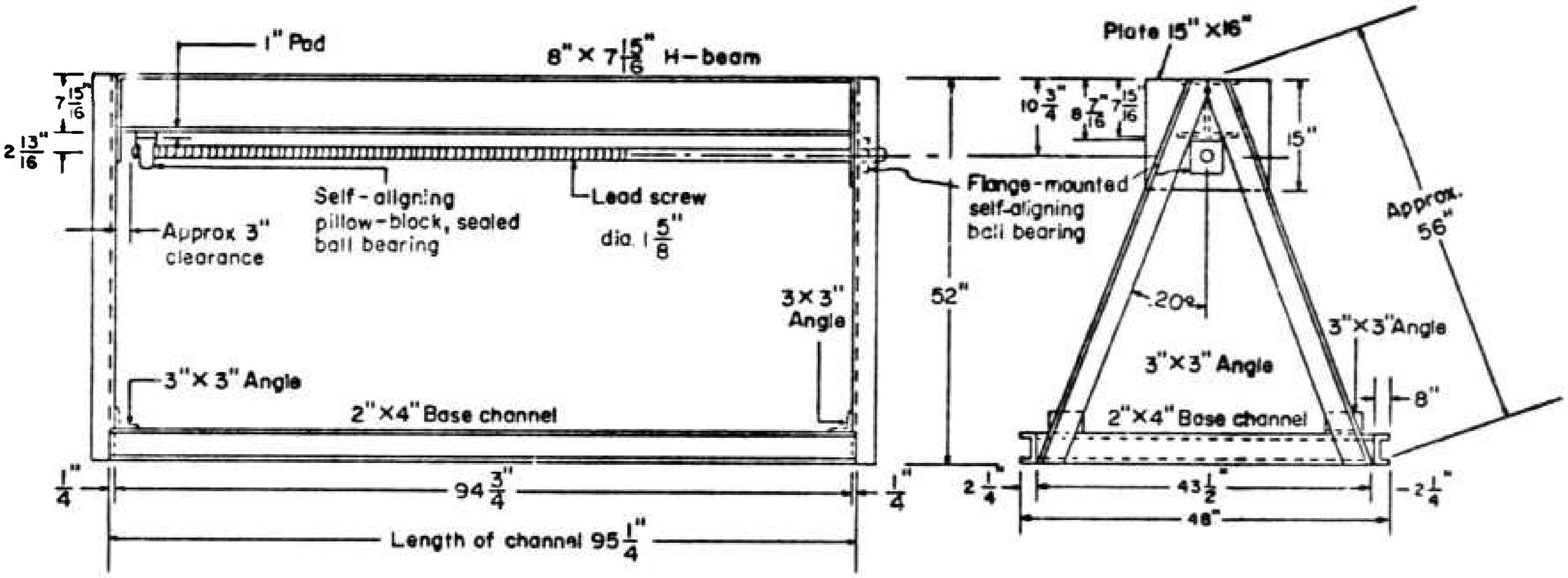
1" Pad
8" × 7 15/16" H-beam
7 15/16"
2 13/16"
Self-aligning pillow-block, sealed ball bearing
Lead screw dia. 1 5/8"
Approx 3" clearance
3 × 3" Angle
3" × 3" Angle
2" × 4" Base channel
1/4"
94 3/4"
1/4"
Length of channel 95 1/4"
52"
Plate 15" × 16"
10 3/4"
8 7/16"
7 15/16"
15"
Flange-mounted self-aligning ball bearing
Approx. 56"
20°
3" × 3" Angle
3" × 3" Angle
8"
2" × 4" Base channel
2 1/4
43 1/2"
2 1/4"
48"

Fig. 1-5 Welded steel frame and drive screw for large cutting apparatus

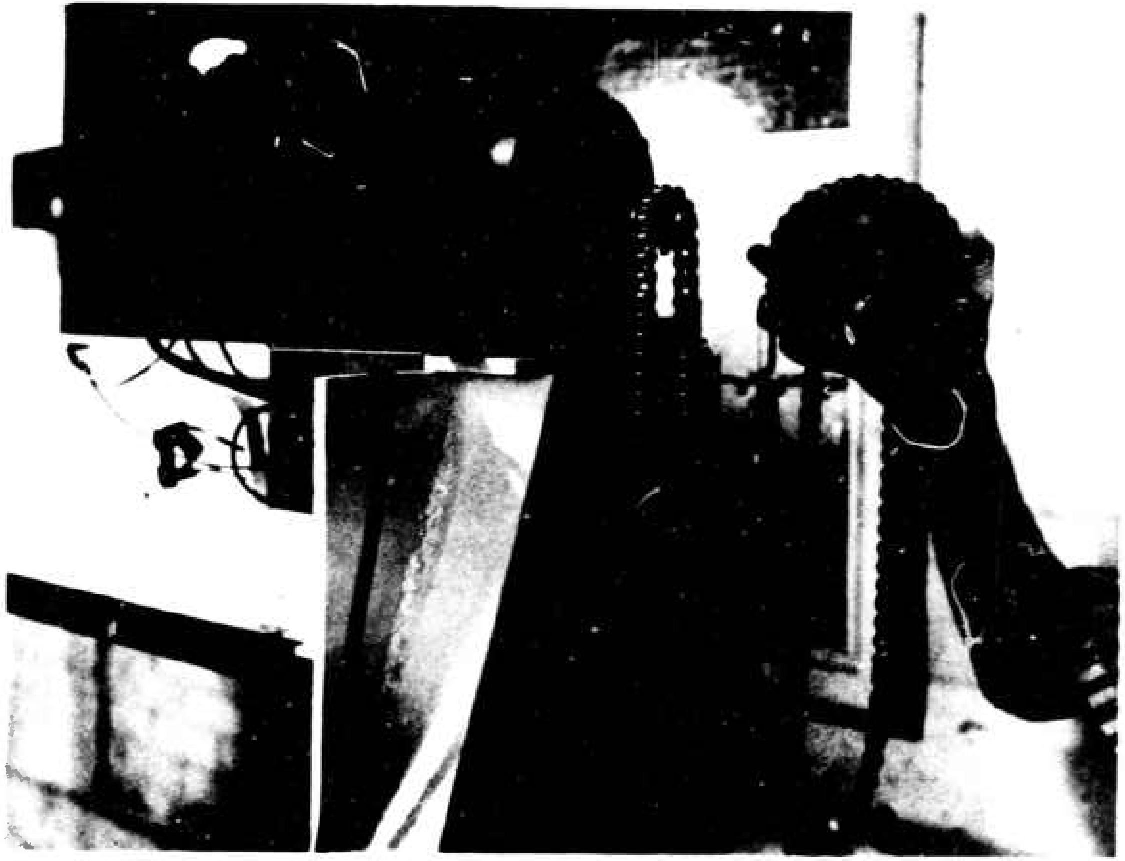

Fig. 1-6 Electric motor and chain drive for layer cutting apparatus

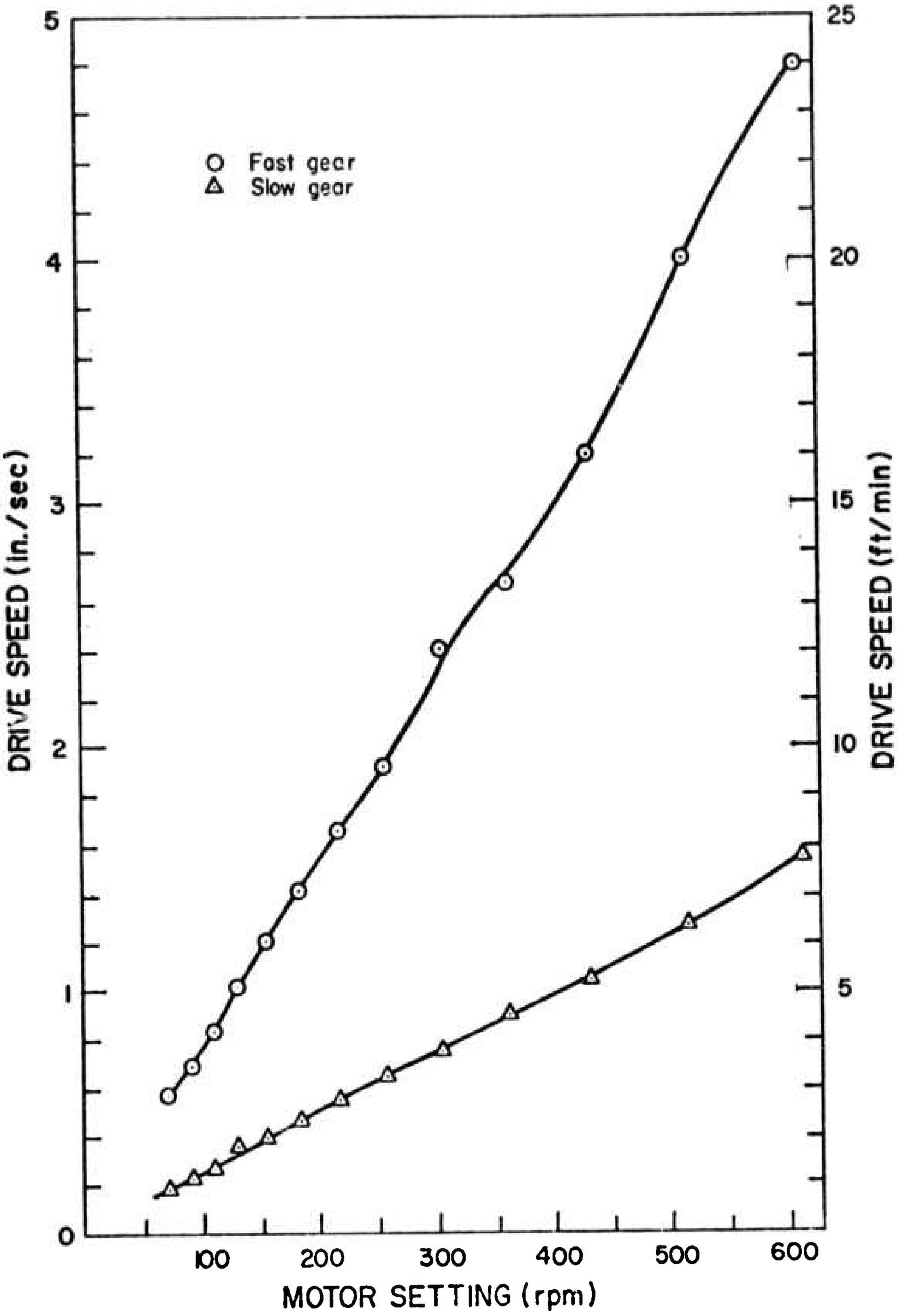

Fig. 1-7 Traverse speed versus motor and gear setting

In carrying out typical layer cutting tests, attention was given to the following items:

(1) Transducer Resonant Frequency. In advance of any series of test runs utilizing a fixed-frequency power supply with a sonic transducer, it is desirable to first establish the initial resonant frequency of the transducer. In this work, the initial resonant frequency of the transducer was measured at no-load on the Dranetz impedance-admittance meter at the point of minimum impedance while a variable frequency, 3 volts excitation level is applied to the transducer. In actual operation the no-load resonant frequency of the P-11 transducer is found to vary inversely with the applied terminal voltage as previously described.*

Consequently, it was necessary to tune the transducer to a higher frequency than the power supply frequency, to account for the frequency drop due to high voltage. In a typical test run, the P-11 transducer had an initial no-load resonant frequency of 10,140 Hz, the power supply delivered a fixed frequency of 10,054 Hz and the excitation level measured at the transducer terminals under load was about 1000 volts.

(2) Speed of Travel. In the tests using the manual traverse mechanism, it was not possible to measure speed of traverse directly. Measurements were, therefore, made of the time of traverse from one face of the limestone block to the other face. On the other hand, tests using the large console apparatus were made with predetermined speed settings. However, no estimate of the possible speed reduction of the motor due to load was included.

(3) Depth of Cut. In initially establishing the depth of cut to be made, measurements were made of the interference between the tool and the rock face. After the cut was made, further measurements were taken of the depth to which rock was actually removed. The difference between these measurements gave an indication of the relative stiffness of the structure. The depth measurements of the cut in the rock were recorded for calculating the volume of rock removed.

(4) Indication of Overload. It was not possible during these actual test runs to monitor the frequency of impact or to measure the static or average forces required to drive the sonically excited tool across the face of the limestone rock. As mentioned in section 1-1 the frequency of impact is inversely proportional to the static or average force applied to draw the transducer and its tool across the rock face. A very high frequency of impact may indicate the process is fully loaded.

---

*Annual Technical Report on previous Contract H0210010, "Fundamental Studies in the Use of Sonic Power for Rock Cutting," December, 1971.

In sonic impact rock cutting, an excessive traverse velocity or an excessive depth of cut may be defined as one in which the transducer cannot maintain impact-coupling with the tool, but instead becomes coupled solidly and continuously with it. Therefore, the point at which the transducer fails to maintain the impact mode of operation is noted during each test run as a part of the test data. This point corresponds to, and is analogous to, a point in a motor driven process at which the drive motor stalls. To all intents and purposes, the process under investigation ceases to function at this juncture.

(5) Volume of Rock Removed. The volume of rock removed was based on the dimensions of the groove formed in a flat surface of the rock. The cross section of this groove is generally trapezoidal in shape. The width of the narrow base of the trapezoid (w) corresponds to the width of the impact tool. The height of the trapezoid (h) corresponds to the depth of the cut in the rock by the impact tool. The width of the cut at the surface of the rock (v) varies rather widely where large chips are removed. It is in the need to estimate dimension v which results in a reduction of the accuracy of volume measurement to ± 5%.

The area (A) of the trapezoidal section of the cut is calculated from these dimensions; A equals one-half the sum (w + v) multiplied by the height (h). The volume of rock removed is then calculated by multiplying the area A by the effective length of the cut (ℓ). The length of the cut must be estimated due to edge effects. The impact tool tends to break out fairly large portions of the rock, both at the beginning and at the end of a block it is grooving. In estimating volume of rock removed, the break-out volume has been ignored.

The accuracy of volume estimates, based on these measurements has been found to be within 5% of the actual volume of rock removed, measured by displacement means.

(6) Angle of Attack and Face Angle. The angle of attack of the transducer may be defined as the inclination of the transducer's centerline in reference to the horizontal line of the work surface. By increasing this angle it is possible to increase the downward component of externally applied static force. The increased angle of attack has been assumed to be required for harder rock.

It must be recalled that the impact tool position is fixed to the transducer-carriage assembly. The angle between the face of the cutting tool and the rock is therefore not only dependent on the tool design, but on the angle of attack of the overall transducer. Thus, if the angle of attack is varied, generally the tool must be redesigned to account for the variation in face angle relative to the rock.

1-5 RESULTS FOR LIMESTONE

Various tool designs were utilized in the limestone cutting work. A typical impact tool is detailed in Fig. 1-8. The drawing illustrates the 70° face angle of the tool and the carbide insert in the flat cutting face of the tool. The cutting face of this 3/4" wide tool is held perpendicular to a horizontal work surface when the transducer is inclined at 20° from the horizontal. With the transducer at a 30° tilt, the tool face is inclined at about 80° from the horizontal work surface. Other tool designs can be used to modify the relationship between the transducer position, or its attack angle, and the angle which the tool face makes with the work surface.

Figure 1-9 illustrates a second generation tool design in which the impact face of the tool has been modified into a plow-shape with a 130° included angle between the faces of the tool. The cutting angle of the tool is approximately the same as in the flat-faced tool in Fig. 1-8, although the tool width is reduced to 1/2". This narrower tool should allow faster cutting speeds with the same rock, or perhaps cutting of harder rock at the same traverse speed as the 3/4" flat-faced tool. The cutting face of this tool is held perpendicular to the work surface with the transducer inclined at 15° from the horizontal.

(A) Results from Preliminary Apparatus

Figure 1-10 illustrates the first data obtained on layer cutting of limestone. The results were obtained using the manually traversed apparatus of Fig. 1-2. The data presents the rate of rock removal (in.^{3}/sec) versus cutting depth. Because a manual traverse was used, velocity determinations were only approximate.

Figure 1-11 presents the preceding data in a different form, showing the specific energy of rock removal versus cutting depth. The major point of interest is the existence of a pronounced minimum at about 0.5-inch cutting depth.

(B) Results from Large Cutting Apparatus

An illustration of the cutting action in limestone during a typical test is shown in Fig. 1-12. Fairly large rock fragments are shown being dislodged. A large breakout area at the end of the block often existed and was discounted in all data reduction.

Figures 1-13 and 1-14 present data on volume of rock removal versus cutting speed for two different depths of cut (1/2" and 1/4"). The volume of excavation shown on the ordinate of Fig. 1-13 is for a 6" traverse distance in limestone with a 3/4" wide tool. The angle θ is the attack angle of the transducer, that is, its angle of inclination from the horizontal. Note that dotted lines indicate the point at which speed of travel exceeded the level at which impact cutting was possible.

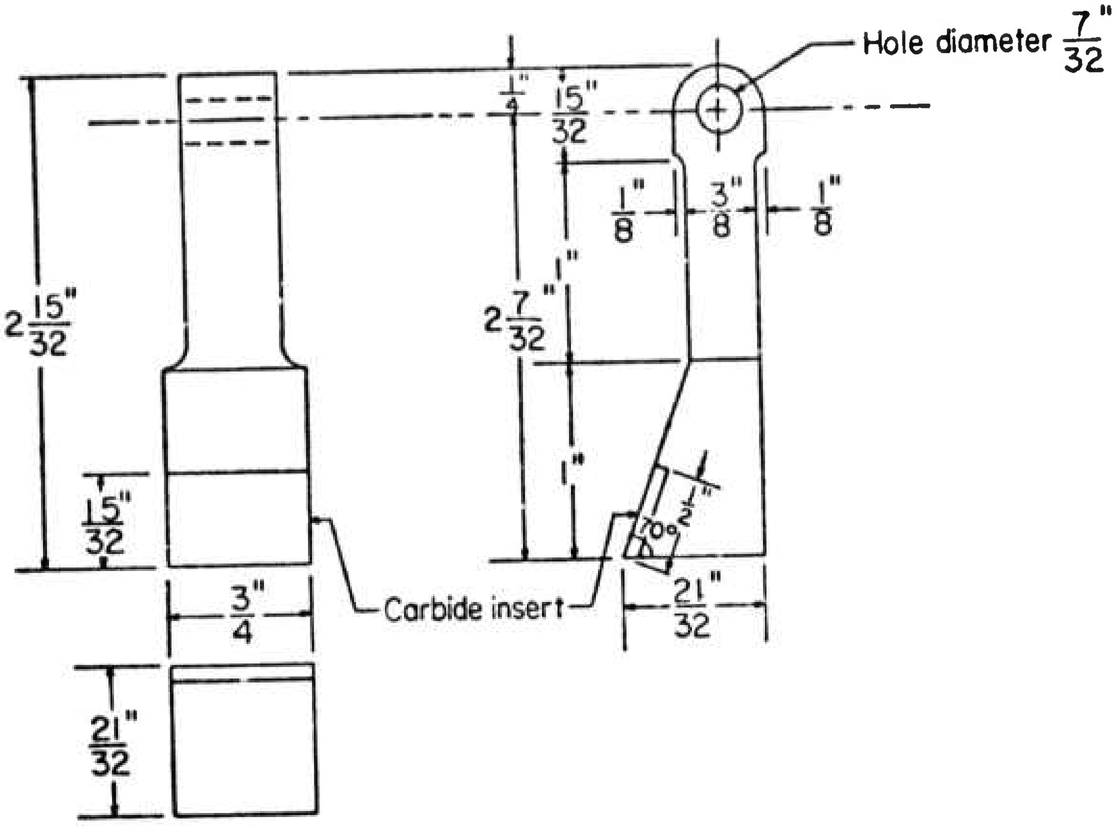
Hole diameter 7"/32
1"/4
15"/32
1"/8
3"/8
1"/8
1"
2 7"/32
1"
1/2"
70°
21"/32
Carbide insert
2 15"/32
15"/32
3"/4
21"/32

Fig. 1-8 Flat-faced cutting tool

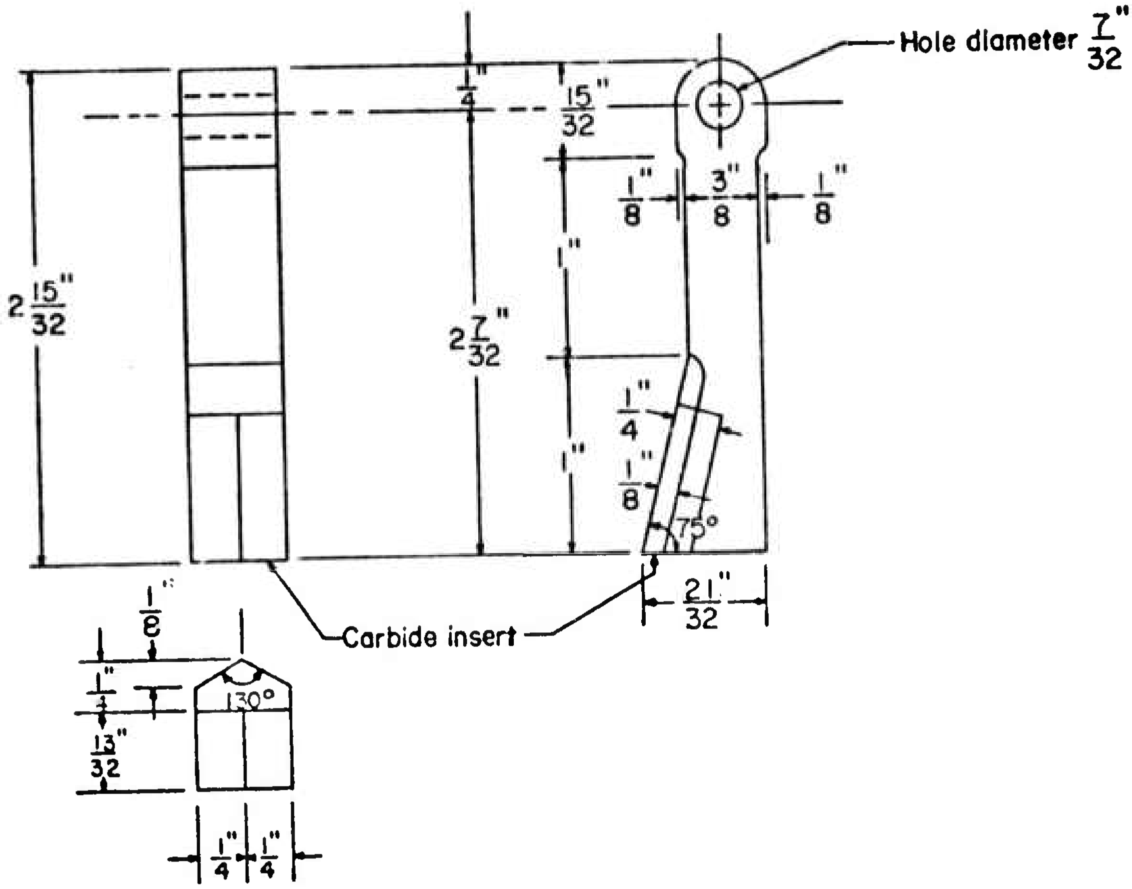
Hole diameter 7"/32
1"/4
15"/32
1"/8
3"/8
1"/8
1"
2 7"/32
2 15"/32
1"/4
1"/8
1"
75°
21"/32
Carbide insert
1"/8
1"/4
130°
13"/32
1"/4
1"/4

Fig. 1-9 Plow-shaped cutting tool

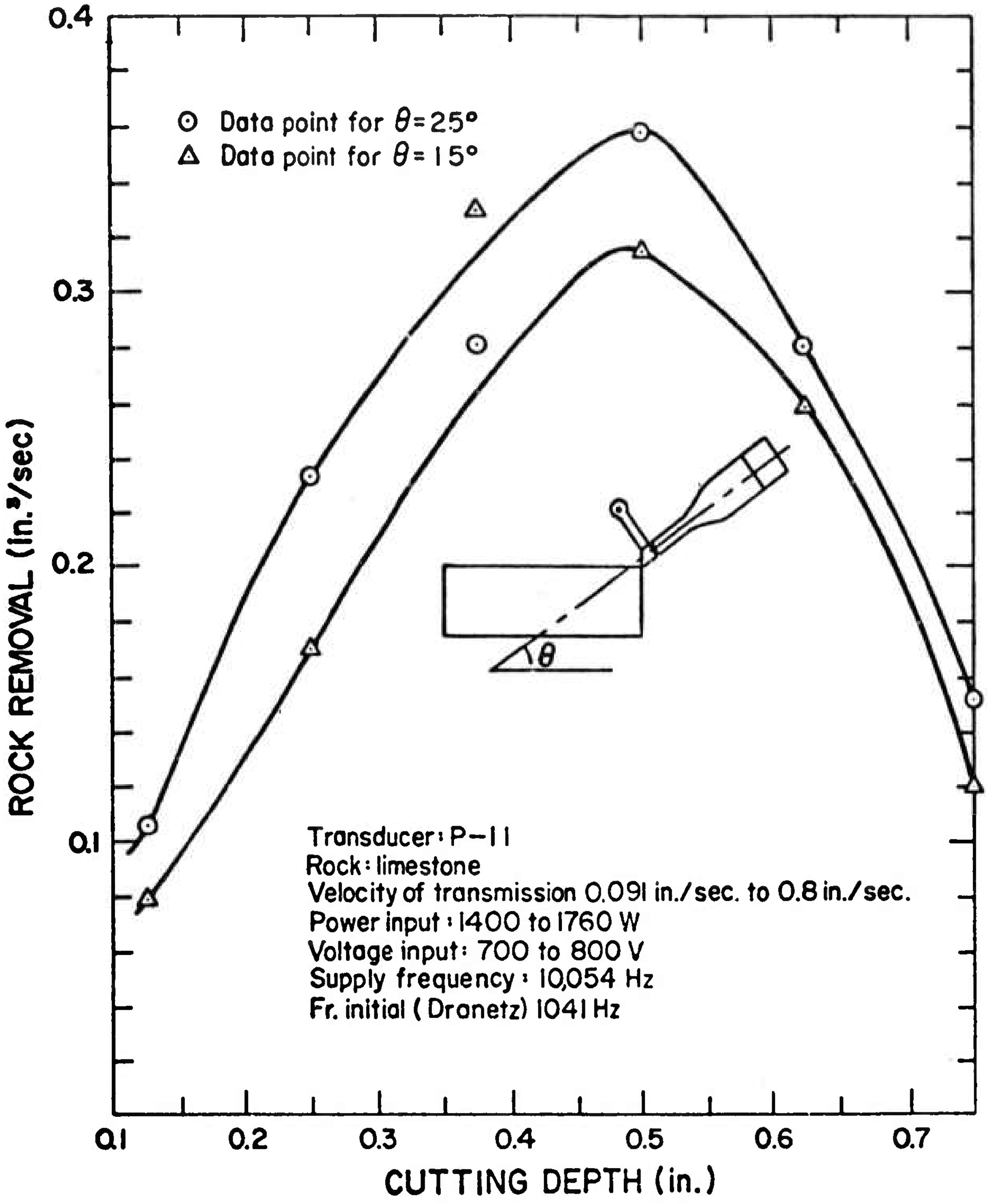

Fig. 1-10 Rate of rock removal for early apparatus

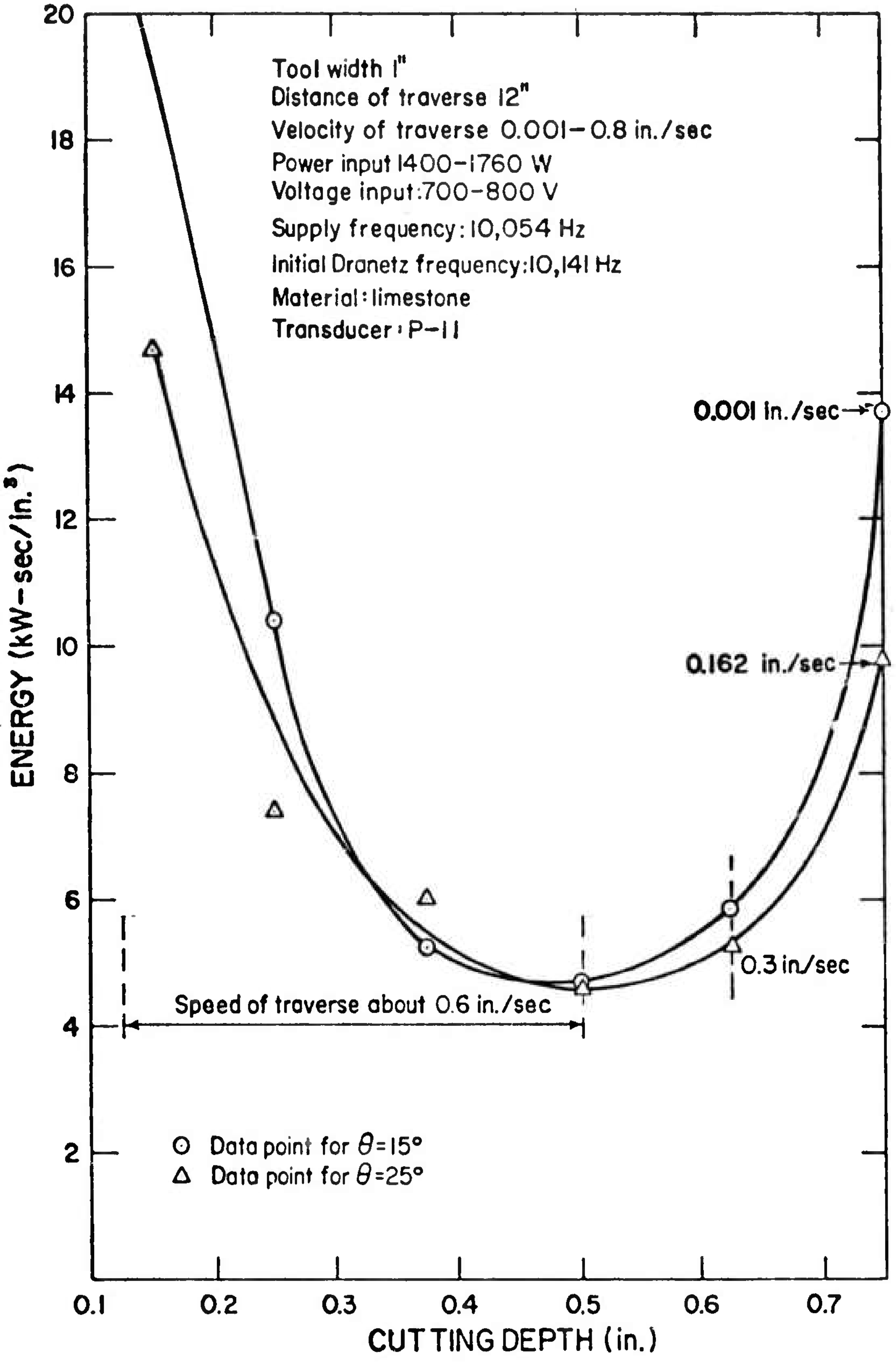

Fig. 1-11 Specific energy of rock removal versus depth of cut for early apparatus

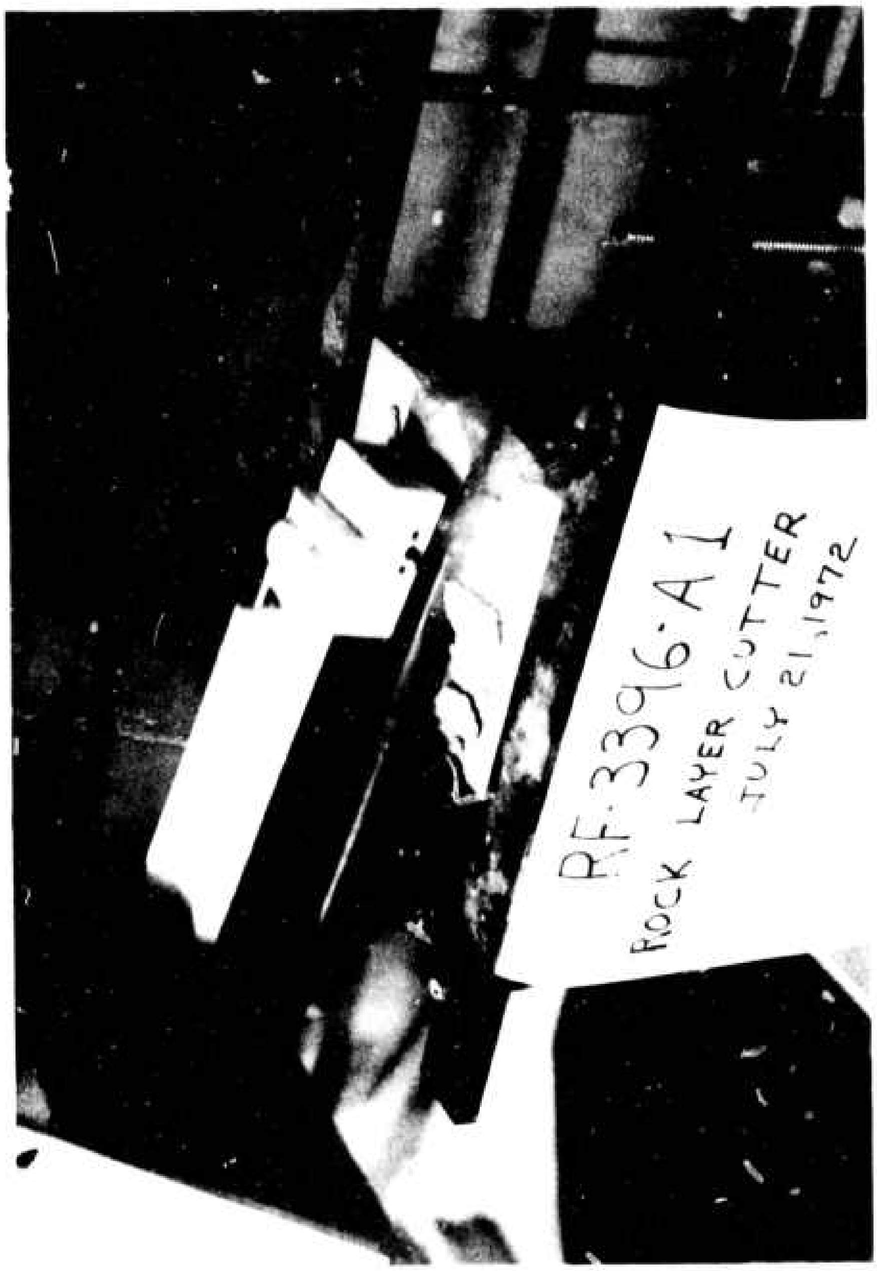
RF-3396-A1
ROCK LAYER CUTTER
JULY 21, 1972

Fig. 1-12 Layer cutting action on large apparatus

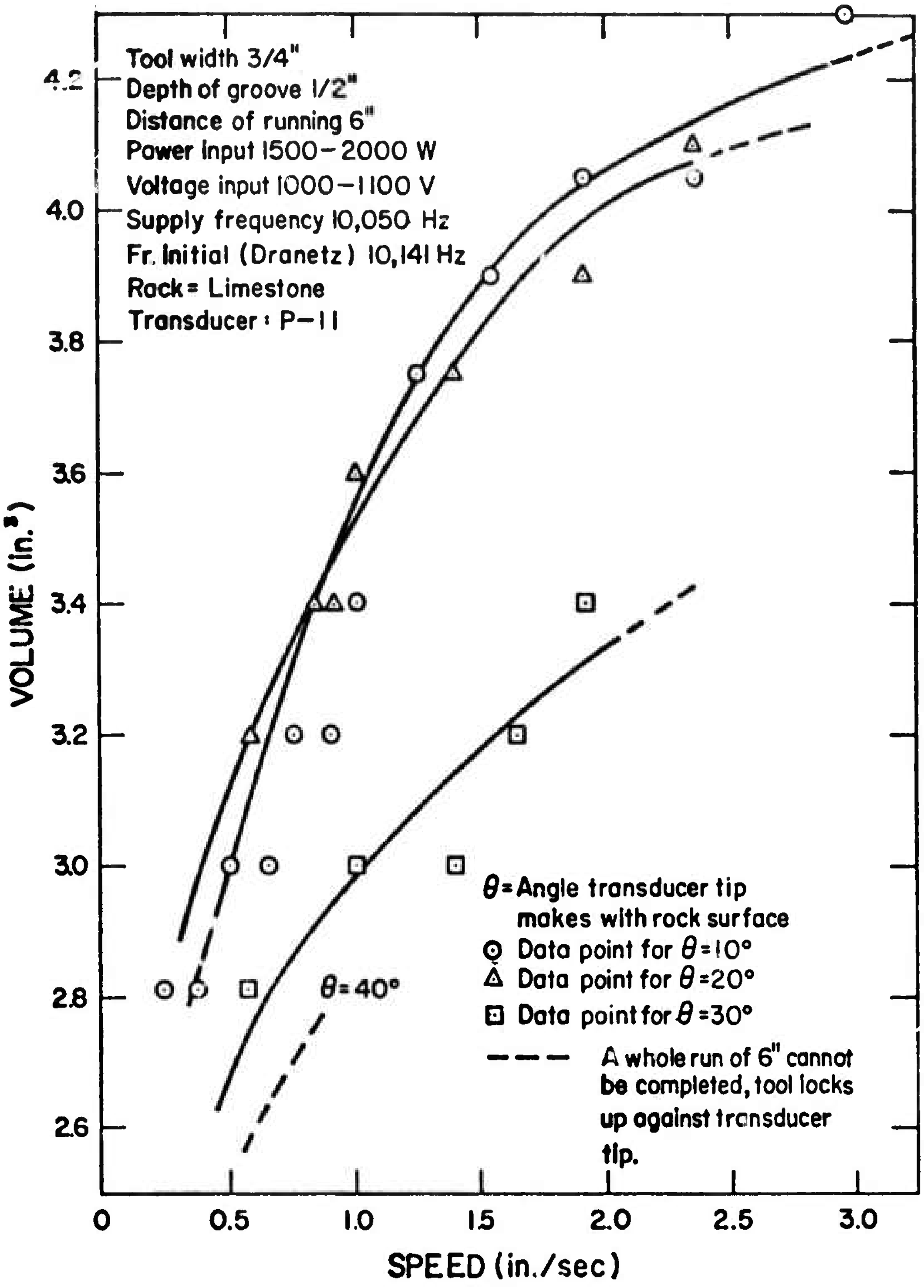

Fig. 1-13 Volume of rock removal versus cutting speed for a 0. 5 inch depth of cut

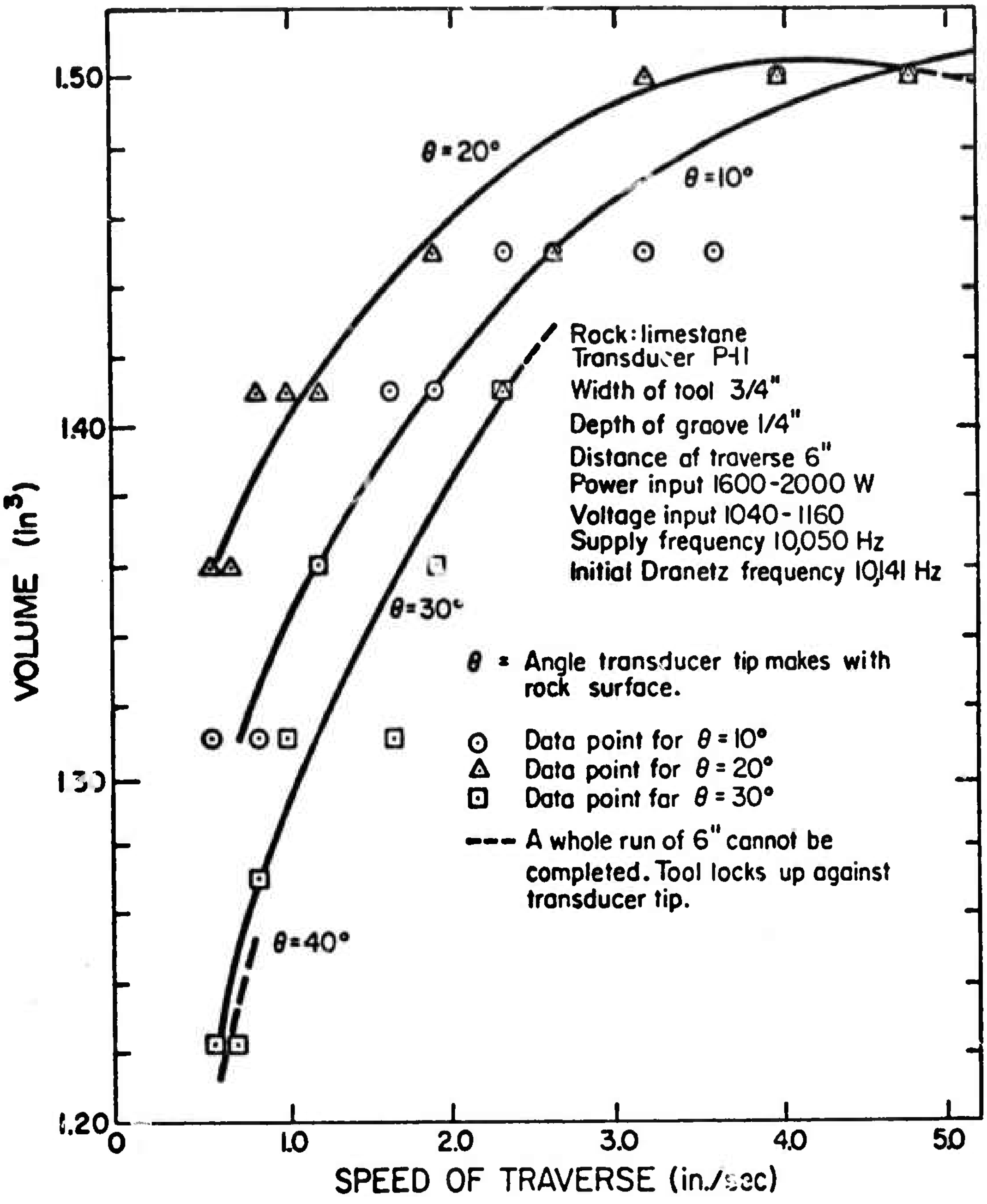

Fig. 1-14 Volume of rock removal versus cutting speed for a 0.25 inch depth of cut

The dotted lines indicate possible extrapolation into an area of overload on the transducer. Figure 1-13 indicates that the impact mode of operation could not be maintained with a 1/2" cut depth, and a 20° angle of attack, for more than 2.25 in./sec traverse speed. At speeds higher than this, the tool maintained constant contact with the transducer, impact cutting ceased, the transducer detuned, its power input dropped and sonic cutting was brought to a halt.

Figure 1-14 shows that with the same tool and half the depth of cut, the velocity of traverse can be almost doubled when compared to Fig. 1-13. The point at which impact cutting ceases with a 20° attack angle and a 1/4" depth of cut is 4.75 in./sec compared to 2.25 in./sec with the 1/2" cut depth. It is to be noted in Figs. 1-13 and 1-14 that the volume of rock removal tends to increase for a shallower angle of attack (exception: the $\theta = 10°$, $20°$ curves of Fig. 1-14).

In Figs. 1-15 and 1-16, data on the specific energy of rock removal versus cutting speed is given. The data is for 1/2" (Fig. 1-15) and 1/4" (Fig. 1-16) depths of cut and for various angles of attack. It is first particularly significant to note the rapid decrease in specific energy requirements for increasing cutting speed for both depths of cut. It is also to be noted that the specific energy of removal is rather insensitive to the attack angle.

It is of particular interest that the specific energy curves are "leveling off" at the higher cutting speeds. Although a clear, lower level asympote does not exist in either Fig. 1-15 or 1-16, it does not appear that specific energies of much less than 500 W-sec/in.^{3} would occur for the 1/2-inch cutting depth or less than 1000 W-sec/in.^{3} for the 1/4-inch cutting depth.

Figure 1-17 presents some of the preceding data in terms of specific energy for various traverse speeds for a fixed angle of attack of 10°. The specific energy is thus seen to decrease with increases in both traverse speed and with depth of cut. Both of these are independent variables and each tends to increase the loading on the transducer. The specific energy, therefore, is improved as the transducer's load increases.

1-6 LAYER CUTTING IN GRANITE

The ultimate objective of the work on rock cutting was to effectively penetrate hard rock, such as Barre Granite, Dresser Basalt and Sioux Quartzite. After some success in cutting limestone, the effort was made to transition the same cutting techniques to hard rock. All work reported in the following was carried out on granite specimens obtained locally.

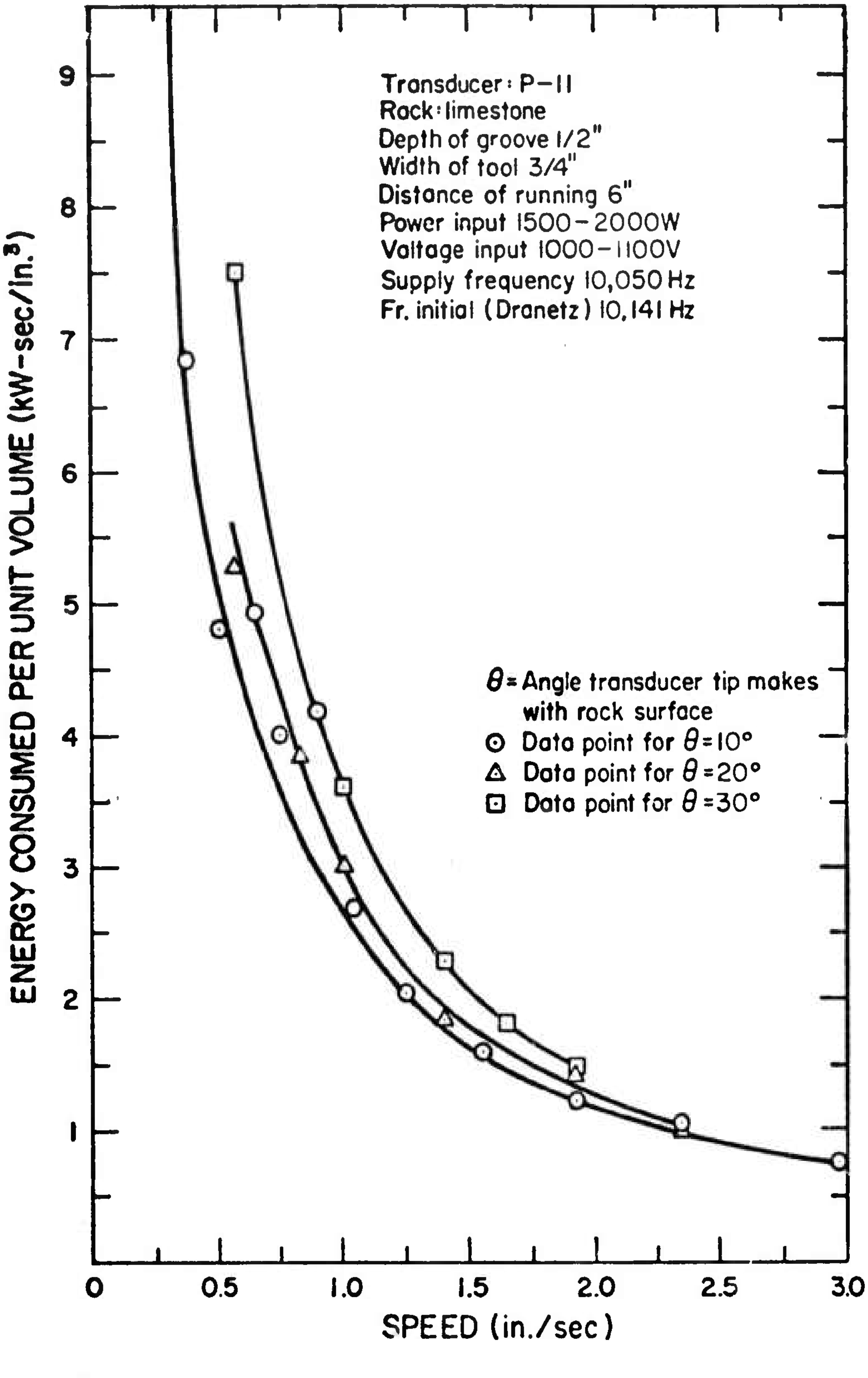

Fig. 1-15 Specific energy of rock removal versus cutting speed for 0.5 inch cutting depth

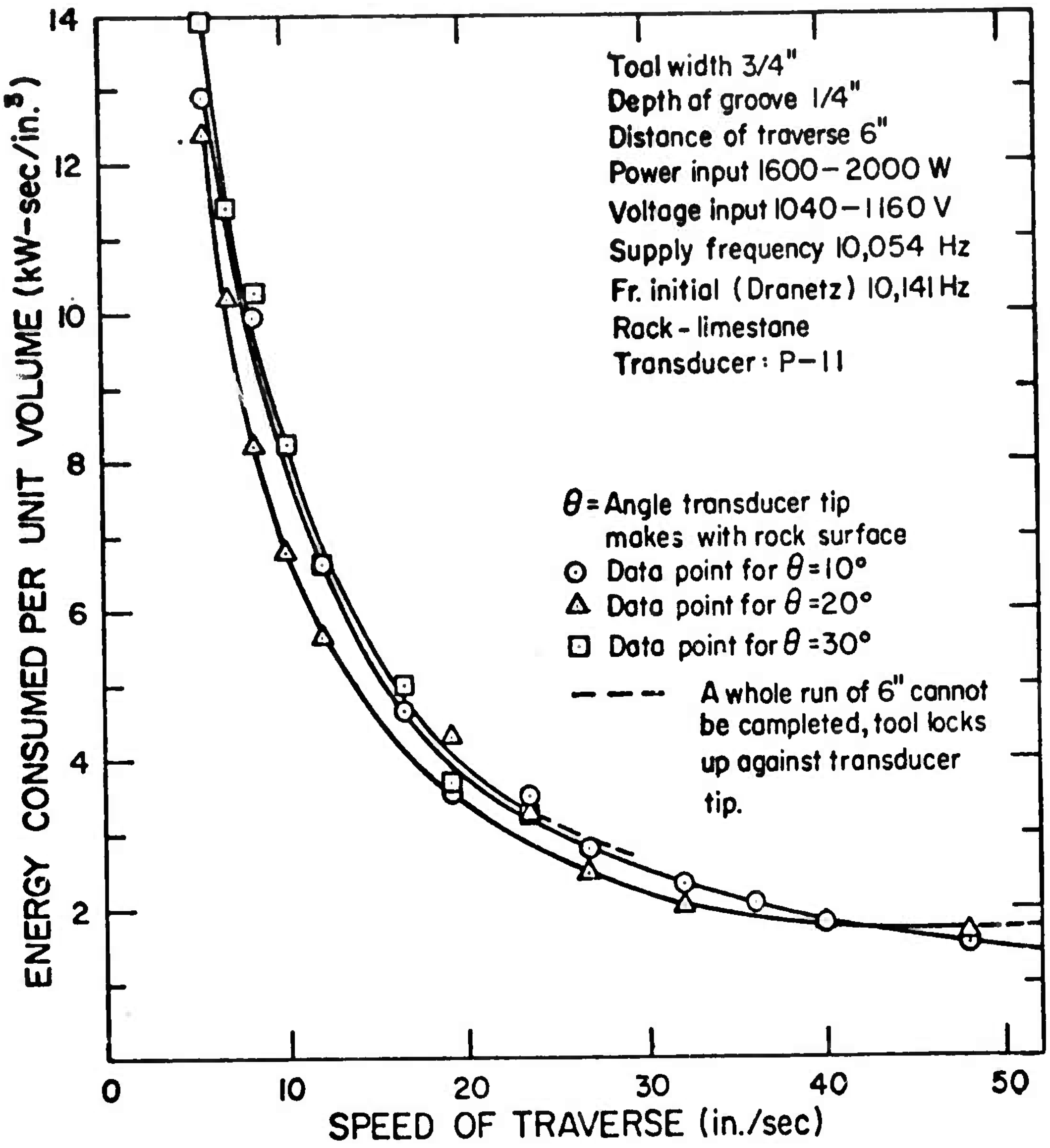

Fig. 1-16 Specific energy of rock removal versus cutting speed for 0.25 inch cutting depth

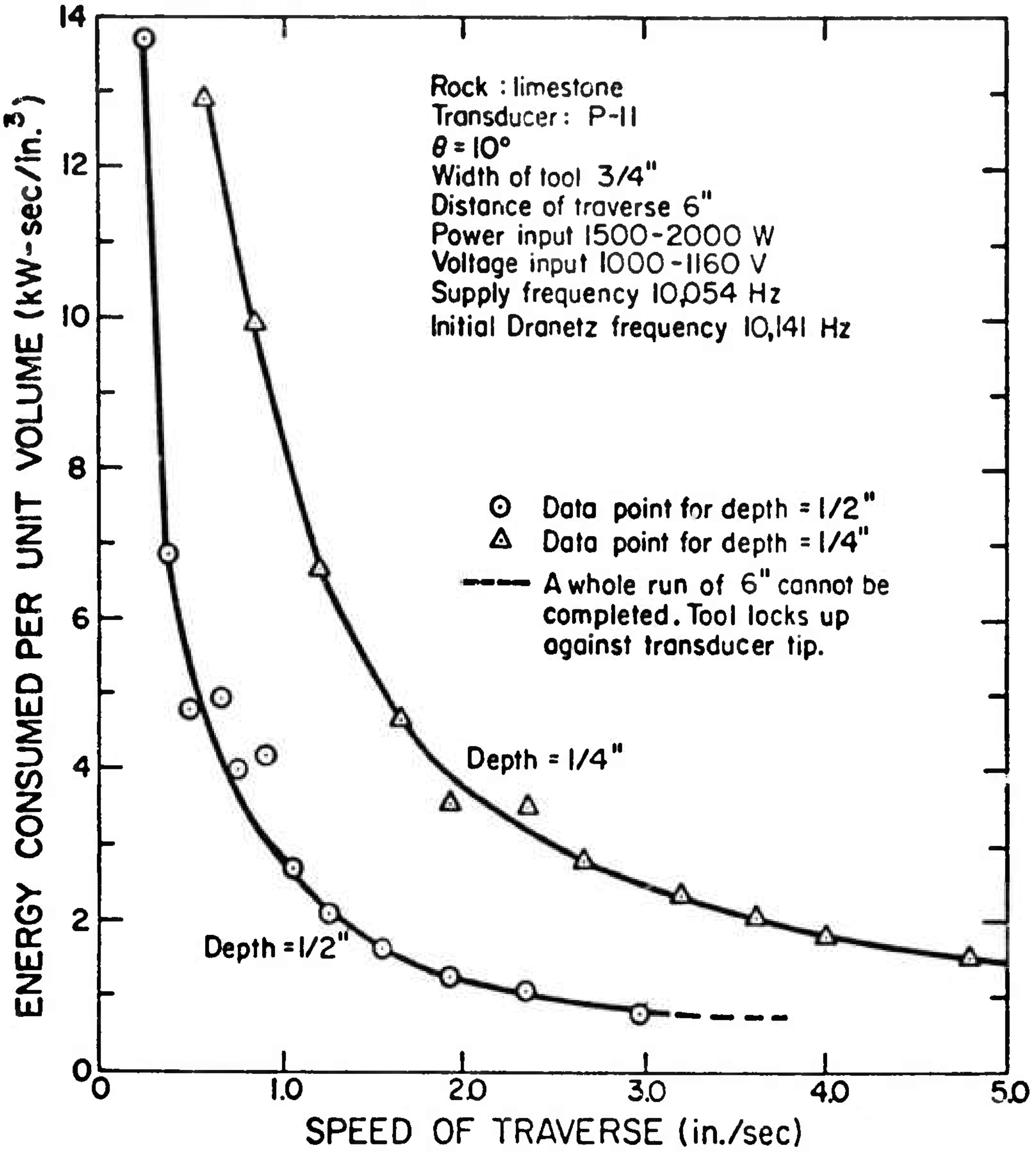

Fig. 1-17 Specific energy of removal versus cutting speed for two depths of cut (attack angle at 10°)

(A) General Difficulties Encountered

Difficulties were immediately encountered in attempting to cut hard rock; the tools and operating conditions sufficient to penetrate limestone were simply not adequate for cutting granite. It was found, for example, that cutting depths of 1/2-inch were not possible. Nearly all subsequent work was restricted to 1/16- to 3/16-inch attempted depths of cut. Secondly, the previous voltage level applied to the transducer of 1200 volts was inadequate. All reported tests, therefore, were run at 2500 volts, which was close to the maximum voltage rating of the transducer. Finally, traverse speeds of several inches per second, possible in limestone, were not possible in granite. Speeds of approximately 1 in./sec were used on most tests, with higher speeds being attained only near the end of the research work.

(B) Attack Angle

Shallow attack angles of 10 to 20° were found most successful in limestone. However, it was found that in granite shallow attack angles generally did not yield satisfactory cutting. What usually occurred was that the cutting tool would "ride up" on the rock. That is, instead of maintaining a given depth of cut, the cut depth would diminish until the tool was skidding along the rock surface.

The fact that the tool was able to ride up was a result of some elasticity and backlash in the system. The cantilever tool support was the major source of elastic deformation. Some slight looseness between the wheels of the carriage and the track was the major source of system backlash.

One approach to the ride up problem was merely to increase the depth of cut beyond the deformation-backlash range of the system. A depth of 1/2-inch was sufficient for this. However, as previously indicated, the transducer system was generally incapable of penetrating the granite at these depths.

The approach generally used was to increase the angle of attack from 30 to 40°. This increased somewhat the downward cutting action of the tool and thus tended to maintain the depth of cut. Probably equally important, it decreased the bending on the cantilevered tool support arm and thus reduced the elastic deformation of the system.

Additionally, stiffening was added to the tool support arm. Shims were placed between the carriage wheels and the track to reduce system backlash. Even with these modifications and the change in attack angle, ride up of the tool continued to occur occasionally.

A last, more or less impromptu, measure taken near the end of work was to manually force the tool downward by pressing against the cantilever tool support fixture. This, in conjunction with the other measures taken enabled fairly consistent cuts to be made in granite near the end of the work period.

(C) Tool Designs

Cutting tool widths, 3/4-inch to 1 inch, were used in limestone. In granite, tool widths were decreased to 1/2-inch to increase the contact stress against the rock. Initial tests were run using the plow-shaped tool previously shown in Fig. 1-9. With this tool, it was found that the carbide tip was repeatedly fractured during cutting. Sharp corners were broken away. Fractures through the carbide near the interface between steel and carbide were noted. Finally, fractures along the narrow neck of the tool occurred. Some of these failures are shown in Fig. 1-22.

One of the tool redesigns was a heavier, plow-shaped tool, shown in Fig. 1-18. It is to be noted that the neck region of the tool is considerably thickened over that of Fig. 1-9. Additionally, it was felt that a more massive tool would increase the energy transfer during the impact coupling process.

Another design was the saw-edged or stepped tool, shown in Fig. 1-19. The idea was to modify the plow tool to obtain a stepped cutting action, with the cutting steps on the order of the cutting depth of a single edged tool. Accordingly, two 1/8-inch steps were placed in the tool.

A chisel-shaped tool, shown in Fig. 1-20 was also tested. This tool used a slightly more complicated pivoting action than the simple pivots of the previous tools. In addition, it had an even narrower cutting edge (1/4"). During test, it was found that the looseness of the pivot arrangement caused the tool to ride up quite easily.

A two-piece round impact tool was designed, as shown in Fig. 1-21. The cutting tool itself had a rounded transducer impact point to improve energy transfer to the tool during impact coupling. The cutting edge of the tool had no particularly new design features. The second part of the tool was the holder, designed to pivot in the manner of earlier tool designs and to rigidly hold the tool. The overall intent of this design was to enable a number of easily replaceable tool designs to be tested. In operation, it was generally found that the tool could not be rigidly retained in the holder during impact action.

Several of the tool configurations are shown in Fig. 1-22. Mainly, the figure depicts some of the fractures and failures that occurred in the tools. Thus, carbide inserts are seen to be fractured or missing in two of the tools. A fracture across the neck of one of the tools also is evident. A heavy plow-shaped tool is shown as is the stepped

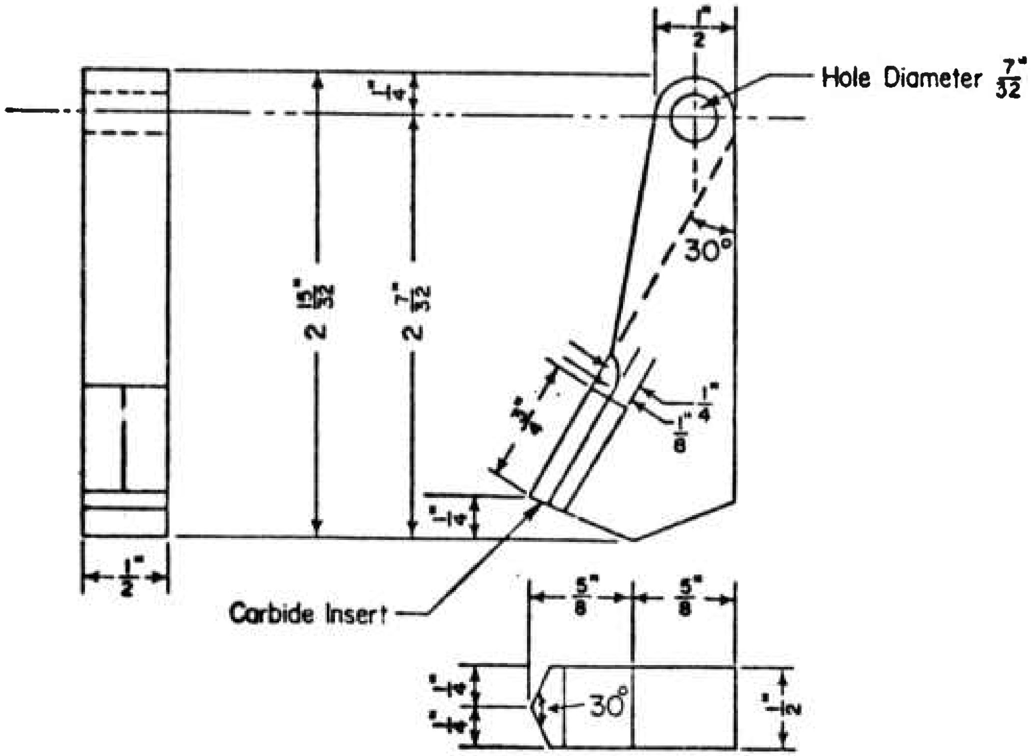
1/2"
Hole Diameter 7/32"
1/4"
30°
2 15/32"
2 7/32"
3/4"
1/4"
1/8"
1/4"
1/2"
Carbide Insert
5/8"
5/8"
1/4"
1/4"
30°
1/2"

Fig. 1-18 Heavy plow tool

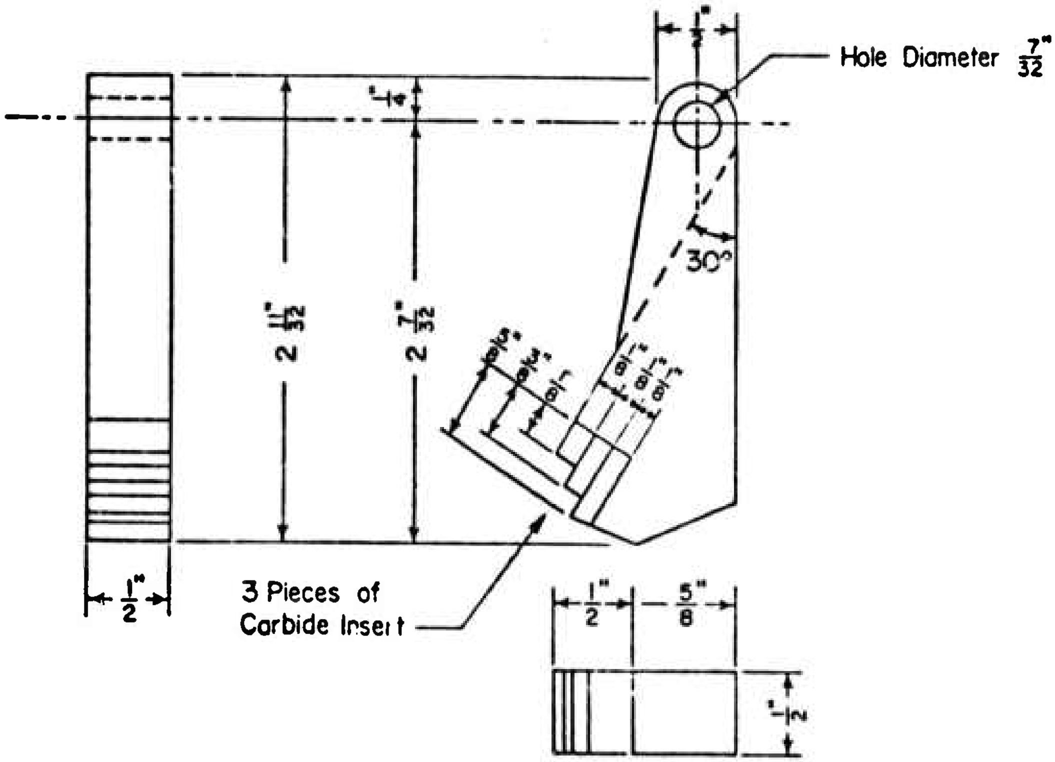
1/2"
Hole Diameter 7/32"
1/4"
30°
2 11/32"
2 7/32"
5/8"
3/8"
1/8"
1/8"
1/8"
1/8"
1/2"
3 Pieces of
Carbide Insert
1/2"
5/8"
1/2"

Fig. 1-19 Stepped cutting tool

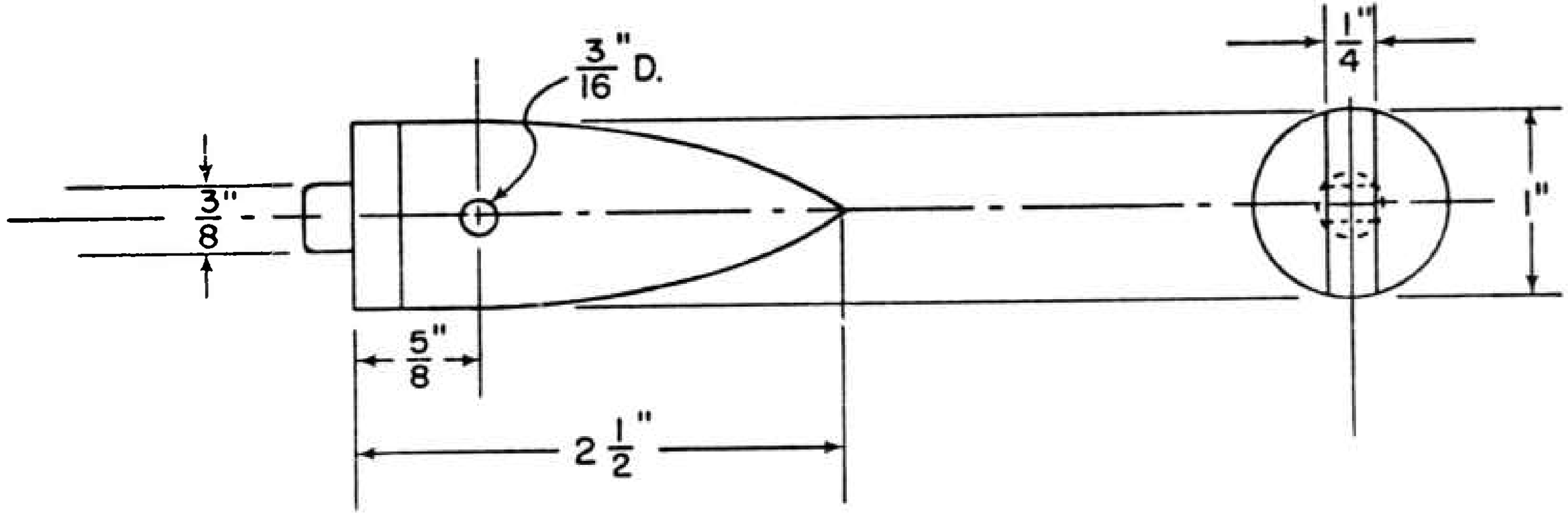
$\frac{3}{16}$" D.
$\frac{1}{4}$"
1"
$\frac{3}{8}$"
$\frac{5}{8}$"
$2\frac{1}{2}$"

Fig. 1-20 Chisel-type tool

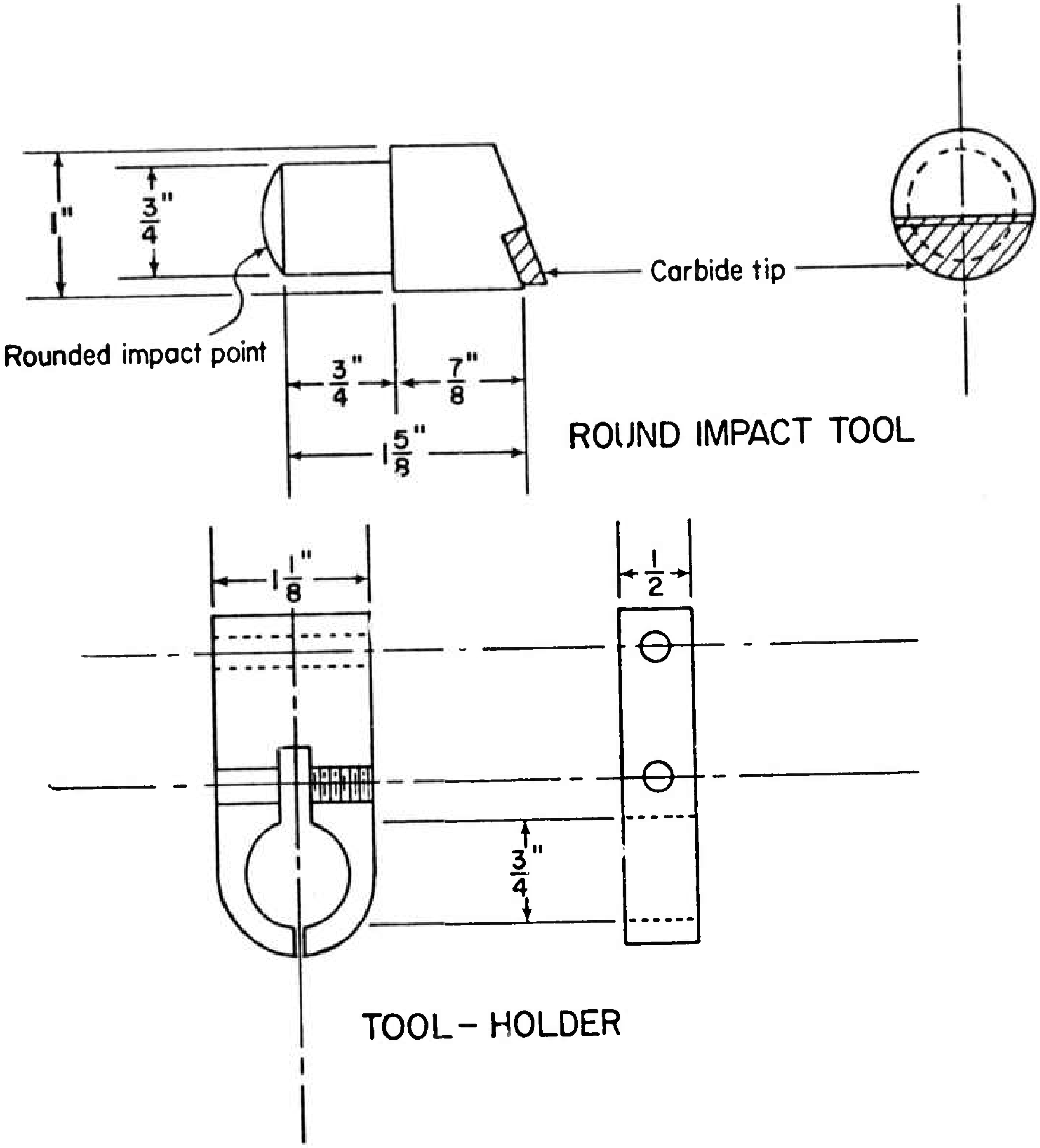
1"
3/4"
Rounded impact point
3/4"
7/8"
1 5/8"
Carbide tip
ROUND IMPACT TOOL
1 1/8"
1/2
3/4"
TOOL-HOLDER

Fig. 1-21 Two-piece impact tool

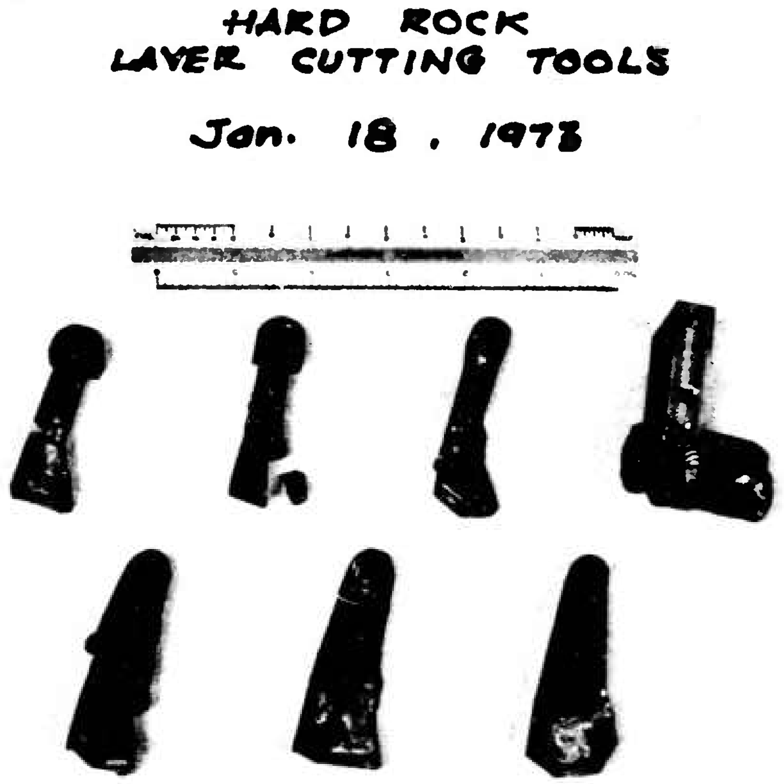
HARD ROCK
LAYER CUTTING TOOLS
Jan. 18 . 1973

Fig. 1-22 Various layer cutting tools

cutting tool, although the stepped edges are not revealed clearly in the latter.

(D) Spring-Return System

An important step of the impact-coupling process is the phase of tool rebound from the load. In particular, if tool rebound is too low, energy pickup from the transducer is also low, leading to rather weak impact against the load. It was felt that a spring-assisted return of the tool against the transducer would enhance the cutting process. A spring was installed in front of the tool to increase tool rebound velocity.

Mechanical springs of different stiffnesses were tried. Eventually, a small block of silicone rubber, yielding a fairly stiff spring, was found to work best. The configuration of spring and tool is shown in Fig. 1-23.

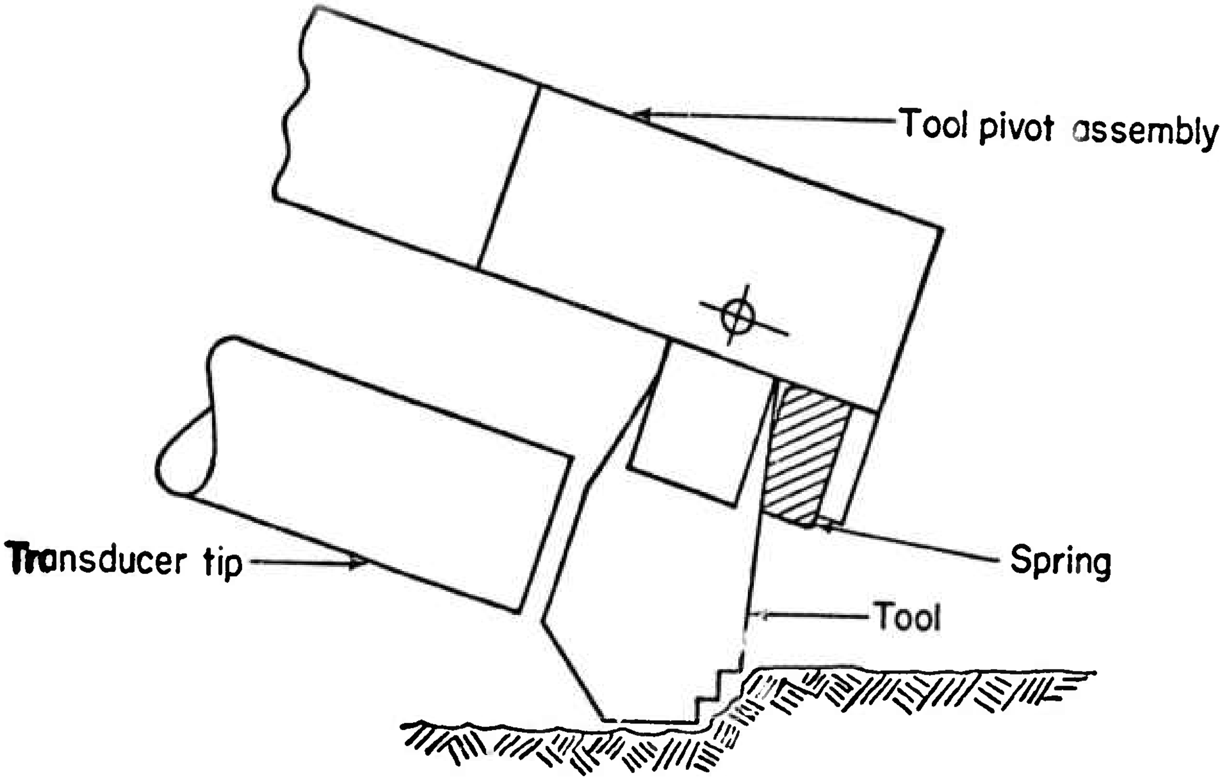

Fig. 1-23 Spring assisted tool return assembly

(E) Transmission Line Optimization

Two fixed frequency motor-generators were available for supplying high frequency power to the transducer. The output frequencies of the generators were slightly different, one being 9,720 Hz, the other 10,054 Hz. For optimum action, it was naturally desirable that the transducer-transmission line resonance be as close as possible to generator frequency at operating voltages. However, the operating conditions of high voltage and temperature increases tend to lower transducer resonance from the no-load, low voltage conditions under which it is tuned. Consequently, it was felt desirable to conduct a series of tests to determine the optimum transmission line length to achieve tuned operation under load.

The tests started with a transducer fitted with a long transmission line, so that the system resonant frequency was considerably lower than the supply frequency. A layer cutting run was then performed, with the transducer input power being noted. The transmission line was then trimmed by 1/16 inch and the cutting process repeated. As the line was shortened, the power input increased, up to a point, and then started to diminish. The process was continued until it was obvious that the optimum length had been reached and passed.

Figure 1-24 shows the low voltage, no-load resonant frequencies for various transmission line lengths. The slope of the average straight line is 25 Hz drop per 1/16 inch increase in line length. In Fig. 1-25, the input power to the transducer under cutting conditions for various transmission line lengths is shown. Obviously, a very pronounced peak is reached at a length of 10-1/16 inches. Referring to Fig. 1-24, it is seen that this length has a no-load resonant frequency of 10,125 Hz.

1-7 RESULTS FOR GRANITE

Although many difficulties were encountered in layer cutting of granite, some successful cuts were accomplished. Figure 1-26 shows a cut being made with the heavy, plow-shaped tool of Fig. 1-18, with the spring-assist device of Fig. 1-23 also being utilized. Figure 1-27 gives a general indication of the depth and profiles of some of the cuts.

Figure 1-28 shows data obtained on the volume of rock removal for various cutting speeds, at two different angles of attack. The specific energy of rock removal versus cutting speed is shown in Fig. 1-29 for the two different angles of attack. The data at the 40° angles of attack is "well behaved" in both Fig. 1-28 and 1-29, in that it resembles the general results obtained in limestone cutting. The results for 30°, however, indicate a marked decrease in removal efficiency for speeds beyond about 1/2 inch per second. This result mainly reflects the tendency of the tool to ride to the surface at lower angles of attack.

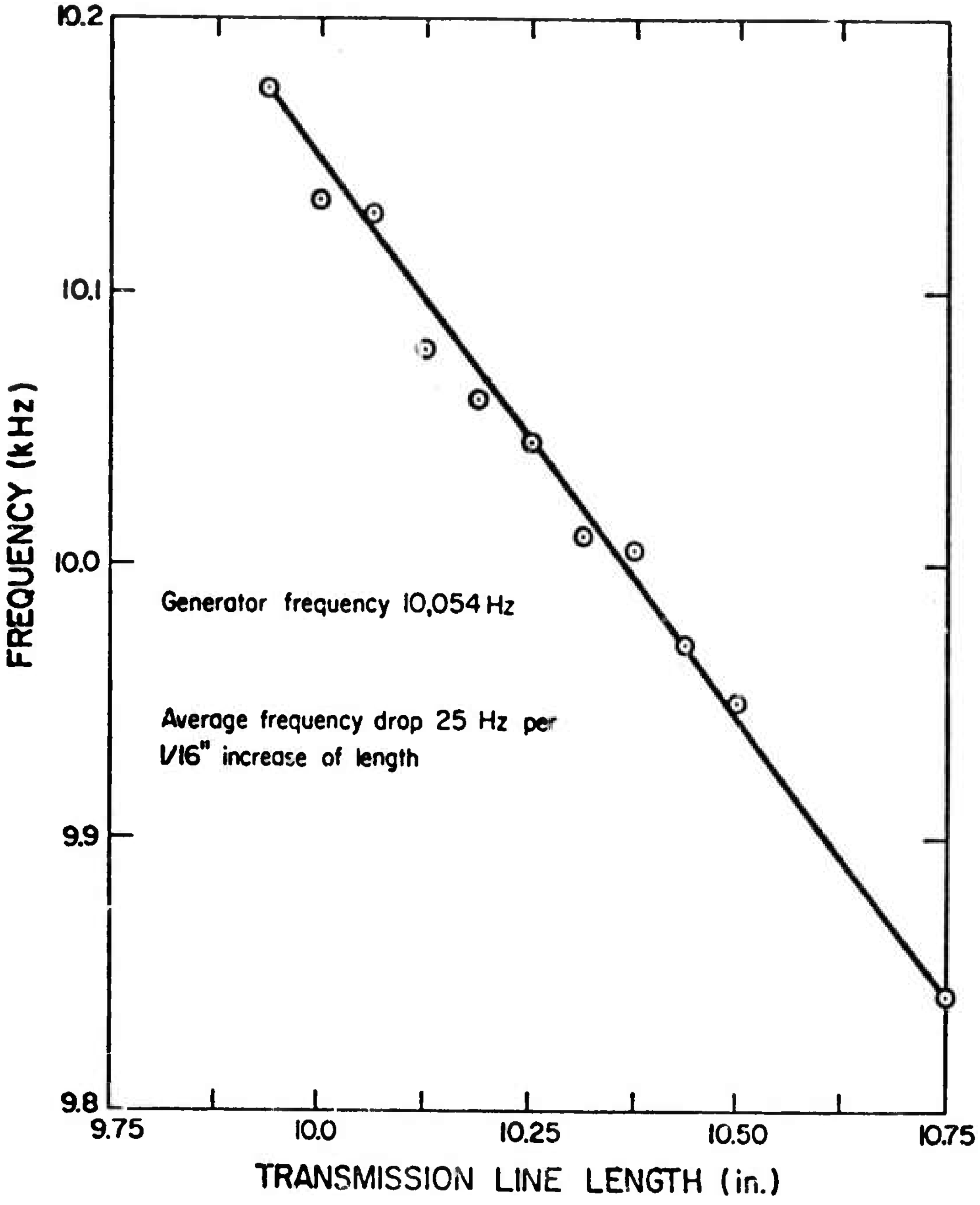

Fig. 1-24 No-load, low-voltage resonant frequency change with change in line length

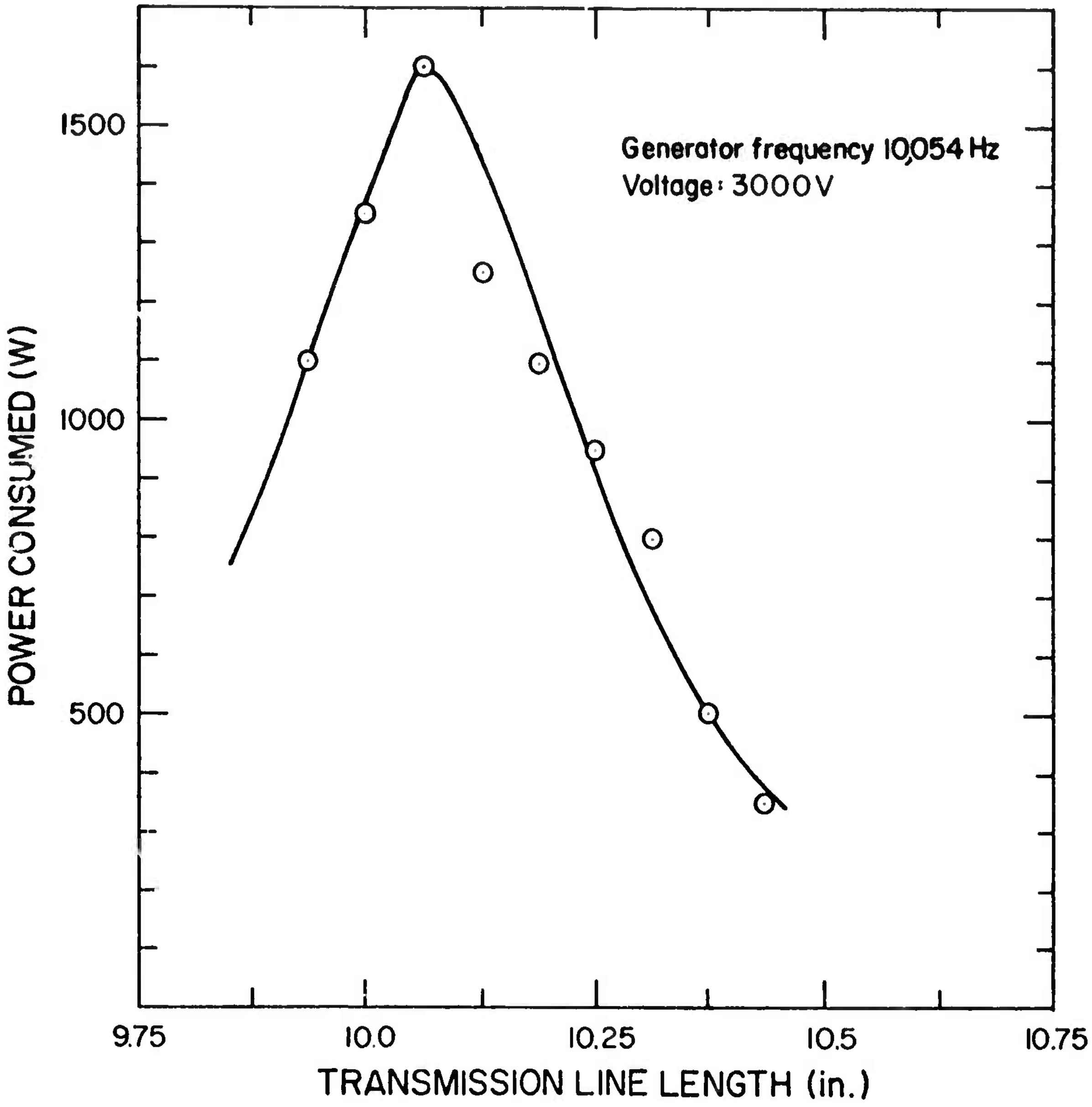

Fig. 1-25 Input power versus line length under cutting conditions

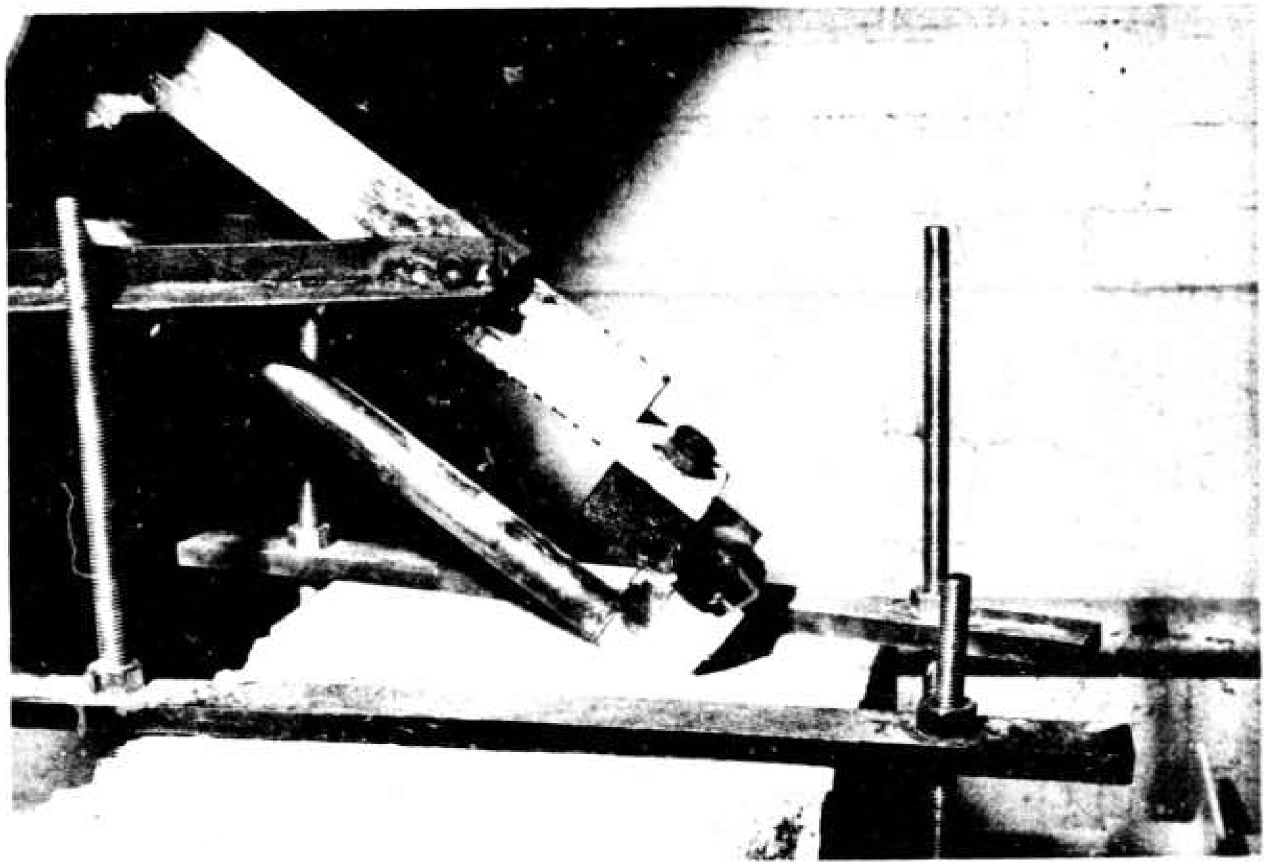

Fig. 1-26 Layer cutting action in granite

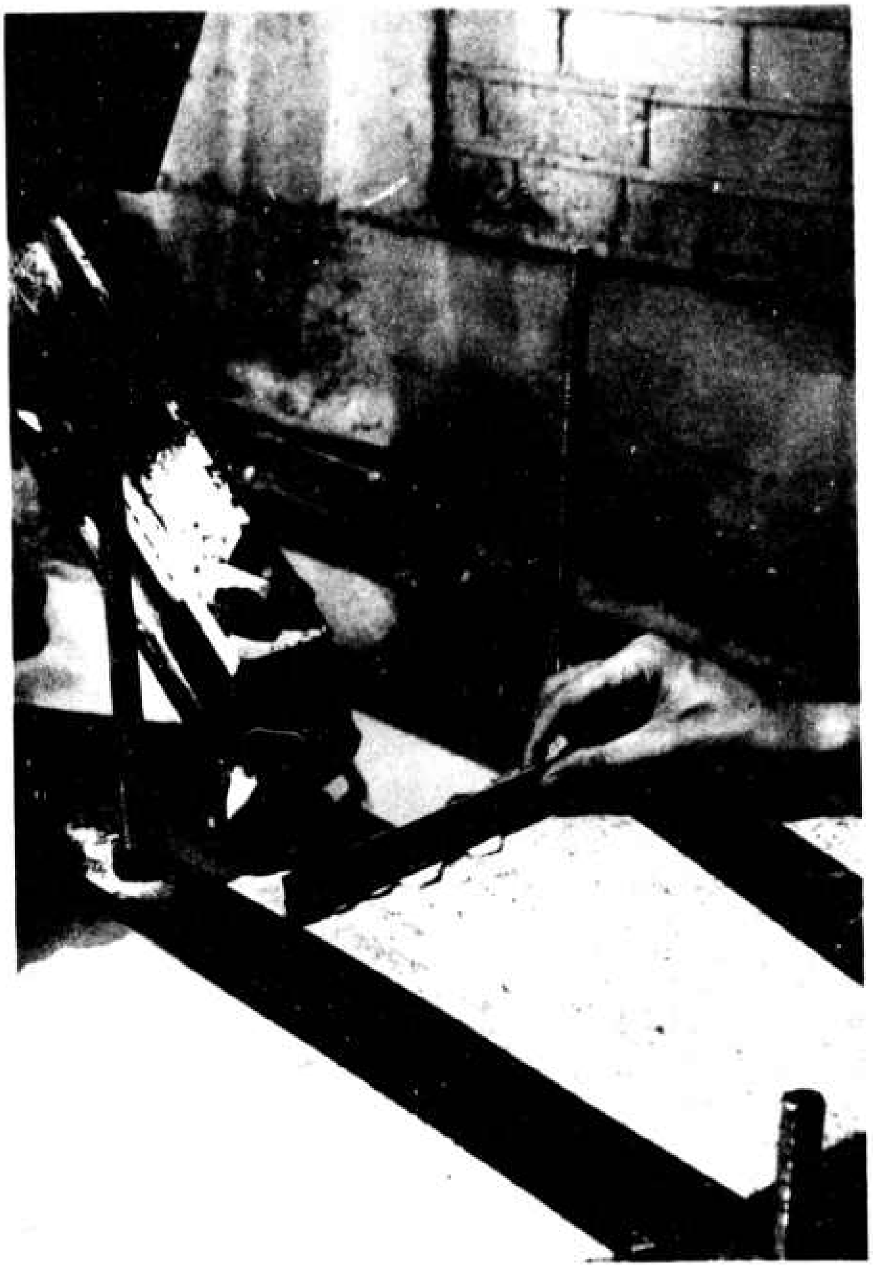

Fig. 1-27 Typical cuts in granite

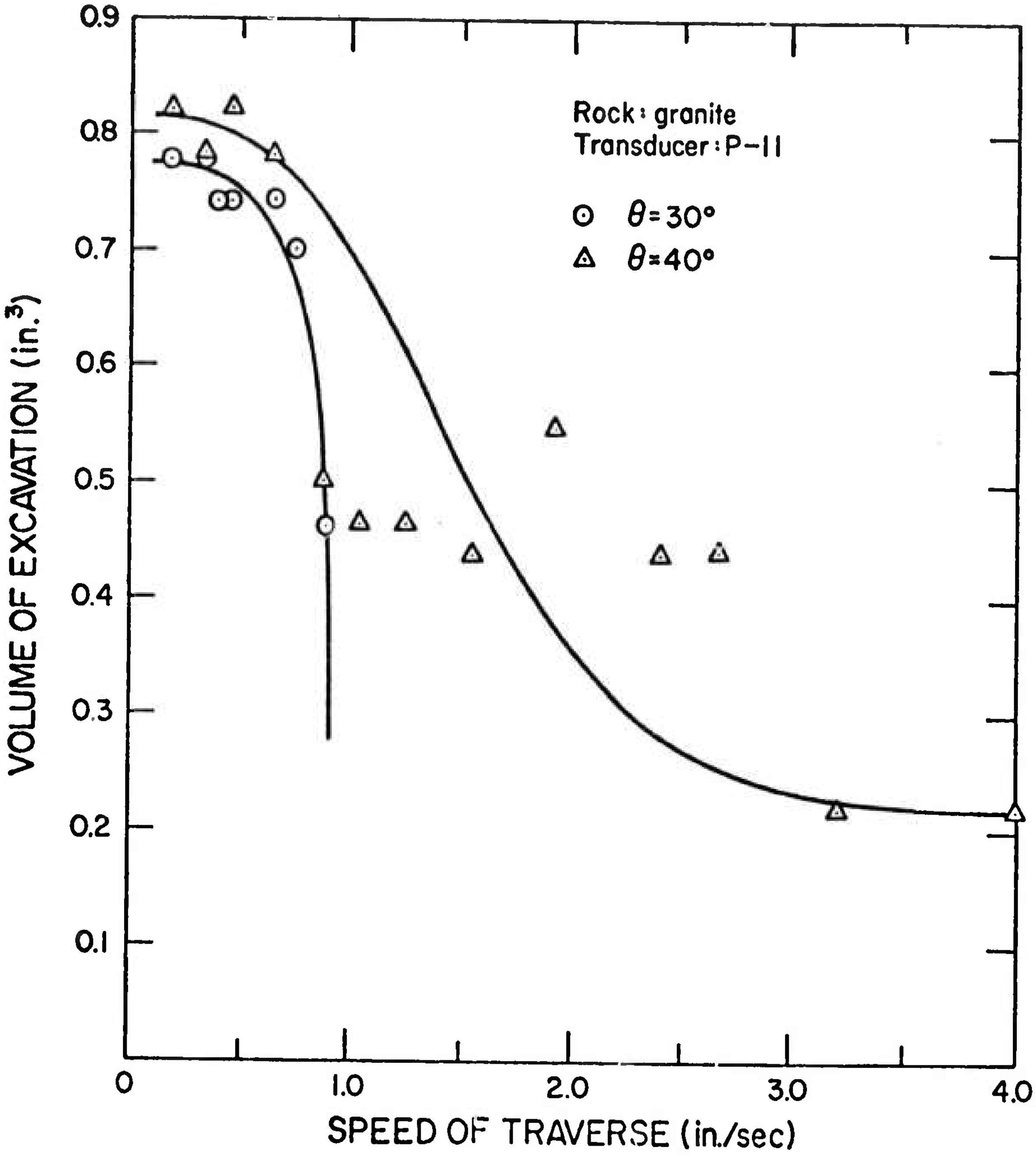

Fig. 1-28 Volume of rock removal versus speed of cutting

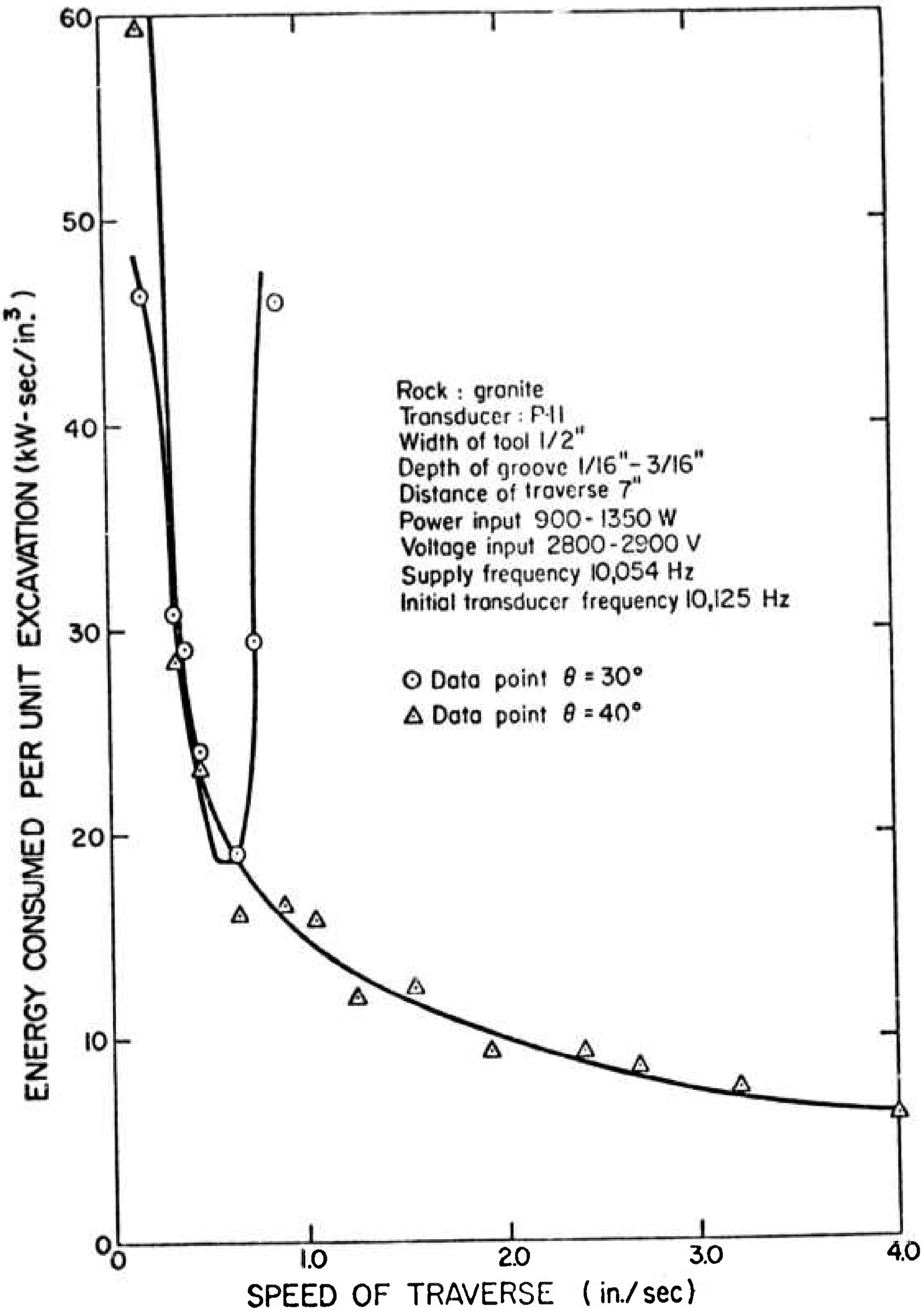

Fig. 1-29 Specific energy of rock removal versus cutting speed

While some success was ultimately achieved in cutting granite, the overall results must be interpreted as highly marginal in hard rock. With the general tendency of the system to stall or couple to the rock when too great a depth of cut was attempted, and the tendency to avoid the rock by tool "ride up" when shallow cuts were attempted, a rather precarious balance of parameters was necessary to achieve successful cuts. This unstable situation was, it seemed, merely indicative of the fundamental problem of inadequate power transfer to rock for cutting.

2. TECHNICAL LITERATURE APPLICABLE TO ANALYSIS OF LAYER CUTTING

2-1 INTRODUCTION

Sonic layer cutting or rock utilized a transducer vibrating at high frequency (10 kHz for the present application) as the energy source. The mechanical vibrational energy is transmitted from the transmission line of the transducer to the rock by a bouncing tool via an impact coupling process. Although significant amounts of energy are transmitted to the work piece by the rapid impacts, the energy transfer involved in a single blow is relatively small compared to, say, conventional percussive drilling. In order to induce failure of the rock through many small increments of energy is a different process than a low frequency, high energy per blow process; therefore, it is most important to understand the effects of process parameters such as depth of cut and tool geometry on rock fracture. A better understanding of the rock fracture mechanics was required. With this in mind, a brief review on the failure theories of rock is given before proceeding to the technical literature applicable to the layered cutting process

2-2 FAILURE THEORIES OF ROCK

It is well known that rocks generally are highly inhomogeneous, anisotropic and porous. The constituents and structures vary from rock to rock. It is indeed very difficult to give a universal failure theory to cover all rocks. Nevertheless, some observations have been made on the general failure modes of most rocks. Rocks are said to be brittle under low confining pressure. A number of failure theories have been proposed and reviewed in several papers [1], [2].* The various theories can be divided into three categories: (A) the empirical criteria, (B) the phenomenological failure theories, and (C) the statistical failure theories. In the following, a brief review will be presented on the above three categories.

(A) The Empirical Criteria

This category includes the maximum shear stress theory and the Coulomb-Navier-Mohr theory. The maximum shear theory states that failure occurs at the point where the maximum shear stress becomes equal to a critical value called the shear strength of the material which is independent of the stress state. If $\sigma_1 \geq \sigma_2 \geq \sigma_3$ denote the three principal stresses, this theory predicts that failure will occur on the plane inclined to the maximum stress σ_1, and whose normal bisects the (σ_1, σ_3) axis. According to this theory, the uniaxial tensile and compressive strengths should be the same. Ductile materials (such as metals) appear to be the only materials which fail in this way.

---

*Numbers in brackets refer to references at the end of this chapter.

However, for most rock materials, the strengths are usually dependent on the stress state in that their strength increases with an increasing confining pressure. Moreover, the compressive strength of a rock is usually much greater than its tensile strength. The failure planes are inclined less than 45° (about 30°, with a tendency to increase slightly as the confining pressure increases) to the direction of maximum compression. Therefore, it is not proper to apply the maximum shear theory to rocks.

To overcome some of the deficiencies of the maximum shear criterion, the Coulomb-Navier Criterion was proposed by Navier (see, for example, King [3]) by utilizing the Coulomb friction concept (see, for example, Nadai [4]). This criterion may be stated as follows: Suppose that $\sigma_1 > \sigma_3$ are the principal stresses (compressive) in two dimensions. The normal compressive stress σ and the shear stress τ on a plane inclined to σ_3 by an angle θ (see Fig. 2-1) may be written as

$$\sigma = \frac{1}{2}(\sigma_1 + \sigma_3) + \frac{1}{2}(\sigma_1 - \sigma_3)\cos 2\theta$$

$$\tau = \frac{1}{2}(\sigma_1 - \sigma_3)\sin 2\theta \qquad (2\text{-}1)$$

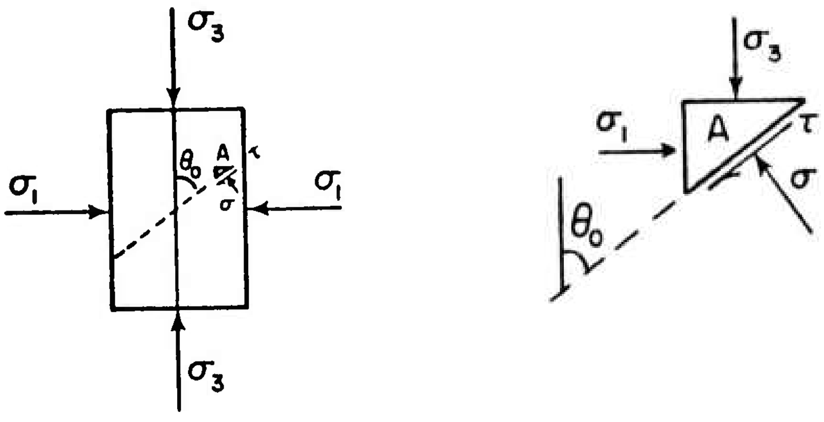

(a) (b)

Fig. 2-1 A two-dimensional stress state

Assume that when failure occurs, element A (Fig. 2-1(b)) will slip along the failure plane $\theta = \theta_0$, as the shear stress along the failure plane exceeds the resisting strength T, which was proposed by Navier to be

$$T = \tau_0 + \mu\sigma \tag{2-2}$$

where τ_0, a material constant, is called the intrinsic shear strength of the material and μ is the internal Coulomb friction coefficient. Physically, μ is the coefficient of sliding friction of one portion of the rock against the other. Incorporating eq. (2-2) into the assumed failure criterion, the failure condition is obtained as

$$|\tau| \geq \tau_0 + \mu\sigma \tag{2-3}$$

Thus, failure occurs, when

$$\begin{aligned} \tau_0 &= |\tau| - \mu\sigma \\ &= -\frac{1}{2}\mu(\sigma_1 + \sigma_3) + \frac{1}{2}(\sigma_1 - \sigma_3)(\sin 2\theta_0 - \mu \cos 2\theta_0) \end{aligned} \tag{2-4}$$

From eq. (2-3) it is seen that for a given τ_0, σ_1 and σ_3, the potential failure plane can be decided by the angle θ_0 which makes the right hand side of eq. (2-3) a maximum or it is the angle θ_0 which makes the stress state satisfy eq. (2-3), whichever occurs first. This θ_0 is found to be

$$\tan 2\theta_0 = -\frac{1}{\mu} \tag{2-5}$$

Substituting eq. (2-5) into eq. (2-4) gives

$$\sigma_1(\sqrt{\mu^2 + 1} - \mu) - \sigma_3(\sqrt{\mu^2 + 1} + \mu) = 2\tau_0 \tag{2-6}$$

or,

$$2\tau_0 = \frac{1}{\tan 2\theta_0}(\sigma_1 + \sigma_3) + (\sigma_1 - \sigma_3)\frac{1}{\sin 2\theta_0} \tag{2-7}$$

This may be written as

$$\sigma_1 = 2\tau_0 \tan \theta_0 + \sigma_3 \tan^2 \theta_0 \tag{2-8}$$

From eq. (2-8), the relation between σ_1 and σ_3 is seen to be a straight line (see Fig. 2-2). Denoting $2\theta_0 = \pi/2 + \varphi$, then $\sin 2\theta_0 = \cos \varphi$, $\cos 2\theta_0 = -\sin \varphi$ and thus $\mu = \tan \varphi = -1/\tan 2\theta_0$, so that eq. (2-4) becomes

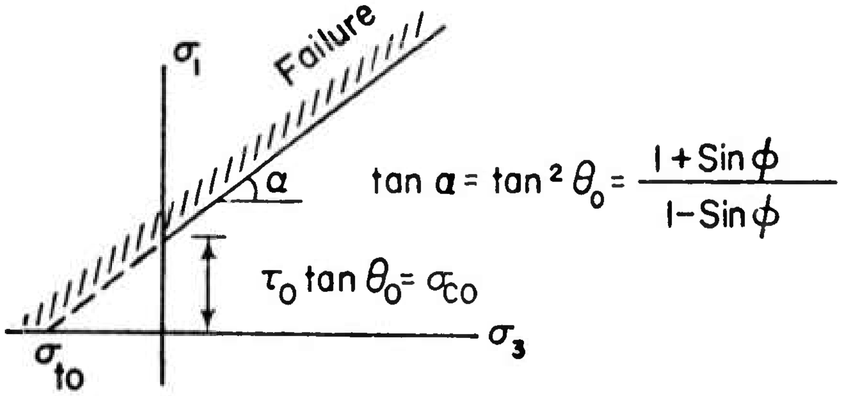
σ_1
Failure
α
$\tan\alpha = \tan^2\theta_0 = \frac{1+\sin\phi}{1-\sin\phi}$
$\tau_0 \tan\theta_0 = \sigma_{co}$
σ_3
σ_{to}

Fig. 2-2 The σ_1-σ_3 failure boundary

$$2\tau_o = \sigma_1 \frac{1 - \sin\varphi}{\cos\varphi} - \sigma_3 \frac{1 + \sin\varphi}{\cos\varphi} \qquad (2\text{-}9)$$

or,

$$\tau_m = \tau_o \cos\varphi + \sigma_m \sin\varphi \qquad (2\text{-}10)$$

where $\tau_m = \frac{1}{2}(\sigma_1 - \sigma_3)$ is the maximum shear and $\sigma_m = \frac{1}{2}(\sigma_1 + \sigma_3)$ is the mean stress. From eq. (2-5), it is seen that $\theta_o > \pi/4$ which is in accord with the experimental observations. From eq. (2-6), it is seen that the tensile strength σ_{to} is given by letting $\sigma_1 = 0$ so that the equation becomes

$$\sigma_{to} = -\sigma_3 = \frac{2\tau_o}{\sqrt{\mu^2 + 1} + \mu} \qquad (2\text{-}11)$$

The compressive strength σ_{co} is given by substituting $\sigma_3 = 0$, or

$$\sigma_{co} = \sigma_1 = \frac{2\tau_o}{\sqrt{\mu^2 + 1} - \mu} \qquad (2\text{-}12)$$

Therefore, $\sigma_{to} \neq \sigma_{co}$, and their ratio is

$$\frac{\sigma_{to}}{\sigma_{co}} = \frac{\sqrt{\mu^2 + 1} - \mu}{\sqrt{\mu^2 + 1} + \mu} \qquad (2\text{-}13)$$

which is less than 1 and, thus, is in accord with the experimental observations. Equation (2-4) can also be expressed as

$$\tau_o = |\tau| - \tan\varphi \cdot \sigma \qquad (2\text{-}14)$$

which is plotted in Fig. 2-3, and is again a straight line. Note that the circles tangent to the straight lines are the Mohr's circles which give the stress states at failure. The failure line is also called the Mohr envelope.

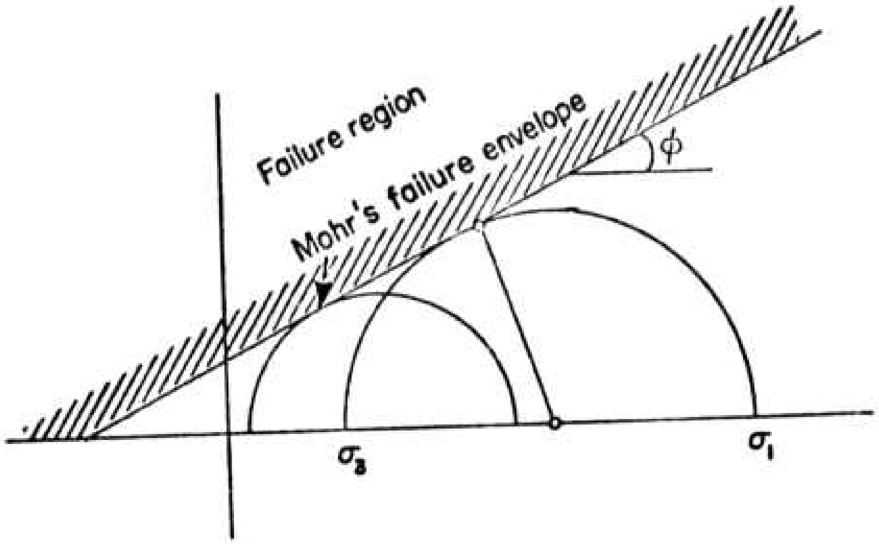

Fig. 2-3 Mohr envelope of failure

Several shortcomings also exist with this criterion, such as; (i) the theory cannot predict the value of the principal stresses at failure, and (ii) μ is difficult to obtain. However, the failure envelope does have fairly good agreement with the observed results for rock-like materials. Moreover, the relative simplicity of the criterion aids in making it one of the most widely used failure theories.

Later development in the area of shear failure followed closely the work in the theory of plasticity. Usually, the failure theories are expressed in terms of stress invariants. For example, Von Mises' criterion [5], [6]

$$J_2 = \frac{1}{6}\left[(\sigma_1 - \sigma_3)^2 + (\sigma_3 - \sigma_1)^2 + (\sigma_1 - \sigma_2)^2\right] = k^2 \qquad (2\text{-}15)$$

where J_2 is called the second stress invariant and k is a material constant associated with the yield stress in simple shear. Other criteria are associated with Tresca [5], [6], Freudenthal [7] and Bresler and Pister [8].

(B) Phenomenological Failure Theories

This category includes Griffith theory, McClintock and Walsh's modified Griffith theory, and Murrel's generalized Griffith theory in three dimensions.

Griffith suggested that there are a great number of micro-cracks existing in a brittle solid. Failure occurs when the existing micro-cracks spread. The condition of crack extension was proposed to depend on energy balance; i.e., if an increase in crack size (length) leads to a diminution of the total free energy, the system becomes unstable and the crack spreads. The uniaxial critical stress σ_0 (tensile), is found to be

$$\sigma_0 = \begin{cases} \left(\dfrac{2\gamma Y}{\pi c}\right)^{1/2}, & \text{for plane stress} \\ \left(\dfrac{2\gamma Y}{\pi c(1 - \nu)}\right)^{1/2}, & \text{for plane strain} \end{cases} \tag{2-16}$$

where ν, Y, are the Poissons' ratio and Youngs' modulus of the material, γ is the surface energy of the material, and 2c is the length of the crack. The maximum stress at the crack tip is found to be

$$\sigma_t = \sigma_0\sqrt{\frac{4c}{\rho}} \tag{2-17}$$

where ρ is the radius of curvature at the crack tip.

The Griffith theory has been extended to the case of a biaxial stress field with an elliptical flaw. It takes the form

$$(\sigma_1 - \sigma_3)^2 - 8\sigma_{to}(\sigma_1 + \sigma_3) = 0 \tag{2-18}$$

when $\sigma_1 + 3\sigma_3 \geq 0$ and σ_{to} is the tensile strength of the material. For $\sigma_1 + 3\sigma_3 < 0$, the failure criterion is

$$\sigma_3 - \sigma_{to} < 0 \tag{2-19}$$

The Mohr envelope for eq. (2-18) can be shown to be

$$\tau^2 = 4\sigma_{to}(\sigma + \sigma_{to}) \tag{2-20}$$

which is a parabola.

Under compression, the Griffith cracks can be closed. Griffith theory was modified by McClintock and Walsh to account for the friction along the crack surfaces. The failure criterion takes the form

$$-\mu'(\sigma_1 + \sigma_3) + (\sigma_1 - \sigma_3)\sqrt{1 + \mu'^2} = 4\sigma_{to} \tag{2-21}$$

where μ' is the coefficient of friction along the crack surfaces. This can also be written as

$$\sigma_1 = \frac{4\sigma_{to}}{\sqrt{1 + \mu'^2} - \mu'} + \frac{\sqrt{1 + \mu'^2} + \mu'}{\sqrt{1 + \mu'^2} - \mu'}\sigma_3 \tag{2-22}$$

Comparing eq. (2-22) with (2-6), it is easily seen that the two results will be the same if

$$\mu' = \mu \ , \qquad 2\sigma_{to} = \tau \tag{2-23}$$

Therefore, if again we let $\mu = \tan \varphi$, the modified Griffith failure criterion can be expressed as

$$\tau = 2\sigma_{to} + \mu\sigma \tag{2-24}$$

Graphically, the Griffith theory, eq. (2-19) and the modified Griffith theory, eq. (2-24) are shown in Fig. 2-4, where μ is assumed to be $0.8 \leq \mu \leq 1.0$.

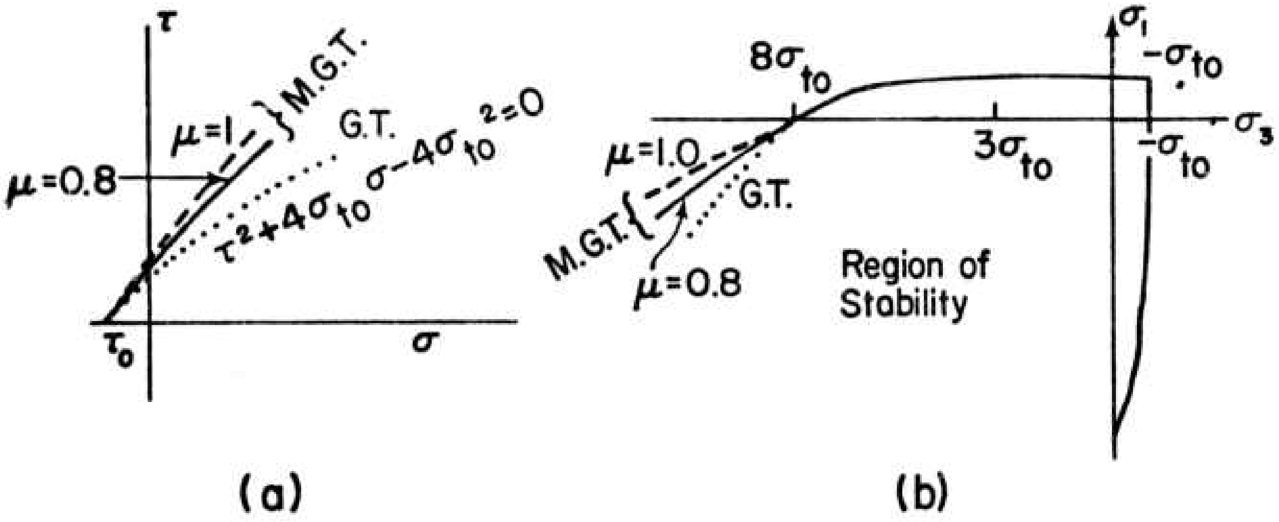

Fig. 2-4 Griffith Theory (G.T.) and Modified Griffith Theory (M.G.T.)

From the above, it is seen that the Griffith theories can predict the tensile strength of a brittle material in terms of crack length, elastic constants and surface energy. It is capable of predicting the stresses for failure subject to a two-dimensional stress state. However, the Griffith theories cannot evaluate σ_{co} and σ_{to} directly; thus the theory is not applicable to the failure of rock material.

Murrell [9] extended the Griffith theory to three dimensions. The failure surface was found to consist of a portion of a paraboloid of revolution, symmetrical about the line $\sigma_1 = \sigma_2 = \sigma_3$ and passing through the origin. The equation is

$$(\sigma_2 - \sigma_3)^2 + (\sigma_3 - \sigma_1)^2 + (\sigma_1 - \sigma_2)^2 = 24\sigma_{to}(\sigma_1 + \sigma_2 + \sigma_3) \qquad (2\text{-}25)$$

(C) Statistical Failure Theories

The statistical models propose that the strengths of materials are decided by the weakest link of the random distribution of Griffith flaws in the materials. Thus there will be a distribution of strengths in a given specimen because a different stress is required to fracture a specimen at one or another point. Several papers based on this concept are reviewed in Brady [2], and will not be further discussed here.

2-3 LITERATURE APPLICABLE TO LAYER CUTTING

There is considerable literature available that applies to the problem of rock drilling mechanics in both the theoretical and experimental areas (see for example, Maurer [10], Dutta [11], Mahban [12], Hustrulid [14], Cheatham and Gnirk [14], Pariseau and Fairhurst [15], etc.). Most of these, however, relate to percussive drilling configurations and have little application to layer cutting. Literature directly concerning layer cutting of rock is rather sparse. There have been numerous studies in metal cutting problems, however, that can provide a starting point for some analysis. Literature concerning the metal cutting mechanics will be reviewed first. Then the literature pertaining to the layer cutting mechanics of brittle materials will be reviewed.

Merchant [16] considered simple models of metal cutting processes, which included the "orthogonal cutting," with a straight-edged cutting tool moving relative to the work piece in a direction perpendicular to its cutting edge, and the "oblique cutting," with the cutting edge oblique to the direction of relative motion of tool and work piece.

Several assumptions were made for the orthogonal cutting: (i) the chip is continuous with mass density ρ unchanged in the cutting process; (ii) shear failure occurs on a shear plane A_s at an angle φ (see Fig. 2-5 for the geometry, and Fig. 2-6 for the shear failure model); (iii) the chip is in static equilibrium, as shown in Fig. 2-7; and (iv) the cutting force required R, is equal to the shear strength of the material τ_o, multiplied by the area of the shear plane A_s.

To attack this problem, first the chip thickness ratio t_c/t_o was geometrically related to the shear angle ψ and the rake angle α. The shear strain in the chip can also be related to ψ and α. Finally the chip velocity V_c may be related to the tool velocity V_o. Applying force equilibrium to the chip, Merchant was able to obtain the various force relations. He obtained:

$$\frac{Q}{P} = \tan(\varphi - \alpha) \qquad (2\text{-}26)$$

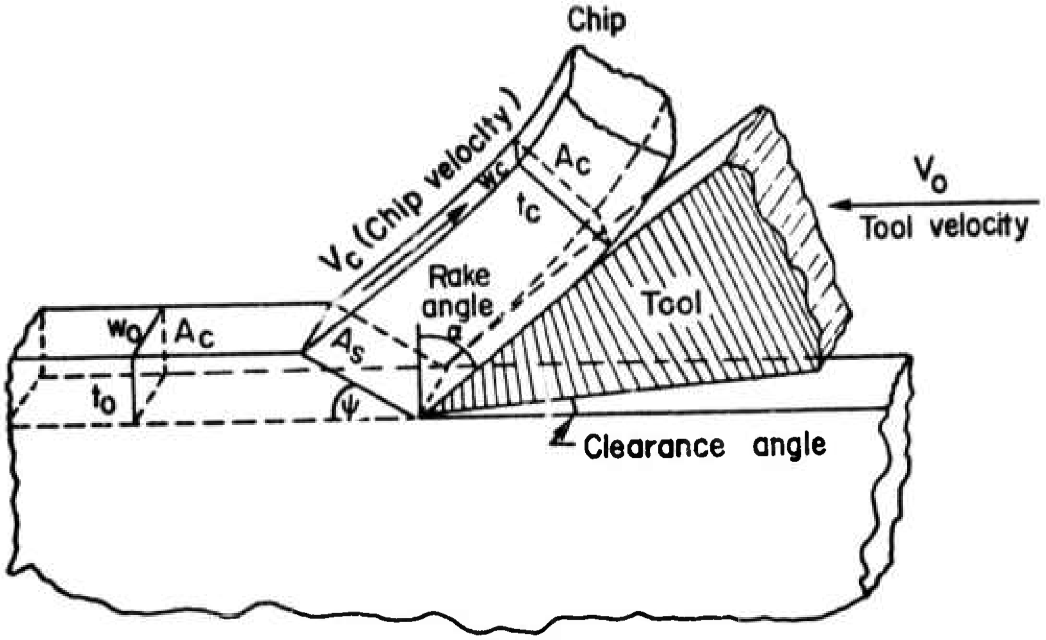
Chip
V_c (Chip velocity)
w_c
A_c
t_c
Rake angle α
Tool
V_o
Tool velocity
w_o
A_c
A_s
t_o
ψ
Clearance angle

Fig. 2-5 Merchants' metal cutting model

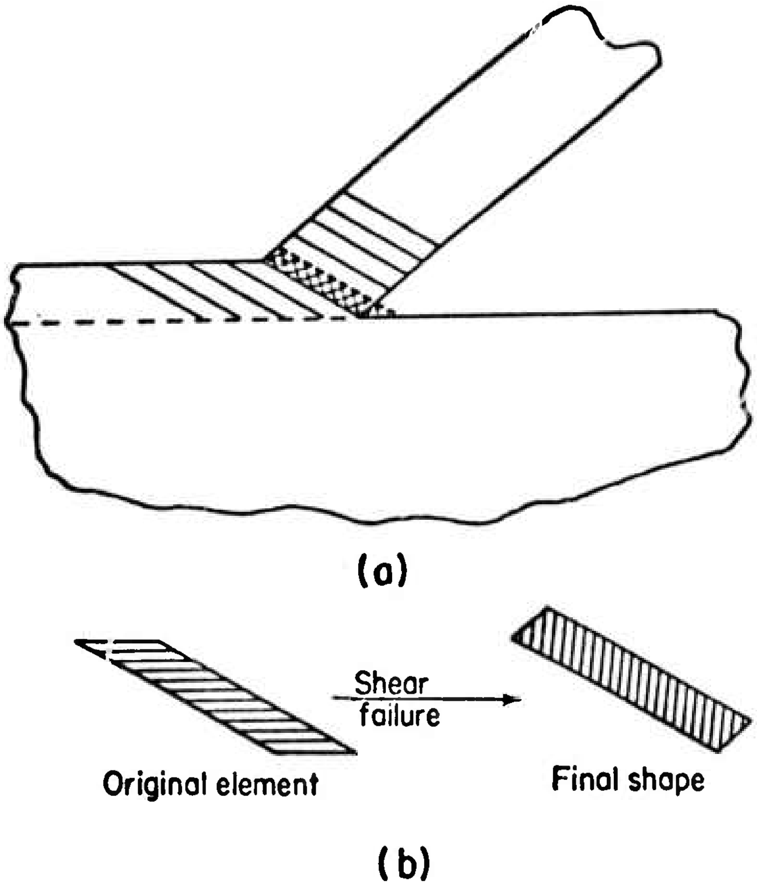
(a)
Shear failure
Original element
Final shape
(b)

Fig. 2-6 Merchants' shear failure model

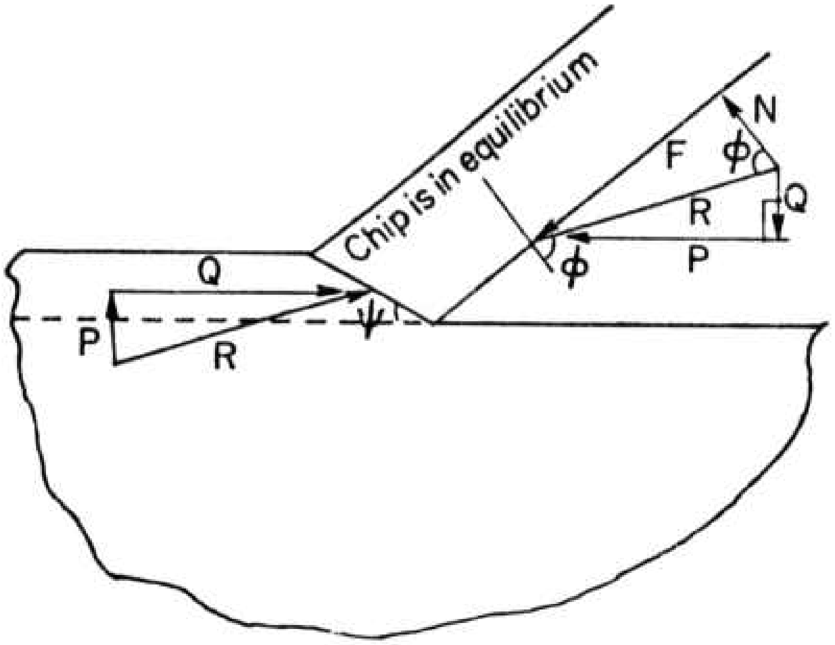

$\phi = \tan^{-1}\mu$

μ = friction coefficient

Fig. 2-7 Merchants' force components on a chip

where Q = thrust force and P = cutting force. Also,

$$\tau_o = \frac{P}{A_o}\left[\sin\psi\cos\varphi - \tan(\varphi - \alpha)\sin^2\psi\right] \qquad (2\text{-}27)$$

or

$$P = \tau_o A_o \frac{\cos(\alpha - \varphi)}{\sin\psi\cos(\varphi + \psi - \alpha)} \qquad (2\text{-}28)$$

where τ_o is the shear strength of the material.

From these results, one can see that since P, Q, A_o, φ, and α can be measured experimentally, τ_o can be determined from eq. (2-27). Alternately, if τ_o is known, and if α, φ, ψ and A_o are measured, the cutting force required, P, can be calculated from eq. (2-28). Figure 2-8 shows $P/2\tau_o A_o$ versus α using $\varphi = \tan^{-1}\mu$ as a parameter.

From Fig. 2-8, one can see that the cutting force required to break a layer of metal is directly proportional to the area of cutting and the shear strength of the material. It also shows that the cutting force required is larger for a smaller rake angle α. Furthermore, friction between the tool and the chip also increases the cutting force needed.

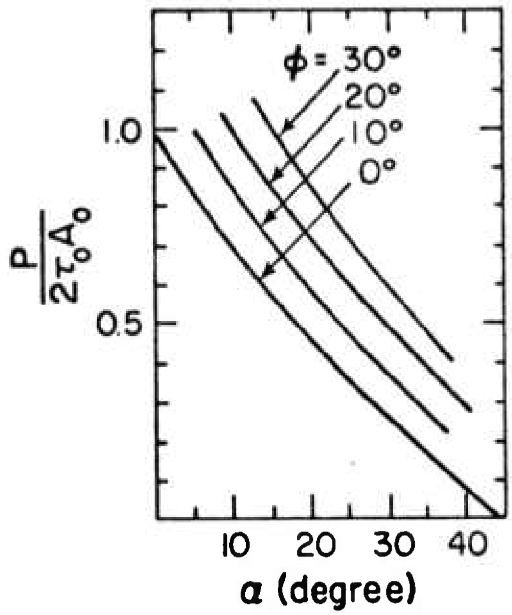

Fig. 2-8 Cutting force P versus rake angle α relations from Merchants' theory

There are certain deficiencies in the theory. For one, it is implied that the cutting force P is independent of the cutting speed V_c, which at least implies that the dynamic effect in metal cutting is not considered. Moreover, the assumption of a single shear plane does not agree with experimental observations. The model proposes an external surface which is not smooth at the junction of the chip and the original surface. Theoretically, an infinite shear gradient exists in this shear plane and an infinite acceleration of the chip is involved, which is physically impossible. A transition zone of plastic deformation (chip formation zone) is definitely necessary to modify the original theory.

Zorev [17] described several modified models which included the transition zone. He discussed, for example, the models of Briks [18] and Krivoukhov [19]. He analyzed a modified model with chip deformation zone which provides for smooth joining of outer boundaries of the cut layer as shown in Fig. 2-9.

The chip formation zone takes the shape of a fan. The stressed state arising is characterized by the fact that the lines of the constant tangential stresses are a fan-shaped pattern of straight lines passing through the cutting edge. The initial and final boundaries of the plastic zone, OL and OM, are determined from the plasticity conditions. It is assumed that the transformation from the layer being removed into a chip occurs by successive shear along a family of slip

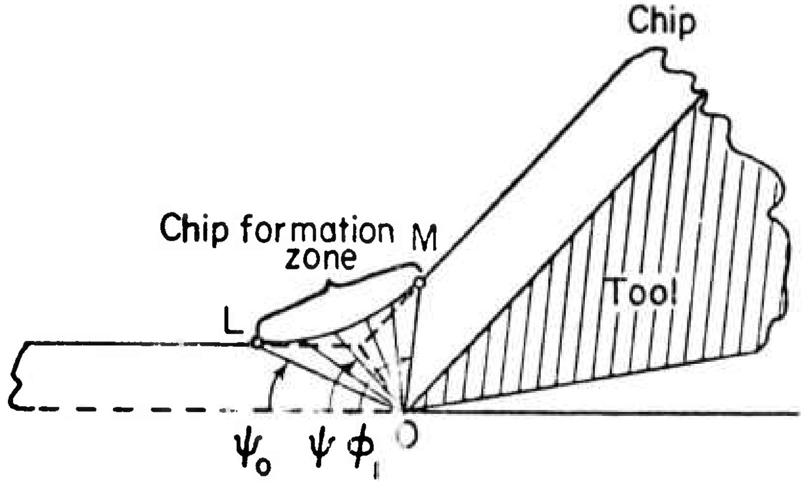

Fig. 2-9 Chip formation zone

lines passing through the cutting edge O. Shear along the second family of slip lines is considered to be comparatively small, and therefore is neglected. The direction of the shear lines is taken to coincide with the direction of the lines of maximum tangential stress.

As in Merchant's treatment, again the shear train is related to geometry. The shear stress acting on a shear plane is related to the resultant force on the chip by considering the equilibrium of the chip, neglecting the moment acting on the chip. Experiments have shown that the shear stress obtained for the initial chip formation boundary is 20% too large. Zorev modified the shear angle ψ to ψ^* to offset the discrepancy. The necessity for this modification is that the actual slip lines are not necessarily straight as proposed earlier. Actually, they are more like those shown in Fig. 2-10.

By these procedures, Zorev was able to obtain a more accurate cutting force, the final, the outer, and the initial boundaries of the chip formation zone, the principal axes of deformation and the true deformation of the chip. The resultant force on the tool has the expression:

$$R = \frac{\tau_0 \omega_0 t_0}{\cos(\psi_1^* + \omega)\,\sin\psi_1^*(0.9 - 0.5\cot\psi_1)} \qquad (2\text{-}29)$$

where ψ_1^* is the modified angle, which is about 0.8 ψ_1.

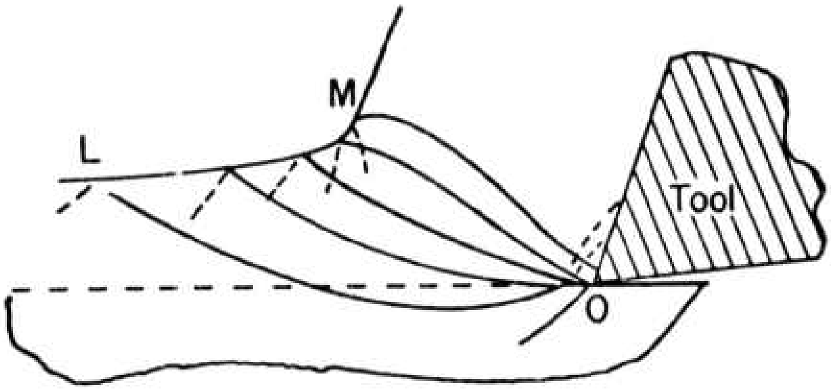

Fig. 2-10 Lines of slip in the chip formation zone

Evans [20] considered the problem of plowing brittle materials (coal) with a symmetric shaped wedge. A scheme similar to Merchants' metal cutting mechanics was proposed in that the chip is in static equilibrium. However, chips formed in plowing brittle material are discontinuous and the fracture mode is assumed essentially tensile in nature.

The model to be treated is a right-angled quarter-space of brittle material, as shown in Fig. 2-11. The breakage curve is assumed to be a circular arc initiated from the tip of the wedge. The chip is acted upon by three resultant forces. The tensile force T is the resultant of the tensile stress acting along the circular arc. The force R' making an angle φ with the normal of the tool surface is exerted by the tool. Thirdly, a concentrated force S, acting on point D, produces static equilibrium of the chip.

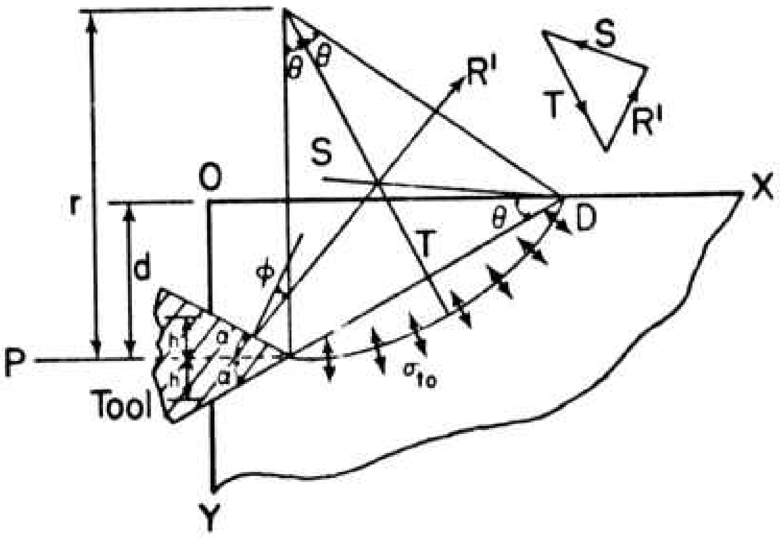

Fig. 2-11 Evans' plowing problem

Immediately before the fracture occurs, the stress acting on the circular arc is assumed to reach the tensile strength of the material $\sigma_{to}d$. Thus, T can be expressed as a function of depth of cut d, and angle θ. Equilibrium of the chip gives P, the horizontal thrust as a function of θ and α, multiplied by $\sigma_{to}d$; thus

$$P = 2R' \sin \alpha$$

$$= \frac{2\sigma_{to}d(1 + \cot^2\theta) \sin^2(\alpha + \varphi)}{h/d + 2 \cot \theta \sin(\alpha + \theta) \cos(\alpha + \varphi) - 2 \sin^2(\alpha + \varphi)} \qquad (2\text{-}30)$$

The assumption of minimum work done by the horizontal thrust P, i.e., $\partial P/\partial\theta = 0$ is employed. In addition, the findings of Evans and Murrell [21] are used; namely, that the force required to push a wedge in normal to a face can be accounted for in terms of a "penetration resistance" closely allied to the compressive strength σ_{co} of the coal. The resulting two supplemental equations are then

$$\frac{\partial P}{\partial\theta} = \cot^2\theta \sin(\alpha+\varphi) \cos(\alpha+\varphi) + \cot \theta \left[\frac{h}{d} \quad 2 \sin^2(\alpha+\varphi)\right]$$

$$- \sin(\alpha+\varphi) \cos(\alpha+\varphi) = 0 \qquad (2\text{-}31)$$

$$P = 2\sigma_{co}h \qquad (2\text{-}32)$$

From the last three equations, one can solve for P as a function of α, with φ and $K = \frac{\sigma_{co}}{\sigma_{to}}$ ($K \approx 10$ for brittle materials) as parameters. The results are plotted in Fig. 2-12. The angle θ can also be calculated. From Fig. 2-12, it is readily seen that the effect of parameter K is small (for $\varphi = 0°$). This , in turn, implies that the penetration of the wedge before breakage takes place is small. If one assumes that the penetration is negligibly small, the expression for P is simplified to be

$$P = 2\sigma_{to}d \frac{\sin(\alpha + \varphi)}{1 - \sin(\alpha + \varphi)} \qquad (2\text{-}33)$$

Equation (2-33) was used to plot the results in Fig. 2-12 for $\varphi = 10$, 20 and 30°.

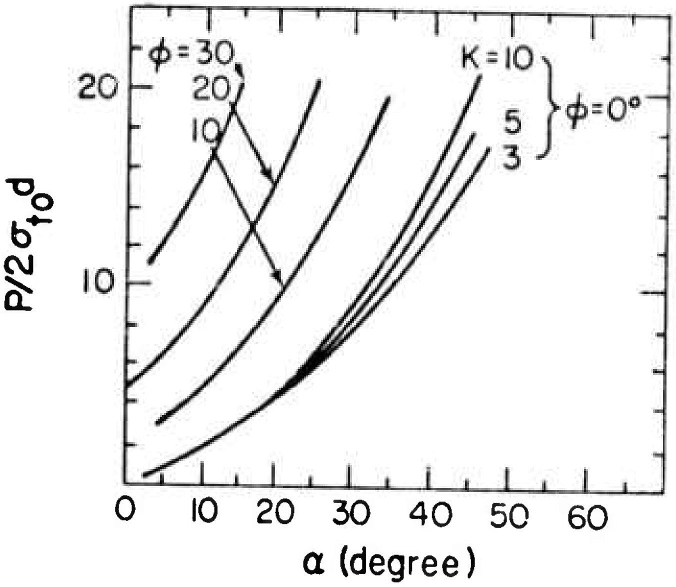

Fig. 2-12 The horizontal thrust force P versus the half-wedge angle α

Experiments were carried out by Evans on several coals. The results compared favorably to his theoretical results. However, a discrepancy was noted in the theoretical and experimental tensile strengths. Evans attributed this discrepancy to the assumption that the mode of failure is a sudden uniform disruption, which does not take into account the crack propagation effect. He proposed a way to compensate for this effect by assuming that the tensile stress varies along the circular arc according to the law $\sigma_{to}(x/\ell)^n$. Comparing with the experimental results, he found that $n = 8$ gave a good result.

Evans [22] continued his study on plowing to consider the effect of bluntness of the wedge. The geometry of the problem as shown in Fig. 2-13. He assumed that the compressive force on the half-band of the wedge needed to initiate the crack is of the form $\frac{\sigma_c}{2}\left(\frac{2b}{d}\right)^m d$, where σ_c is the compressive stress and m is a generalized parameter to be determined (which was found to be in the vicinity of $\frac{1}{2}$). Again, the scheme of a tensile failure along a circular arc was assumed. The chip equilibrium condition plus the minimum work hypothesis enabled the horizontal force on the wedge needed to initiate fracture to be calculated. For the case of zero penetration of the wedge before crack initiation, he obtained

$$P = 2\sigma_{to}d\left[\frac{\sin(\alpha+\varphi)}{2\sin\theta\cos(\theta+\alpha+\varphi)} + 2^{m-1}\left(\frac{\sigma_c}{\sigma_{to}}\right)\left(\frac{b}{d}\right)^m\left(1 + \frac{\sin\theta\sin(\alpha+\varphi)}{\cos(\theta+\alpha+\varphi)}\right)\right] \tag{2-34}$$

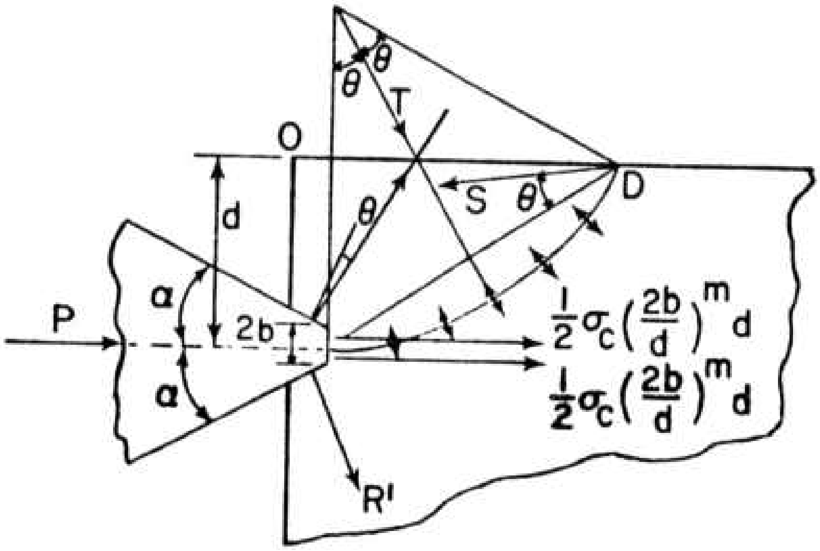
θ
θ
θ
T
O
D
S
θ
d
α
α
P
2b
R'
$\frac{1}{2}\sigma_c\left(\frac{2b}{d}\right)^m d$
$\frac{1}{2}\sigma_c\left(\frac{2b}{d}\right)^m d$

Fig. 2-13 Evans' blunt wedge plowing model

where the angle θ is given by

$$\frac{\cos(2\theta + \alpha + \varphi)}{1 - \cos 2\theta} = 2^{m-1}\left(\frac{\sigma_c}{\sigma_{to}}\right)\left(\frac{b}{d}\right)^m \cos(\alpha + \varphi) \qquad (2\text{-}35)$$

Experimental results on Cwintillery coal were given for comparison. He found that if m = 2/3, his theoretical results were very close to the experimental ones, as shown in Fig. 2-14.

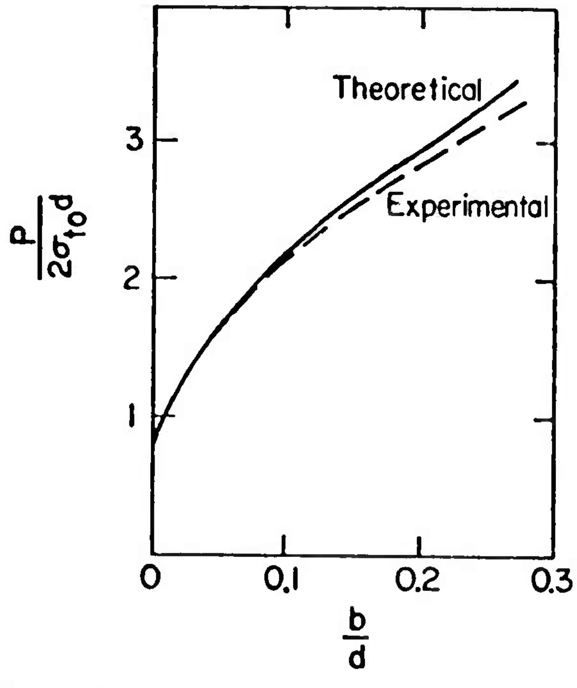

Fig. 2-14 Comparison between experimental and theoretical results, continuous cutting with blunted picks

Recently, Nishimatsu [23] has treated a two-dimensional rock cutting model. He observed that the failure process of rock cutting is as given in Fig. 2-15. The crushed zones can be divided into two categories: (i) the major crushed zone and, (ii) the secondary zone. The tool first chips off several small pieces (minor chips), then a large fragment of rock is fractured (major chip). This process repeats for the entire cutting process.

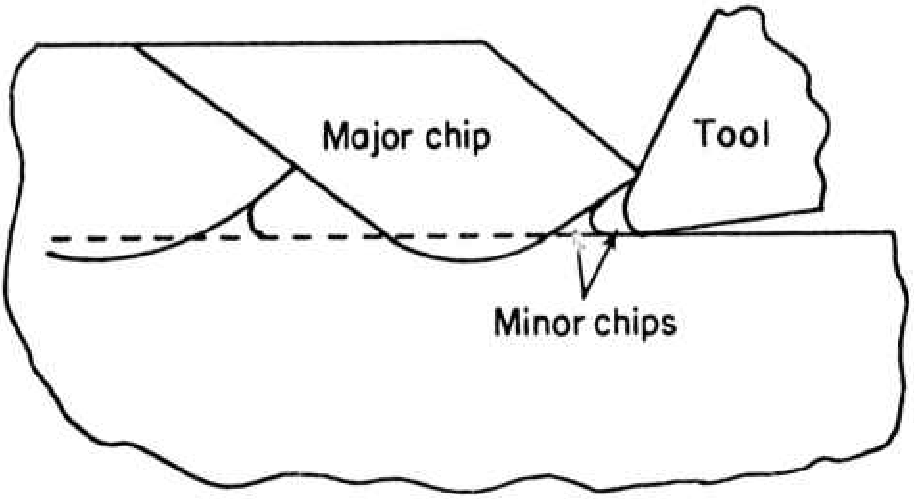

Fig. 2-15 Failure process of rock cutting

With the above observation, the author proceeded to analyze the major chip crushing model as shown in Fig. 2-16.

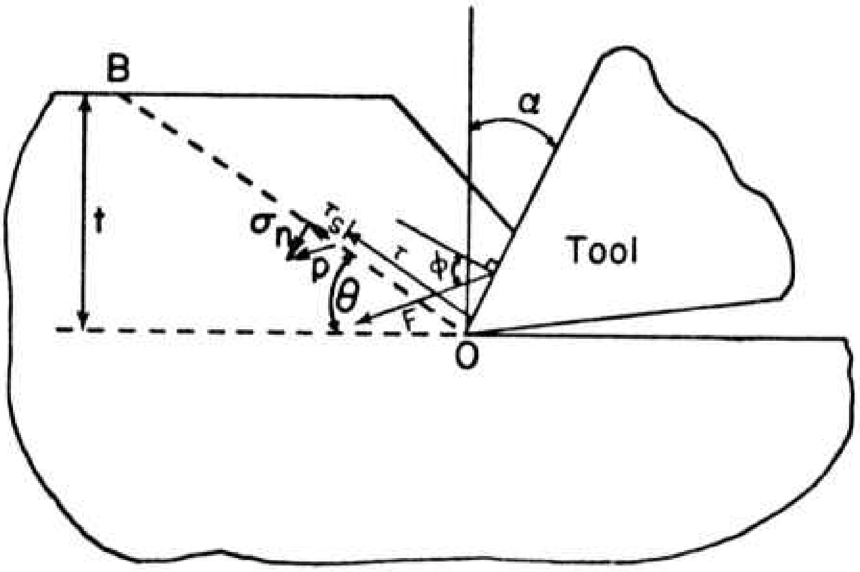

Fig. 2-16 Stress distribution and cutting forces for orthogonal rock cutting

He assumed that the stress distribution along an arbitrary straight line OB in the rock mass to be

$$p = p_0\left(\frac{t}{\sin\theta} - \lambda\right)^n \tag{2-36}$$

where $(\lambda, 0)$ is the polar coordinate of a point p on line OB, and n is the stress distribution factor to be determined. Furthermore, he assumed that the stress p has a constant direction along AB, and the resultant force R will be in equilibrium with the acting force F, from the tool. In so doing, p_0 in eq. (2-36) can be found to be

$$p_0 = -(n + 1)\left(\frac{\sin\theta}{t}\right)^{n+1} F \tag{2-37}$$

One can resolve p into the tangential and normal components along AB. Since fracture will be initiated at the maximum stress concentration point O, the Navier-Coulomb-Mohr criterion can be applied to the above stress components at point O to obtain

$$F = -\frac{1}{n+1}\,\frac{t}{\sin\theta}\,\frac{\tau_0}{\tan k\,\sin(\theta - \alpha + \varphi) - \cos(\theta - \alpha + \varphi)} \tag{2-38}$$

where k is the internal friction angle of the material and τ_0 is the shear strength of the material. The direction of the line OB on which the failure stress acts should be the line which makes the cutting force a minimum. Thus the resulting cutting force is found to be

$$F_c = \frac{2}{n+1}\,\tau_0 t\,\frac{\cos k}{1 - \sin(k - \alpha + \varphi)} \tag{2-39}$$

Thus, F_c is a linear function of the depth of cut t. The horizontal cutting force P and the vertical thrust Q are

$$P = F_c \cos(\varphi - \alpha)$$

$$Q = F_c \sin(\varphi - \alpha) \tag{2-40}$$

Nishamatsu also gave experimental values of P and Q versus rake angle α for sandy tuff and cement mortar. The forces were measured with a circular plate-type dynamometer. He found that φ is a linear function of rake angle α as shown in Fig. 2-17. The experimental cutting force is a linear function of t as predicted by the theory. The stress distribution factor n is found to have a value

$$n = 11.3 - 0.18\,\alpha \tag{2-41}$$

where α is expressed in degrees.

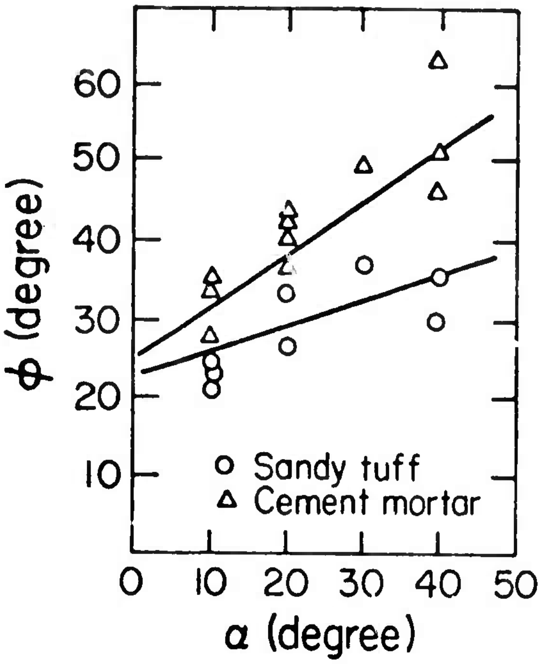

Fig. 2-17 The angle of friction of rock cutting

Svensson and Freshwater [24] gave some experimental studies on rock cutting by employing a photoelastic technique on Catalin 800 and polystyrene. Fringe patterns for various cutting processes were obtained and he was able to deduce the stress distribution during cutting. From his studies, he made the following conclusions:

> A photoelastic stress analysis of chip formation in brittle materials, Catalin 800 and polystyrene, has established that chip formation is a process of crack initiation and propagation due to tensile stresses normal to the crack path. No justification could therefore be found for the application of any analysis based on a shear theory of failure.
>
> The results show that fracture begins at a very small tool penetration and the crack propagates slowly whilst the cutting force is increasing. At some critical crack length, propagation becomes more rapid and the cutting force decreases rapidly. The photoelastic analysis shows there is an intense concentration of tensile stress in the immediate vicinity of the incipient crack. This stress rapidly decays and over the latter portion of the completed crack path, the normal stress becomes compressive. The stress distribution along the crack path, except for regions near the tool tip, agrees with the theoretical results obtained by Shepherd.

The crack path is not a principal stress trajectory and shear stresses of the same order of magnitude as the normal stresses act along most of its length. Near the tool tip, however, the stresses normal to the crack path are principal stresses. Equilibrium of the incipient chip is therefore maintained by the tool force acting on the chip and the normal and shear stress distribution along the crack path. This stress distribution is far more complex than that assumed by Evans. Other observations made during the investigation showed that the crack path was not a circular one. As the crack length increases, the bending effect of the tool force becomes more pronounced. This causes a rotation of the principal stress directions such that the radius of curvature of the resulting crack diminishes as it penetrates further.

There are two aspects which are of importance in studying the machining of brittle materials.

(a) The maximum force required to initiate the crack,
(b) The energy required to remove a unit volume of material.

From the results of these investigations it appears that the maximum force is largely dependent of the depth of cut but would possible depend upon depth of cut in addition to tool angle.

Further work is necessary to establish the mechanism of crack initiation, the concept of a critical crack length (which governs the maximum force) and the effect of tool angle on these.

Other methods of rock cutting which may be applied to layer cutting analysis include crater indexing with a sharp wedge or with a blunted tool. Garner [25] gave possible fractures for crater indexing (Fig. 2-18) and Cheatham [26] gave possible slip lines for indexing in a plastic rock (Fig. 2-19).

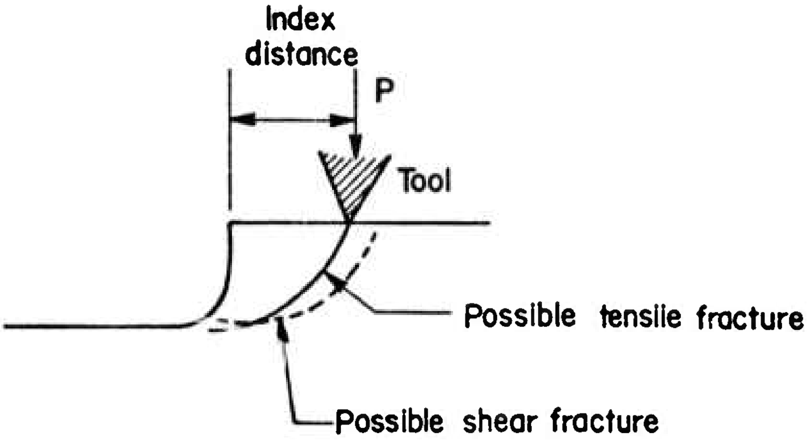
Index distance
P
Tool
Possible tensile fracture
Possible shear fracture

Fig. 2-18 Garners possible fractures for crater indexing

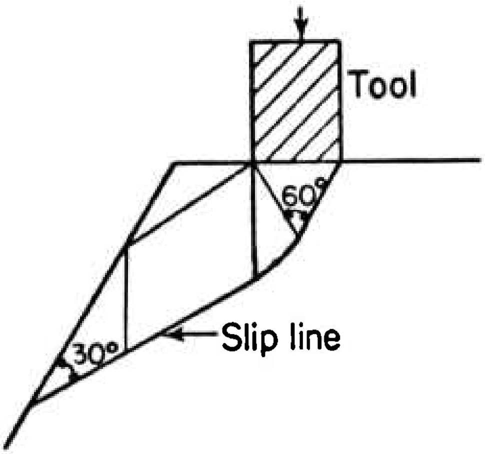
Tool
60°
30°
Slip line

Fig. 2-19 Cheathams' possible slip lines for indexing in a plastic rock

2-4 REFERENCES

1. Jaeger, J. C., "Brittle Fracture of Rocks," Chap. 1, Failure and Breakage of Rocks, The 8th Symposium on Rock Mechanics, The American Institute of Mining, Metallurgical and Petroleum Engineers, Inc., 1967.

2. Brady, B. T., "A Statistical Theory of Brittle Fracture for Rock Material, Part 1--Brittle Failure Under Homogeneous Axisymmetric States of Stress," Int. J. Rock Mech. Min. Sci. 6, pp. 21-42, 1967.

3. King, L. V., "On the Mathematical Treatment of the Internal Friction and Limiting Strength of Rocks Under Conditions of Stress Existing in the Interior of the Earth," J. Geol., 25, pp. 638-658, 1917.

4. Nadai, A., Theory of Fracture and Flow of Solids, 2nd Ed., McGraw-Hill, Inc., N. Y., Vol. 1, pp. 176, 220, 222, 242, 1950.

5. Hill, R., The Mathematical Theory of Plasticity, Oxford: Clarendon Press, 1950.

6. Prayer, W., and Hodge, P. T., Jr., Theory of Perfectly Plastic Solids, N. Y., Wiley, 1951.

7. Freudenthal, A., "The Inelastic Behavior and Failure of Concrete," Proc. 1st U. S. Nat. Congress of Appl. Mech., Chicago, pp. 641-646, 1951.

8. Bresler, B. and Pister, K. S., "Failure of Plain Concrete Under Combined Stress," Trans. Amer. Soc. Civil Engrs., 122, pp. 1049-1068, 1957.

9. Murrell, S. A. F., "A Criterion for Brittle Fracture of Rocks and Concrete Under Triaxial Stress and the Effect of Pore Pressure on the Criterion," Rock Mechanics, ed. by C. Fairhurst, pp. 563-577 Pergamon Press, 1963.

10. Maurer, W. C., "The State of Rock Mechanics Knowledge in Drilling," presented at the 8th Symposium on Rock Mechanics; appears in Failure and Breakage of Rock, ed. by C. Fairhurst, pp. 410-460, The Amer. Inst. of Mining, Metallurgical and Petroleum Engineers, Inc. N. Y. 1967.

11. Dutta, P. K., "A Theory of Percussive Drill Bit Penetration," Int. J. Rock Mech. Min. Sci. 9, pp. 543-567, 1972.

12. Mahban, H., "Rock Behavior Under Impulsive Load," Ph.D. Dissertation, The Ohio State University, 1970.

13. Hustrulid, W. A. and Fairhurst, C., "A Theoretical and Experimental Study of the Percussive Drilling of Rock--Part 1-Theory of Percussive Drilling," Int. J. Rock Mech. Min. Sci. 8, pp. 311-333, 1971.

14. Cheatham, J. B. and Gnirk, P. F., "The Mechanics of Rock Failure Associated With Drilling at Depth," at 8th Symposium on Rock Mechanics, appears in Failure and Breakage of Rock, ed. by C. Fairhurst, pp. 410-460, The Amer. Inst. of Mining, Metallurical and Petroleum Engineers, Inc., N. Y., 1967.

15. Pariseau, W. G. and Fairhurst, C., "The Force-Penetration Characteristic for Wedge-Penetration into Rock," Int. J. Rock Mech. Min. Sci. 4, pp. 165-180, 1967.

16. Merchant, M. E., "Basic Mechanics of the Metal-Cutting Process," J. Appl. Mech., pp. A-168-A-175, 1944.

17. Zorev, N. N., Metal Cutting Mechanics, translated by H. S. H. Massey, ed. by M. C. Shaw, Pergamon Press, 1966.

18. Briks, A. A., "Cutting of Metals," Rezaniye Metallov, 1896.

19. Krivoukhov, V. A., "Deformation of Surface Layers of Metal During the Cutting Process," Deformirovaniye poverkhmostnyrh Sloyev metalla v protsesse rezaniya, Mashgis, 1945.

20. Evans, I., "Theoretical Aspects of Coal Plowing," in Mechanical properties of Non-Metallic Brittle Materials," ed. by W. H. Walton, Interscience Publishers Inc., 1958.

21. Evans, I. and Murrell, S. A. F., "The Forces Required to Penetrate a Brittle Material with a Wedge-Shaped Tool," in Mechanical Properties of Non-Metallic Brittle Materials, ed. by W. H. Walton, pp. 432-450, Interscience Publishers Inc., 1958.

22. Evans, I. "The Force Required to Cut Coal with Blunt Wedges," Int. J. Rock Mech. Mining Sci., 2, pp. 1-12, 1965.

23. Nishimatsu, Y., "The Mechanics of Rock Cutting," Int. J. Rock Mech. Min. Sci., 9, pp. 261-270, 1972.

24. Svensson, N. L. and Freshwater, I. J., "Stress Analysis of Mechaning Brittle Materials," (1963) The Tewksbury Symposium, appears in Fracture, ed. by C. J. Osborn, Univ. of Melbourne, 1965.

25. Garner, N. E., "The Photoelastic Determination of the Stress Distribution Caused by a Bit Tooth on an Indexed Surface," M. S. Thesis, Univ. of Texas, January 1961.

26. Cheatham, J. B., Jr., "Indexing Analysis for Plastic Rock," *Proceedings of the 7th Symposium on Rock Mechanics*, 1965, Pennsylvania State Univ., p. 175.

3. SONIC ROCK DRILLING

Study of the basic drilling configuration was begun in the first year of sonic rock cutting and has been previously reported.* In the current phase of work, the basic sonic drilling techniques previously developed were utilized, with certain modifications and refinements. The basic technique was to force a P-11 transducer vertically downward with a static force. A small, bouncing mass drilling tool at the tip of the transducer performed the cutting action through repeated impacts with the rock surface. This impact coupling drilling technique also has been previously described.

The basic parameters of the drilling process have been identified as the transducer drive voltage, the mass and geometry of the impact tool, the static force and the rock properties. A limited number of tests were conducted to establish optimum static force values. Particular attention was given in this phase of work to various tool designs. The parameter of drive voltage was held constant during most of the drilling tests. Some attention was given to using variable frequency versus fixed frequency drive to the transducer. This phase of work continued drilling tests in Indiana limestone and initiated drilling tests on granite.

3-1 APPARATUS

The basic drilling apparatus has been described and shown in an earlier report.** Some modifications were incorporated in this apparatus. First, the external static force applied at the nodal point of the transducer by dead weights was replaced by a pneumatic cylinder capable of applying static forces of up to 200 pounds. Secondly, an air-vacuum system has been incorporated for removal of rock debris. This system includes an air hose on the one side of a cylindrical-shaped plastic container at the transducer tip, and a vacuum system on the other side. The advantages of this set-up are (1) increased drilling penetration rate due to debris removal from the cutting surface, (2) considerable noise reduction in the drilling process, (3) prevention of dust from escaping to the laboratory, and (4) removing some of the heat from the sonic tool. Although items (2) through (4) are desirable benefits, the main objective of the air-vacuum system was for rock debris removal. A schematic of the modified system is shown in Fig. 3-1.

---

* See Annual Technical Report on previous Contract H0210010, "Fundamental Studies in the Use of Sonic Power for Rock Cutting," December, 1971.

**Ibid., p. 37.

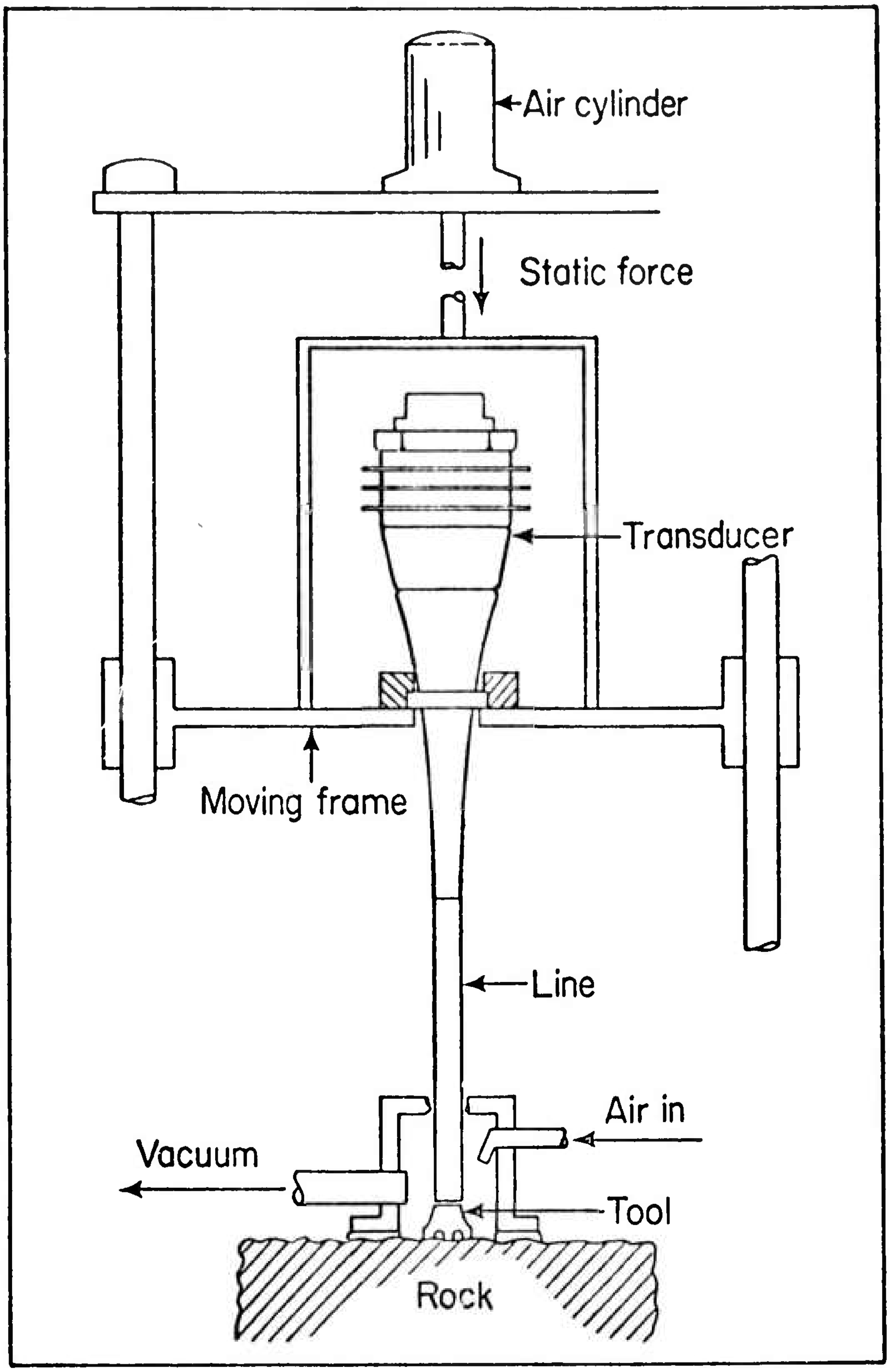
Air cylinder
Static force
Transducer
Moving frame
Line
Air in
Vacuum
Tool
Rock

Fig. 3-1 Drilling apparatus

A system was devised for automatically measuring and recording depth of penetration versus time during drilling. The distance of transducer motion was indicated by the electrical output of a ten-turn potentiometer. This signal was, in turn, fed to an electronic processing unit and from there to an XY recorder. The processing unit also generated a time base signal for the XY recorder. A simple schematic of the system is shown in Fig. 3-2.

3-2 TOOL DESIGN

A number of tool configurations were developed during the course of work. It will be noted that tools used in the earlier phase of work on rock cutting* had large amounts of flat surface area on the impact face of the tools. Such designs were highly inefficient, since rock penetration occurred mainly by crushing action. Tool designs during the current phase of work were aimed at reducing flat areas and increasing edges where stress concentrations could occur.

Drawings of several of the tools tested for limestone drilling are shown in Fig. 3-3. It was generally found that finely pulverized limestone would compact in the recesses and material egress holes in these configurations. Photographs of a second series of tools is shown in Fig. 3-4. It was found that the configuration of Fig. 3-4(b) yielded best drilling results in limestone. Finally, a configuration designed and fabricated for granite cutting is shown in Fig. 3-5. Unfortunately, time did not permit cutting tests to be conducted using this tool.

3-3 DRILLING RESULTS IN LIMESTONE

A series of drilling tests in limestone were carried out to assess the effects of variation in static force on drilling. This was done for Tools #1, 2, 3 and 4, shown in Fig. 3-3. The results are shown in Fig. 3-6. There is a marked lack of uniformity in these results in that the characteristics of each curve differ. Thus, Tool #1 exhibits an irregular behavior with increasing force, having a pronounced dip at about 60 pounds. Tool #2 shows a moderate but continually increasing cutting depth with increasing force, while Tool #3 shows marked increases in cutting at higher forces. Tool #1 exhibits a weak maximum point at about 140 pounds.

The main conclusion drawn from these results was that static force did not appear to be a highly sensitive controlling parameter of the drilling process. Consequently, in most later drilling tests, static force was set at about 200 pounds, which was the largest value obtainable with the available air supply, pneumatic cylinder system.

---

*Ibid., p. 23, 29, 33, 34.

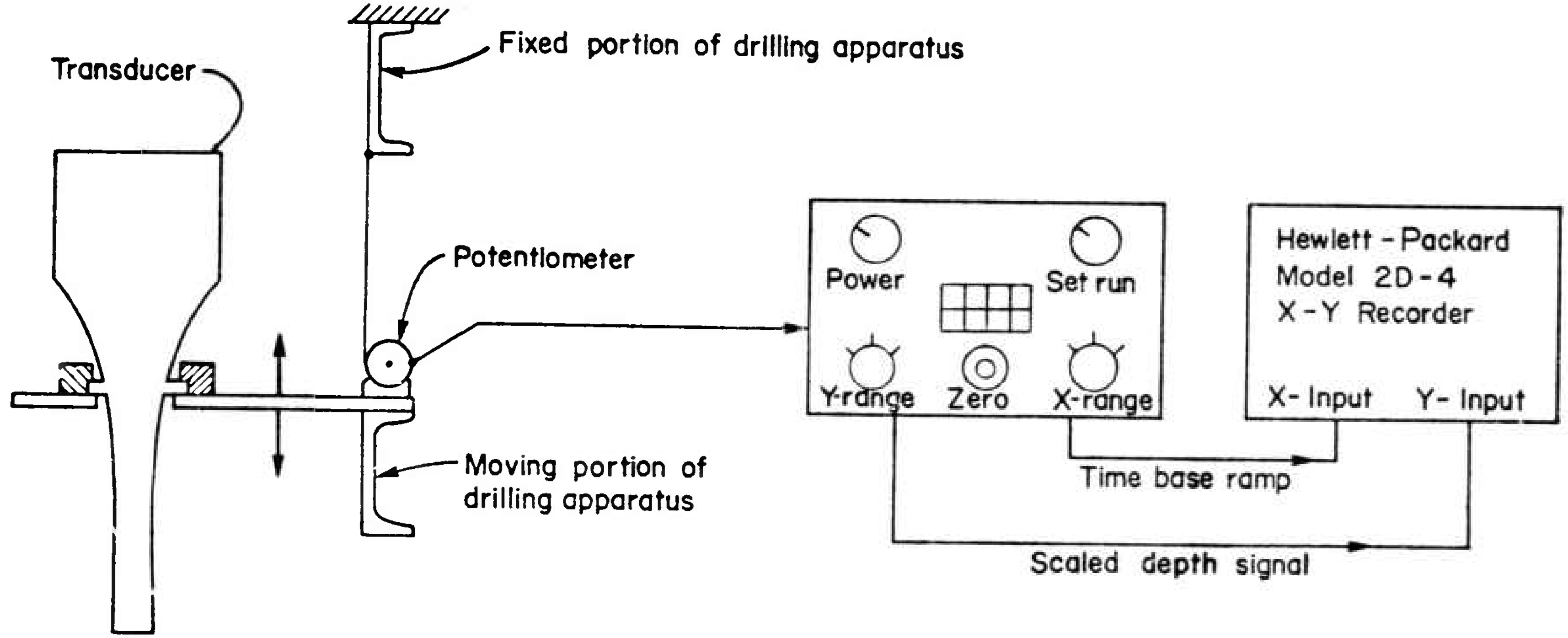
Transducer
Fixed portion of drilling apparatus
Potentiometer
Moving portion of drilling apparatus
Power
Set run
Y-range
Zero
X-range
Hewlett - Packard
Model 2D-4
X-Y Recorder
X- Input
Y- Input
Time base ramp
Scaled depth signal

Fig. 3-2 Schematic of depth-time measuring system

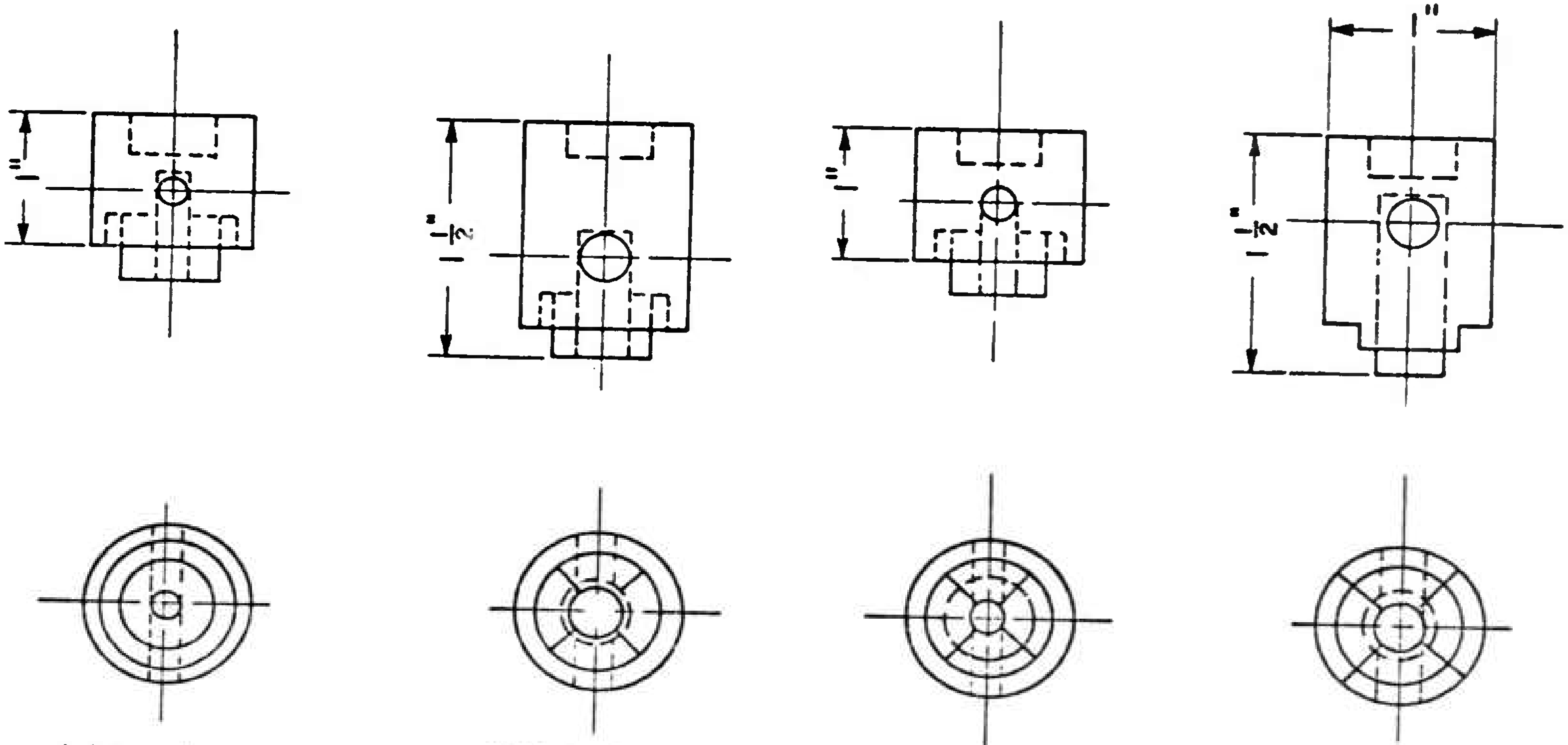

(a) Tool #1 (b) Tool # 2 (c) Tool # 3 (d) Tool # 4

Fig. 3-3 Tool designs used in limestone drilling

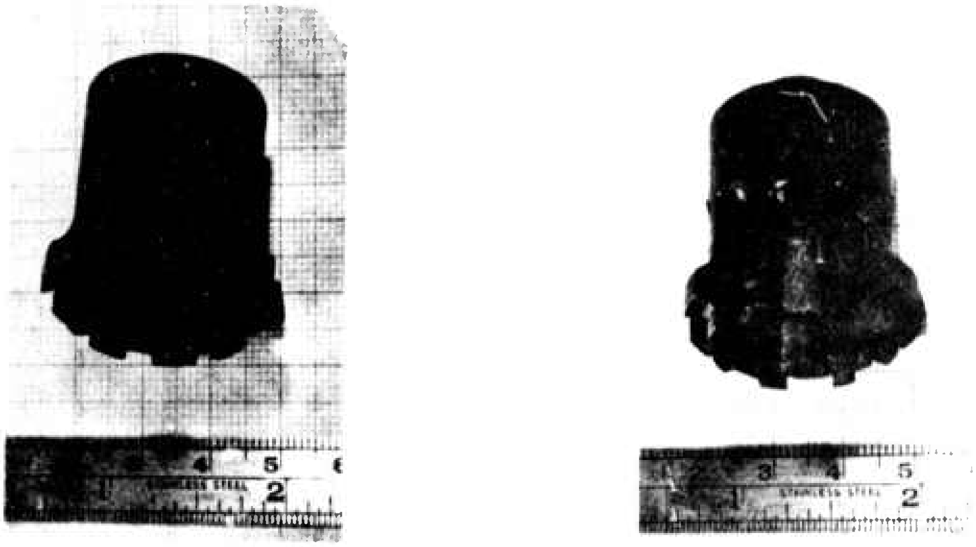

(a) Tool #5 (b) Tool #6

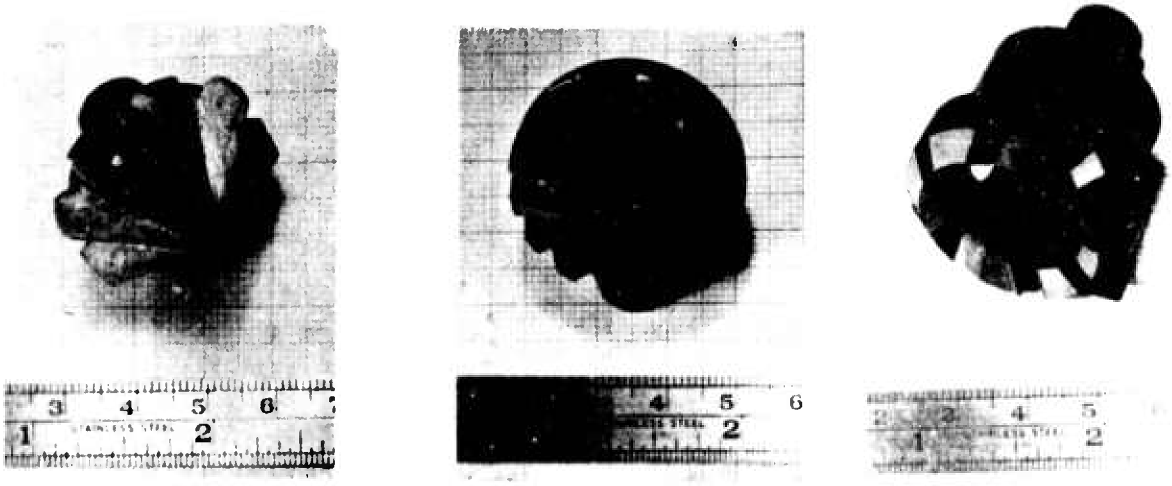

(c) Tool #7 (d) Tool #8 (e) Tool #9

Fig. 3-4 Second series of tool designs

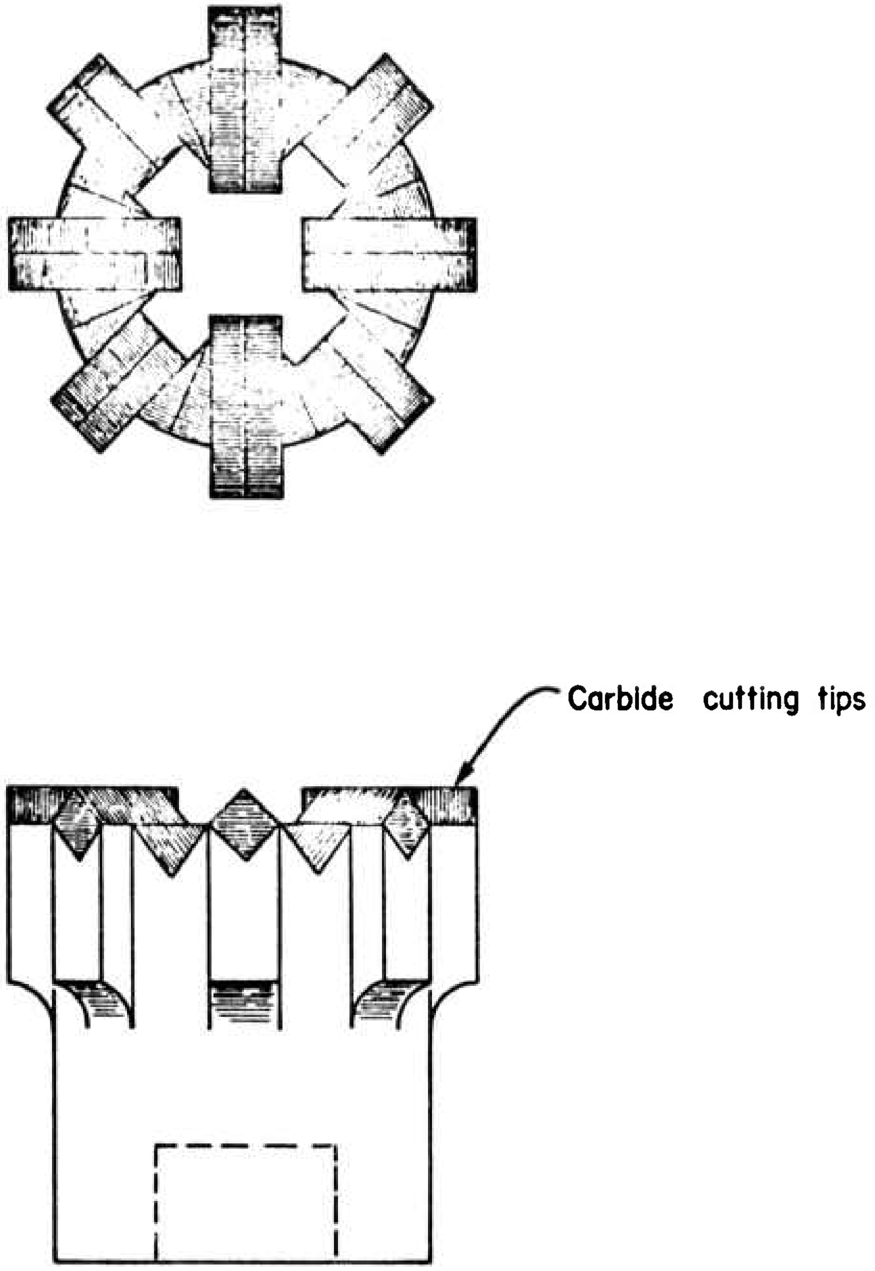

Carbide cutting tips

Scale 2:1

Fig. 3-5 Tool design for granite cutting

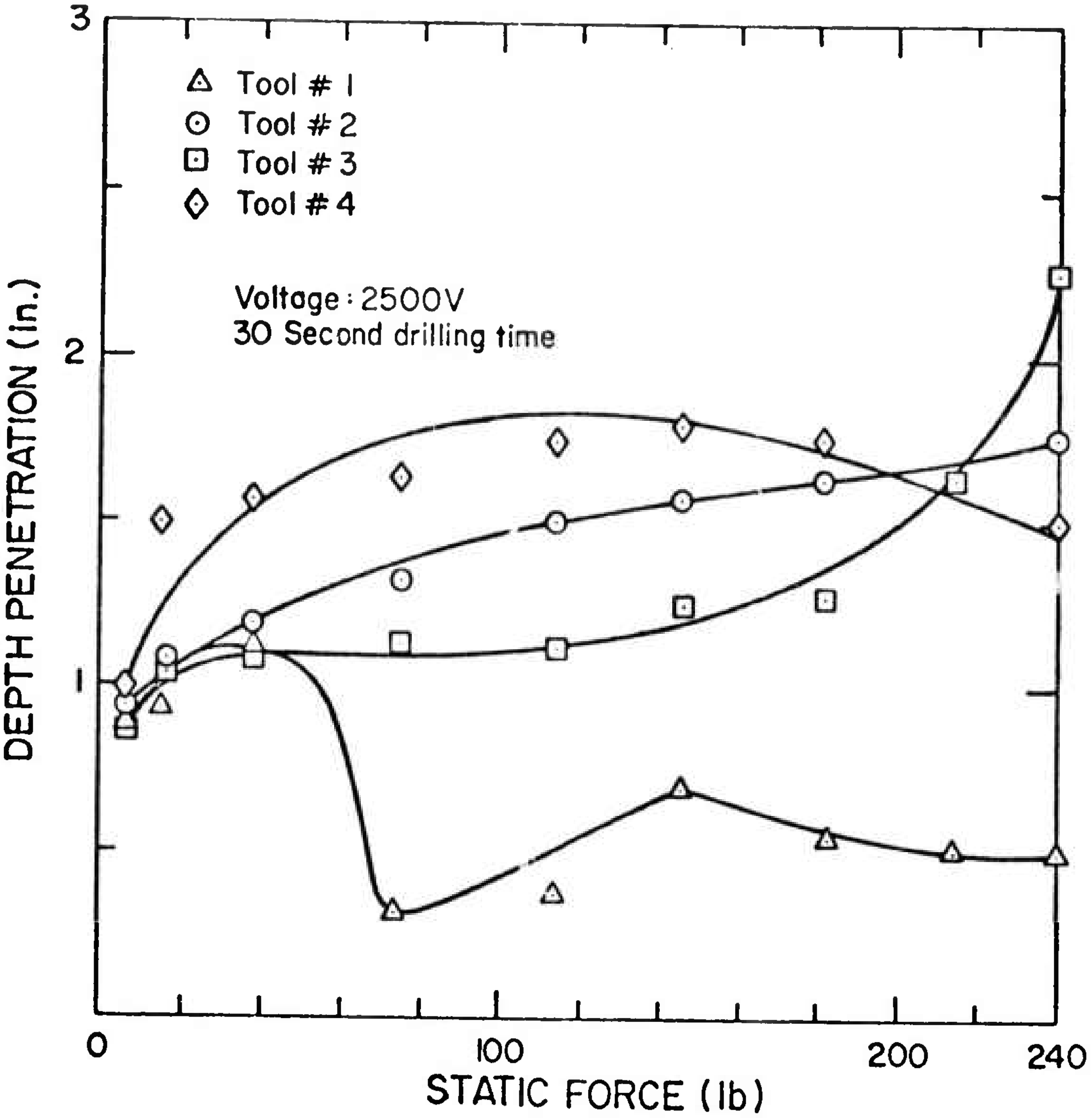

Fig. 3-6 Effects of static force on drilling for various tools

A specific set of tests was run to assess the effectiveness of the air-vacuum system on improving drilling. A specific tool, static force value and drive voltage was selected, and depth of penetration versus time measured with and without the air-vacuum system operating. The results are shown in Fig. 3-7. Without the air-vacuum system to remove drilling debris, it is seen that a point is reached at which penetration practically ceases (lower curve of Fig. 3-7 at about 90 seconds). With debris removal, it is seen that a steady penetration rate is achieved. In both cases, initial penetration rates are quite rapid and about comparable. This is to be expected in the early stages when both the lack of debris and the aspect of cutting into the initially flat surface combine to speed cutting.

The influence of variable frequency versus fixed frequency drive to the transducer was also assessed, with the results shown in Fig. 3-8. The basis for conducting this test was the known difficulty in achieving a transducer resonance frequency at the fixed power supply frequency at high voltage operating conditions. Secondly, there was also the known problem of shifting transducer frequency during operation due to temperature effects. A drilling test at fixed frequency was conducted. Then, a drilling test was conducted during which the drive frequency was varied during the test in a manner to maintain peak power into the transducer.

As is evident from Fig. 3-8, the difference in penetration becomes fairly significant for increasing time (say, beyond 30 seconds). The probable cause of fall-off of the fixed frequency data is transducer detuning resulting from temperature increase within the transducer.

Figures 3-9 and 3-10 show penetration tests for several of the cutting tools (Tools #3, 7, 8 and 6). The data shown was obtained with the automatic recording equipment previously described and indicated in Fig. 3-2. All of the results show the similar characteristic of initial rapid penetration (up to 120 in./min initial rate) and then a reduction to a steady cutting speed. The best results obtained were those for Tool #6 (Fig. 3-10, lower trace), which had the following performance characteristics:

Drilling Test, Tool #6

Material: Indiana Limestone
Hole diameter: 1 1/4 in.
Drilling rate (steady): 11 1/2 mi/min
Volume removal rate: 14 in.^{3}/min
Specific energy: 10,700 W-sec/in.^{3}

3-4 DRILLING TESTS IN GRANITE

As in layer cutting, difficulties were encountered in cutting granite. Unlike the layer cutting work discussed previously, where

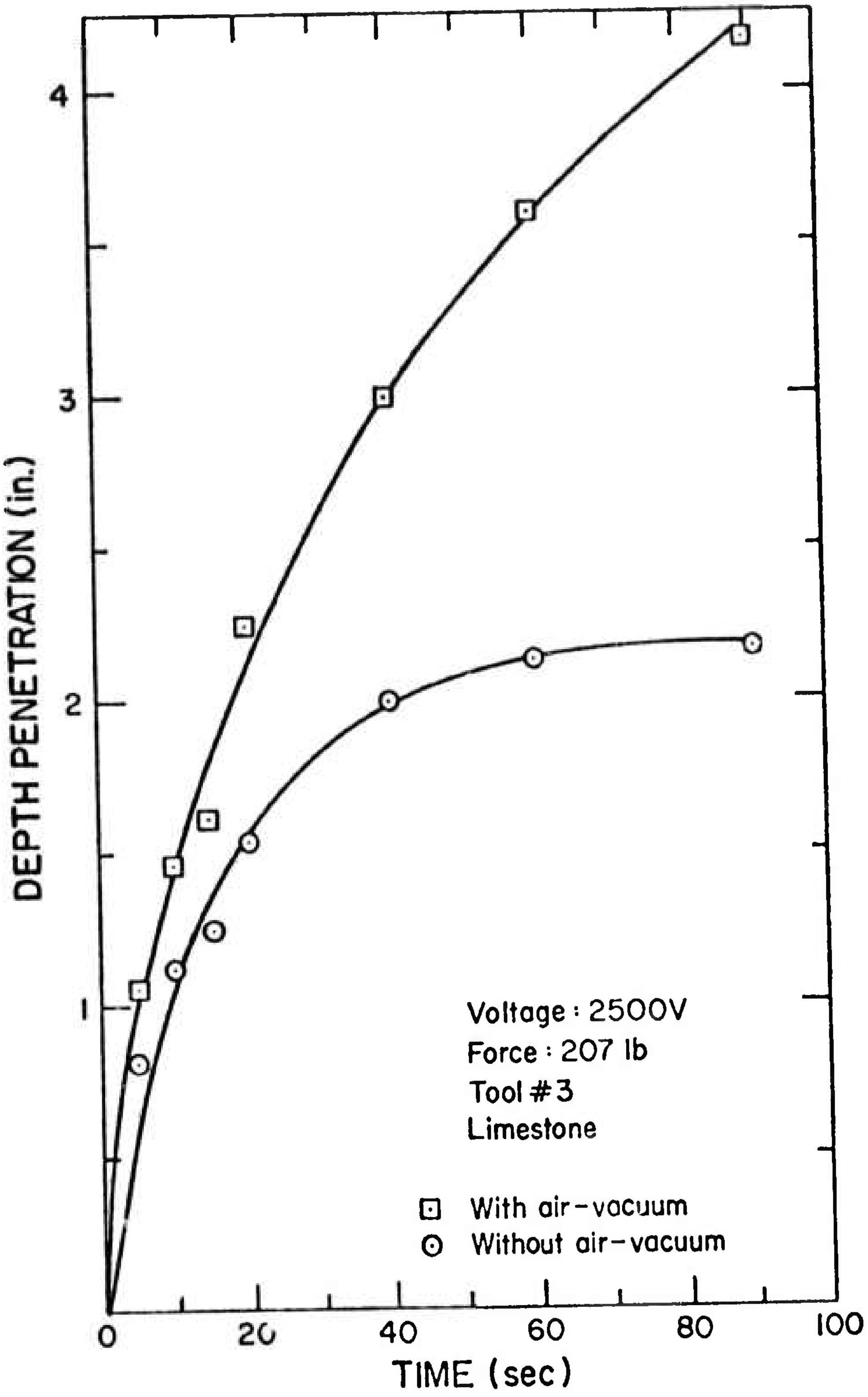

Fig. 3-7 Penetration rate with and without the air-vacuum system

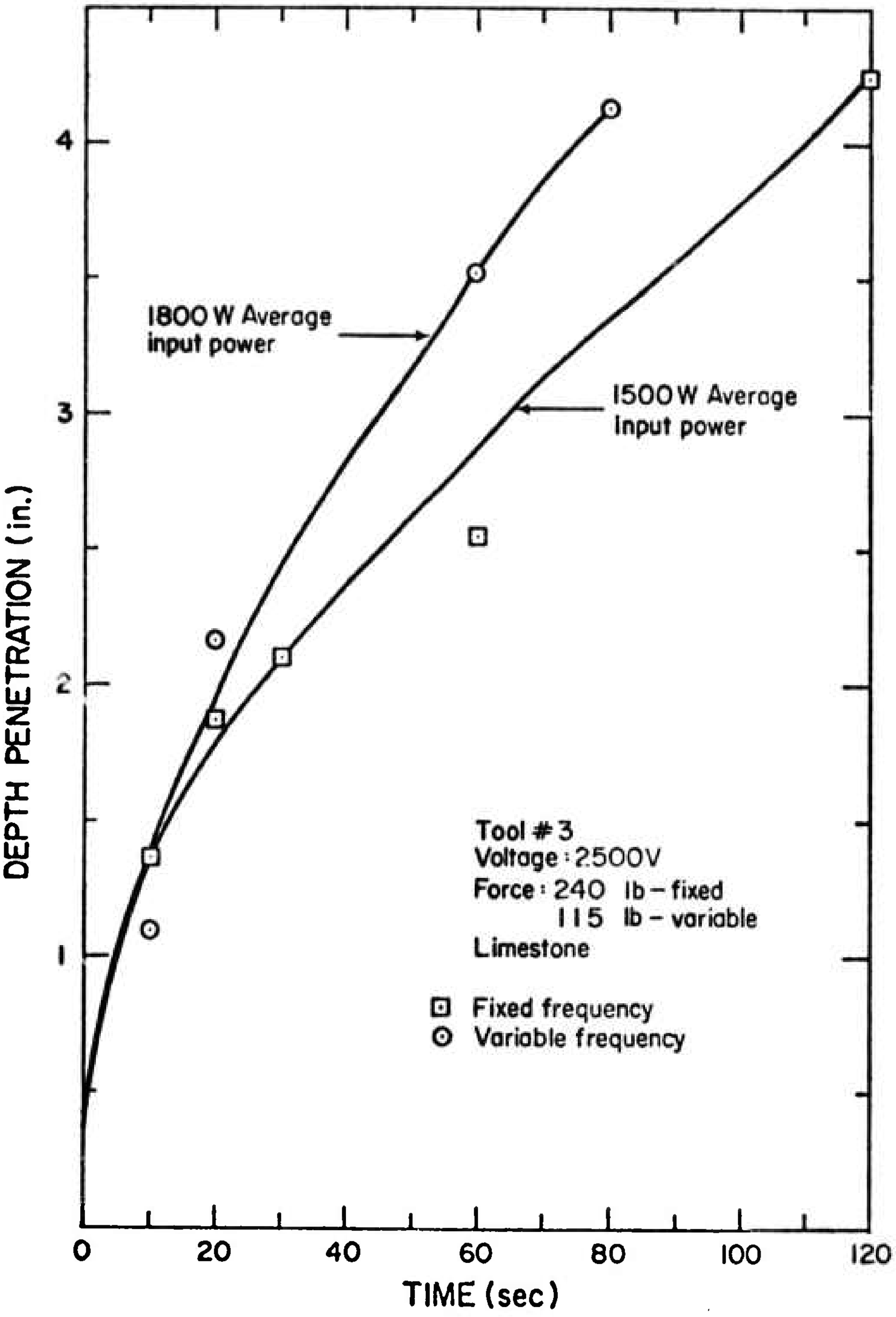

Fig. 3-8 Depth of penetration versus time for fixed and variable frequency operation

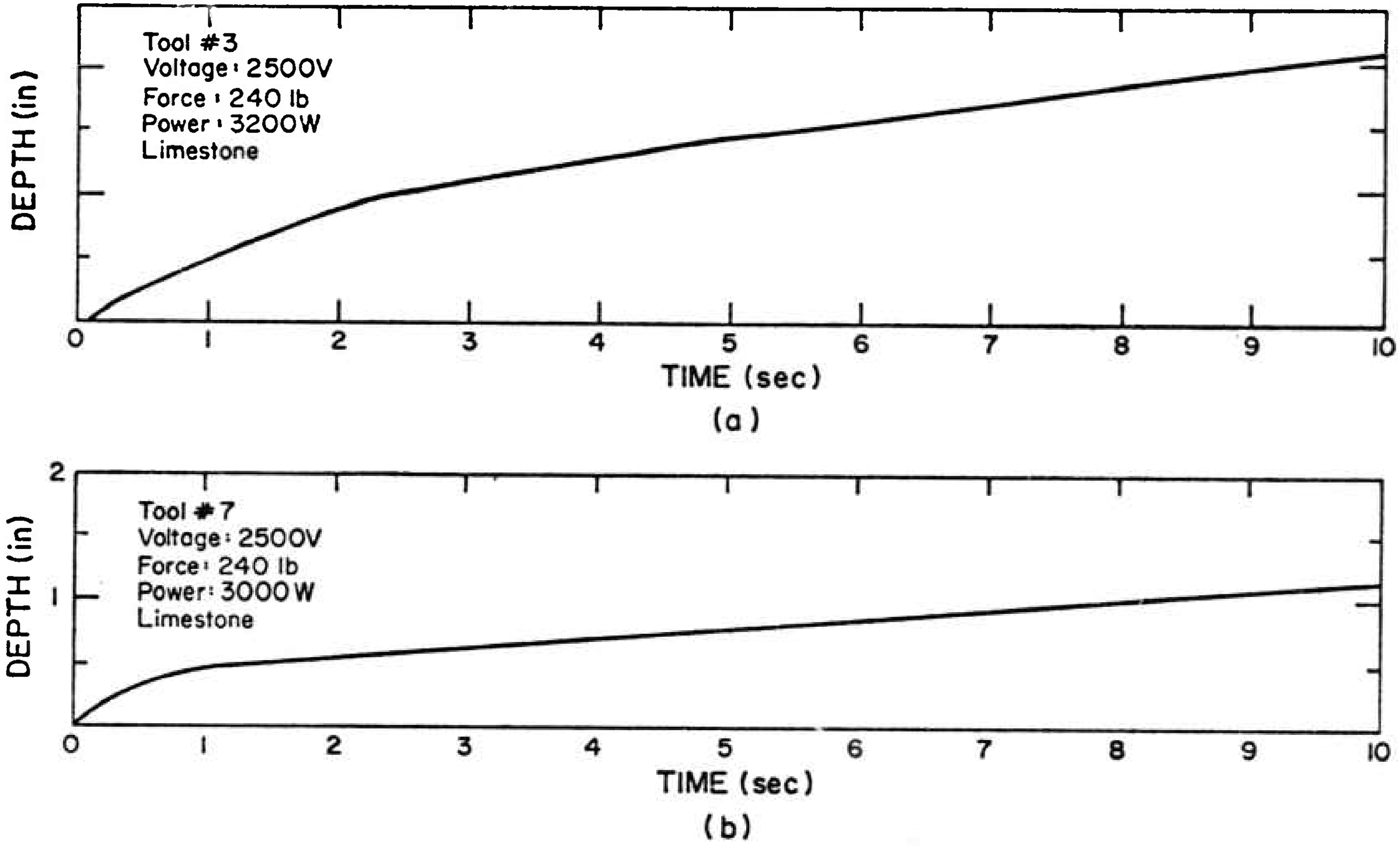

Fig. 3-9 Depth of penetration versus time for (a) tool # 3 and (b) tool # 7

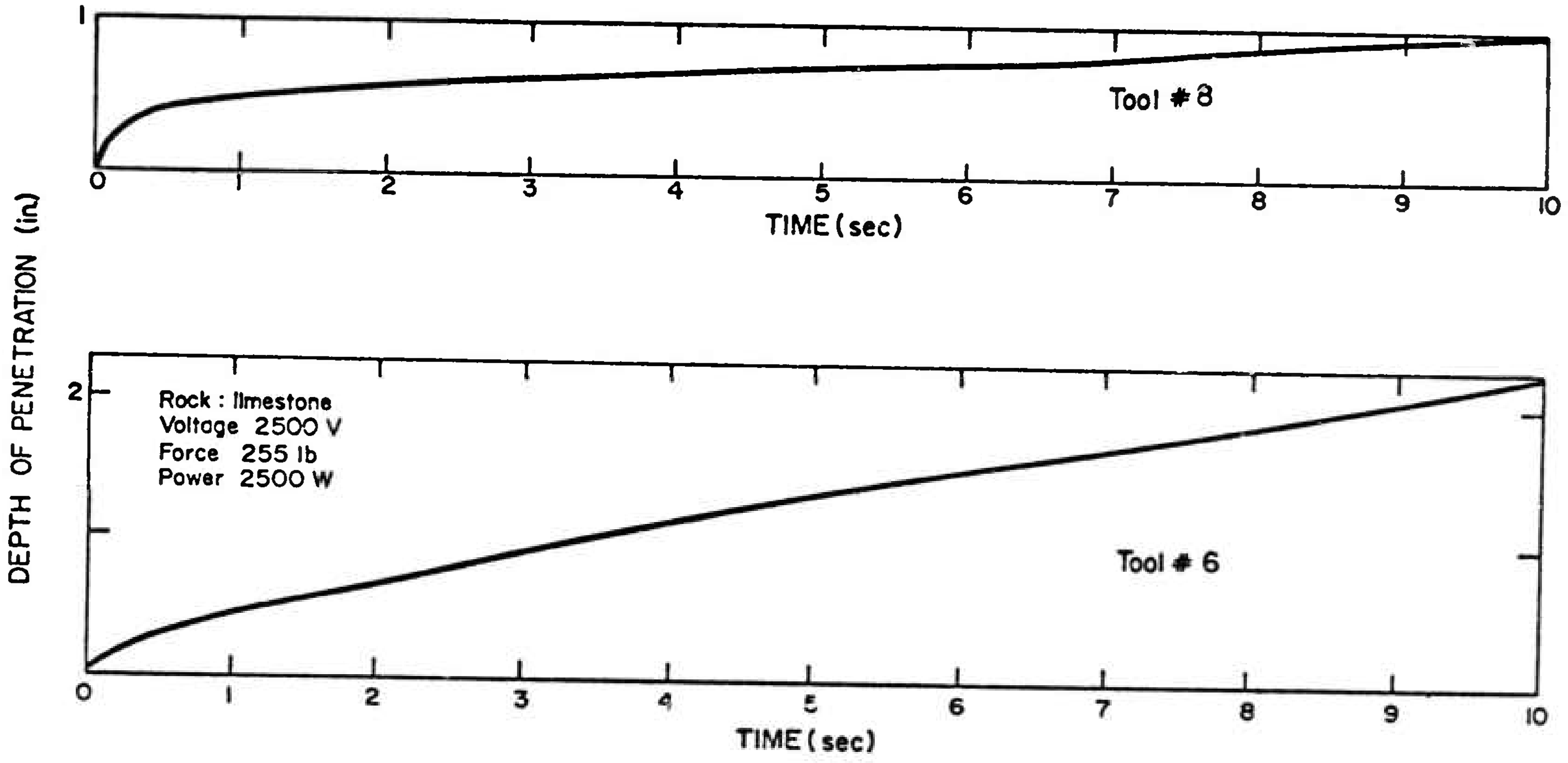

Fig. 3-10 Depth of penetration versus time for tools # 8 (upper trace) and # 6 (lower trace)

some success was finely achieved, the efforts at drilling in granite were essentially negative throughout. The various cutting tools developed for limestone drilling had little effect on granite specimens. Hardened steel tools dulled in matters of seconds or fractured at stress concentration points. Drilling tests, while frequently ineffective, were nearly always spectacular. The region of the tool-rock interface would reach a red heat and showers of sparks would be thrown from the impact area.

Several tests were done on granite drilling using slightly unusual types of tools. The main tools were carbide-tipped steel and pieces of ceramic. The ceramic tools were made of zirconia. It was possible to drill about 1/2" into granite boring a 3/4"-diameter hole. The ceramic would chip into smaller pieces. It appeared the drilling was achieved by heating and fracturing of the rock. As the ceramic was impacted by the P-11, the interface between the ceramic and granite actually became red hot. Next, an impact tool with two carbide inserts was tried, with the inserts mounted in a sloped manner. During drilling the carbide tips penetrated the granite to a depth of 3/16". The flat surfaces of the tool then impacted the rock and no further drilling was achieved.

Drilling tests were also done using a sharp wedge tool made of tool steel. Before using the transducer, tests were done on a static testing machine. With a few thousand pounds of force it was possible to force the wedge tool into granite about 3/16" with no signs of tool deformation. The same tool was then used with a P-11 transducer drilling into granite. The tool penetrated about 3/16" with considerable wear. A possible method of reducing this wear would be to use carbide tips and rotate the tool.

The end of the project work period arrived before tool rotation schemes or additional drill configurations could be tested. For example, the tool configuration of Fig. 3-5 was not completed in time for testing. Although it is likely that these modifications would have somewhat improved granite drilling, it is questionable whether drilling rates of practical significance would have resulted.

4. ANALYSIS OF ROCK DRILLING

The feasibility of utilizing sonic energy for drilling brittle materials, such as concrete or rock, has been under study for some time. The basic process employs a sonic transducer mounted on a support structure and a slug of metal, called the "tool", as shown in Fig. 4-1 and as previously described in this report. The tools are of a general cylindrical shape with various tip and end geometries. Sonic energy is transmitted by means of impact coupling, or in other words, by repeated impact of the tool between the transducer and load at rates of hundreds to thousands of cycles per second. The tool impacts against the rock after impacting with and acquiring energy from the vibrating transmission line. Some energy of the tool is transmitted into the rock and results in some fracture of the rock surface. The tool then rebounds from the rock surface due to elastic recovery and again impacts against the transmission line tip. Because of the energy withdrawal from the transducer by the tool during tool-line impact, the internal energy of the transducer is at a lower level right after impact. It recovers before the next impact occurs.

Although the impact coupling process is rapid and somewhat random, it is a continual sequence of two clearly defined events: (1) impact and rebound of the tool against the vibrating line, and (2) impact and rebound of the tool from the load. Therefore, a rational analysis of impact coupling becomes possible and can be divided into three areas of study -- tool-line impact, tool-load impact and transducer analysis. Each area of these analyses involves several controlling parameters. The mass and tip geometry of the tool, the rock properties, and the energy level of each impact affect the incident-rebound velocity relationship as well as the characteristics of the impact zone. The end geometry and mass of the tool and the geometry and vibration amplitude of transmission line tip contribute to the characteristics of tool-line impact. The transducer is a rather complicated energy conversion system. Many parameters, aside from the supplied terminal voltage, affect its vibration characteristics. All of the previously mentioned parameters interact with each other; any one parameter can easily affect several others in the overall performance of the sonic system. The static force applied by the support structure is another factor in determining the energy transfer of the impact coupling process.

A considerable amount of work has been done previously on various aspects of the sonic impact coupling process, with a fairly complete summary being given in [1],* pp. 184-186. Similarly, study in the area of transducer characteristics has been extensive, although much is yet unknown on the performance of these devices. McMaster, Dettloff and Minchenko [2] reviewed the basic principles of piezoelectric materials, while Dettloff and Minchenko [3] studied the resonant horn.

---

*Numbers in brackets refer to references at the end of this chapter.

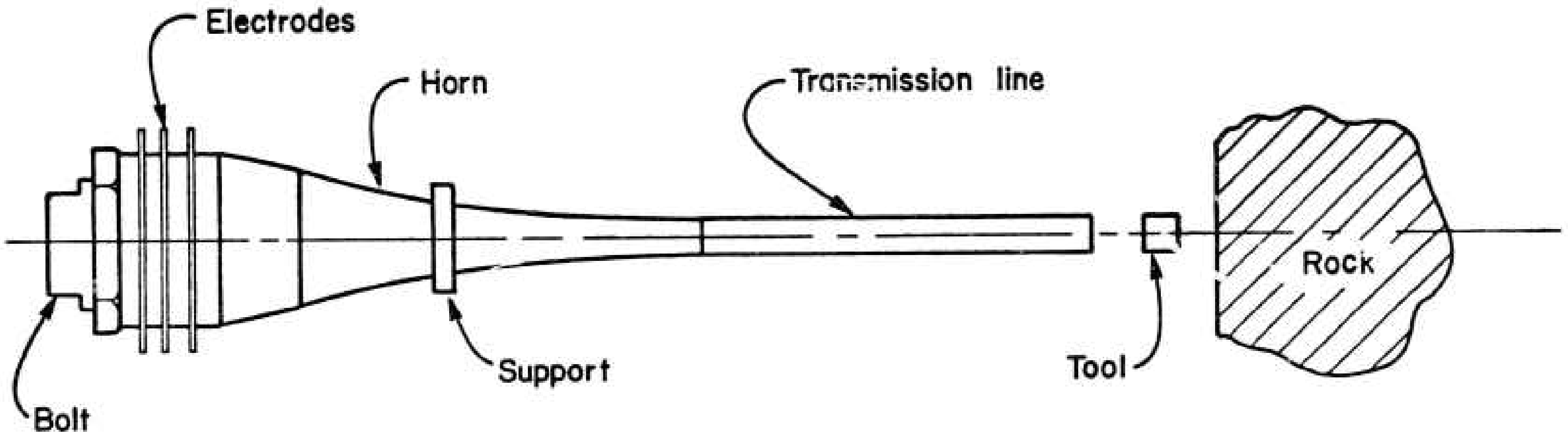
Electrodes
Horn
Transmission line
Bolt
Support
Tool
Rock

Fig. 4-1 Sonic rock drilling system

The overall transducer characteristics was first touched on from the viewpoint of classical circuit and transmission line theory by Hoffman and Swartz [4]. Following this line of approach, Mahtan and Graff [5] developed the transfer function of a sonic power system. Graff [6], [7], in 1969, reviewed the problems of vibrations of crystals and stepped horn resonators. The energy dissipation in a vibrating transmission line was analyzed by Fretwell [8] and Graff [9]. Ma [10], as part of an extensive study of the transducer, has measured the transient response of the transducer to impact. In Section 5 of this report, results obtained by Feng on transducer analysis are given. A more complete description of transducer studies appears in [11].

In the analysis of the rock drilling process, work on the tool-rock and the tool-transmission lines has been previously reported.* Additionally, a qualitative explanation of the general interaction process has been put forth.** In the first section of this chapter, certain additional information on tool-rock impact is presented. In the second section, additional results are given in the tool-transmission line aspects of the process. The third section of the chapter will bear additionally on the transducer aspects of the process.

In section four there is presented an analysis of the effects of various parameters, such as drive voltage, transducer energy storage, static force, tool-load and tool-line parameters on drilling. Finally, all the analyses are united in the prediction of sonic drilling rate of rocks. A numerical example is given at the end of the chapter. A comprehensive treatment of all aspects of the problem may be found in [12].

4-1 TOOL IMPACT ON ROCK--SPECIFIC ENERGY

Previous results on sonic tool impact on rock have appeared in [1], Chapters 1 and 4. During the current phase of work, additional tool-rock impact studies were conducted using apparatus and techniques described in the cited reference. The objective of the work was to establish specific energy data for rock.

To study the specific energy of rock removal for granite, a tool design having a sharp tip made of carbide inserts was used. The tool was propelled into a series of impacts with the rock surface at a specific location. The total energy used was the sum of all the individual impact energies, and the volume of rock removal was obtained by dividing the total weight of the chips and dust collected by the average density of the rock.

---

* Reference [1], Part II, Chapters 1, 4 and 5.

**Ibid, Chapter 6.

Figure 4-2 shows the relationship between incident velocity V_o, specific energy e_s, and volume v for the tool impacting on granite. The tool design is also shown. A linear relationship between v and V_o is observed. This result strengthens the belief that the higher the energy level per impact the more fracture occurs for an equal amount of work. Rock as well as concrete is a brittle material. It is weak in both tension and shear. Fracture occurs when the tensile and shear stress reach a certain level. High energy level impact would cause not only more fractures but also cause them to propagate a greater distance. Therefore, it would cause larger fractures than would a low energy impact and save energy by not breaking rock into smaller fragments than necessary.

4-2 TOOL IMPACT ON A VIBRATING TRANSMISSION LINE

Many aspects of tool impact on a static transmission line were described in [1], Chapter 5, including the effects of a slightly curved tool surface on the rebound. The analysis of the drilling process requires consideration of impact on a vibrating line. Feng [13] has solved the impact problem of a spherical ball against a vibrating transmission line, with some of these results also reported in [14]. The approach used by Feng will be applied to the present case of a cylindrical tool having a slightly curved contact surface impacting a vibrating line.

The tip displacement of a resonant transducer (or transmission line) can be expressed as:

$$u_o(t) = c_i \sin(\omega t + \varphi) \qquad (4\text{-}1)$$

where

φ = phase angle
c_i = amplitude of tip displacement
ω = angular frequency of resonance
t = time measured from the start of tool-line impact

The displacement β_1 of the center of the transmission line tip during impact is a combination of: (i) the displacement due to transducer tip vibration $[u_o(t) - u_o(0)]$, (ii) the displacement due to the stress wave traveling down the transmission line, u_1, and (iii) the local deformation, w_1. The positive directions of β_1, u_1 and w_1 are shown at the upper left hand corner of Fig. 4-3. Therefore, we have

$$\beta_1 = u_1 + w_1 + u_o(t) - u_o(0) \qquad (4\text{-}2)$$

Similarly, the displacement at the tip of the tool, β_2, is

$$\beta_2 = u_2 + w_2 \qquad (4\text{-}3)$$

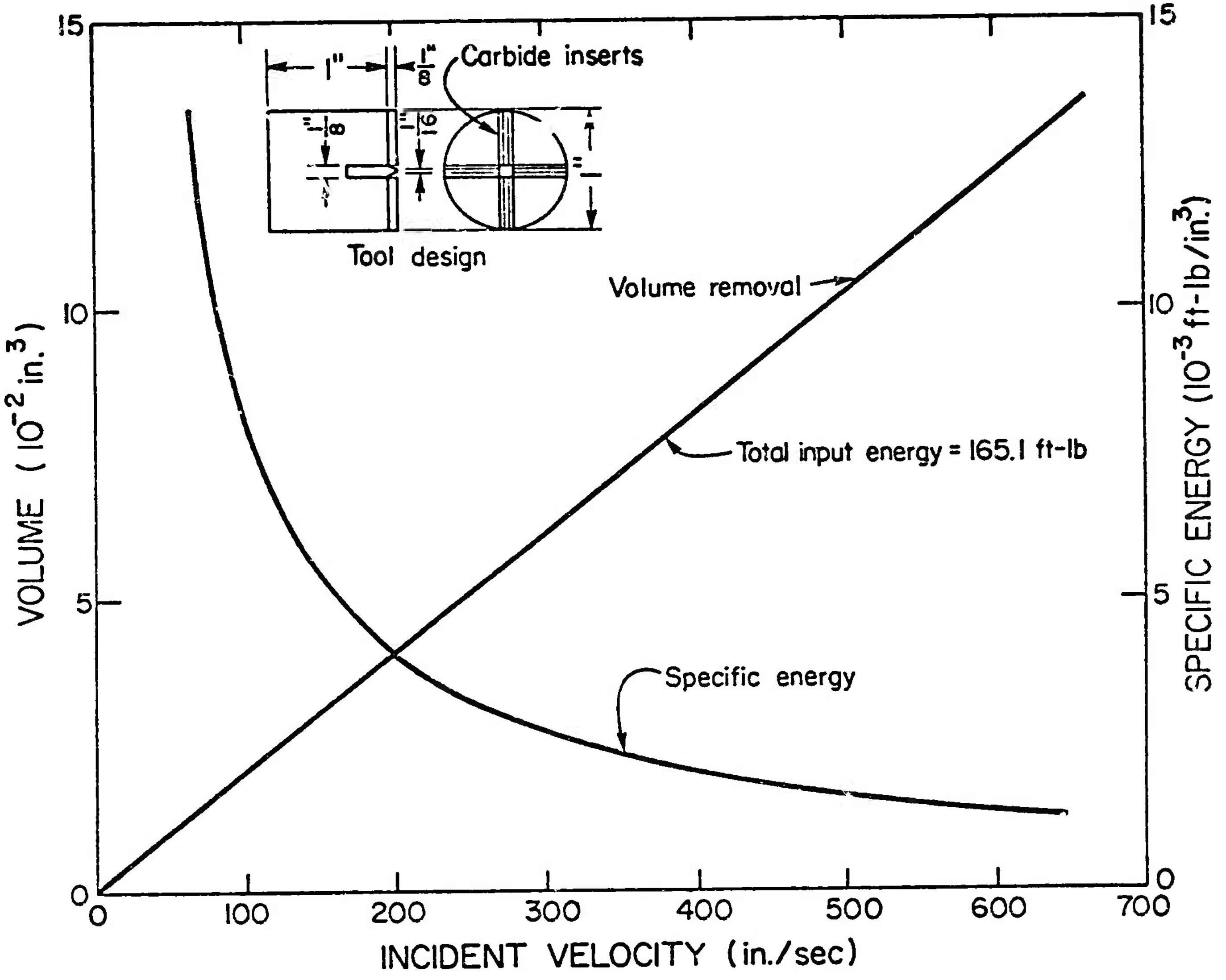

Fig. 4-2 Variations of specific energy and volume removal
(m_e = 1.08 inch)

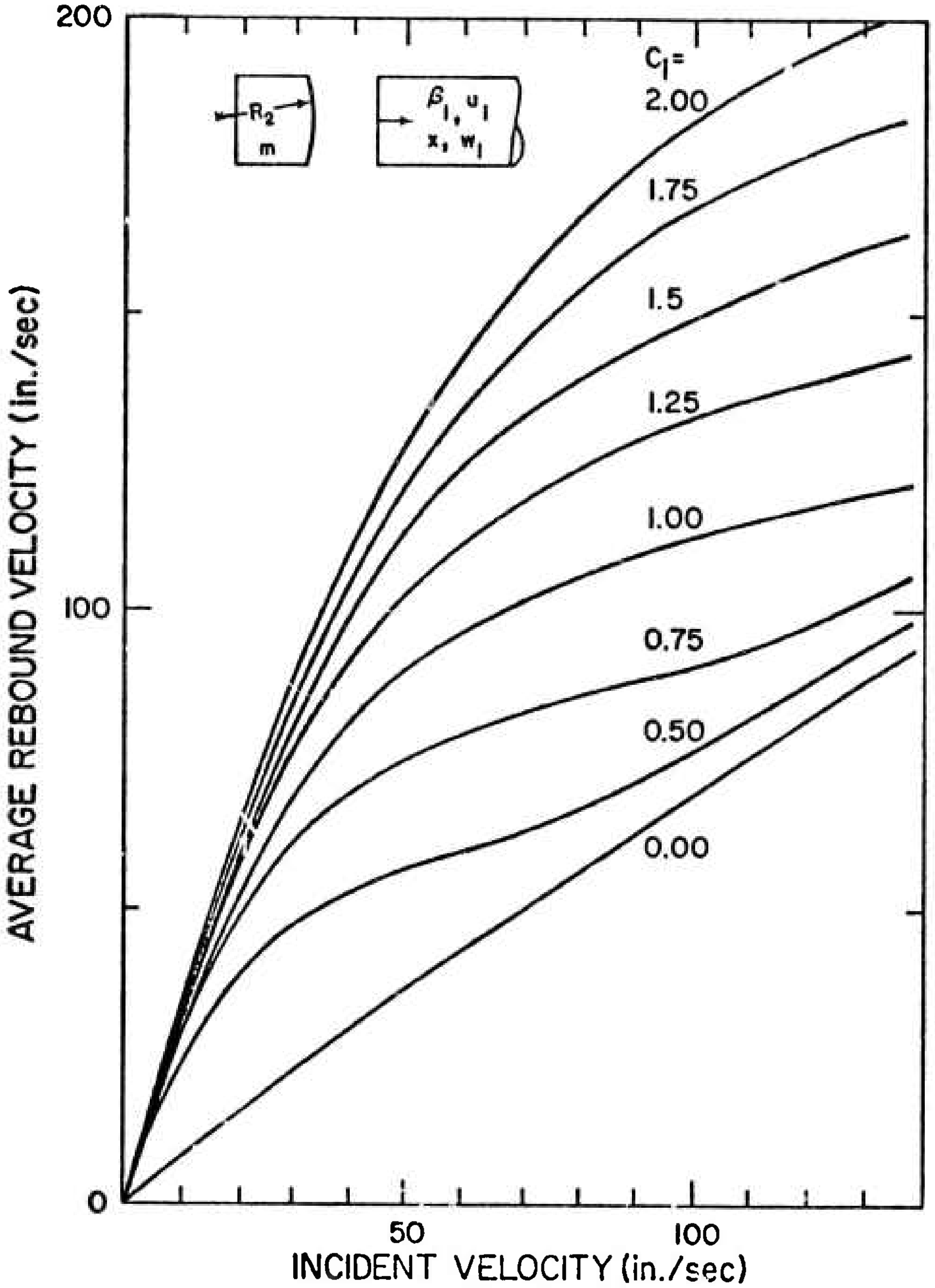

Fig. 4-3 Incident-rebound velocity relationship (R = 10" and m_e = 0.5")

where u_2 is the rigid body displacement of the tool, and w_2 is the local deformation of the tool tip. The positive direction is assumed to be the same as β_1.

During the course of impact,

$$\beta_1 = \beta_2$$

or

$$w_2 - w_1 = u_1 - u_2 + u_0(t) - u_0(0) \qquad (4\text{-}4)$$

The impact period is short and the transmission line is usually long enough that the wave front of the reflected stress wave will not reach the tip during this period. We also assume that the stress wave, due to previous impact, has been damped out. Then the displacement u can be expressed as

$$u(x,t) = f(x - c_0 t) \qquad (4\text{-}5)$$

From eq. (4-5), we can obtain

$$\dot{u} = - c_0 f'(x - c_0 t) \qquad (4\text{-}6)$$

and

$$F = EA \frac{\partial u}{\partial x} = EA\ f'(x - c_0 t) \qquad (4\text{-}7)$$

Eliminating $f'(x - c_0 t)$ in eq. (4-6) and eq. (4-7), we obtain

$$\dot{u} = - \frac{F}{\rho A c_0} \qquad (4\text{-}8)$$

and

$$\dot{u}_1 = \dot{u}_0(0,t) = - \frac{F}{\rho A c_0}\bigg|_{x=0} \qquad (4\text{-}9)$$

By considering the conservation of linear momentum of the tool, one gets the following equation

$$\frac{du_2}{dt} = V_0 + \frac{1}{m}\int_0^T F\,dt \qquad (4\text{-}10)$$

Substituting eqs. (4-9) and (4-10) into eq. (4-4), and defining the "approach", α, as $(w_1 - w_2)$, we have

$$\dot{\alpha} = V_0 + \frac{1}{m}\int_0^T F\,dt + \frac{F}{\rho\,A c_0}\bigg|_{x=0} - c_1\omega\cos(\omega t + \varphi) \qquad (4\text{-}11)$$

Hertz contact theory states that

$$F = -K\alpha^{3/2} \tag{4-12}$$

where K is a constant depending on elastic properties and geometry of the contact surface, and is given as

$$K = 2ER_2^{1/2}/3(1 - \nu^2) \tag{4-13}$$

for a flat transmission line tip where it is assumed that tool and line are made of the same material. Also, R_2 is the radius of curvature of the tool end, and ν is Poisson's ratio. With eqs. (4-11), (4-12) and (4-13), a differential equation for α is given by

$$\frac{d^2\alpha}{dt^2} + \frac{F}{\rho A c_o}\frac{d\alpha^{3/2}}{dt} + \frac{K}{m}\alpha^{3/2} = c_i\omega^2 \sin(\omega t + \varphi) \tag{4-14}$$

A computer program similar to Feng's was written to solve the incident-rebound relationship for tools of different mass and various curvature at the impact end. Figure 4-3 is a typical example of the impact-rebound relationship for various tip vibration amplitudes. All the tools are one inch in diameter but with different tip and end geometries. The mass of the tools is designated as m_e. In the figure, a tool with curved surface of ten inches radius is used. The tool has a one-half inch equivalent length ($m_e = \frac{1}{2}''$); i.e., the tool has a mass which is equivalent to a flat ended rod of one inch in diameter and one-half inch in length. One observation that should be noted is that the rebound velocity is calculated in the sense of average as stated by Feng [13], because the actual rebound velocity varies as to where the tool comes into contact with the transmission line tip.

Figure 4-4 shows the results for four different values of m_e. The main purpose of such a plot is to examine the effect of tool mass on the rebound velocity. It is easy to see that the rebound velocity drops as the mass increases. The value of rebound velocity not only depends upon the mass of the tool but also depends upon the curvature of tool tip.

4-3 TRANSDUCER VIBRATION

As pointed out previously, study in the area of transducer characteristics has been extensive, yet, much is still unknown of transducer performance. This holds particularly for the response of the transducer during and immediately after impact from the sonic tool. Thorough theoretical as well as experimental study is needed to get a complete understanding on this matter. However, it is not the purpose at this stage to go into detailed research in that area. Instead, it is simply to study the internal energy and tip vibration amplitude of a sonic transducer for the purpose of analyzing the sonic interaction process

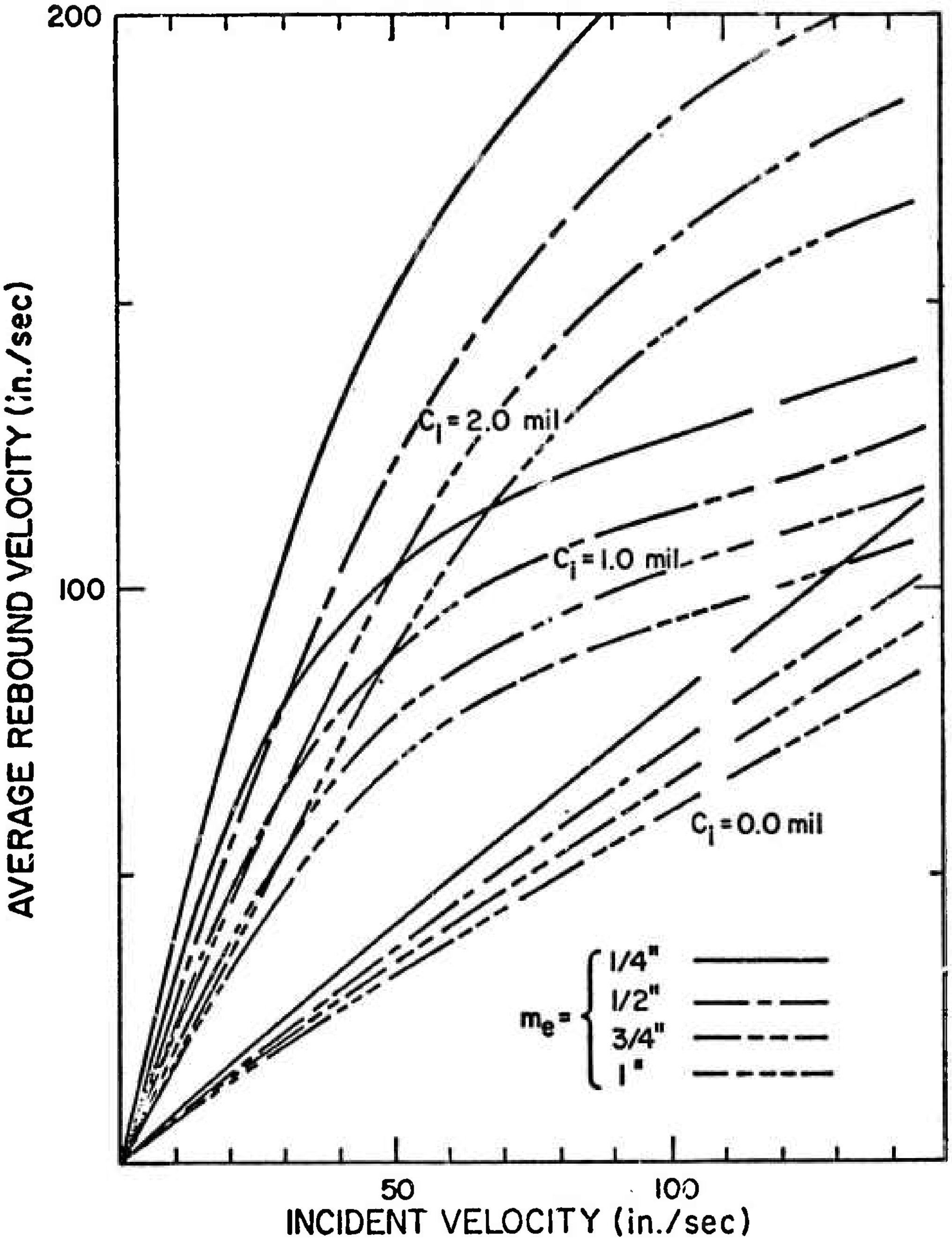

Fig. 4-4 Variation of incident-rebound velocity relationship with respect to equivalent length m_e ($R = 5''$)

and finding the power transmission of the transducer system. The transducer response to impact will be modeled based on observed transducer behavior and basic vibrational principles governing solid materials.

Ma [10] conducted an experiment in the study of energy removal and transducer recovery during tool impact. From this experiment, an interesting phenomenon can be observed. The recovery of the tip vibration amplitude (velocity as well as displacement) is along an exponential curve as shown within the dotted region of Fig. 4-5. Two experimental results of such removal and recovery curves, after data reduction, are shown in Fig. 4-6. The ordinate is nondimensionalized with respect to the total amount of amplitude drop immediately after impact. Some theoretical background, in addition to the previous experimental observations will be given to justify the resulting modeling of the recovery of a sonic transducer after impact.

For convenience of analysis, the discussion will start with the most simple and basic piezoelectric resonator, a cylindrical sandwich type, as shown in Fig. 4-7. Then, the results of this analysis will be expanded to the study of the vibration and damping characteristics of a more complicated sonic resonator.

(A) Forced Vibration of a Cylindrical Sandwich Type Resonator

The most simple and basic piezoelectric resonator is the cylindrical sandwich type as shown in Fig. 4-7. Because of its simple geometry, the analysis is straightforward compared with resonators of more complicated shape.

Usually two kinds of damping exist in a vibration system, viscous damping and Coulomb damping. In a sonic transducer, viscous damping is present within the metal and ceramic materials while the Coulomb damping exists as interfacial friction between the metal and ceramic parts. The viscous damping force is along the direction of particle velocity. In the sonic transducer, radial vibration is always coupled with longitudinal vibration even though the first radial resonant mode is usually a higher order mode than the first longitudinal mode. In the discussion of longitudinal resonance of a transducer, the effect of radial motion is usually neglected and the problem treated as one-dimensional. The direction of the Coulomb friction force in the sonic resonator is radial. The effect of interfacial friction on longitudinal vibration is, therefore, indirect. With the above arguments, the Coulomb friction and viscous damping force in the radial direction can be neglected if the approximation is made to discuss longitudinal vibration only.

In a steady state resonance condition, the amplitude of longitudinal vibration is a constant. The force that the ceramic applies to the metal part also reaches a steady state constant amplitude. The

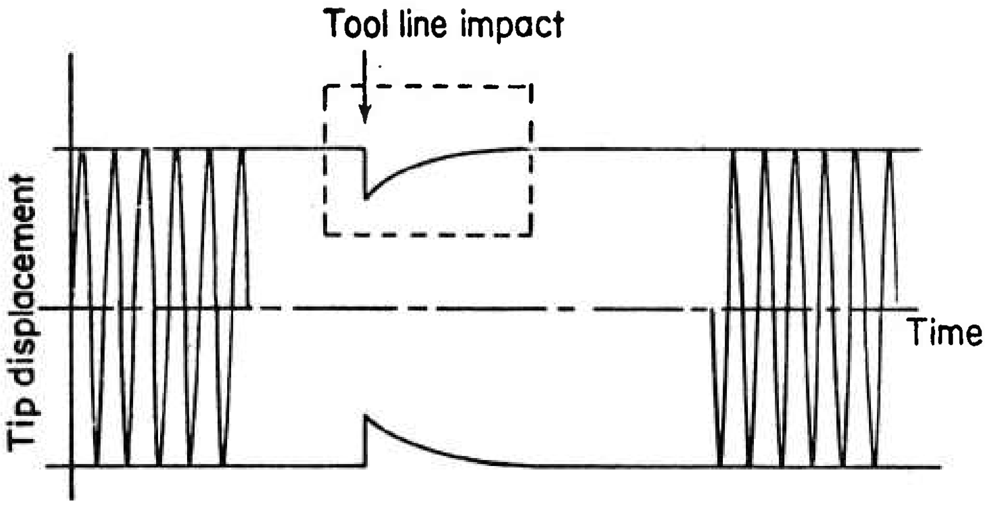
Tool line impact
Tip displacement
Time

Fig. 4-5 Transducer tip vibration under impact

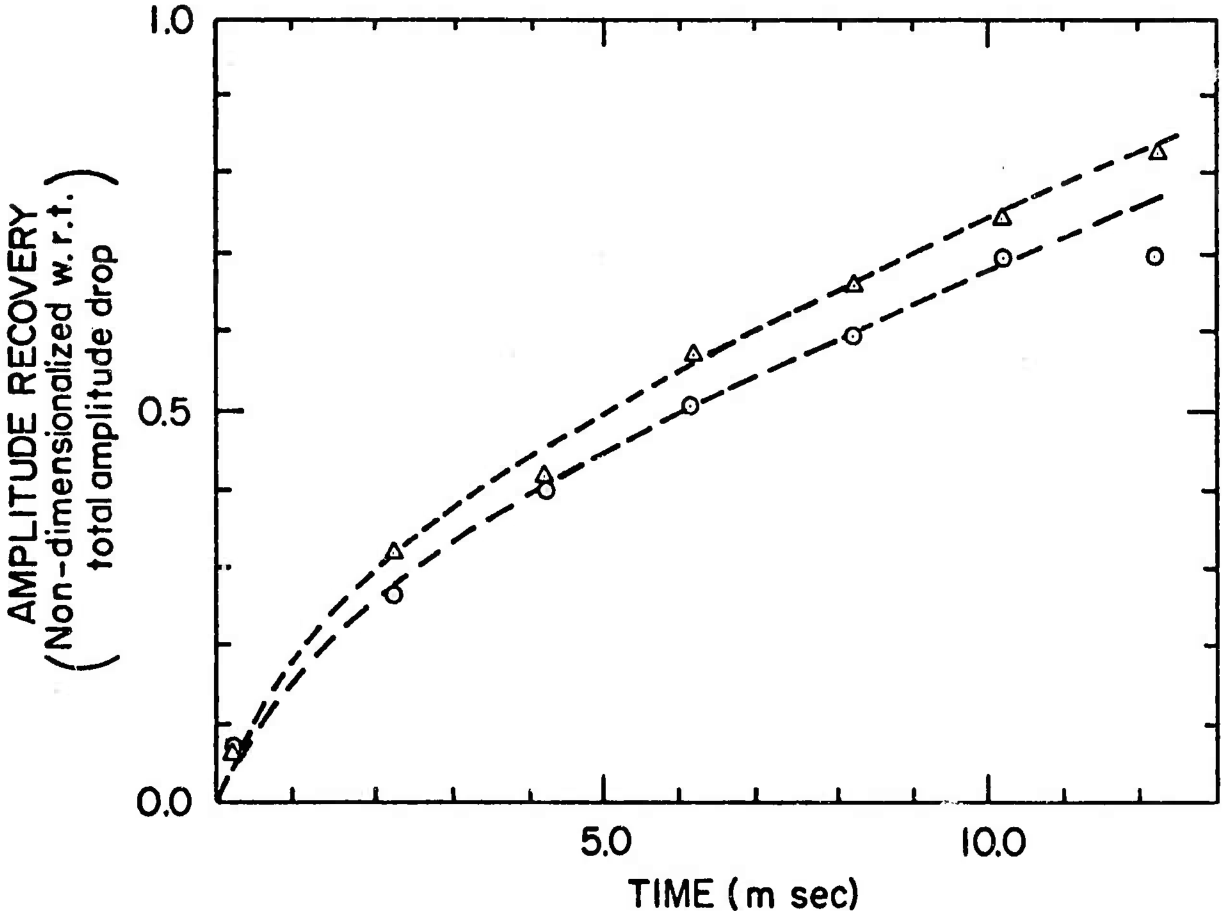

Fig. 4-6 Recovery of tip vibration amplitude

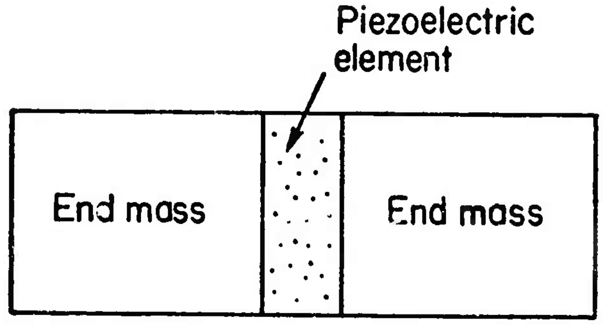
Piezoelectric element
End mass
End mass

Fig. 4-7 Cylindrical sandwich type resonator

following discussion analyzes the vibrational characteristics of a simplified model of a cylindrical sandwich type resonator as shown in Fig. 4-8. Two equal and opposite forces $P_o \sin \omega t$ are applied on a cylinder of length ℓ and area A at each side of the midpoint.

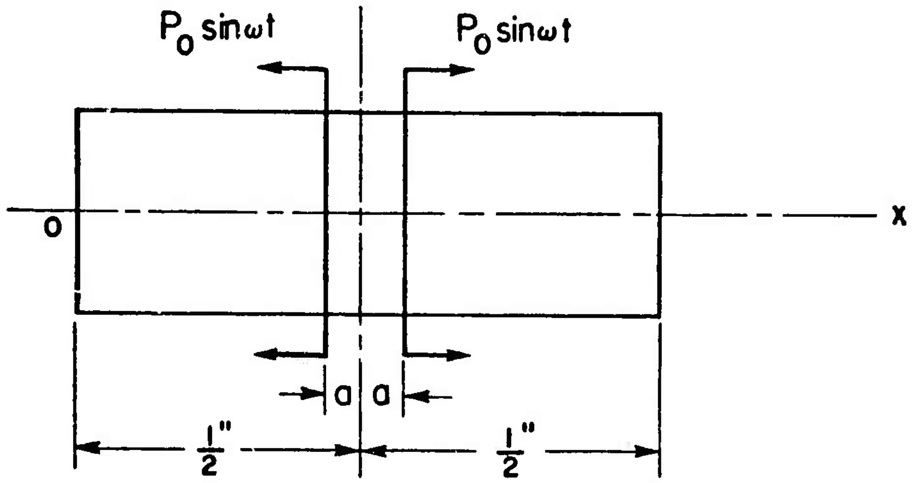
$P_o \sin\omega t$
$P_o \sin\omega t$
O
X
a
a
$\frac{l}{2}$''
$\frac{l}{2}$''

Fig. 4-8 Simplified model of cylindrical sandwich type resonator

Viscous damping in metal is usually of the Voigt type [15], [16]. The stress-strain relation can be expressed as

$$\sigma_x = Y\,\epsilon_x + Y'\,\frac{\partial \epsilon_x}{\partial x} \qquad (4\text{-}15)$$

where x is the direction of stress and strain, Y is the Young's modulus, and Y' is a damping factor [17], [18]. The one-dimensional equation governing the cylinder is

$$Y\,\frac{\partial}{\partial x}\left(A\,\frac{\partial u}{\partial x}\right) + Y'\,\frac{\partial}{\partial x}\left(A\,\frac{\partial^2 u}{\partial x \partial t}\right) = \rho A\,\frac{\partial^2 u}{\partial t^2} \qquad (4\text{-}16)$$

$A(x)$ = cross-sectional area at point x
$u(x,t)$ = longitudinal displacement

For the simplified model, we can express $u(x,t)$ as an infinite series of orthogonal vibrational modes $U_n(x)$ as follows

$$u(x,t) = \sum^{\infty} \varphi_n(t)\, U_n(x) \qquad (4\text{-}17)$$

with

$$U_n(x,t) = \cos(p_n x)$$

$$p_n = \frac{n\pi}{l} \qquad (n = 1,2,3,....)$$

Using the principle of virtual work, a set of differential equations for $\varphi_m(t)$ can be obtained as

$$M_o\ddot{\varphi}_m + \eta_m\dot{\varphi}_m + E_m\varphi_m = -2P_o\,\sin\left(\frac{m\pi a}{\ell}\right)\,\sin\left(\frac{m\pi}{2}\right)\,\sin\omega t \qquad (4\text{-}18)$$

where

$M_o = A\rho\ell/2,$ $\eta_m = AY'm^2\pi^2/2\ell,$

$E_m = AYm^2\pi^2/2\ell$ $P_m = -2P_o\,\sin\left(\frac{m\pi a}{\ell}\right)\,\sin\left(\frac{m\pi}{2}\right)$

The transient solution of eq. (4-18) is

$$\varphi_m = \exp[-(\eta_m t/2M_o)]\,\{A_m \sin q_m t + B_m \cos q_m t\} \qquad (4\text{-}19)$$

where

$$q_m = \left\{\frac{E_m}{M_o} - \frac{\eta_m^2}{4M_o^2}\right\}^{1/2}$$

The steady state solution is

$$\varphi_m = \frac{P_m}{\omega Z_m} \sin(\omega t - \psi_m)$$

where

$$Z_m = \left(\frac{E_m}{\omega} - M_O\omega\right)^2 + \eta_m^2 \qquad , \qquad \psi_m = \frac{\omega\eta_m}{E_m - M_O\omega^2}$$

and, the steady state displacement $u_s(x,t)$ is

$$u_s(x,t) = \sum_{n=1}^{\infty} \frac{P_m}{\omega Z_m} \sin(\omega t - \psi_m) \cos(p_m x) \tag{4-21}$$

When the exciting frequency ω reaches the value $[(E_1/M_O) - (\eta_1^2/2M_O^2)]^{1/2}$, the coefficient $P_1/\omega Z_1$ in eq. (4-20) becomes a maximum, and

$$\frac{P_1}{\omega Z_1} = \frac{P_1}{\eta_1 q_1} = \frac{-2P_O \sin(\pi a/\ell)}{\eta_1 q_1} \tag{4-22}$$

In this condition, the system resonates at its lowest mode because the terms higher than one in eq. (4-21) can be neglected in comparison with the first term. Therefore,

$$u_s(x,t) = \frac{-2P_O}{\eta_1 q_1} \cos\left(\frac{\pi x}{\ell}\right) \sin(\omega t - \psi_1) \sin\left(\frac{\pi a}{\ell}\right) \tag{4-23}$$

Since Y' (or η_1) is usually very small for metals, we have

$$\omega \approx q_1 = \sqrt{\frac{E_1}{M_O}} = \frac{\pi}{\ell}\sqrt{\frac{Y}{\rho}}$$

$$\eta_1 q_1 = \frac{A\pi^3 c_O Y'}{2\ell^2} \sqrt{1 - \left(\frac{\omega Y'}{2Y}\right)^2} \tag{4-24}$$

It is known that [15]

$$Q \text{ (factor of merit)} = \frac{F}{\Delta F} = \frac{2\pi I}{\Delta I} = \frac{Y}{\omega Y'} \tag{4-25}$$

where

F = resonant frequency,
ΔF = bandwidth (between half-power points),
I = internal energy, and
ΔI = energy dissipated in a cycle.

Equation (4-24) can be rewritten as

$$\eta_1 q_1 = \frac{A\pi^3 c_O Y'}{2\ell^2} \sqrt{1 - \left(\frac{1}{2Q}\right)^2} \tag{4-26}$$

Q is usually very large (on the order of 50 to 10^4), so we can neglect the second term in the radical sign and get

$$\eta_1 q_1 \approx \frac{A\pi^3 c_0 Y'}{2\ell^2} \tag{4-27}$$

With eqs. (4-19), (4-23), and (4-27), we have for the general solution for the vibration of the resonator

$$u(x,t) = \sum_{n=1}^{\infty} \exp[-(\eta_n t/2M_0)] \{A_n \sin(q_n t) + B_n \cos(q_n t)\} \cos\left(\frac{n\pi x}{\ell}\right)$$

$$- \frac{4P_0\ell^2 \sin(\pi a/\ell)}{A\pi^3 c_0 Y'} \cos\left(\frac{\pi x}{\ell}\right) \sin(\omega t - \psi_1) \tag{4-28}$$

In actual operation, the value of P_0 depends on the terminal voltage applied to the ceramics and prestress in the transducer. These two variables are assumed to be fixed during vibration in this study. Another variable that affects the value of P_0 is the previously mentioned interfacial friction. Since the interfacial friction force depends upon the dynamic behavior of the transducer, the value of P_0 is a function of time. In the previous analysis, the effect of interfacial friction is neglected and the value of P_0 is assumed to be constant to simplify the problem.

The time factor S_n, which is equal to $2M_0/\eta_n$ in eq. (4-28), is a function of Y'; the exponential coefficient $\exp(-t/S_n)$ represents the effect of damping in the system. We know that

$$S_n = \frac{2M_0}{\eta_n} \tag{4-25}$$

Since $\omega^2 \approx E_1/M_0$, we have

$$S_n = \frac{2Q}{\omega_n^2} = \frac{S_1}{n^2} \tag{4-30}$$

where

$$S_1 = \frac{2Q}{\omega} \tag{4-31}$$

(B) Transducer Vibration and Recovery of Transducer Tip Amplitude

In the previous section, the forced vibration of a simplified cylindrical sandwich type resonator was discussed. It was found that the resonator will vibrate in a natural mode if the exciting frequency is close to the natural mode. On the transient part of the solution, the time factor S_n depends on the damping characteristics of the materials used. The amplitude of steady state vibration is controlled by damping as well as the voltage applied to the ceramics.

The results obtained for a simple cylindrical sandwich type resonator will now be expanded to a more complicated resonator such as the P-11 transducer with body, resonant horn and transmission line. It is believed that the same type of solution will exist, except with different mode shapes, time factor and steady state amplitude; i.e., there will be a steady state solution with a lowest natural mode if the frequency of excitation is at that mode, and an amplitude which increases as the terminal voltage increases and damping decreases. The transient solution is an infinite series combination of all the natural modes with exponential time functions. The time factors depends on all the damping characteristics of transducer. In written form, we have the following;

$$u(x,t) = Af_1(x)\sin(\omega t - \psi_1) - \sum_{n=1}^{\infty} \exp(-t/S_n)\,[A_n \sin(q_n t) + B_n \cos(q_n t)]\,f_n(x) \tag{4-32}$$

where $f_n(x)$ is the nth mode shape. The lowest mode of vibration is $f_1(x)$.

In general, since the mass of the tool is rather small, the energy loss of the transducer for each impact is small compared to the total stored energy. If, for example, a tool of mass 0.003439 slug ($m_e = \frac{1}{2}$") impacts against a transducer, which has a tip vibration amplitude of 1.15 mils, and the incident and rebound velocity of the tool are equal to 66.6 in./sec and 111 in./sec, respectively; the energy loss of the transducer is equal to the energy gain of the tool and is about 1.124 in.-lb while the internal energy is approximately equal to 17.25 in.-lb. The percentage of energy loss is about 7.54%. Since the energy loss of the transducer is small per impact, the mode of vibration after impact is essentially $f_1(x)$; i.e., the value of A_n and B_n are small compared to A.

According to previous analysis,

$$S_n = S_1/n^2 \tag{4-33}$$

This tells us that the higher-order terms in the transient solution damp out much faster than the lowest mode. Therefore, another assumption is made here to neglect the effect of higher order terms in eq. (4-32), giving

$$u(x,t) \approx f_1(x)\{A \sin(\omega t - \psi_1) - \exp(-t/S_1)[A_1 \sin(q_1 t) + B_1 \cos(q_1 t)]\} \tag{4-34}$$

The above equation represents approximately a harmonic vibration with gradually varying amplitude. In another words, the recovery of the transducer from energy loss due to tool-line impact is exponential. The above analysis has been confirmed by the experimental results stated early in this section. Therefore, we may model the recovery of transducer tip vibration amplitude c(t) as follows,

$$c(t) = C - A \exp(-t/S) \qquad (4\text{-}34)$$

where C represents the maximum amplitude at the no-load condition, A is the amplitude drop of the transducer after impact and is dependent on the energy drain by the tool. Immediately after impact, t = 0, the tip amplitude is

$$c(0) = C - A$$

As time goes on, c(t) increases in an exponential order with a time factor S which depends on the total damping characteristics of a sonic transducer, i.e., the damping in ceramic as well as in metal is also considered.

(C) Internal Energy and Tip Vibration Amplitude

The ability of a sonic transducer to do work is dependent on the amount of energy in the transducer. It is known that internal stored energy in a longitudinally vibrating resonator is in the form of strain and kinetic energy. The amount of energy is proportional to the square of maximum displacement (or amplitude) at any point. In Section 4-2, the tip vibration amplitude was used in discussing the tool impact-rebound relationship on a vibrating transmission line. The amount of tip vibration amplitude will again be used as the measurement of the internal energy of a transducer.

It is not difficult to find the stored energy in terms of tip amplitude in the resonant horn and transmission line once the mode of vibration is known. It is more difficult to find the energy which is stored in the body of the transducer. This difficulty arises from the complicated structure of this part. An approximate value is obtained by assuming the approximate mode shape in the body and neglecting the energy stored in the ceramics. The proportional constant, K, for the P-11 transducer with a 10-inch transmission line in the equation

$$I = K c^2 \qquad (4\text{-}36)$$

is found approximately to be equal to 11.2 in.-lb/(mil)^2. In this equation I is the internal energy, and c is the tip vibration amplitude. The energy stored in the body of a stepped transducer has been calculated and is much smaller than in the resonant horn and transmission line. Hence the approximate value of K thus obtained is expected to be close to the true value. The reason is that the stored energy in the resonant horn and transmission line can be calculated exactly while approximation is made only in calculating the stored energy in the body. If the energy in the body is small, the approximation just made would not affect the total stored energy drastically. The value of K can be considered as a measurement of the energy storage capacity of a sonic transducer. The larger the value of K the more the energy can be stored.

The value of the tip displacement is important in the impact coupling process and difficult to obtain from purely theoretical analysis. The value is also dependent on the terminal voltage of the electric supply and temperature of the transducer system. An experiment was conducted to find the effect of temperature and voltage on the tip amplitude of an unloaded P-11 transducer with a ten-inch transmission line. It was found that the amplitude of vibration increases as the applied voltage increases as shown in Fig. 4-9. Figure 4-10 shows the peak-to-peak amplitude and power supply as a function of frequency of vibration. The applied voltage is approximately 1,200 V.

To find the effect of temperature change on the vibration characteristics of the P-11 transducer with a 10-inch transmission line, a set of curves similar to Fig. 4-10 but at different temperatures is shown in Fig. 4-11. The resonant frequency, amplitude and input power varies as the temperature changes. At room temperature the amplitude is largest while the power required to maintain steady state vibration is least. As time goes on, the heat accumulates in the transducer and causes the temperature to rise. The amplitude drops drastically while more energy is required to maintain resonance, which means that more energy is consumed as heat and acoustic noise at high temperature. Undoubtedly the temperature has a large effect on the properties of the piezoelectric material since the properties of metal are fairly stable for such small ranges of temperature change. Another important fact is the drop in resonant frequency of the system as the temperature rises. This is not particularly desirable if a single frequency power supply is to be used.

4-4 DRILLING ANALYSIS

As stated previously, the sonic rock cutting process is achieved by using an intermittent tool between the transmission line tip and the work surface. The tool acquires energy from impacting with the vibrating transmission line tip; it then impacts against the rock and rebounds from the surface. During impact between tool and rock, the tool loses part of its energy and causes some fracture of the rock.

The resonant frequency of a sonic transducer can be affected by many factors, such as voltage, temperature, and static force. The direct result of these detuning effects is to change the tip vibration amplitude. Since the sonic transducer is a high Q system, any small amount of frequency change can affect the tip vibration amplitude drastically. This, in turn, reduces the capability of the transducer to do work. Future efforts should be given to making the transducer resonant at all times during operation. In other words, the system interaction only on the assumed conditions that the transducer is always in a resonant state, and that the tip vibration amplitude is a constant during steady state, no load operation will be discussed.

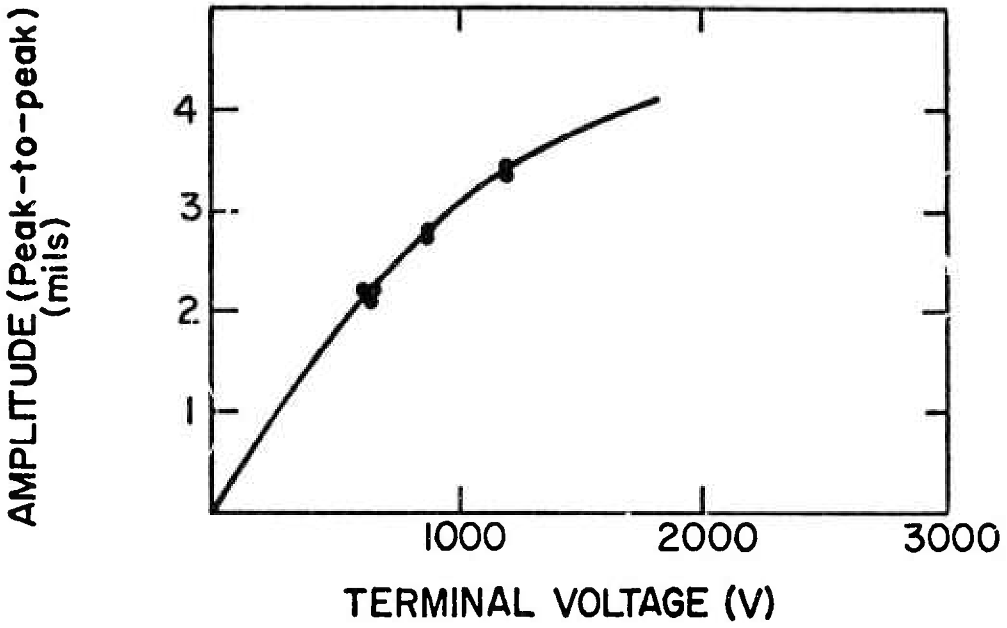

Fig. 4-9 Amplitude-voltage relationship (transducer temperature = 75°F

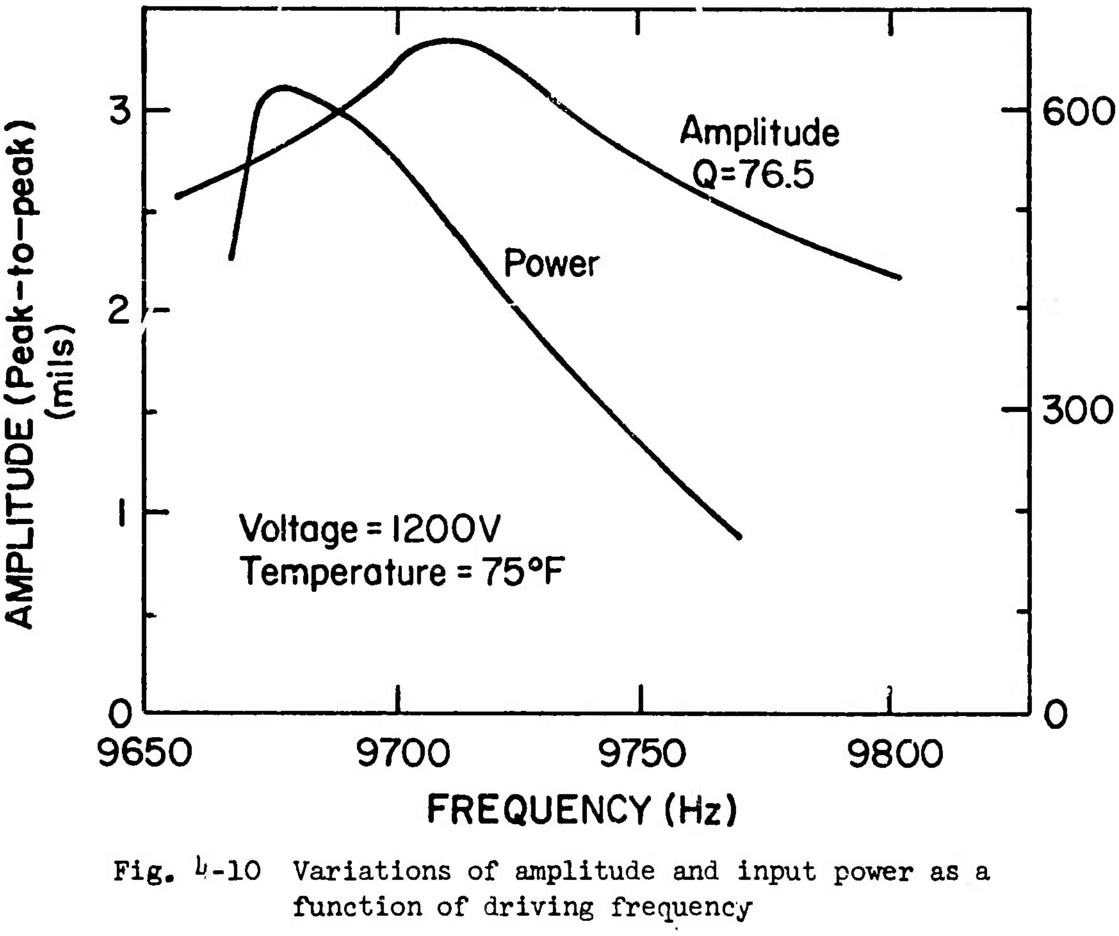

Fig. 4-10 Variations of amplitude and input power as a function of driving frequency

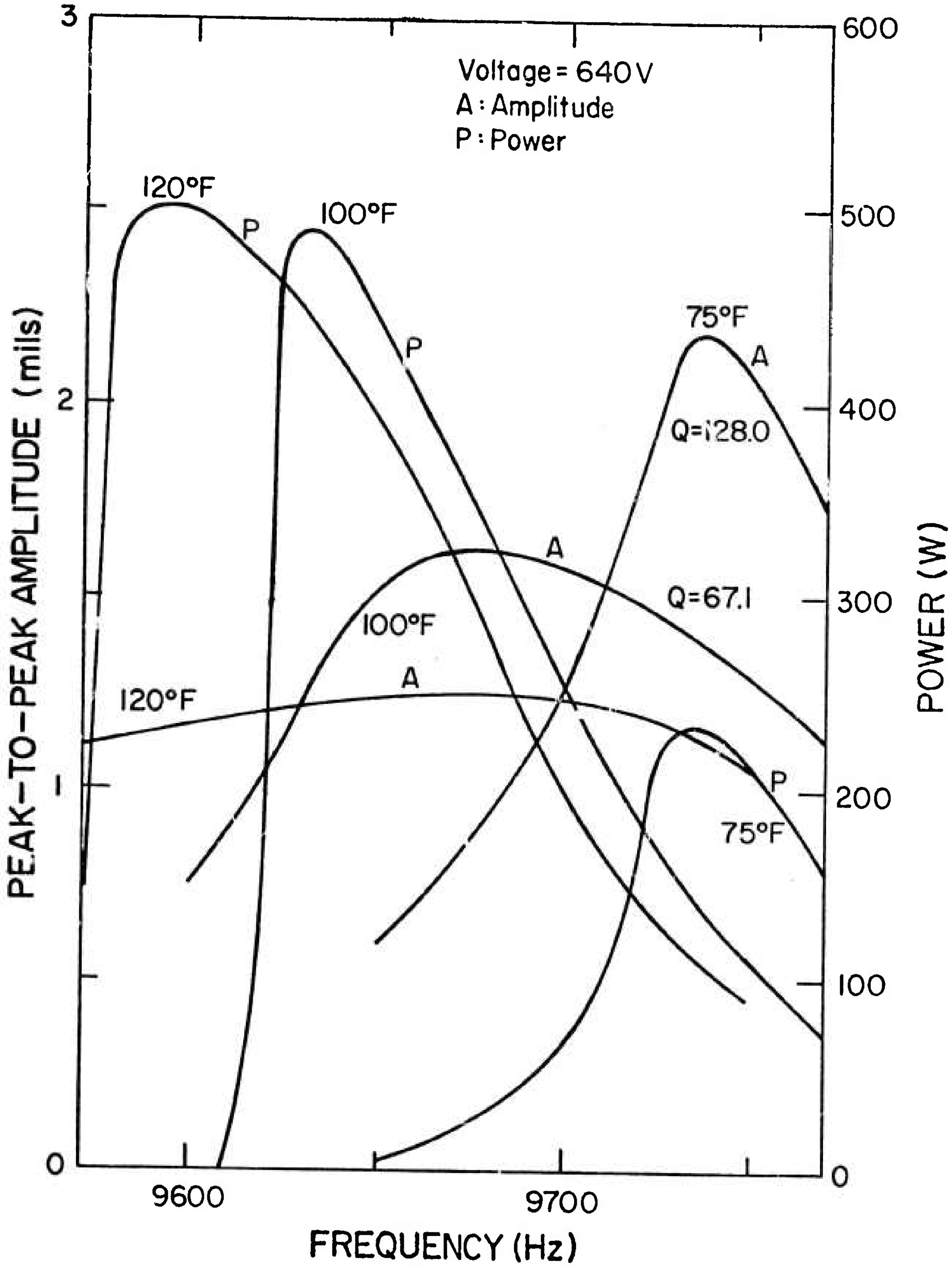

Fig. 4-11 Effect of transducer temperature on amplitude, resonant frequency and power

(A) Internal Energy During Steady State Operation

The recovery of the transducer after tool-line impact has been discussed. It was found that the tip vibration amplitude will recover in an exponential manner. If no further impacts occur, the tip vibration amplitude will eventually reach the steady state no-load amplitude. In actual operation, the tool will bounce back and forth in the gap between the transmission line tip and load. The impacts of the tool against the tip can be at hundreds and even thousands of times per second. The tip amplitude has no chance of fully recovering back to its steady state no-load condition because the second impact follows the first one in a short period. Hence, the internal energy during the steady state, no-load vibration represents a maximum value.

As discussed in Section 4-3, the tip vibration amplitude is assumed to be $c(t) = C - A \exp(-t/S)$. The corresponding internal energy, according to eq. (4-36) is

$$I(t) = K[C - A \exp(-t/S)]^2 \qquad (4\text{-}37)$$

Figures 4-12 and 4-13 represent the variation of tip vibration amplitude and internal energy during operation. The tip amplitude and internal energy at the steady state unloaded condition are C and I_0, respectively. When a load is applied to the system, the tool acquires energy from impacting with the transmission line tip. As time goes on, the amplitude and internal energy recovers due to the power supply input. Before the transducer recovers to its full energy, the tool bounces back from the rock surface, and again drains energy from the transducer. This process continues until a steady state condition is reached. The dashed lines represent the recovery curves of the transducer if no further drain of energy from the tool occurs.

If eq. (4-37) is expanded, one obtains

$$\begin{aligned} I(t) &= K\{C - A + A[1 - \exp(-t/S)]\}^2 \\ &= K(C - A)^2 + 2K(C - A)A[1 - \exp(-t/S)] + KA^2[1 - \exp(-t/S)]^2 \end{aligned} \qquad (4\text{-}38)$$

The first term represents the internal energy right after impact. The second and third terms represent the recovery. It is easy to see that, in the second term, the recovery is also dependent on C and K as well as the time factor S. The larger the value of C and K the faster the energy recovery.

In the steady state operating condition, the energy recovered equals the energy drained from the transducer, assuming T_i is the impact interval. Therefore,

$$I_i = I(T_i) = K[C - A \exp(-t/S)]^2 = K(C - A)^2 + \Delta \qquad (4\text{-}39)$$

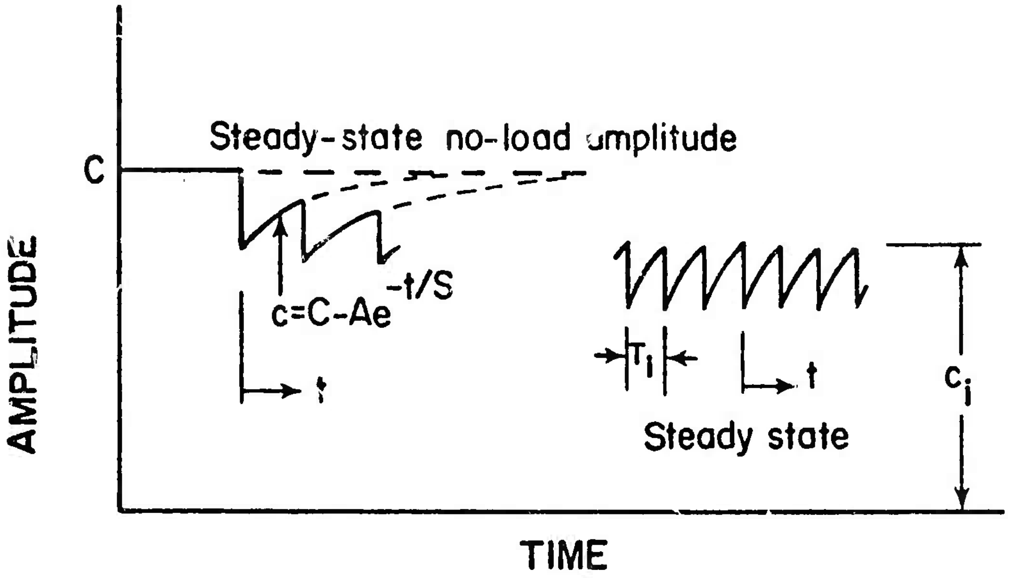

Fig. 4-12 Variation of tip vibration amplitude

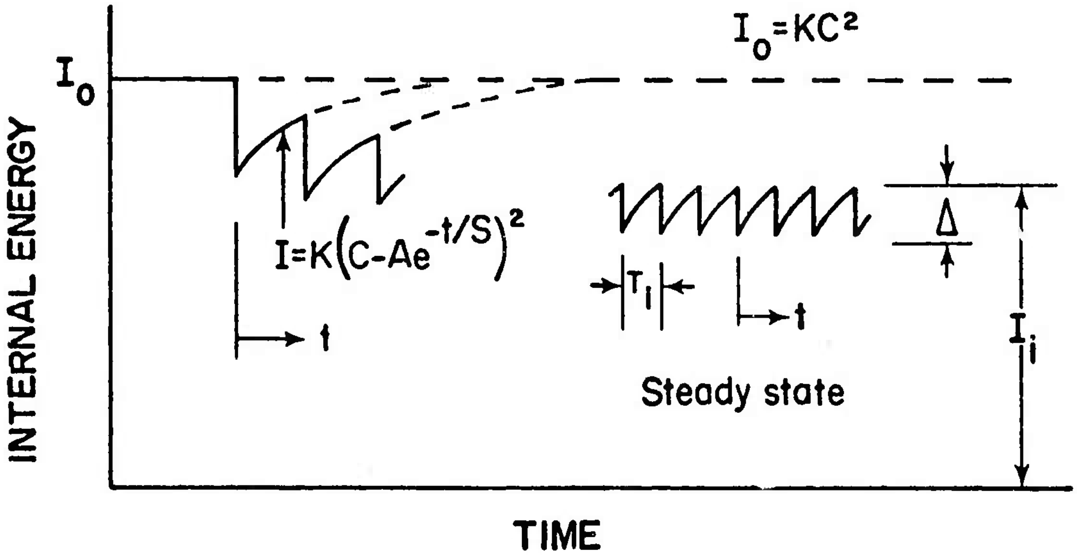

Fig. 4-13 Variation of internal energy

where Δ is the energy that the tool acquired from the transducer; i.e.,

$$\Delta = \frac{1}{2} m(V_2^2 - V_1^2) + E_L \qquad (4\text{-}40)$$

with E_L being the energy loss due to impact. V_1 and V_2 are the velocities of the tool before and after impact, respectively. If the transmission line tip and tool are made of hard material, not much plastic deformation should occur. Therefore, E_L is considered to be small compared to $m(V_2^2 - V_1^2)/2$ and can be neglected. Thus,

$$\Delta = m(V_2^2 - V_1^2)/2 \qquad (4\text{-}41)$$

During this steady state condition, the internal energy is at a specific value before impact which implies that the tip vibration amplitude is also at a specific value. Now, there are several questions to be answered: What is the value of the internal energy and tip vibration amplitude? What are the values of impact and rebound velocity of the tool against the transmission line tip and rock? These problems will be answered as the discussion procedes.

In actual operation, the impact and rebound velocity of the tool is somewhat random and so is the internal energy and tip vibration amplitude; but, in the sense of averages, they are assumed to be deterministic in the above analysis.

(B) Impact Coupling

The general idea of internal energy during the steady state operating condition was discussed in the preceding section. Now the tool behavior during this condition will be studied. The tool-rock and tool-line phases of the impact coupling process have been studied extensively. The present task is to combine them for the study of this coupling process. Feng [13] studied the impact coupling of a spherical ball between a static and a vibrating transmission line. The present analysis follows his method of approach.

In [1], Part II, Chapter 4, the incident-rebound velocity relationship of a tool impacting against rock was represented by a best-fit straight line while in Section 4-2 of this chapter, the incident-rebound velocity relationship of a tool impacting against a vibrating transmission line was obtained. If these two relationships are plotted on the same figure with the notation of incident and rebound velocity as shown in the lower-right-hand corner of Fig. 4-14, we obtain an example figure as shown. In this case, a tool with 1/2-inch equivalent length ($m_e = \frac{1}{2}$") and 10-inch radius of curvature of the tool-tip contact surface is used. The rebound-incident velocity ratio and tip amplitude c_1 are assumed to be equal to 0.6 and 1.0, respectively. The steady state velocities happen to be at the point of intersection of these two relationships, i.e., the point W(V_1 = 57.5 in./sec and V_2 = 96.0 in./sec). To illustrate this, let the tool start at a velocity V_{01} and impact

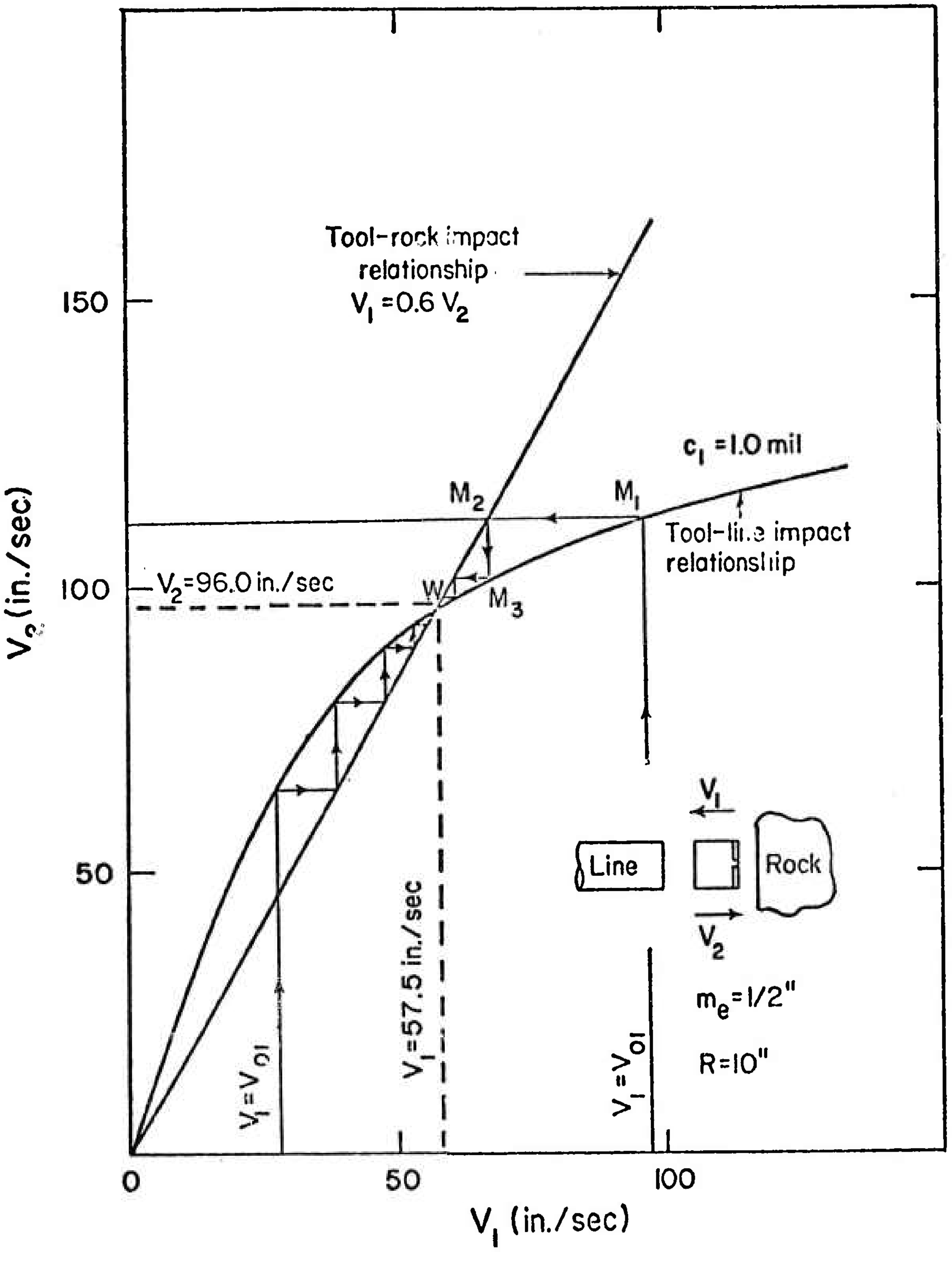

Fig. 4-14 Steady-state velocities for $c_1 = 1.0$ mil, $m_e = 0.5$ inch and $R = 10''$

against the vibrating line (point M_1). The rebound velocity V_2 from the line becomes the incident velocity V_2 for tool-rock impact (point M_2). With this rebound velocity V_1 from rock, the tool impacts again against the transmission line tip (point M_3). This process continues until the point of intersection W is reached. The same result will be obtained if we start at a lower velocity V'_{01}. The above is true as long as the tip vibration amplitude remains unchanged. If the amplitude c_i changes so does the point W representing the steady state velocities. Therefore, we can say that steady state velocities V_1 and V_2 are functions of c_i since the tool-rock impact relation and the geometry of the tool are assumed to remain unchanged during operation.

It is interesting to note that the situation may arise where the slope of the rebound-incident velocity relationship for tool-rock impact (slope = V_1/V_2) is so small that no point of intersection W can be obtained. This means that no steady state velocities can be reached and the problem then becomes more complicated. It is believed that, in some instances, the tool tip is in close contact with the rock while the transmission line hits the tool at the end; i.e., the tool-rock and tool-line impacts happen at more or less the same time. The slope of the rebound-incident velocity relationship for tool-rock impact (V_1/V_2) depends on the tip geometry of the tool and the properties of the rock. Usually harder rock yields higher values of V_1/V_2. In the remainder of this analysis, only the case where steady state impact coupling occurred was considered. Therefore, our study was restricted to hard rock drilling in which intersection point W exists for a specific tool geometry.

Another interesting observation in previous analysis of impact coupling is that the steady state velocities do not change so long as the tip vibration amplitude remains unchanged; the static force F_s applied by the support structure of the transducer plays no direct role. It seems to have no effect on the impact process. Actually the static force affects the steady state velocities via affecting the value of steady state tip vibration amplitude c_i. This will be clear as the discussion of impact coupling continues.

The discussion of static force is started by looking at the dynamics of a sonic transducer considered by Graff [19] (Fig. 4-15). The rigid body motion is governed by

$$M \ddot{x} = F_s - f(t) \qquad (4\text{-}42)$$

where M is the mass of the transducer, f(t) is the time varying force at the tip of the transducer due to the impact of a sonic tool, and F_s is the static force applied by the support structure. Force f(t) is a combination of a sequence of impact forces, each impact force is high in magnitude but short in duration. It usually is less than 50 μsec. Actually, the impact forces would be of various amplitudes and intervals, but thinking in terms of averages it is justifiable to consider equal amplitudes and spacings. The interval of impacts is quite long compared

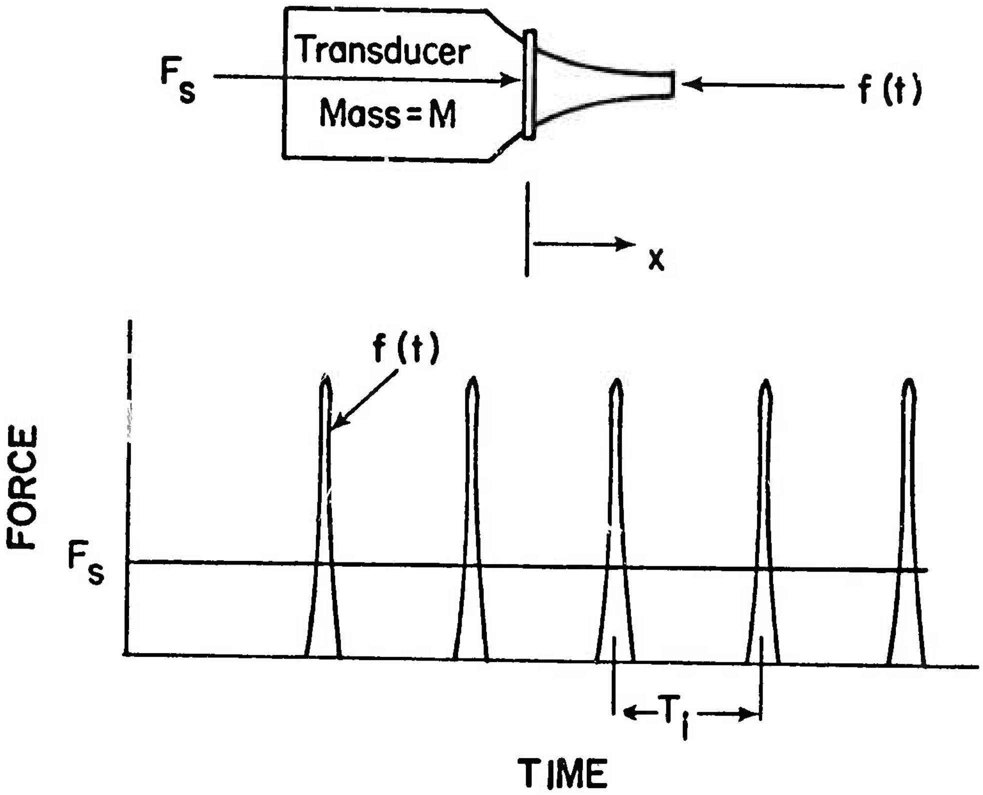

Fig. 4.15 Trandsucer acted upon by static force F_s and impact force f(t)

with each impact duration in sonic processes. For example, if the frequency of impact is 1000 impacts/sec, the time interval is in the order of 1000 μsec.

Integrating eq. (4-42) gives

$$M(\dot{x} - \dot{x}_0) = F_s t - \int_0^t f(t)dt \tag{4-43}$$

Since it was assumed that each impact force is the same and the duration is short, it is justifiable to represent the second term as follows

$$\int_0^t f(t)dt = I_m \sum_{n=1}^{N} H(t - t_n) \tag{4-44}$$

where N is the number of impacts between the time interval 0 and t and H is a Heaviside function. Now, rewriting eq. (4-43)

$$M(\dot{x} - \dot{x}_0) = F_s t - I_m \sum_{n=1}^{N} H(t - t_n) \tag{4-45}$$

This equation shows that the velocity of a sonic transducer has a sawtooth form as shown in Fig. 4-16. Thus, the constant force F_s causes a linear increase in velocity, but this is periodically offset by sudden velocity decreases due to the impact pulses. If the proper balance holds between the static force and the impulse I_m and inpulse interval T_i, the increase in velocity is completely offset by the drop caused by impact, so that

$$F_s T_i = I_m \tag{4-46}$$

This is a statement of impulse balance, so that the average net change in momentum of the transducer is zero.

According to the definition of impulse,

$$I_m = m(V_1 + V_2) \tag{4-47}$$

Therefore, from eq. (4-46), we have

$$T_i = \frac{m(V_1 + V_2)}{F_s} \tag{4-48}$$

The value of T_i consists of impact times and the travelling times of the tool between the transmission line tip and the rock surface. The frequency of impact coupling is just equal to the reciprocal of T_i; or,

$$f = 1/T_i = \frac{F_s}{m(V_1 + V_2)} \tag{4-49}$$

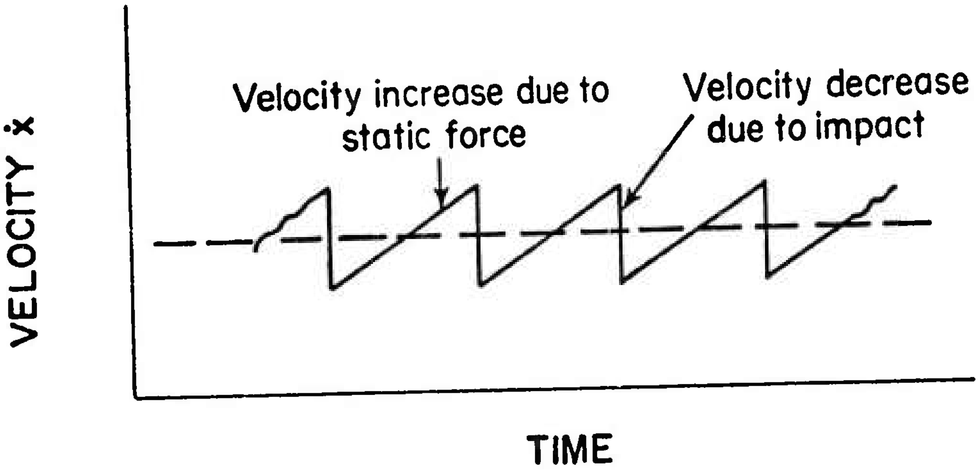

Fig. 4-16 Rigid body motion of a transducer acted upon by static force and impact

As stated previously, steady state velocities, V_1 and V_2, are functions of tip vibration amplitude c_i. Thus, the relationship between impact frequency and the tip vibration amplitude c_i are related to each other according to eq. (4-49). Generally, the increase or decrease of V_1 and V_2 follows the trend of the value of c_i. When we increase the impact frequency, the amplitude drops, therefore reducing the internal stored energy of the transducer. If the static force is kept constant during operation, it is easy to see from eq. (4-48) that T_i is a function of c_i.

(C) Power Transmission

Now again consider the internal energy of the transducer, and rewrite eqs. (4-35), (4-39), (4-41) and (4-47) as follows:

Internal energy just before impact is

$$I_i = K(C - A)^2 + \Delta = K[C - A \exp(-T_i/S)]^2 \qquad (4\text{-}50)$$

The energy drain in each impact is

$$\Delta = m(V_2^2 - V_1^2)/2 \qquad (4\text{-}51)$$

Tip vibration amplitude was given previously by $c(t) = C - A \exp(-t/S)$, while the interval of impulse is

$$T_i = 1/f = \frac{m(V_1 + V_2)}{F_s} \qquad (4\text{-}52)$$

Eliminating Δ is eqs. (4-39) and (4-41), and solving for A, we obtain

$$A = \frac{C \exp(T_i/S) \pm \sqrt{\{C[1 - \exp(-T_i/S)]^2\} - (m/2K)(V_2 - V_1)[1 - \exp(-T_i/S)]}}{1 - \exp(-T_i/S)} \qquad (4\text{-}53)$$

Substituting (4-53) is eq. (4-35) and letting $t = T_i$, we get

$$c(T_i) = \frac{C \exp(T_i/S) \pm \sqrt{C^2 - (m/2K)(V_2^2 - V_1^2)[1 + \exp(T_i/S)]/[-1 + \exp(T_i/S)]}}{1 + \exp(T_i/S)} \qquad (4\text{-}54)$$

To decide whether the positive or negative sign in the above equation should be chosen, consider a transducer with large K, i.e., a transducer whose energy storage capacity is very large. Then, by neglecting the second term in the radical sign, we have

$$c_i = c(T_i) \approx C[\exp(T_i/S) \pm 1]/[\exp(T_i/S) + 1] \qquad (4\text{-}55)$$

If we choose the positive sign, we have

$$c_i = c(T_i) = C$$

This means that, for a transducer with large energy storage capacity, the steady state vibration amplitude before impact is close to the unloaded vibration amplitude C. This is consistent with the statement made in Section (A) of this chapter that the larger the value of K the faster the energy recovery. If we choose the negative sign, we have

$$c(T_i) = C[\exp(T_i/S - 1)]/[\exp(T_i/S) + 1]$$

This has no special physical meaning. Therefore, we choose the positive sign in eq. (4-53) and (4-54), i.e.,

$$c_i = c(T_i)$$

$$= \frac{C \exp(T_i/S) + \sqrt{C^2 - (m/2K)(V_2^2-V_1^2)[1 + \exp(T_i/S)]/[-1 + \exp(T_i/S)]}}{1 + \exp(T_i/S)} \tag{4-56}$$

As discussed at the end of Section (B), the static force F_s is kept constant, and V_1, V_2, and T_i are functions of c_i [or $c(T_i)$]. Then, the right hand side of eq. (4-56) is a function of c_i only. Therefore, the value of c_i can be solved numerically if not analytically, since no mathematical relationship between V_1, V_2 and c_i exists.

The questions stated at the end of Section (A) become clear once the values c_i, or $c(T_i)$, is obtained. The values of V_1 and V_2 can be found according to Section (B). The value of T_i can be obtained by using eq. (4-52) with the values of V_1 and V_2 just found. The internal energy just before impact can also be evaluated according to eq. (4-36).

With all the information obtained previously, the power transmission into rock can be calculated by considering the energy loss of tool to rock in each impact and the frequency of the sonic process. The energy absorbed per impact, Δ, is

$$\Delta = m(V_2^2 - V_1^2)/2 \tag{4-57}$$

Therefore, the power transmission P is the product of Δ and f, i.e.,

$$P = \Delta f \tag{4-58}$$

Substituting f of eq. (4-53) in the above equation, we have

$$P = F\ (V_2 - V_1)/2 \tag{4-59}$$

With the value of c_i known, the value of $V_2 - V_1$ (or P) can be obtained. Figure 4-17 shows the values of $V_2 - V_1$ for R = 10" and various values of equivalent length of the tool, m_e. The ratios of the rebound-incident velocity relationship in tool-rock impact used here are equal to 0.7 and 0.6.

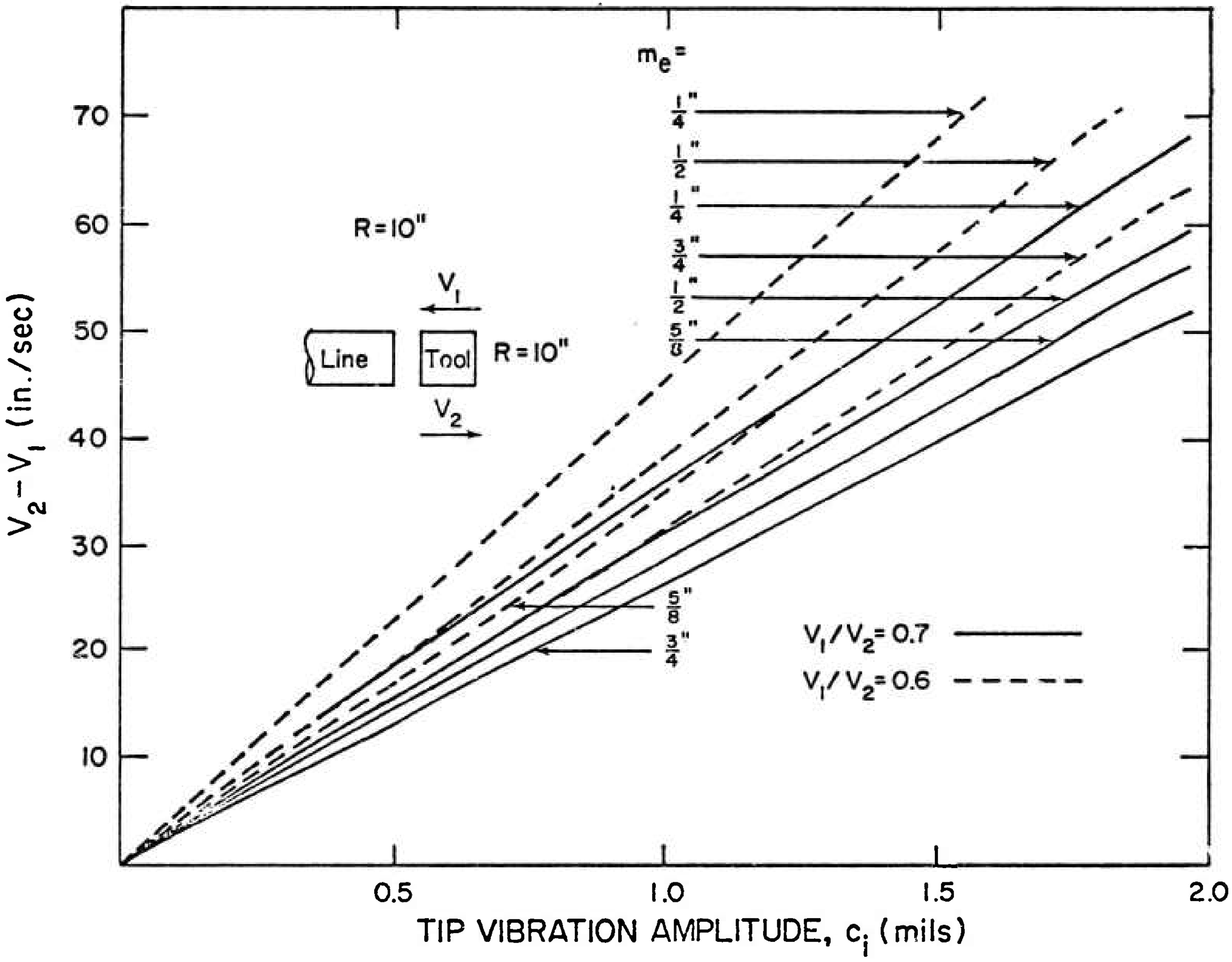

Fig. 4-17 Velocity difference for various values of equivalent length of the tool

(D) Drilling Rate of a Sonic Transducer

As we mentioned previously in discussing the specific energy (e_s) of rock removal, the time required to remove a certain volume of rock is important in the discussion of economy of a drilling system. Therefore, drilling rate is the focusing point for any kind of rock drilling system. With the power transmission (P) and specific energy known for a sonic transducer system and rock, the drilling rate (R) can be found very easily as follows

$$R = P/e_s \tag{4-60}$$

With all the studies on the sonic rock drilling being completed, an example problem using the information presented is given. This will aid in understanding the previous studies and also give a general idea of a practical situation in a sonic rock drilling process.

(E) Numerical Example

The information with regard to the transducer, static force applied, the tool and the rock are given as follows:

TRANSDUCER:	P-11 transducer with 1-inch diameter and 10-inch long transmission line Resonant frequency = 9750 Hz Applied terminal voltage = 1200 V
STATIC FORCE:	100 lb.
TOOL:	Dimensions - Type F tool Radius of curvature of the tool end = 10" Equivalent length $m_e = \frac{1}{2}$"
ROCK:	Granite $V_1/V_2 = 0.6$ (Laboratory experiment shows that the value of rebound-incident ratio is between 0.54 to 0.60 for Type F tool impacting against granite. 0.6 is used here for analysis.) Specific energy e_s - Fig. 4-2

- -

The internal energy I according to eq. (4-36) is $I = Kc^2$ where K is equal to 11.2 in.-lb/(mil)^2 for P-11 transducer with a 10 in. transmission line [following eq. (4-36)].

Angular frequency $\omega = 2\pi f = 61{,}260$ rad/sec.

No-load amplitude $C = 3.4/2 = 1.7$ mils according to Fig. 4-9.

Time factor S is dependent upon the total damping characteristics of the transducer. Assuming that eq. (4-31) still holds after the modeling of transducer tip vibration amplitude recovery is made, then $S = 2Q/\omega$ where Q can be obtained by using eq. (4-25); i.e., $Q = F/\Delta F$, and data from Fig. 4-10. The value of Q is found to be equal to 76.5 for the terminal voltage of 1200 V and temperature of 75°F. Therefore,

$$S = 2 \times 76.5/61{,}260 = 2.498 \text{ m sec.}$$

$$T_i = m(V_1 + V_2)/F_s = 0.0055027\ V_2$$

$$T_i/S = 0.001147536\ V_2$$

and

$$\frac{(m/2K)(V_2^2 - V_1^2)[1 + \exp(T_i/S)]}{[-1 + \exp(T_i/S)]} = 8.1885 \times 10^{-6}\ V_2^2\ \frac{1 + \exp(T_i/S)}{-1 + \exp(T_i/S)}\ (\text{mil})^2$$

With the above information, the curves for the left-hand side and right-hand side of eq. (4-60) are $\varphi = c(T_i)$,

and

$$\varphi = \frac{C\exp(T_i/S) + \sqrt{C^2 - (m/2K)(V_2^2 - V_1^2)[1 + \exp(T_i/S)]/[-1 + \exp(T_i/S)]}}{\exp(T_i/S) + 1}$$

and are plotted in Fig. 4-18. The solution of eq. (56) is the intersection of the above two curves, i.e.,

$$c_i = c(T_i) = 1.15 \text{ mils}$$

From Fig. 4-17,

$$V_1 - V_2 = 44.4 \text{ in./sec}$$
$$V_1 = 66.6 \text{ in./sec}$$
$$V_2 = 111.0 \text{ in./sec}$$
$$T_i = 0.504 \text{ m sec}$$
$$I_i = 11.2 \times (1.15)^2 = 17.25 \text{ in.-lb}$$
$$\Delta = \tfrac{1}{2} m(V_2^2 - V_1^2) = 1.124 \text{ in.-lb}$$
$$\Delta/I_i = 1.124/17.25 = 7.54\%$$

Power transmission P is

$$P = \tfrac{1}{2} F_s(V_2 - V_1) = 2{,}220 \text{ in.-lb/sec} = 11{,}100 \text{ ft-lb/min}$$
$$= 250.8 \text{ W}$$

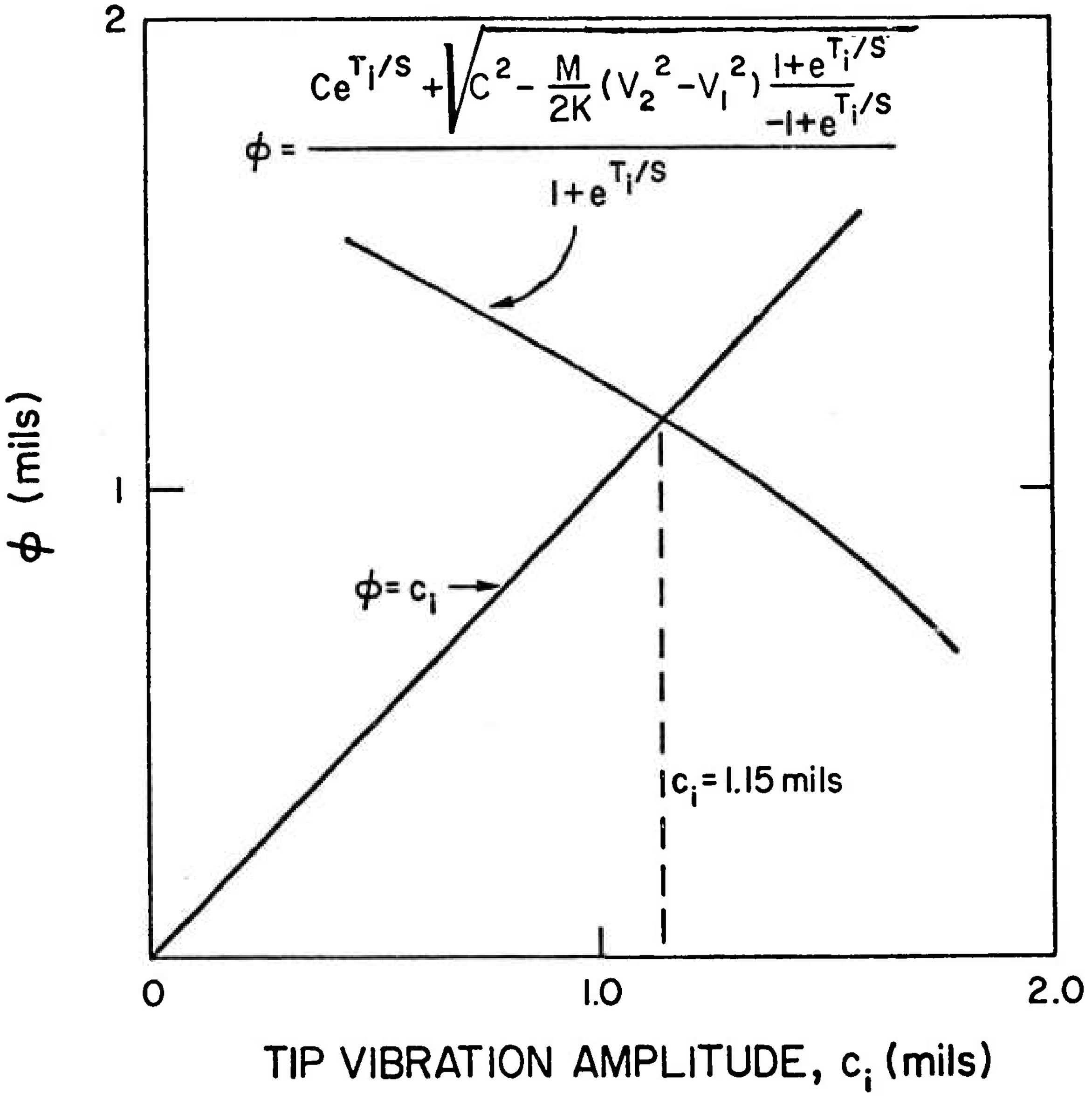

Fig. 4-18 Solution of c_i (graphical method)

We do not have the specific energy chart for $m_e = \frac{1}{2}$ in. but do have it for $m_e = 1.08$ in. (Fig. 4-2). To find the specific energy for $m_e = 0.5$ in. and $V_2 = 111.0$ in./sec, assume that equal incident energy of the tool would cause equal amount of damage to the rock if tip geometries are the same for tools of different mass (or m_e); then the corresponding incident velocity V_2' of the tool with m_e' can be found as follows

$$\frac{1}{2} m_e V_2^2 = \frac{1}{2} m_e' V_2'^2$$

for

$$m_e = \frac{1}{2} \text{ in. and } m_e' = 1.08 \text{ in.}$$

$$V_2' = 75.5 \text{ in./sec}$$

The value of e_s corresponding to $V_2' = 75.5$ in./sec and $m_e' = 1.08$ in. is 11,000 ft-lb/in.^{3} according to Fig. 4-2. Therefore, the drilling rate in volume per minute is

$$R_V = P/e_s = 11100/11000 = 1.01 \text{ in.}^3/\text{min}$$

and the drilling rate in in./min is

$$R_L = R_V/A = 1.01/\pi(\tfrac{1}{2})^2 = 1.29 \text{ in./min}$$

Drilling rates and power transfer are also calculated for the case when the terminal voltage and static force applied to the transducer are equal to 2000 V and 200 lb, respectively. An estimated value of Q is used (Q = 60) in this calculation since no experimental result is available for a transducer driven at 2000 V. The results are listed in the following table along with the previous example.

Table 4-1 - Sonic Drilling of Granite

	Drilling rate R_L in./min	Drilling rate R_V in.^{3}/min	Power transfer W	Power transfer ft-lb/min	T_i, m sec.	Δ/I_i, %
V = 1200 V F_s = 100 lb.	1.29	1.01	250.8	11,100	0.504	7.54
V = 2000 V F_s = 200 lb.	8.58	6.75	819.0	36,250	0.416	7.60

The drilling rates of 1.29 and 8.58 in./min obtained are lower than conventional percussive drilling. Bruce [20], in a study, found the drilling rate with two special bits (four-wing) and percussive drilling apparatus is within the range of 5 to 40 in./min while the maximum piston energy consumed is in the range of 46,000 ft-lb/min to 162,000 ft-lb/min. Considering the power consumed and the drilling rate of a sonic transducer system, it is easy to see that the system is in the low range of percussive drilling systems.

4-5 REFERENCES

1. Graff, K. F., "Fundamental Studies in the Use of Sonic Power for Rock Cutting," Annual Technical Report, Bureau of Mines Contract No. H0210010, Dec., 1971.

2. McMaster, R. C., Dettloff, B. B. and Minchenko, H. M., "Piezoelectric Transducers: Theory and Basic Principles," EES 220-1, 1963, The Ohio State University.

3. Dettloff, B. B. and Minchenko, H. M., "Theory and Design of Sonic and Ultrasonic Concentrators," EES 220-1, 1963, The Ohio State University.

4. Hoffman, R. B. and Swartz, J. M., "Analysis of the P-7 Ultrasonic Transducer Using Classical Circuit and Transmission Line Theory," EES 220-Q2, 1967, The Ohio State University.

5. Mahban, H. and Graff, K. F., "System Characteristics of Sonic Energy Transfer," EES 220-Q3, 1968.

6. Graff, K. F., "Vibrations of Crystals and Transducers," EES 220-Q3, 1969, The Ohio State University.

7. Graff, K. F., "Analysis of Stepped Horn Resonators," EES 220-Q3, 1969, The Ohio State University.

8. Fretwell, C. C., "Energy Losses in a Transmission Line," EES 220-Q4, 1967.

9. Graff, K. F., "Energy Storage and Dissipation in a Vibrating Rod," EES 220-Q3, 1969.

10. Ma, N. T., "Vibrational Characteristics of a Sonic Transducer," Part II, Section 3, Annual Technical Report on "Fundamental Studies in The Use of Sonic Power for Rock Cutting," Dec., 1971, The Ohio State University.

11. Feng, Ching-chiou, "Analysis of Sonic Transducers," Ph.D. Dissertation, The Ohio State University, 1972.

12. Lo, Ting-yu, "Fundamental Studies in the Use of Sonic Power for Rock Cutting," Ph.D. Dissertation, The Ohio State University, 1972.

13. Feng, C. C., "Energy Transfer in Sonic Impact Coupling," M.S. Thesis, The Ohio State University, 1969.

14. Feng, C. C. and Graff, K. F., "Impact of a Spherical Tool Against a Sonic Transmission Line," *J. Accoust. Soc. Amer.*, July, 1972.

15. Lazan, B. J., *Damping of Materials and Members in Structural Mechanics*, First Edition, Pergamon Press.

16. Kolsky, H., *Stress Waves in Solids*, Dover.

17. Thompson, J. H. C., *Phil. Mag.*, *41*, 1933.

18. Honda, K. and Konno, S., *Phil. Mag.*, *42*, 1905.

19. Graff, K. F., "A Description of the Sonic Interaction Process," Section 6, Part II, Annual Technical Report on "Fundamental Studies in the Use of Sonic Power for Rock Cutting," Dec., 1971.

20. Bruce, W. E., "How to Predict the Penetration Rate of Percussive Drills," *Mining Engineering*, Nov., 1970.

5. TRANSDUCER ANALYSIS

Although sonic and ultrasonic power transducers are widely used, the design of transducers is still more an art than a science. Concepts such as the half wavelength design and the full wavelength design are the dominant approaches in industry. Theoretical design based on more exact theories is lacking, especially for the high power applications. Possibly this may be because of the complicated geometry of an actual transducer. Here, attempts will be made to apply the more "exact" theory of linear piezoelectricity to predict the resonant frequency of a transducer. However, the lack of an applicable short piezoelectric rod theory leaves the long rod and large plate theories as the only remaining alternatives. Thus, these two models will be followed throughout the report.

Additionally and, possibly more importantly, is the objective of determining the causes for shifts in the resonant frequency of transducers operating in different environments. In the Sonic Power Laboratory of The Ohio State University, the resonant frequency of a transducer in operation has been observed to shift with different levels of prestress on the ceramics. A change of the transducer temperature or the driving voltage will also produce a shift of the resonant frequency. Although the shift is not necessarily drastic, it is sufficient to throw the transducer out of its designed operational bandwidth. This drastically reduces the working capability of the transducer. The usual way to correct this problem is to retune the transducer to its original designed frequency by changing transducer length, or to employ a variable frequency power supply to change the operation frequency. Experience reveals that the retuning process is tedious and time consuming. On the other hand, variable frequency power supplies are expensive. This situation presents a problem in attempting to use the less expensive, fixed frequency power supply approach to sonic processes. In order to overcome this difficulty, causes of the shifting must be understood; proper measures may then be taken to reduce the shifting or to make allowance in advance for the shifting and to offset it. In this chapter some experimental data will be given to show the extent of the shift with the prestress, temperature and voltage. Theoretical analysis of the shifting will also be given.

In the following theoretical formulations for various resonators and transducers will be given and the frequency equations will be solved numerically. The shifts of resonant frequency will then be treated from two approaches: (i) from the effects of the material property changes, and (ii) for the effect of prestress from determining an equivalent spring constant for the ceramics from measuring the resonant frequency of the simple resonator at different prestress levels. The theoretical results will be compared with the experimental values in the final section.

5-1 SONIC RESONATORS

A sonic resonator generally takes the form of a sandwich which consists of several piezoelectric discs or rings clamped between metal cylinders. This arrangement lowers the resonant frequency of the resonator drastically from that of the free piezoelectric elements alone, since the piezoelectrics used are generally thin.

To analyze the vibrational behavior of the resonators the equations of motion for each part of the assembly must be formulated. The general solutions must be found and the boundary conditions at the ends and the interfaces must be applied. The frequency equations can then be obtained and solved for the resonant frequencies. Finally mode shapes of vibration may be determined. If energy dissipation effects in the materials are included, the amplitudes of vibration can also be calculated.

In the following, three resonator designs will be analyzed assuming there is no energy dissipation in the materials. The three resonators are: (1) the symmetrical simple resonator, (2) the asymmetrical simple resonator, and (3) the P-7 resonator (which is an OSU P-7 transducer with the horn removed). The thickness plate and the longitudinal rod models will be used in the analysis. Finally, experimental results will be compared to the theoretical ones.

(A) The Symmetrical Simple Resonator

A symmetrical simple resonator has two PZT ceramic rings sandwiched between two steel end rods connected by a center bolt. A thin copper electrode is placed at the center of the resonator to serve as the high voltage lead. Figure 5-1 shows the schematic diagram of this resonator.

To analyze the above, one-dimensional wave theory will be applied to the metal cylinders. The ceramic rings are short and hollow and, strictly speaking, can neither be classified as rods nor infinite plates. However, because of the complexity of the models for other than the rod or the plate, for this study, they will be approximated as one or the other. On the other hand, the copper electrode is very thin (less than 0.1") and is treated as rigid and massless. In the following, the resonator will be analyzed by modeling the ceramics as plates and rods.

The thickness plate model--Taking advantage of the symmetry property, the equivalent circuit of this system can be obtained by straightforward techniques [1].* The resultant equivalent circuit is shown in Fig. 5-2. The various symbols have the expressions:

---

*Numbers in brackets refer to references at the end of this chapter.

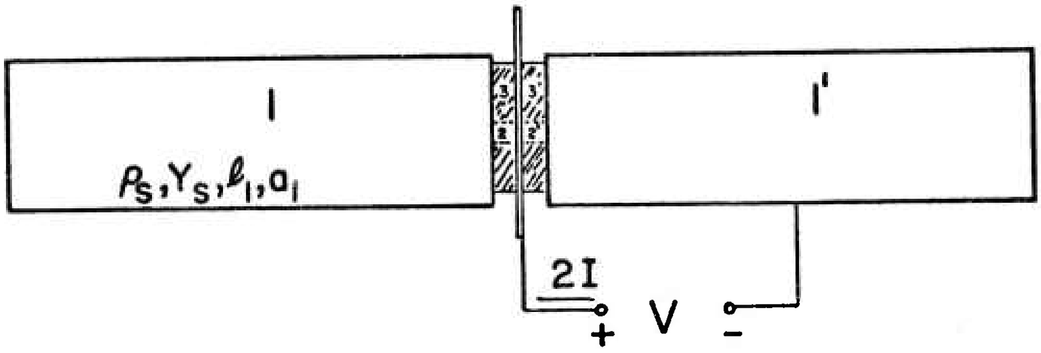
1
1'
ρ_S, Y_S, ℓ_1, a_1
3
2
3'
2'
2I
+
V
-

Fig. 5-1 The symmetrical simple resonator

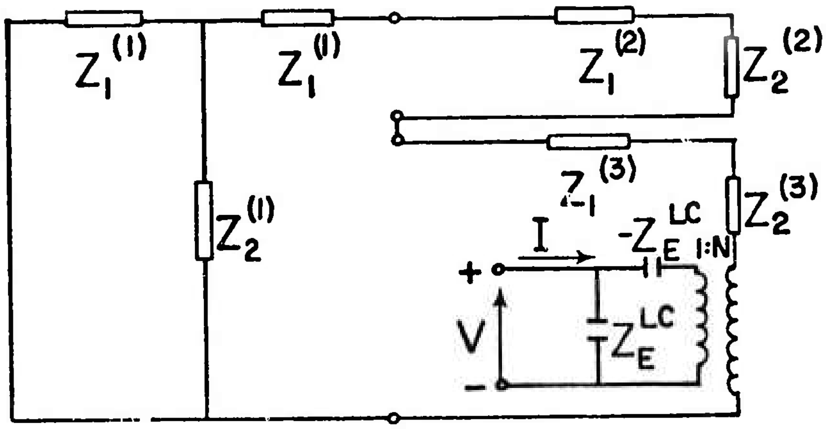
$Z_1^{(1)}$
$Z_1^{(1)}$
$Z_1^{(2)}$
$Z_2^{(2)}$
$Z_1^{(3)}$
$Z_2^{(3)}$
$Z_2^{(1)}$
I
$-Z_E^{LC}$
1:N
+
V
-
Z_E^{LC}

Fig. 5-2 Equivalent circuit for the symmetrical simple resonator -- thickness plate model

$$Z_1^{(i)} = ja_i z_o^{(i)} \tan \tfrac{1}{2} \Gamma_i \ell_i \qquad (5\text{-}1)$$

$$Z_2^{(i)} = - ja_i z_o^{(i)} / \sin \Gamma_i \ell_i \qquad (5\text{-}2)$$

where $i = 1, 2, 3$ for elements 1, 2, 3, respectively (referring to Fig. 5-1) and

$$z_o^{(1)} = z_o^{(2)} = (\rho_s Y_s)^{1/2} \quad \text{(metal elements 1 and 2)}$$

$$z_o^{(3)} = (\rho_c c_{33}^D)^{1/2} \quad \text{(ceramic plates)}$$

$$\Gamma_1 = \Gamma_2 = \omega / c_b, \quad c_b = (Y_s / \rho_s)^{1/2}$$

$$\Gamma_3 = \omega / (c_{33}^D / \rho_c)^{1/2} \qquad (5\text{-}3)$$

The other quantities are

$$Z_E^{LC} = \beta_{33}^S \ell_3 / j\omega a_3$$

$$N = h_{33} a_3 / \beta_{33}^S \ell_3 = h_{33} / j\omega Z_E^{LC} \qquad (5\text{-}4)$$

The equivalent circuit can be simplified to that of Fig. 5-3 (a), which, in turn, is equivalent to Fig. 5-3 (b).

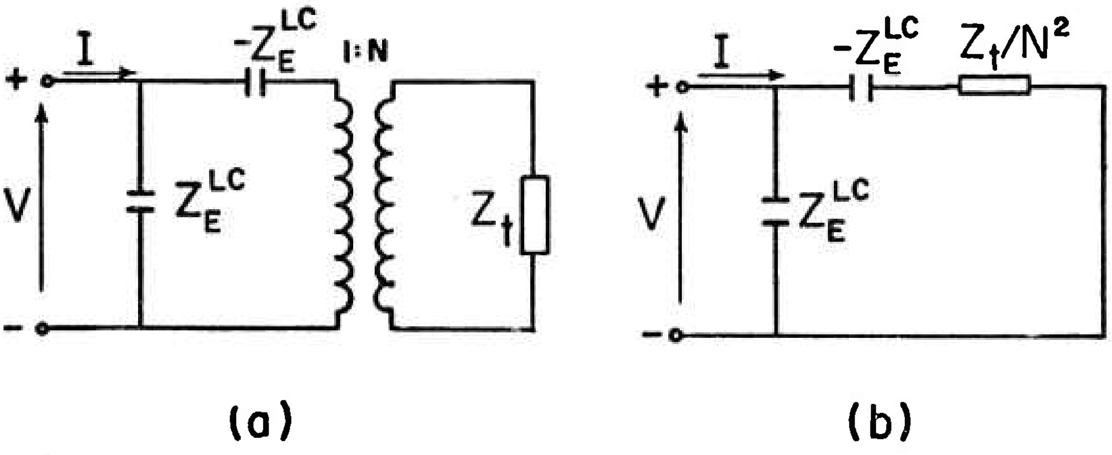

Fig. 5-3 Simplified equivalent circuits

The impedance Z_t in Fig. 5-3(a) can be written as

$$\begin{aligned} Z_t &= Z_1^{(1)} + Z_1^{(2)} + Z_2^{(2)} + Z_1^{(3)} + Z_2^{(3)} \\ &\quad + Z_1^{(1)} Z_2^{(1)} \Big/ \left(Z_1^{(1)} + Z_2^{(1)}\right) \\ &= ja_1 z_0^{(1)} \tan \Gamma_1 \ell_1 - ja_2 z_0^{(2)}/\tan \Gamma_2 \ell_2 - ja_3 z_0^{(3)}/\tan \Gamma_3 \ell_3 \end{aligned} \tag{5-5}$$

Thus, the terminal impedance Z is as follows:

$$Z^{-1} = I/V = \left(Z_E^{LC}\right)^{-1} + \left(-Z_E^{LC} + Z_t/N^2\right)^{-1}$$

$$Z = Z_E^{LC}\left(1 - N^2 Z_E^{LC}/Z_t\right) \tag{5-6}$$

The resonant frequency is given by $Z = 0$, or,

$$Z_t = N^2 Z_E^{LC} = - jh_{33}{}^2 a_3/\omega \ell_3 \beta_{33}^S \tag{5-7}$$

Substituting the definitions of Z_t, N and Z_E^{LC}, the following frequency equation is obtained;

$$a_1 z_0^{(1)} \tan \Gamma_1 \ell_1 - a_2 z_0^{(2)}/\tan \Gamma_1 \ell_2 - a_3 z_0^{(3)}/\tan \Gamma_3 \ell_3 = -h_{33}^2 a_3/\omega \ell_3 \beta_{33}^S \tag{5-8}$$

Since $z_0^{(3)}$ and $z_0^{(1)}$ are comparable, $\Gamma_1 \ell_1 \gg \Gamma_2 \ell_2$, $\Gamma_1 \ell_1 \gg \Gamma_3 \ell_3$, thus when $\omega \ell_1/c_b \rightarrow \pi/2$, the value of the first term in eq. (5-8) is large and increasing, while the value of the third term is also large but decreasing. This implies that the lowest frequency solution to eq. (5-8) will occur near $\omega \ell_1/c_b = \pi/2$. Therefore, for the lowest resonant frequency, the approximation $\tan \Gamma_2 \ell_2 \doteq \Gamma_2 \ell_2$, $\tan \Gamma_3 \ell_3 \doteq \Gamma_3 \ell_3$, can be made and eq. (5-8) becomes

$$\tan \Gamma_1 \ell_1 = [(a_2 \ell_1/a_1 \ell_2) + a_3 \ell_1/a_1 \ell_3)(c_{33}^D - \epsilon_{33}^S h_{33}^2)/Y_s]/\Gamma_1 \ell_1 \tag{5-9}$$

One can show that $c_{33}^D - \epsilon_{33}^S h_{33}^2 = c_{33}^E$. Thus eq. (5-9) is simplified to

$$\tan \Gamma_1 \ell_1 = [(a_2 \ell_1/a_1 \ell_2) + (a_3 \ell_1/a_1 \ell_3)(c_{33}^E/Y_s)]/\Gamma_1 \ell_1 \tag{5-10}$$

To understand the physical meaning of this result, eq. (5-10) will be compared to the frequency equation obtained by replacing the ceramic rings by an isotropic elastic rod with Young's modulus equal to Y_c. It is easy to show that the frequency equation for this system is

$$\tan \Gamma_1 \ell_1 = [(a_2 \ell_1/a_1 \ell_2) + (a_3 \ell_1/a_1 \ell_3)(Y_c/Y_s)]/\Gamma_1 \ell_1 \tag{5-11}$$

Comparing eq. (5-10) to eq. (5-11) one can see that the two frequency equations are identical if one substitutes Y_c in eq. (5-10) for c_{33}^E. Thus the following conclusion is made: for the thickness plate model, the resonant frequency of a simple resonator is given by the pure elastic system in which the ceramic has an equivalent Young's modulus equal to c_{33}^E. Stated differently, the resonant frequency is the natural frequency of the system with the piezoelectric rings short circuited.

Equation (5-10) can be solved numerically. For the OSU simple resonator, the following numerical data were used:

Table 5-1 - Numerical Data for the OSU Simple Resonator

For steel elements:

$a_1 = 2.074$ in.^{2}
$\ell_1 = 5.0$ in.
$Y_s = 20.02 \times 10^{10}$ N/m^2
$= 29.0 \times 10^6$ psi

$a_2 = 0.1964$ in.^{2}
$\ell_2 = 0.265$ in.
$c_b = 5050$ m/sec
$= 19.88 \times 10^4$ in./sec

For the PZT-4 rings:

$a_3 = 1.325$ in.^{2}
$c_{33}^E = 11.5 \times 10^{10}$ N/m^2
$= 16.7 \times 10^6$ psi
$Y_3^E = 6.45 \times 10^{10}$ N/m^2
$= 9.35 \times 10^6$ psi

$\ell_3 = 0.25$ in.
$c_{33}^D = 15.9 \times 10^{10}$ N/m^2
$= 23.1 \times 10^6$ psi
$Y_3^D = 12.65 \times 10^{10}$ N/m^2
$= 18.2 \times 10^6$ psi

After substitution of the above data into eq. (5-10), the frequency equation becomes

$$\tan(\omega\ell_1/c_b) = 9.197/(\omega\ell_1/c_b) \tag{5-12}$$

The solution is $\omega\ell_1/c_b = 1.418$, thus $f_r^{plate} = 0.226\, c_b/\ell_1 = 8980$ Hz. While the resonant state is characterized by the zeros of the reactance, the antiresonant state is characterized by the zeros of susceptance. For this problem, the antiresonant frequency is given by $Z \to \infty$, or $Z_t = 0$. Again using the approximation $\tan \Gamma_2\ell_2 \doteq \Gamma_2\ell_2$, $\tan \Gamma_3\ell_3 \doteq \Gamma_3\ell_3$, the result is

$$\tan \Gamma_1\ell_1 = [(a_2\ell_1/a_1\ell_2) + (a_3\ell_1/a_1\ell_3)(c_{33}^D/Y_s)]/\Gamma_1\ell_1 \tag{5-13}$$

Physically, from this result it is equivalent to say that the ceramic has an equivalent Young's modulus equal to c_{33}^D. Hence, the antiresonant frequency is the natural frequency of the system with the ceramic open circuited. Substitution of the numerical data yields

$$\tan(\omega\ell_1/c_b) = 12.01/(\omega\ell_1/c_b) \qquad (5\text{-}14)$$

Thus $f_a^{plate} = 0.2309\ c_b/\ell_1 = 9180$ Hz

The longitudinal rod model--For the longitudinal rod model, the only modification to be made is in the part of the equivalent circuit representing the ceramic. The equivalent circuit for a longitudinally vibrating ceramic for the rod is incorporated and the new equivalent circuit of this model is shown in Fig. 5-4. Some of the symbols appearing in the figure were given previously in eqs. (5-1), (5-2) and (5-3). Additional definitions are

$$z_o^{(3)} = (\rho_c Y_3^D)^{1/2} \quad \text{for the ceramic rod}$$

$$\Gamma_3 = \omega/c_{bc} \quad , \quad c_{bc} = (Y_3^D/\rho_c)^{1/2}$$

$$Z_E^{LC} = s_{33}^E\ell_3/j\omega a_3\epsilon_{33}^T s_{33}^D$$

$$N = g_{33}/j\omega s_{33}^D Z_E^{LC} = a_3 d_{33}/\ell_3 s_{33}^D \qquad (5\text{-}15)$$

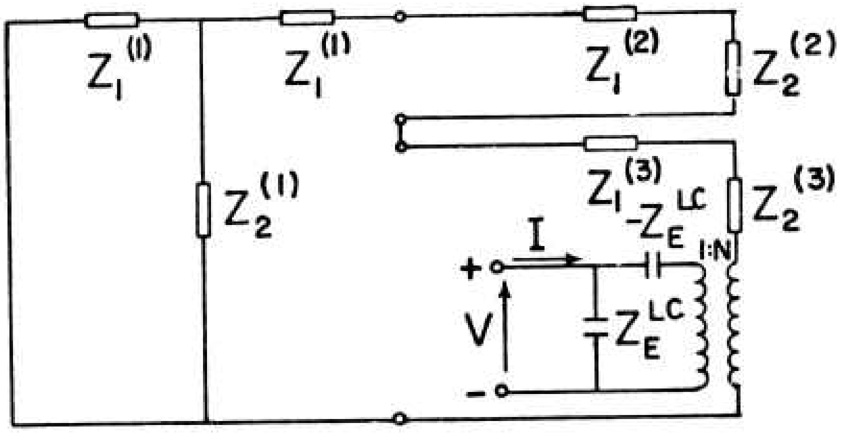

Fig. 5-4 Equivalent circuit for the symmetrical simple resonator-longitudinal rod model

Again, the equivalent circuit is simplified. The resulting circuit is exactly the same as that of Fig. 5-3 for the plate model, except that the symbols have different definitions. After manipulation, the impedance is found to be

$$Z = Z_E^{LC}\left(1 - N^2 Z_E^{LC}/Z_t\right) \tag{5-16}$$

where

$$Z_t = ja_1 z_o^{(1)} \tan \Gamma_1 \ell_1 - ja_2 z_o^{(2)}/\tan \Gamma_1 \ell_2 - ja_3 z_o^{(3)}/\tan \Gamma_3 \ell_3 \tag{5-17}$$

For the resonant frequency, $Z = 0$ yields

$$\tan \Gamma_1 \ell_1 = a_2 z_o^{(2)}/a_1 z_o^{(1)} \tan \Gamma_1 \ell_2 + a_3 z_o^{(3)}/a_1 z_o^{(1)} \tan \Gamma_3 \ell_3$$

$$- (a_3/a_1 \omega \ell_3)(s_{33}^E - s_{33}^D)/s_{33}^E s_{33}^D z_o^{(1)} \tag{5-18}$$

With the same argument given previously, the approximations, $\tan \Gamma_1 \ell_2 \doteq \Gamma_1 \ell_2$, $\tan \Gamma_3 \ell_3 \doteq \Gamma_3 \ell_3$, can be made. Thus, eq. (5-18) becomes

$$\tan \omega \ell_1/c_b = [(a_2 \ell_1/a_1 \ell_2) + (a_3 \ell_1/a_1 \ell_3)(Y_3{}^E/Y_s)]/(\omega \ell_1/c_b) \tag{5-19}$$

Equation (5-19) can be regarded as representing a mechanical system with a short circuit across the faces of the ceramic. Substituting the numerical data given in Table 5-1, eq. (5-19) reduces to

$$\tan(\omega \ell_1/c_b) = 5.975/(\omega \ell_1/c_b) \tag{5-20}$$

This has a solution, $(\omega \ell_1/c_b) = 1.3488$, or $f_r^{rod} = 8540$ Hz. The antiresonant frequency is given by $Z_t = 0$, which yields

$$\tan \omega \ell_1/c_b = [(a_2 \ell_1/a_1 \ell_2) + (a_3 \ell_1/a_1 \ell_3)(Y_3{}^D/Y_s)]/(\omega \ell_1/c_b) \tag{5-21}$$

Equation (5-21) can be regarded as representing a mechanical system with an open circuit across the faces of the ceramic. Using the data of Table 5-1, eq. (5-21) becomes

$$\tan \omega \ell_1/c_b = 9.937(\omega \ell_1/c_b) \tag{5-22}$$

A solution to this equation is $\omega \ell_1/c_b = 1.4281$, or $f_a^{rod} = 0.2273\ c_b/\ell_1 = 9038$ Hz.

Comparing f_r^{plate}, f_r^{rod}, f_a^{plate}, f_a^{rod} to one another, one can see that the resonant frequencies of the above two models differ considerably, while the antiresonant frequencies do not differ very much.

The spring model--The third model being formulated is the "spring model". For this model, the crystals are approximated by a linear spring with its spring constant remaining to be determined. A simple resonance test is required to assign the equivalent spring constant. It is hoped that this constant can be applied to other resonators of similar configuration. In this way, the complicating factors which result in discrepancies between experimental resonant frequencies and the one-dimensional theoretical results can be disposed of simply. Furthermore, the complicated piezoelectric relations can be eliminated. Figure 5-5(a) shows this model schematically. Taking advantage of the symmetry property of this problem, the problem is simplified as shown in Fig. 5-5(b). The equations of motion are similar to those used earlier. The general solutions are

$$u_1(x_1,t) = (A_1 \cos \omega x_1/c_b + B_1 \sin \omega x_1/c_b)\, e^{j\omega t}$$

$$u_2(x_2,t) = (A_2 \cos \omega x_2/c_b + B_2 \sin \omega x_2/c_b)\, e^{j\omega t} \qquad (5\text{-}23)$$

The boundary conditions are

$$\partial u_1/\partial x_1 \Big|_{x_1 = 0} = 0$$

$$u_2(0,t) = 0$$

$$u_1(\ell_1,t) = -\, u_2(\ell_2,t)$$

$$a_1 Y_s \partial u_1/\partial x_1 \Big|_{x_1 = \ell_1} = a_2 Y_s \partial u_2/\partial x_2 \Big|_{x_2 = \ell_2} + 2K\, u_2(\ell_2,t) \qquad (5\text{-}24)$$

Substituting eq. (5-23) into eq. (5-24) yields

$$B_1 = A_2 = 0$$

$$A_1 \cos \omega\ell_1/c_b = -\, B_2 \sin \omega\ell_2/c_b - A_1 a_1 Y_s(\omega/c_b) \sin \omega\ell_1/c_b$$

$$= B_2 a_2 Y_s(\omega/c_b) \cos \omega\ell_2/c_b + 2K\, B_2 \sin \omega\ell_2/c_b \qquad (5\text{-}25)$$

The frequency equation is obtained from eq. (5-25) for nontrivial solutions of A_1 and B_2. It is

$$\tan \omega\ell_1/c_b = (a_2/a_1)/\tan \omega\ell_2/c_b + 2K/(a_1 \omega Y_s/c_b) \qquad (5\text{-}26)$$

Since $\ell_1 >> \ell_2$, $\tan \omega\ell_2/c_b \doteq \omega\ell_2/c_b$ so that

$$\tan \omega\ell_1/c_b = [a_2\ell_1/a_1\ell_2 + 2K/(Y_s a_1/\ell_1)]/(\omega\ell_1/c_b) \qquad (5\text{-}27)$$

Substituting the numerical data of Table 5-1 into the above equation, the solution for the lowest natural frequency can be plotted against

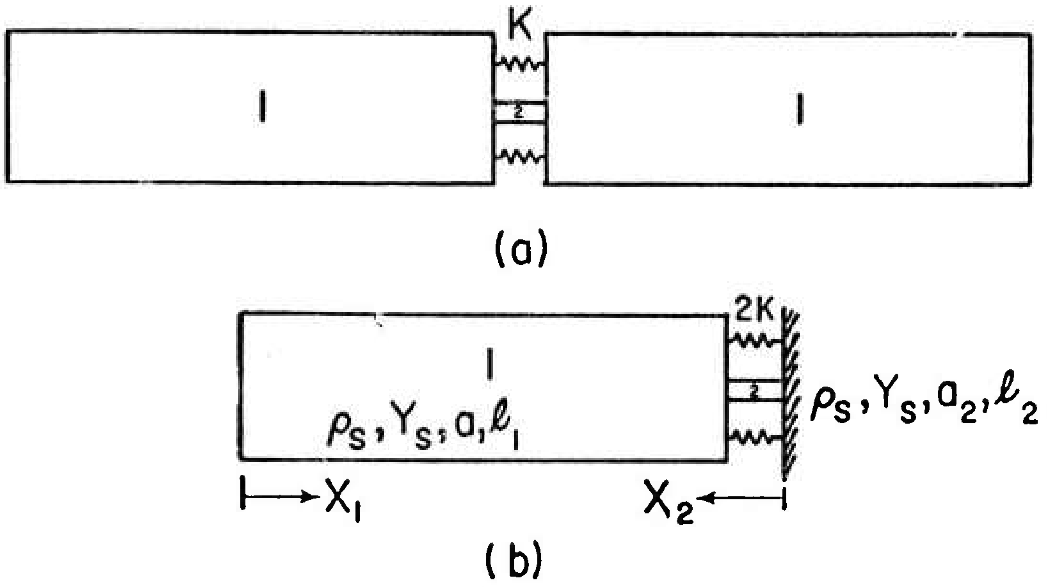

Fig. 5-5 The spring model for the symmetrical simple resonator

the unknown K value as shown in Fig. 5-6. Specifically, if one uses the strength of material K values, i.e., if $2K = Y_3^E a_c/\ell_c = 5.00 \times 10^7$ lb/in., eq. (5-27) becomes

$$\tan \omega\ell_1/c_b = 6.01/(\omega\ell_1/c_b) \tag{5-28}$$

The solution is $\omega\ell_1/c_b = 1.35$. Thus the natural frequency is $f^E = 8545$ Hz. If the value $2K = Y_3^D a_c/\ell_c = 9.70 \times 10^7$ lb/in. is used, one obtains

$$\tan \omega\ell_1/c_b = 9.95/(\omega\ell_1/c_b) \tag{5-29}$$

The solution is $\omega\ell_1/c_b = 1.4283$, thus the natural frequency is is $f^D = 9040$ Hz. The above two natural frequencies are indicated in Fig. 5-6. Theoretically, comparing eqs. (5-19) and (5-21) to eq. (5-27), the frequencies obtained above should be exactly the same as those for the longitudinal rod model. However, due to the round-off errors, the values are slightly different.

(B) The Asymmetric Simple Resonator

In Fig. 5-7, a schematic diagram of an asymmetric simple resonator is shown. In this figure, Part 1 is considered to be a solid cylinder which consists of the end nut and a portion of the center bolt screwed together; Part 2 is a hollow cylindrical steel sleeve. Part 3

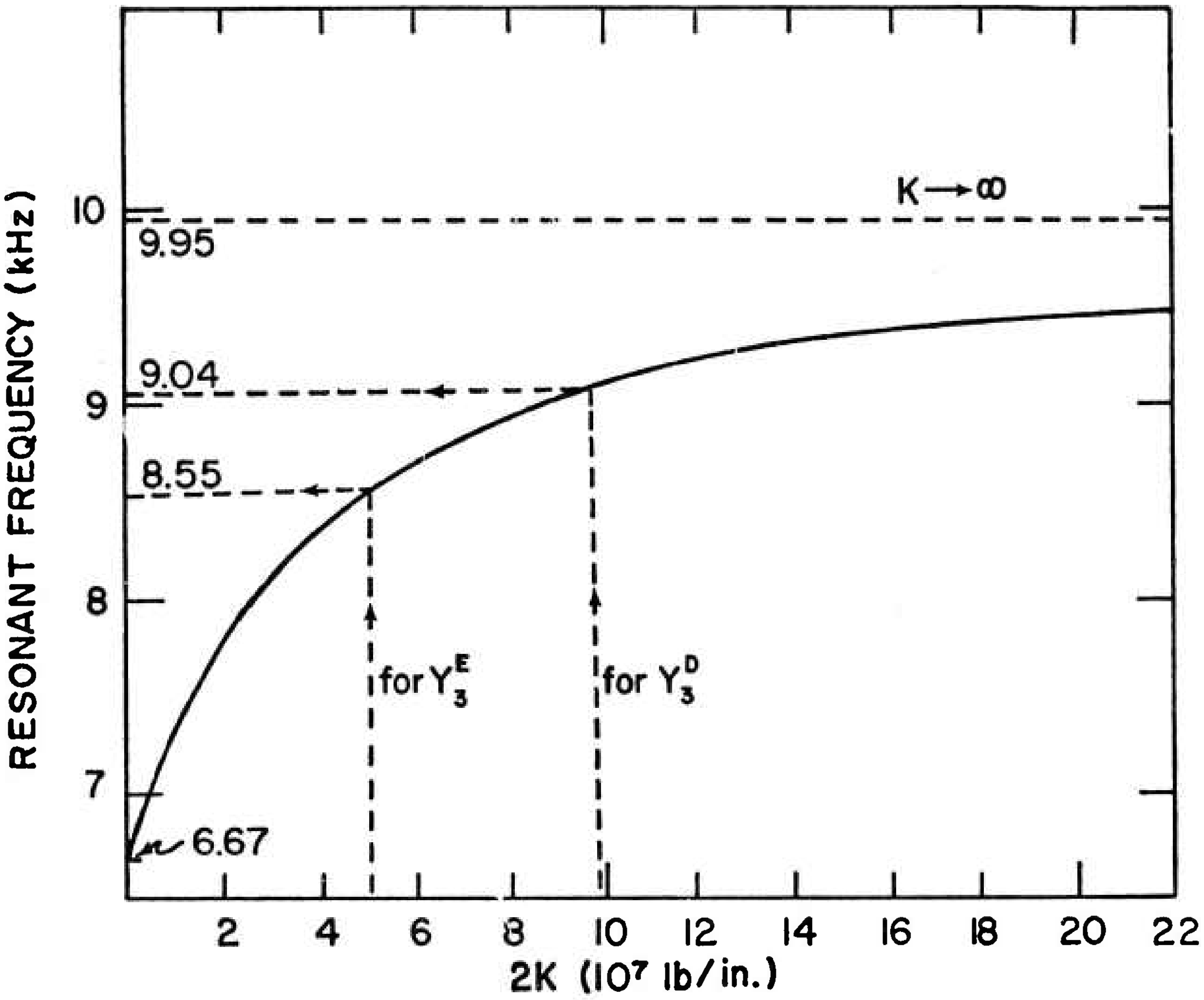

Fig. 5-6 The natural frequency versus the spring constant K

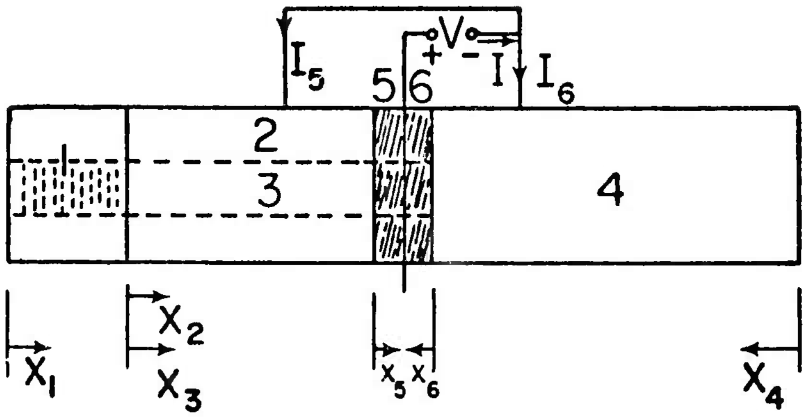

Fig. 5-7 The asymmetric simple resonator

represents the remaining center bolt while Part 4 is the solid steel cylinder on the other side of the ceramic rings, and Parts 5 and 6 are the two ceramic rings.

The one-dimensional wave model--To analyze this problem, one-dimensional wave equations will again be employed to model each part of the resonator. Boundary conditions at the ends and interfaces must be incorporated to solve for the various constants as well as the frequency equation. The equivalent circuits obtained previously can be used to relate the forces and the velocities for the boundary conditions. For this problem, this will yield 26 equations for 26 unknown terminal velocities, forces and currents. Numerical calculation of the resonant frequency is possible by looking for the frequency for which the determinant of coefficients of the above unknowns vanishes. This could be determined by use of an electronic computer but would consume considerable computational time. However, by using the following scheme without resorting to the equivalent circuit method, the procedure can be simplified. Thus, from this point on, the equivalent circuit will not be used again. The general solutions presented previously will be substituted directly into the boundary conditions and the frequency equation, which is obtained from the vanishing determinant of the resulting coefficient matrix, will be solved numerically on the computer.

The general solutions for the steel members 1 through 4 are expressed as follows:

$$u_i(x_i,t) = (A_i \cos \Gamma x_i + B_i \sin \Gamma x_i)\, e^{j\omega t} \qquad (5\text{-}30)$$

where $\Gamma = \omega/c_b$, $c_b = (Y_s/\rho_s)^{1/2}$, and $i = 1, 2, 3, 4$ for members 1, 2, 3, 4, respectively. The velocities and forces can be derived as follows:

$$v_i(x_i,t) = j\omega(A_i \cos \Gamma x_i + B_i \sin \Gamma x_i)\, e^{j\omega t}$$

$$f_i(x_i,t) = Y_s a_i \Gamma(-A_i \sin \Gamma x_i + B_i \cos \Gamma x_i)\, e^{j\omega t} \qquad (5\text{-}31)$$

where again, i = 1, 2, 3, 4. For the ceramics

$$u_p(x_p,t) = (A_p \cos \Gamma_c x_p + B_p \sin \Gamma_c x_p)\, e^{j\omega t}$$

$$v_p(x_p,t) = j(A_p \cos \Gamma_c x_p + B_p \sin \Gamma_c x_p)\, e^{j\omega t}$$

$$f_p(x_p,t) = a_c[\omega z_{oc}(-A_p \sin \Gamma_c x_p + B_p \cos \Gamma_c x_p) - \zeta I_p^a]\, e^{j\omega t}$$

$$V^a = -\, h_{33}[(\cos \Gamma_c \ell_p - 1)A_p + B_p \sin \Gamma_c \ell_p] + Z_E^{LC}\, I_c^a \qquad (5\text{-}32)$$

where p = 5 and 6 for ceramic rings 5 and 6, respectively, and

$$\Gamma_c = \omega/c_{bc}$$

$$c_{bc} = \begin{cases} (c_{33}^D/\rho_c)^{1/2} & \text{for thickness plate model} \\ (Y_3^D/\rho_c)^{1/2} & \text{for longitudinal rod model} \end{cases}$$

$$Z_E^{LC} = \begin{cases} \beta_{33}^S \ell_c/j\omega a_c & \text{for thickness plate model} \\ s_{33}^E \ell_c/j\omega a_c \epsilon_{33}^T s_{33}^D & \text{for longitudinal rod model} \end{cases}$$

$$\zeta = \begin{cases} h_{33}/j\omega a_c & \text{for thickness plate model} \\ g_{33}/j\omega a_c s_{33}^D & \text{for longitudinal rod model} \end{cases}$$

$$z_{oc} = \begin{cases} (\rho_c c_{33}^D)^{1/2} & \text{for thickness plate model} \\ (\rho_c Y_3^D)^{1/2} & \text{for longitudinal rod model} \end{cases}$$

The boundary conditions are

1) at free end $x_1 = 0$
$f_1(0,t) = 0$ (5-33)

2) at interface $x_1 = \ell_1$, $x_2 = 0$ and $x_3 = 0$
$u_1(\ell_1,t) = u_2(0,t)$ (5-34)

$u_1(\ell_1,t) = u_3(0,t)$
$f_1(\ell_1,t) = f_2(0,t) + f_3(0,t)$ (5-35)

3) at interface $x_2 = \ell_2$, $x_5 = 0$
$u_2(\ell_2,t) = u_5(0,t)$
$f_2(\ell_2,t) = f_5(0,t)$ (5-36)

4) at interface $x_5 = \ell_c$, $x_6 = \ell_c$
$u_5(\ell_c,t) = -u_6(\ell_c,t)$
$f_5(\ell_c,t) = f_6(\ell_c,t)$ (5-37)

5) the current versus voltage relations

$$V = \int \overline{E}_5 \cdot d\overline{x}_5$$
$$V = \int \overline{E}_6 \cdot d\overline{x}_6 \qquad (5\text{-}38)$$

6) at end $x_4 = 0$

$$f_4(0,t) = 0 \qquad (5\text{-}39)$$

7) at interface $x_4 = \ell_4$, $x_3 = \ell_3$, and $x_6 = 0$

$$u_3(\ell_3,t) = - u_4(\ell_4,t)$$
$$u_6(0,t) = - u_4(\ell_4,t)$$
$$f_3(\ell_3,t) + f_6(0,t) = f_4(\ell_4,t) \qquad (5\text{-}40)$$

In summary, there are 14 equations for the 14 unknown A's, B's, and I's resulting from substituting the general solutions into the above boundary conditions. This is quite a simplification compared to the equivalent circuit approach which has 26 equations for 26 unknowns. The reason for this simplification can easily be explained: from minimum energy principle, it can be proved that one cannot specify force and velocity at the same end simultaneously. Thus, all the end forces and velocities appeared in the equivalent circuit approach cannot be mutually independent. Therefore there must be one equation relating the end force and velocity at each end. For our problem, there are 6 members and thus 12 ends. This is why there are 12 equations and 12 unknowns. In the following, the general solutions will be substituted into the boundary conditions and then the relations will be simplified to give a frequency equation of a 7 x 7 determinant.

The substitutions yield,

$$B_1 = 0$$

$$A_1 \cos \Gamma \ell_1 = A_2$$

$$A_1 \cos \Gamma \ell_1 = A_3$$

$$-a_1 A_1 \sin \Gamma \ell_1 = a_2 B_2 + a_3 B_3$$

$$A_2 \cos \Gamma \ell_2 + B_2 \sin \Gamma \ell_2 = A_5$$

$$a_2 \omega z_o(-A_2 \sin \Gamma \ell_2 + B_2 \cos \Gamma \ell_2) = a_5(\omega z_{oc} B_5 - \zeta I_5^a)$$

$$A_5 \cos \Gamma_c \ell_c + B_5 \sin \Gamma_c \ell_c = -(A_6 \cos \Gamma_c \ell_c + B_6 \sin \Gamma_c \ell_c)$$

$$(-A_5 \sin \Gamma_c \ell_c + B_5 \cos \Gamma_c \ell_c + A_6 \sin \Gamma_c \ell_c - B_6 \cos \Gamma_c \ell_c) \\ - (\zeta/\omega z_{oc})(I_5^a - I_6^a) = 0$$

$$V^a = - h_{33}[(\cos \Gamma_c \ell_c - 1)A_5 + B_5 \sin \Gamma_c \ell_c] + Z_E^{LC} I_5^a$$

$$V^a = - h_{33}[(\cos \Gamma_c \ell_c - 1)A_6 + B_6 \sin \Gamma_c \ell_c] + Z_E^{LC} I_6^a \qquad (5\text{-}41)$$

$$B_4 = 0$$

$$A_3 \cos \Gamma \ell_3 + B_3 \sin \Gamma \ell_3 = - A_4 \cos \Gamma \ell_4$$

$$A_6 = A_4 \cos \Gamma \ell_4$$

$$\begin{aligned} a_3 \omega z_0 (-A_3 \sin \Gamma \ell_3 + B_3 \cos \Gamma \ell_3) + a_c(\omega z_{oc} B_6 - \zeta I_6^g) \\ = a_4 \omega z_0 (-A_4 \sin \Gamma \ell_4) \end{aligned} \qquad (5\text{-}41)$$

The simplified relations are

$$B_1 = 0,\ B_4 = 0,\ A_2 = A_3 = A_1 \cos \Gamma \ell_1$$

$$A_4 = - (A_1 \cos \Gamma \ell_1 \cos \Gamma \ell_3 + B_3 \sin \Gamma \ell_3)/\cos \Gamma \ell_4$$

$$A_5 = A_1 \cos \Gamma \ell_1 \cos \Gamma \ell_2 + B_2 \sin \Gamma \ell_2$$

$$A_6 = - (A_1 \cos \Gamma \ell_1 \cos \Gamma \ell_3 + B_3 \sin \Gamma \ell_3) \qquad (5\text{-}42)$$

$$\begin{bmatrix} \\ \\ D_{ij} \\ \text{(a } 7 \times 7 \text{ matrix)} \\ \\ \\ \end{bmatrix} \begin{bmatrix} A_1 \\ B_2 \\ B_3 \\ B_5 \\ B_6 \\ I_5 \\ I_6 \end{bmatrix} = \begin{bmatrix} C_1 \\ C_2 \\ C_3 \\ C_4 \\ C_5 \\ C_6 \\ C_7 \end{bmatrix} \qquad (5\text{-}43)$$

where $D_{ij} = 0$ and $C_i = 0$ except for

$$D_{11} = \sin \Gamma \ell_1, \quad D_{12} = a_2/a_1, \quad D_{13} = a_3/a_1$$

$$D_{21} = (a_2/a_1) \cos \Gamma \ell_1 \sin \Gamma \ell_2, \quad D_{22} = - (a_2/a_1) \cos \Gamma \ell_2$$
$$D_{24} = (a_c/a_1)(z_{oc}/z_o), \quad D_{25} = - (a_c/a_1)(\zeta/\omega z_o)$$

$$D_{31} = \cos \Gamma \ell_1 \cos \Gamma \ell_2 \cos \Gamma_c \ell_c - \cos \Gamma \ell_1 \cos \Gamma \ell_3 \cos \Gamma_c \ell_c$$
$$D_{32} = \sin \Gamma \ell_2 \cos \Gamma_c \ell_c, \quad D_{33} = - \sin \Gamma \ell_3 \cos \Gamma_c \ell_c$$
$$D_{34} = \sin \Gamma_c \ell_c, \quad D_{35} = \sin \Gamma_c \ell_c$$

$$D_{41} = \cos \Gamma \ell_1 \cos \Gamma \ell_2 \sin \Gamma_c \ell_c + \cos \Gamma \ell_1 \cos \Gamma \ell_3 \sin \Gamma_c \ell_c$$
$$D_{42} = \sin \Gamma \ell_2 \sin \Gamma_c \ell_c, \quad D_{43} = \sin \Gamma \ell_3 \sin \Gamma_c \ell_c$$
$$D_{44} = - \cos \Gamma_c \ell_c, \quad D_{45} = \cos \Gamma_c \ell_c, \quad D_{46} = - \zeta/\omega z_{oc}$$
$$D_{47} = \zeta/\omega z_{oc}$$

$$D_{51} = - (a_3/a_1) \cos \Gamma \ell_1 \sin \Gamma \ell_3 - (a_4/a_1) \tan \Gamma \ell_4 \cos \Gamma \ell_1 \cos \Gamma \ell_3$$
$$D_{53} = (a_3/a_1) \cos \Gamma \ell_3 - (a_4/a_1) \tan \Gamma \ell_4 \sin \Gamma \ell_3$$
$$D_{55} = (a_c/a_1)(z_{oc}/z_o), \quad D_{57} = (a_c/a_1)(\zeta/\omega z_o)$$

$$D_{61} = (\cos \Gamma_c \ell_c - 1) \cos \Gamma \ell_1 \cos \Gamma \ell_2$$
$$D_{62} = (\cos \Gamma_c \ell_c - 1) \sin \Gamma \ell_2$$
$$D_{64} = \sin \Gamma_c \ell_c, \quad D_{66} = - Z^{LC}_E / h_{33}$$

$$D_{71} = (1 - \cos \Gamma_c \ell_c) \cos \Gamma \ell_1 \cos \Gamma \ell_3$$
$$D_{73} = (1 - \cos \Gamma_c \ell_c) \sin \Gamma \ell_3$$
$$D_{75} = \sin \Gamma_c \ell_c, \quad D_{77} = - Z^{LC}_E / h_{33}$$

$$C_6 = - V^a / h_{33}, \quad C_7 = - V^a / h_{33}$$

The frequency equation is given by

$$\det[D_{ij}] = 0 \tag{5-44}$$

The spring model--As for the symmetric simple resonator, the spring model for the asymmetric simple resonator can be obtained by simply modeling the ceramics as an elastic spring (Fig. 5-8). The equations of motion and their corresponding general solutions are the same as previously given in (5-30) to (5-31) for the steel members. Boundary conditions 1, 2 and 6 are the same, while at steel-ceramic interfaces the original set of equations are replaced by the new set of equations involving the spring constant. These new equations are:

1) at $x_2 = \ell_2$,
$$f_2(\ell_2,t) + K[u_2(\ell_1,t) + u_4(\ell_4,t)] = 0 \tag{5-45}$$

2) at $x_4 = \ell_4$, and $x_3 = \ell_3$,
$$u_4(\ell_4,t) = - u_3(\ell_3,t)$$
$$f_4(\ell_4,t) = f_3(\ell_3,t) - K[u_2(\ell_2,t) + u_4(\ell_4,t)] \tag{5-46}$$

Copying down the rest of the valid boundary equations and substituting the general solutions into the above three boundary conditions, one obtains the following relations after some manipulation:

$$B_1 = 0, \; B_4 = 0$$

$$A_2 = A_3 = A_1 \cos \Gamma \ell_1$$

$$A_4 = (-A_1 \cos \Gamma \ell_1 \cos \Gamma \ell_3 - B_3 \sin \Gamma \ell_3) / \cos \Gamma \ell_4 \tag{5-47}$$

$$\begin{bmatrix} D_{11} & D_{12} & D_{13} \\ D_{21} & D_{22} & D_{23} \\ D_{31} & D_{32} & D_{33} \end{bmatrix} \begin{bmatrix} A_1 \\ A_2 \\ A_3 \end{bmatrix} = \begin{bmatrix} 0 \\ 0 \\ 0 \end{bmatrix} \tag{5-48}$$

where

$$D_{11} = \sin \Gamma \ell_1, \quad D_{12} = a_2/a_1, \quad D_{13} = a_3/a_1$$

$$D_{21} = (a_2/a_1) \cos \Gamma \ell_1 \sin \Gamma \ell_2 + \cos \Gamma \ell_1 (\cos \Gamma \ell_3 - \cos \Gamma \ell_2)$$

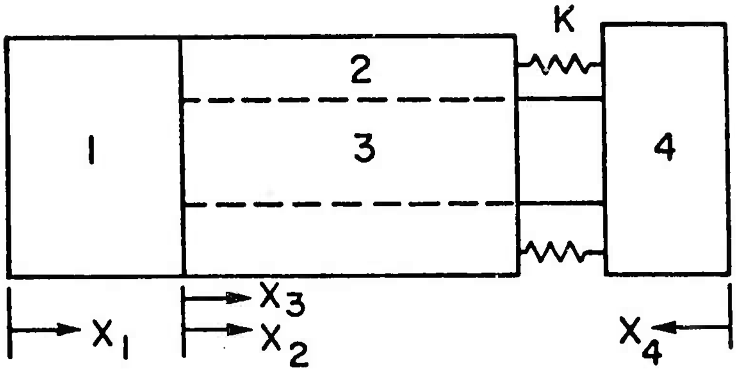

Fig. 5-8 The spring model for the asymmetric simple resonator

$$D_{22} = -(a_2/a_1)\cos\Gamma\ell_2 - \zeta_1 \sin\Gamma\ell_2$$
$$D_{23} = \zeta_1 \sin\Gamma\ell_3$$

$$D_{31} = -(a_3/a_1)\cos\Gamma\ell_1 \sin\Gamma\ell_3 - (a_2/a_1)\cos\Gamma\ell_1 \sin\Gamma\ell_2 - (a_4/a_1)\cos\Gamma\ell_1 \cos\Gamma\ell_3 \sin\Gamma\ell_4/\cos\Gamma\ell_4$$
$$D_{32} = (a_2/a_1)\cos\Gamma\ell_2$$
$$D_{33} = (a_3/a_1)\cos\Gamma\ell_3 - (a_4/a_1)\sin\Gamma\ell_3 \sin\Gamma\ell_4/\cos\Gamma\ell_4$$

In the above, the symbol $\zeta_1 = K\, c_b/Y_s a_1 \omega$ has been used. The frequency equation is given by

$$\det[D_{ij}] = 0 \qquad (5\text{-}49)$$

Again, this can be solved numerically. However, numerical solutions were not actually obtained in this study.

(C) The P-7 Resonator

The P-7 resonator is essentially the OSU P-7 transducer without the stepped horn. It differs from the asymmetric simple resonator only in its dimensions and its cross sections. It does not have a uniform cross-sectional area along its length. Also, it has a hexagonal cylindrical nut and steel sleeve. Figure 5-9 shows the schematic diagram of the P-7 resonator. The set of equations are identical to those of Section (B) except that the geometrical dimensions are different. The following data are used for the P-7 resonator.

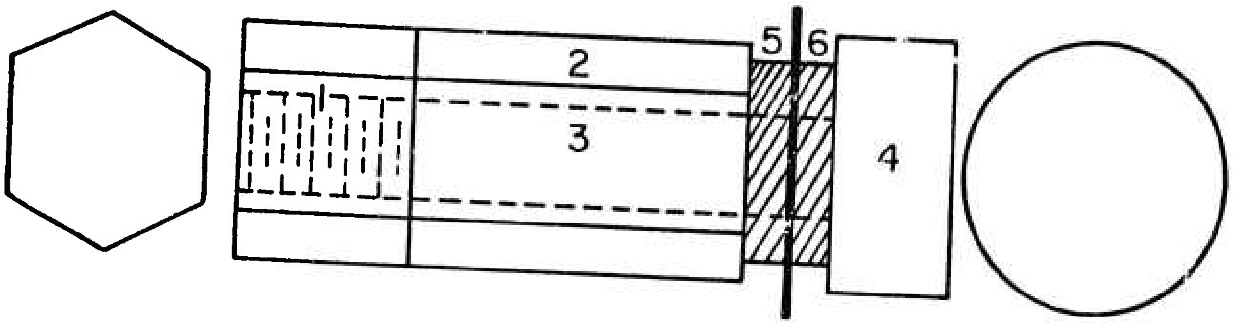

Fig. 5-9 The P-7 resonator

Table 5-2 - Dimensions for the P-7 Resonator

$\ell_1 = 1.25$ in.	$a_1 = 1.947$ in.^{2}
$\ell_2 = 2.75$ in.	$a_2 = 1.505$ in.^{2}
$\ell_3 = 3.35$ in.	$a_3 = 0.442$ in.^{2}
$\ell_4 = 0.97$ in.	$a_4 = 2.405$ in.^{2}
$\ell_5 = \ell_6 = \ell_c = 0.25$ in.	$a_5 = a_6 = a_c = 1.325$ in.^{2}

After substituting the material property coefficients the frequency equation, eq. (5-49) can be solved numerically on an electronic computer. The lowest resonant frequency is $f_r = 15.33$ kHz for the longitudinal rod model of the ceramic.

The spring model--After substituting the static strength of material K's, i.e., $K^E = 2.5 \times 10^7$ lb/in. and $K^D = 4.85 \times 10^7$ lb/in. in eq. (5-49), the lowest resonant frequencies were found to be $f_r^E = 16.4$ kHz, $f_r^D = 17.6$ kHz. Comparing the above two frequencies with the one for the longitudinal rod model, it is apparent that the spring model gives a frequency which is too high.

5-2 THE P-7 TRANSDUCER

The P-7 transducer can be thought of as a P-7 resonator plus a stepped horn. Figure 5-10 is a schematic diagram of the P-7 transducer. Although, as a first approximation the resonant frequency can be determined by using the "half-wavelength" approach, the more exact solution

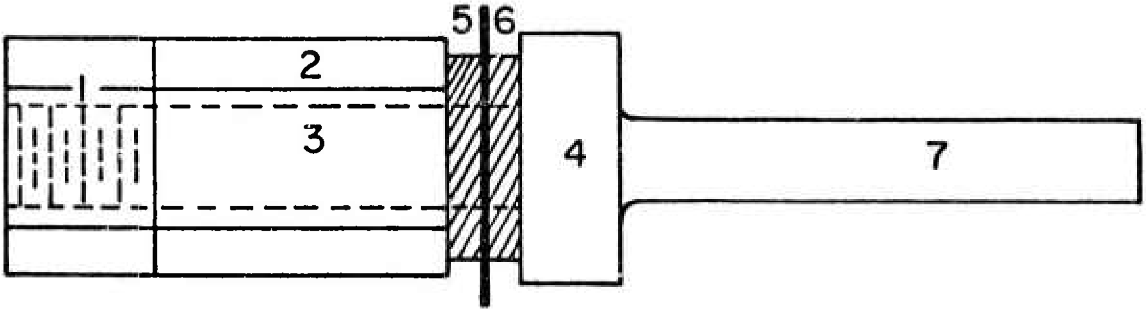

Fig. 5-10 The P-7 transducer

should be calculated from the more exact model. Especially, when the transfer function between the electrical terminals and the tip of the transmission line is to be decided, the piezoelectric equations must be taken into consideration. In this section, the method used in treating the P-7 resonator (Section 5-1 (C)) will be extended to include the stepped horn.

The general solutions for the steel members 1, 2, 3, 4, and 7 are given by eqs. (5-30) and (5-31), while for the ceramic rings 5, 6, eq. (5-30) applies. In addition to the boundary conditions given by eqs. (5-33) to (5-38), the following equations arise from the attachment of the stepped horn 7: They are:

1) at the free end $x_7 = 0$, $f_7(0,t) = 0$, so that
$B_7 = 0$

2) at interface $x_7 = \ell_7$, and $x_4 = 0$, $u_7(\ell_7,t) = u_4(0,t)$ and $f_7(\ell_7,t) = f_4(0,t)$; thus
$A_7 \cos \Gamma\ell_7 = A_4$
$-a_7 A_7 \sin \Gamma\ell_7 = a_4 B_4$

3) at interface $x_4 = \ell_4$, $x_3 = \ell_3$, and $x_6 = 0$, $u_4(\ell_4,t) = u_6(0,t) = - u_3(\ell_3,t)$, and $f_4(\ell_4,t) = f_6(0,t) + f_3(\ell_3,t)$; thus,
$A_4 \cos \Gamma\ell_4 + B_4 \sin \Gamma\ell_4 = A_6$
$a_4\omega z_o(- A_4 \sin \Gamma\ell_4 + B_4 \cos \Gamma\ell_4) = a_c(\omega z_{oc}B_6 - \zeta I_6^g)$
$\quad + a_3\omega z_o(- A_3 \sin \Gamma\ell_3 + B_3 \cos \Gamma\ell_3)$
$A_4 \cos \Gamma\ell_4 + B_4 \sin \Gamma\ell_4 = - (A_3 \cos \Gamma\ell_3 + B_3 \sin \Gamma\ell_3)$

Thus, there are 16 equations for 16 unknowns. Again, the above equations can be simplified and the frequency determinant obtained and solved numerically on an electronic computer. Substituting the numerical data previously given, the lowest resonant frequency versus a 5/8 in. diameter horn with a length of approximately 5 in. is obtained and shown in Fig. 5-11 as the "1-D Rod Model."

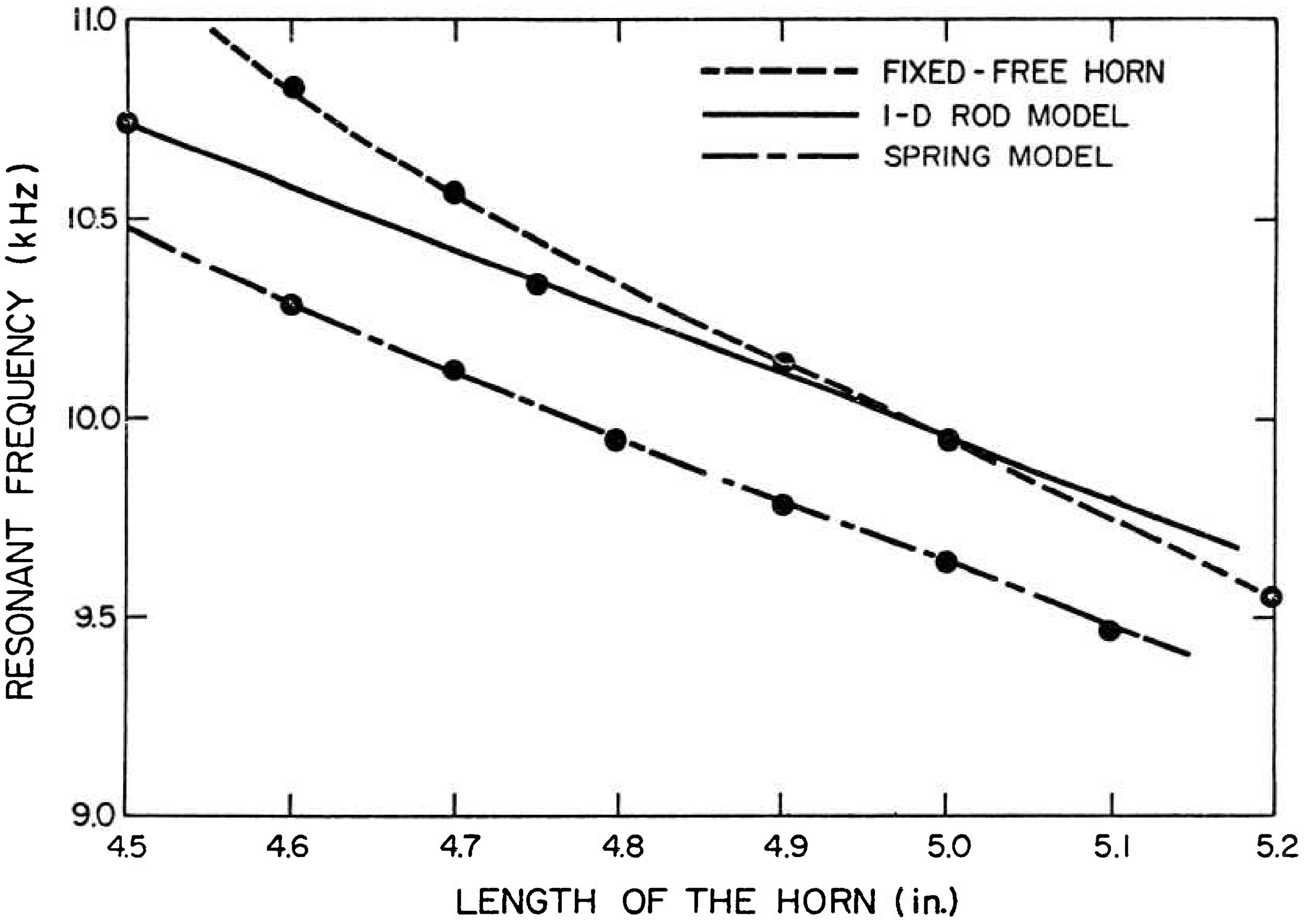

Fig. 5-11 The resonant frequency versus the length of horn of a P-7 transducer

The spring model--Figure 5-12 shows the spring model for the P-7 transducer. It is obtained from Fig. 5-10 by modeling the ceramic rings as an elastic spring with spring constant K. The formulation of the equations of motion are similar to the previous cases and will not be repeated here. After substituting the general solutions into the boundary conditions the frequency equation is found to be

$$\det[D_{ij}] = 0$$

where D_{ij} is a 3 x 3 matrix with

$$D_{11} = \sin\Gamma\ell_1, \quad D_{12} = a_2/a_1, \quad D_{13} = a_3/a_1$$

$$\begin{aligned}
D_{21} &= (a_2/a_1)\cos\Gamma\ell_1 \sin\Gamma\ell_2 + \zeta_1 \cos\Gamma\ell_1 \cos\Gamma\ell_3 \\
&\qquad - \zeta_1 \cos\Gamma\ell_1 \cos\Gamma\ell_2 \\
D_{22} &= -(a_2/a_1)\cos\Gamma\ell_2 - \zeta_1 \sin\Gamma\ell_2 \\
D_{23} &= \zeta_1 \sin\Gamma\ell_3
\end{aligned}$$

$$\begin{aligned}
D_{31} &= (a_4/a_1)[\sin\Gamma\ell_4 + (a_7/a_4)\tan\Gamma\ell_7 \cos\Gamma\ell_4]\cos\Gamma\ell_1 \\
&\quad \cos\Gamma\ell_3/[\cos\Gamma\ell_4 - (a_7/a_4)\tan\Gamma\ell_7 \sin\Gamma\ell_4] \\
&\quad + (a_3/a_1)\cos\Gamma\ell_1 \sin\Gamma\ell_3 - \zeta_1 \cos\Gamma\ell_1 (\cos\Gamma\ell_3 - \cos\Gamma\ell_2) \\
D_{32} &= \zeta_1 \sin\Gamma\ell_2 \\
D_{33} &= (a_4/a_1)[\sin\Gamma\ell_4 + (a_7/a_4)\tan\Gamma\ell_7 \cos\Gamma\ell_4]\sin\Gamma\ell_3/ \\
&\quad [\cos\Gamma\ell_4 - (a_7/a_4)\tan\Gamma\ell_7 \sin\Gamma\ell_4] - (a_3/a_1)\cos\Gamma\ell_3 \\
&\quad - \zeta_1 \sin\Gamma\ell_3
\end{aligned}$$

The resonant frequency (lowest) for $K = K^E = 2.5 \times 10^7$ lb/in. was found numerically for several lengths in the vicinity of 5 in. as shown in Fig. 5-11 as the "Spring Model." For a more direct comparison, the results of the longitudinal rod model and the fixed-free horn are also shown in the same figure. It is seen that the slopes of the one-dimensional model and the spring model are the same, while that of the fixed-free horn is somewhat steeper.

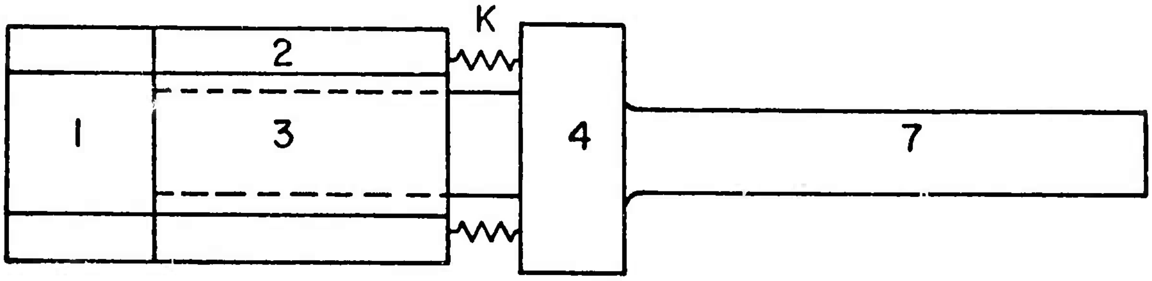

Fig. 5-12 The spring model for the P-7 transducer

In conclusion, it may be worthwhile to differentiate the physical meaning of the resonant frequency from that of the antiresonant frequency. At the resonant frequency the terminal current is infinite for a finite driving voltage, since the terminal impedance is zero. Consequently, the particle velocity is infinite except at the velocity nodal points. Contrarily, the particle velocity will be zero at the antiresonant frequency, since the terminal impedance is infinite and the terminal current is thus zero for a finite driving voltage. However, it must be noted that the pure mechanical systems (neglecting the piezoelectric effects completely) do have a natural frequency at the antiresonant frequency. This is evident from the vanishings of the pure mechanical impedances for the equivalent circuit systems. Therefore, in order to drive the system into its resonant state at the antiresonant frequency, the mechanical forcing function (force or displacement) must be provided at one of the mechanical terminals. An electrical driving voltage will not be able to drive the system into its resonant state at the antiresonant frequency. Therefore, in order to obtain maximum energy transduction, the system must be driven at its resonant frequency.

5-3 STATIC BIAS AND TEMPERATURE EFFECTS ON TRANSDUCER RESONANT FREQUENCIES

As mentioned earlier, ferroelectrics are highly nonlinear in material properties. Their properties are also subject to change with passage of time, a phenomenon called the aging effect. Experiments have shown that a major disturbance such as large temperature change, or high stress level, or intense electric field, will not only change the properties themselves, but also trigger a new cycle of aging. Thus a complete understanding and precise prediction of the behavior of a ferroelectric material is quite difficult. However, thanks to various researchers, sufficient useful information has been accumulated on PZT-4 to make possible a better understanding of its properties.

In the OSU Sonic Power Laboratory, the resonant frequency of a transducer has been observed to shift with different prestress bias levels. It also shifts with the change of temperature of the transducer. Moreover, a higher driving voltage will always decrease the resonant frequency. These effects greatly hamper efforts to operate the transducer at a fixed frequency. Because the shift of resonant frequency of a transducer shifts it away from the fixed supply frequency, the transducer is detuned; i.e., it has an amplitude of vibration much less than the designed amplitude at the power supply frequency. Figure 5-13 illustrates the detuning effect with the shift of resonant frequency. The detuned transducer is seen to have a very small response at the power supply frequency, although the shift of frequency is small compared to the original resonant frequency. When a transducer is detuned, one way to correct this problem is to tune it back to its original resonant frequency by changing the length of the horn, since the resonant frequency of a transducer is very sensitive to

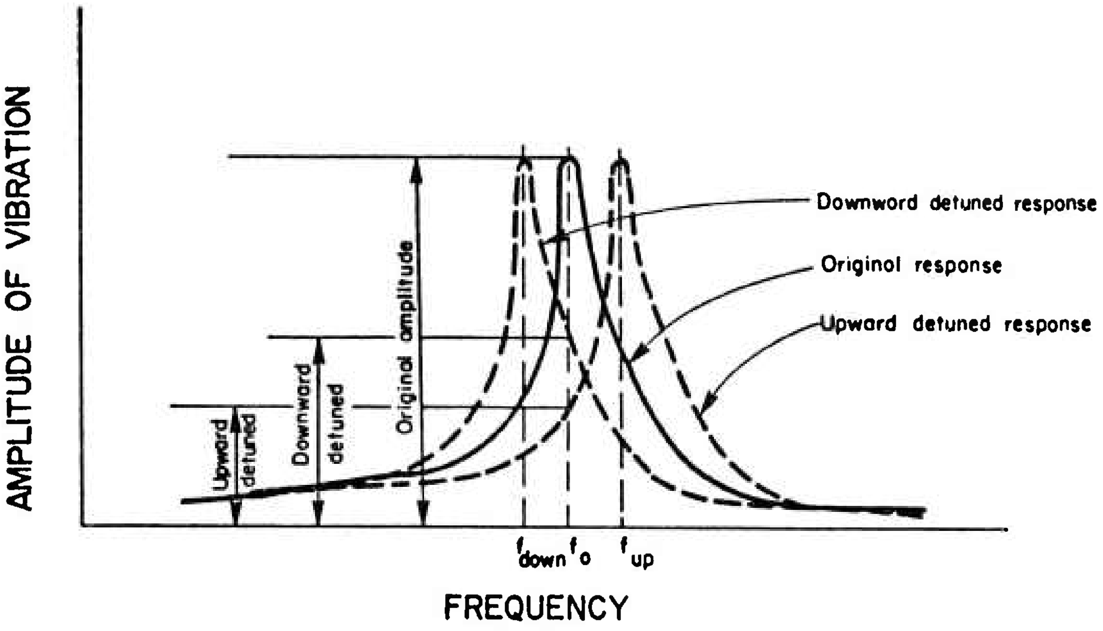

Fig. 5-13 The detuning effect on a transducer

the horn length (see Fig. 5-11). However, this process of correction is rather tedious.

The above problem prompts this investigation. In the following, the shift of resonant frequency of a transducer due to the prestress bias level, the temperature change and the voltage supply amplitude will be investigated. The aging effect will be compared to the experimental ones, where they are available.

Another aspect of the work will be an experimental-theoretical approach utilizing the spring models previously proposed. This approach is used because the ceramic rings are hard to model more precisely since they are neither a plate nor a rod. Although the more exact two-dimensional model can be formulated, the solution is difficult to obtain and will not be used in this study. It is envisioned that the spring model which has a spring constant K, that may be found from experiments with the simple resonator, will enable one to determine the shift of resonant frequencies in the other resonators and transducers using the same ceramics.

(A) Summary of Prestress, Temperature and Voltage on PZT-4 Properties

It has been suggested that the shifts of the material properties of piezoelectrics are dictated by the intrinsic nonlinearities of ferroelectrics [2]. The nonlinearities of the ferroelectric ceramics result from domain effects. This is best explained by the following quotation from Berlincourt and Krueger [3]:

> "... The polar axis of a perovskite ferroelectric may be oriented parallel to an edge (tetragonal), a body diagonal (rhombohedral), or a face diagonal (orthorhombic) of the pseudocubic perovskite cell. The polar direction is elongated with respect to its length in the reference cubic phase. In each case 180 degrees domain reorientation can take place. This will here be termed 'lelectrical' domain reorientation, since this is the main type of orientation which occurs with high electric drive, and since reorientation of this type takes place with no nonpiezoelectric mechanical strain. The other type of domain reorientation is termed 'mechanical' since it involves dimensional changes. This is by 90 degrees in a tetragonal perovskite, by 120 - 60 or 90 degrees in an orthorhombic perovskite, and by 109 - 71 degrees in a rhombohedral perovskite. ...."

Experiments on some ferroelectric ceramics have been carried out by several researchers on the property changes due to environmental effects. Summaries of previous work have been prepared by Berlincourt and co-workers and are presented in Mason [4] and Mattiat [5]. Insofar as PZT-4 is concerned, the data is scattered and incomplete. Brown and McMahon [6], [7] measured the planar Young's modulus, the planar coupling factor, d_{31}, dielectric losses, ϵ_{33}^T, and the aging of its permittivity under maintained planar stress. Krueger and Berlincourt [8] measured the effects of lateral and longitudinal compressive stress on d_{33}, ϵ_{33}, k_{31}, d_{31}, and d_{32} under maintained stress and after stress release. More detailed descriptions were later given by Berlincourt and Krueger [3] which included the ac rms electric field effects on the ϵ_{33}^T and the dielectric loss tangent, the parallel stress effects on ϵ_{33}^T and d_{33}, and some temperature and aging information. In a 1969 Clevite conference, Berlincourt [9] presented a brief discussion on this subject. Nishi [10] also gave data for the one-dimensional pressure, high field, hydrostatic pressure and aging effects on the permittivity and dielectric losses and some coupling factors. The most complete data were given in three papers presented by Krueger [11], [12], [13] which summarized the effects of parallel pressure, lateral stress, ac field, aging and temperature on properties such as the permittivity, the dielectric loss tangent and the piezoelectric constants. But, again the data was far from complete.

Some of this information is summarized in Figs. 5-14, 5-15 and 5-16. Thus, Fig. 5-14 shows the parallel stress effect on d_{33} and ϵ_{33}^T with stress maintained. It has been noted that the coupling factor is less sensitive to the pressure effect [14]. Thus if one assumes a constant coupling factor under various prestress levels, from the relation

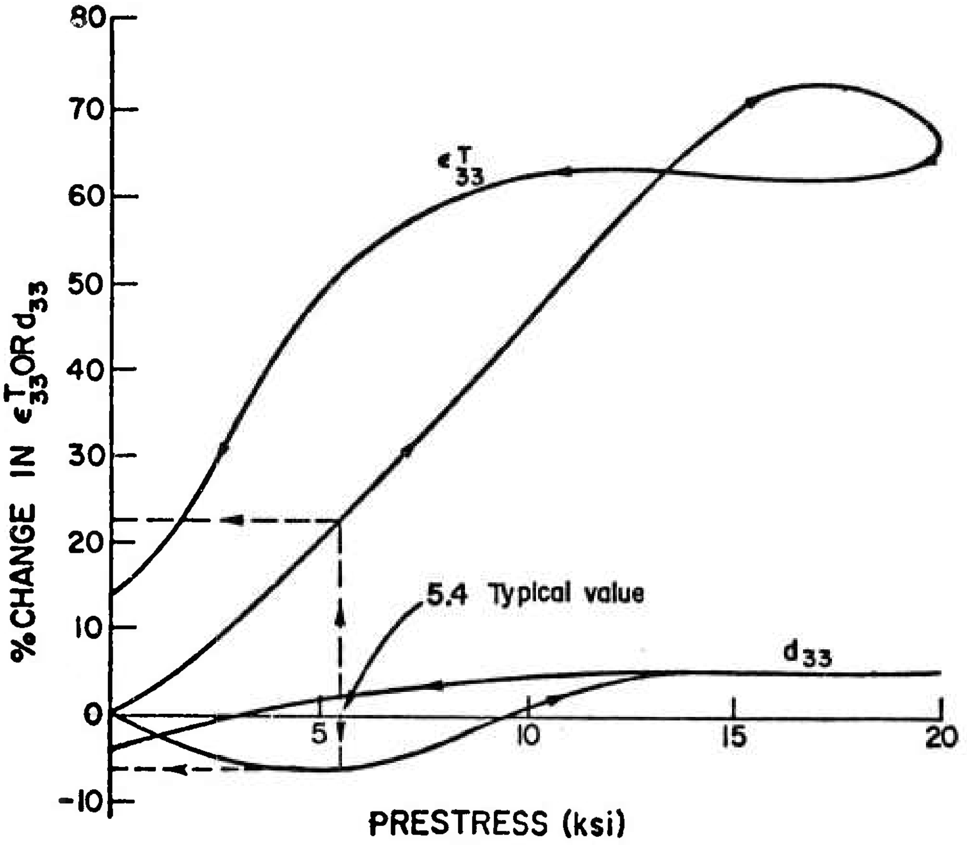

Fig. 5-14 The d_{33} and ϵ_{33}^T versus the parallel stress (from [3] and [14])

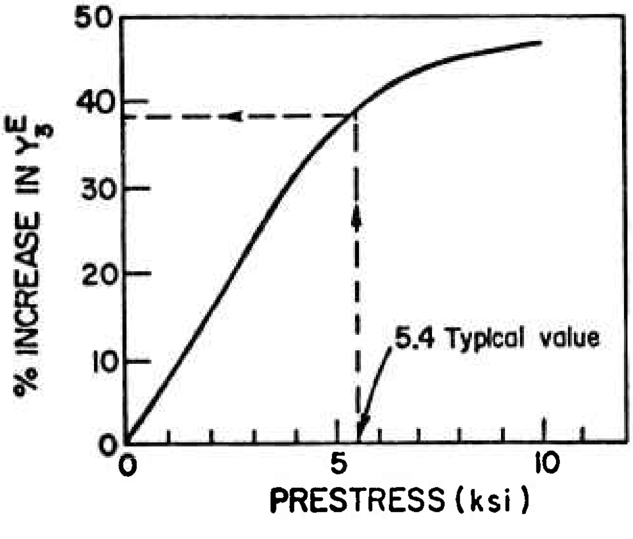

Fig. 5-15 The Youngs' modulus versus the parallel stress

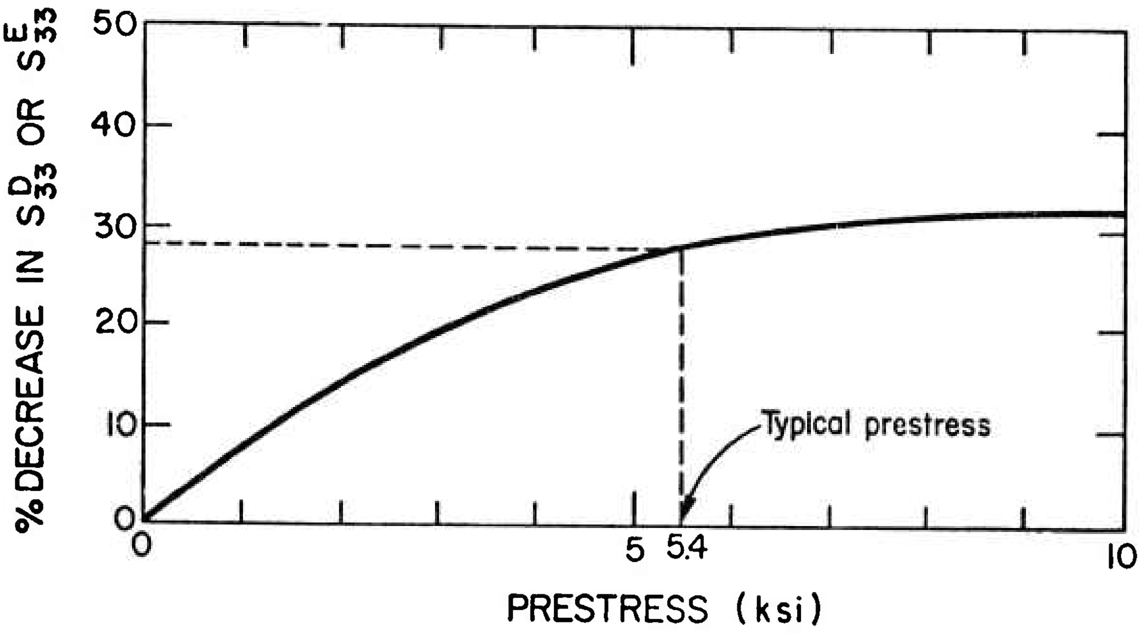

Fig. 5-16 S_{33}^D and S_{33}^E versus prestress as calculated from Fig. 5-14

$$k_{33} = d_{33}/(s_{33}^E \epsilon_{33}^T)^{1/2}$$

the elastic compliance s_{33}^E or the Young's modulus $Y_3^E = 1/s_{33}^E$ can be deduced from Fig. 5-14. The result is shown in Fig. 5-15. The elastic compliance s_{33}^D can be obtained by the relation

$$s_{33}^D = s_{33}^E - (d_{33})^2/\epsilon_{33}^T \qquad (5\text{-}50)$$

Figure 5-16 shows the compliance s_{33}^D and s_{33}^E versus the parallel compressive stress relations. Later, data from these figures will be applied to calculate the effect of prestress on the resonant frequency.

(B) Effects of Prestress, Temperature and Voltage on Resonant Frequency

By applying the changes of material properties given in the literature, as summarized in Section (A), to the frequency equations for the various resonators and transducers, the new resonant frequencies can be calculated. In this way the effects of the prestress, temperature, and voltage may be evaluated. In the following, the prestress effect will be treated and then the temperature and voltage effects will be discussed.

The prestress effect on resonant frequency--In Section (A), Figs. 5-14, 5-15, and 5-16 have shown the material coefficient changes at different prestress levels that are needed for calculating the resonant frequencies. For example, from Fig. 5-15 the Young's modulus, Y_3^E, at a certain prestress level can be obtained. Substituting this value together with other data which are not changed by the prestress into the frequency equation (5-19), one can calculate the resonant frequency at this prestress level for the symmetric simple resonator. The results of this calculation are shown in Fig. 5-17. Similarly, for the P-7 resonator and the P-7 transducer, one can obtain the necessary material coefficient variations from Figs. 5-14, 5-15, and 5-16 at various prestress levels and then substitute them into the frequency eq. (5-43) for the P-7 transducer to get Figs. 5-18 and 5-19. From the above three figures, one can see that the resonant frequencies increase with an increase in prestress level.

The temperature effect on resonant frequency--Not enough data is available in the literature for a direct evaluation of this effect. The only material coefficient variation given [14], [15] pertaining to our problem is ϵ_{33}^E which shows little increase from -60°F to 200°F. Thus, more experiments must be conducted on the variations of the material properties with temperature changes. However, it is possible to show by a fairly simple calculation that an increase in temperature will tend to release a portion of the prestress in the ceramics and to decrease the resonant frequency.

The prestressed ceramic and center bolt of a simple resonator is shown in Fig. 20. Suppose at room temperature the ceramic has a total length ℓ_2. The original prestress at room temperature was f_o. Then, at temperature $\Delta\theta$ above room temperature, the decrease in the prestress $f_o - f$ can be shown to be

$$f_o - f = (\alpha_2\ell_2 - \alpha_c\ell_3)\Delta\theta/(1/K_c + 1/K_2) \qquad (5\text{-}51)$$

where α_2 and α_c are the linear thermal expansion coefficient for steel and the PZT-4 ceramic, respectively, and the K's represent the static spring constants for the ceramic bar and the steel center bolt.

For the simple resonator given in Section 5-1(A), $K_c = 2.5 \times 10^7$ lb/in. and $K_2 = 1.12 \times 10^7$ lb/in. For steel $\alpha_2 = 6.5 \times 10^{-6}/°F$, and for the ceramic $\alpha_c = 2.5 \times 10^{-6}/°C = 1.4 \times 10^{-6}/°F$. Utilizing the values in eq. (5-51), one obtains

$$f_o - f = 20.3\ \Delta\theta \qquad (5\text{-}52)$$

This relation is plotted as shown in Fig. 5-21. Using eq. (5-52) a theoretical-experimental approach will be introduced to evaluate the resonant frequency shift due to the prestress releasing effect. For a P-7 transducer, the typical prestress on the ceramic is $f_o/a_c = 5.4$ ksi (or, 125 ft-lb torque on the 3/4-in. diameter stress bolt). Thus, from eq. (5-52), the prestress f/a_c at any temperature can be calculated for the symmetric simple resonator. After resonant frequency versus

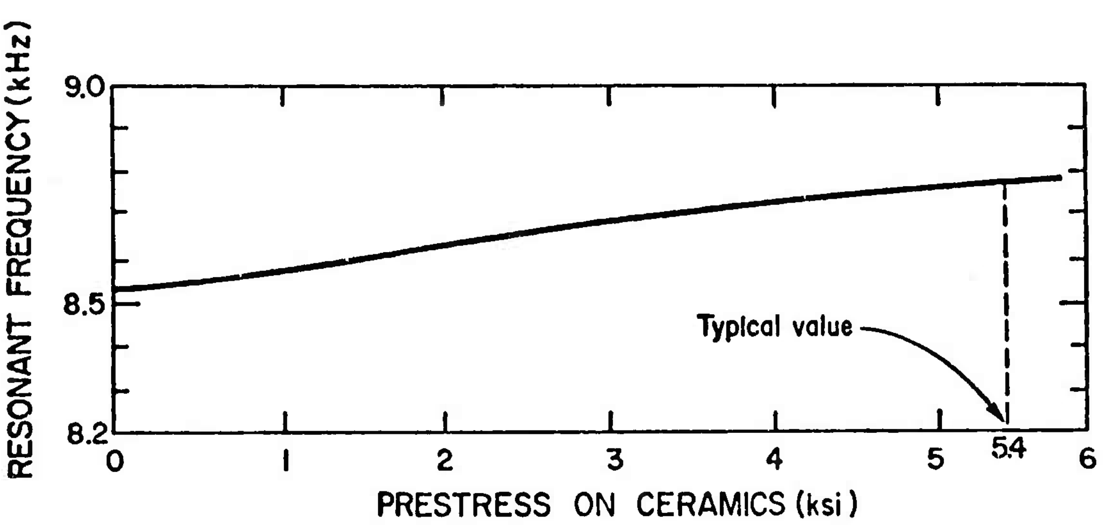

Fig. 5-17 The prestress effect on the resonant frequency of a simple resonator

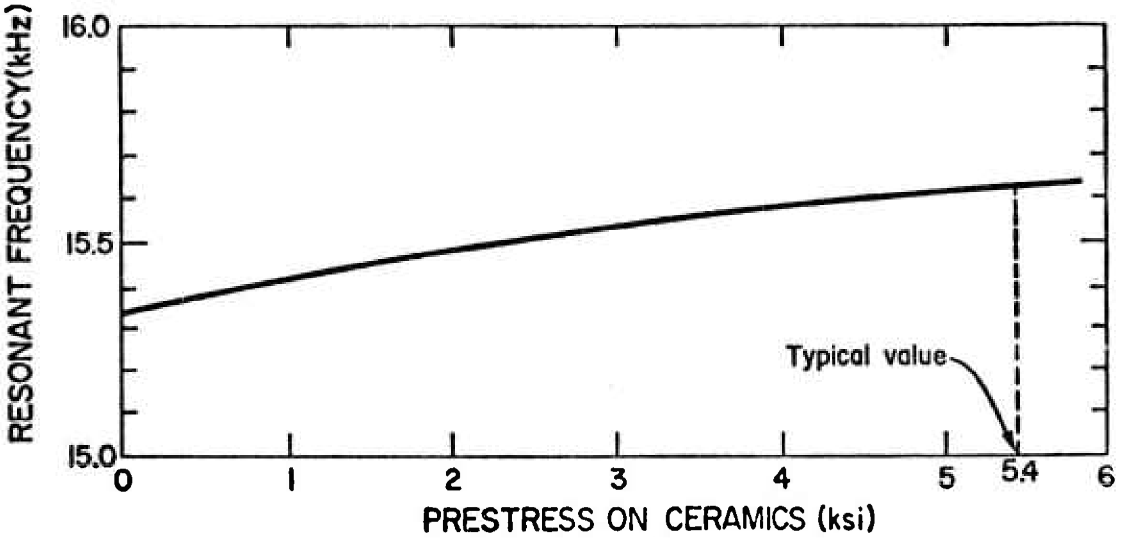

Fig. 5-18 The prestress effect on the resonant frequency of a P-7 resonator

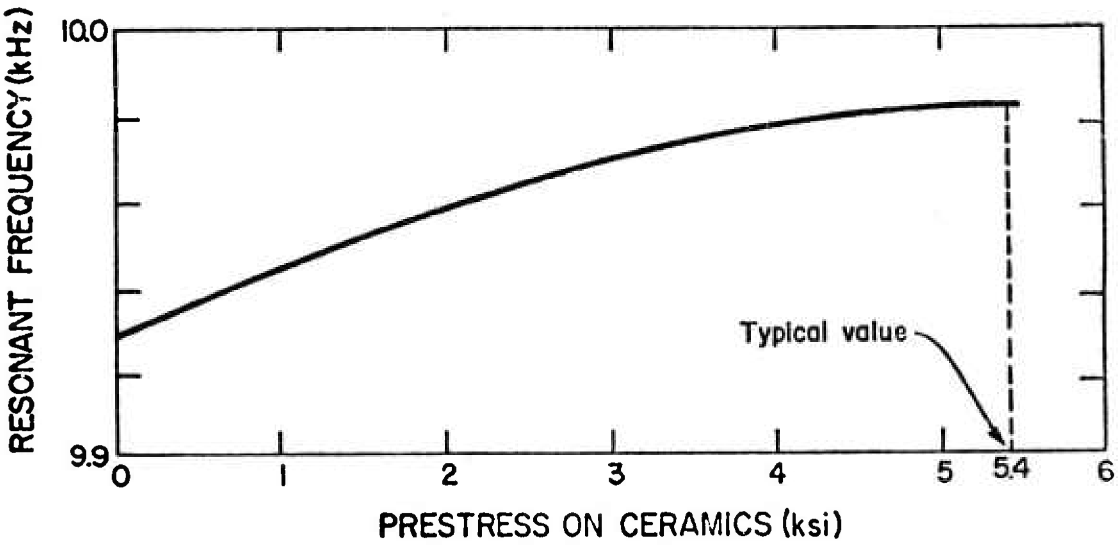

Fig. 5-19 The prestress effect on the resonant frequency of a P-7 transducer

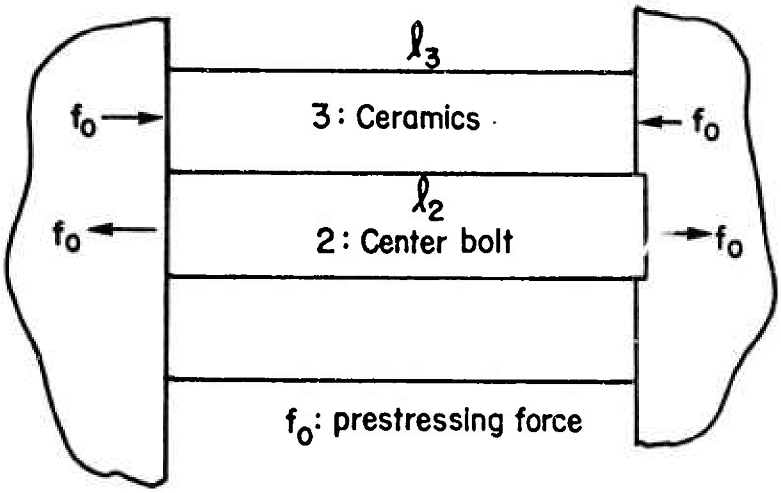
l_3
3: Ceramics
f_o
f_o
l_2
2: Center bolt
f_o
f_o
f_o: prestressing force

Fig. 5-20 The prestressed ceramic and center bolt

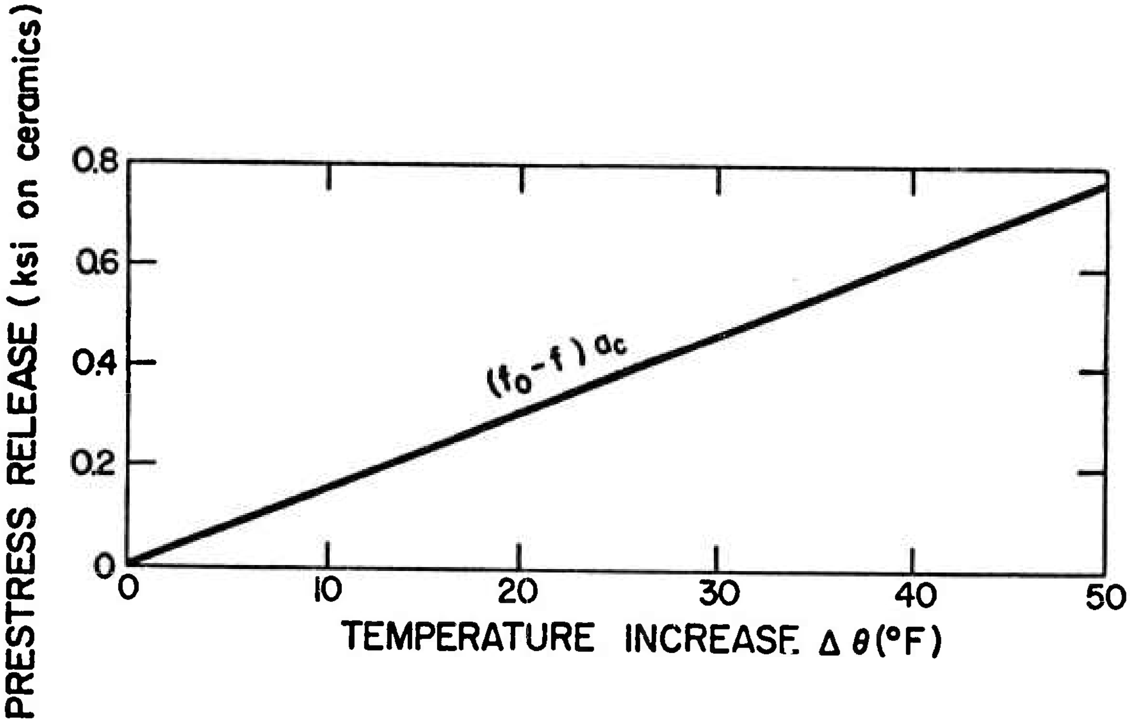

Fig. 5-21 Prestress release versus temperature change on a simple resonator

prestress relations are determined experimentally, the resonant frequency versus temperature relations can be deduced. Particularly, for the symmetric simple resonator, the experimental resonant frequency versus prestress relation is given later in Fig. 5-34 (Section (D)); the result of this approach is shown in Fig. 5-22.

For the asymmetric simple resonator, the P-7 resonator and the P-7 transducer, the prestressed portion is shown in Fig. 5-23. This time the same type of derivation leads to

$$f_o - f = \Delta\theta(\alpha_3\ell_3 - \alpha_2\ell_2 - \alpha_c\ell_5)/(1/K_2 + 1/K_3 + 1/K_c) \qquad (5\text{-}53)$$

Substituting the data given in Table 5-2 and the material properties, one obtains $K_2 = 1.587 \times 10^7$ lb/in., $K_3 = 0.3826 \times 10^7$ lb/in., and eq. (5-53) becomes

$$f_o - f = 8.78\,\Delta\theta \qquad (5\text{-}54)$$

Again, experimental resonant frequency versus prestress relations were obtained, as shown later in Figs. 5-35 and 5-36, for the P-7 resonator and the P-7 transducer, respectively. The stress release effects are obtained and shown in Figs. 5-24 and 5-25 for the P-7 resonator and the P-7 transducer, respectively, by employing eq. (5-54) and Figs. 5-35 and 5-36.

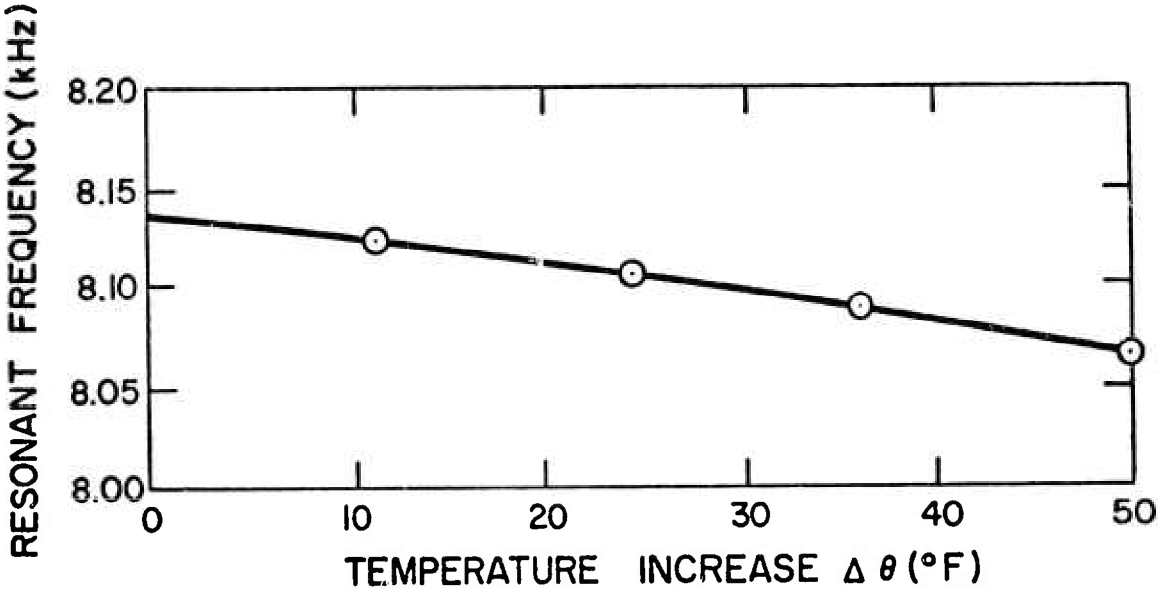

Fig. 5-22 Theoretical-experimental temperature effects on the resonant frequency of a simple resonator

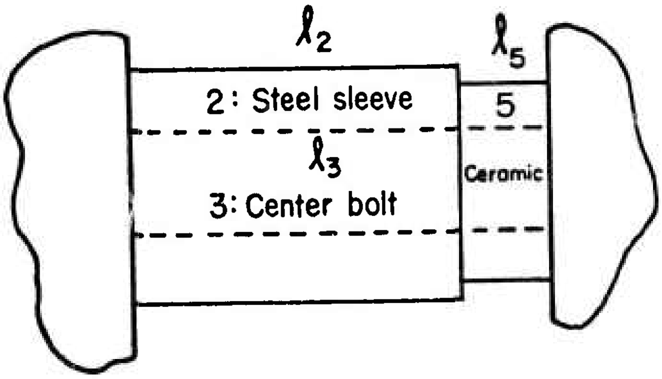
l_2
l_5
2: Steel sleeve
5
l_3
Ceramic
3: Center bolt

Fig. 5-23 The prestressed ceramic, center bolt and metal sleeve

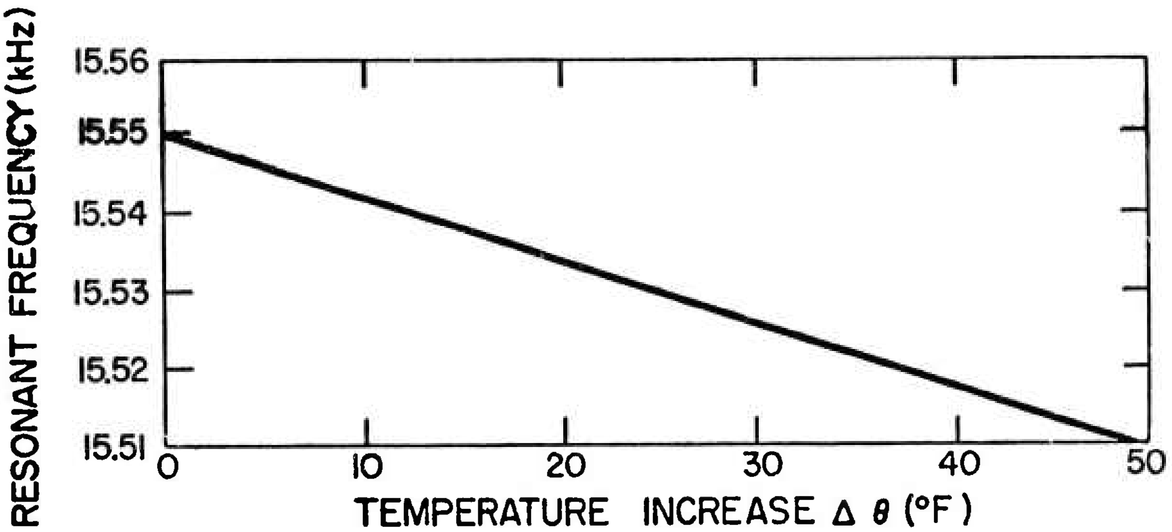

Fig. 24 Theoretical-experimental temperature-prestress release effects on a P-7 resonator

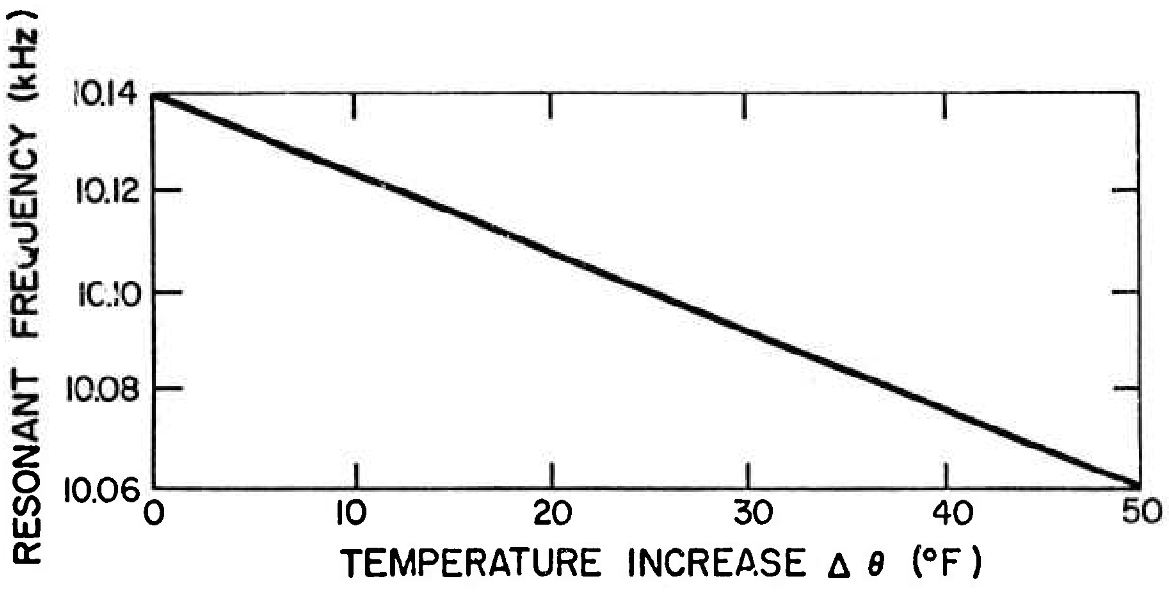

Fig. 5-25 Theoretical-experimental temperature-prestress release effects on a P-7 transducer

From the above results, one can see that the prestress release is a linear function of the temperature change. As a result, the temperature increase always reduces the resonant frequency of a resonator or a transducer. In a later section one will see that this is in accord with the experimental observation.

The electric field effect on resonant frequency--As mentioned in Section (A), there is not sufficient available literature to evaluate this effect. The only plausible reasoning which can be put forth here is that a higher voltage tends to cause a higher amplitude of vibration in the transducer. A bigger dynamic stress will be realized in the ceramics. This according to the literature [15], tends to reduce the Young's modulus which in turn causes a resonant frequency drop. Berlincourt [15] gave data which showed that a peak dynamic stress of 4 ksi corresponded to a 5% decrease in Young's modulus Y_1^E. However, data on the more useful Y_3^E is not available.

(C) Effect of Prestress on Resonant Frequency, Based on the Spring Model

The ceramic rings used in our resonators and transducers can be modeled strictly neither as a plate nor a rod. It was suggested in Section 5-1 to model the ceramic rings as a linear spring leaving the spring constant K to be determined. In so doing, it is envisioned that an experimentally determined K value for the symmetric simple resonator at a certain prestress level can also be applied to the other resonators and transducers. It is envisioned that the spring models so applied will account for the resonant frequency shifts due to the prestress effect. To find the spring constant, K, at a given prestress level, the resonant frequency is obtained from the experimental resonant frequency versus prestress relation for a symmetric simple resonator given by the later Fig. 5-34. Then, the spring constant is determined from Fig. 5-6 at this frequency corresponding to this prestress level. Figure 5-26 gives the K versus the prestress relations so obtained. The data points can be approximated by a straight line which does not pass through the coordinate origin.

Having acquired the K values at different prestress levels, those values may be applied to calculate the resonant frequencies of a P-7 resonator and transducer at different prestress levels utilizing the spring model formulations presented in Section 5-1. For convenience, the numerically obtained resonant frequency of the P-7 resonator and the P-7 transducer versus the spring constant K is plotted in Figs. 5-27, 5-28 and 5-29, respectively. Now at any prestress level, the spring constant K can be obtained from Fig. 5-26. The resonant frequencies can then be obtained from Figs. 5-27, 5-28 and 5-29 for the P-7 resonator and the P-7 transducer, respectively. The resulting resonant frequency versus prestress relations are given in Figs. 5-30 and 5-31. It is seen that the resonant frequency increases with an increase in prestress, also that the rate of increase of the resonant frequency with the prestress

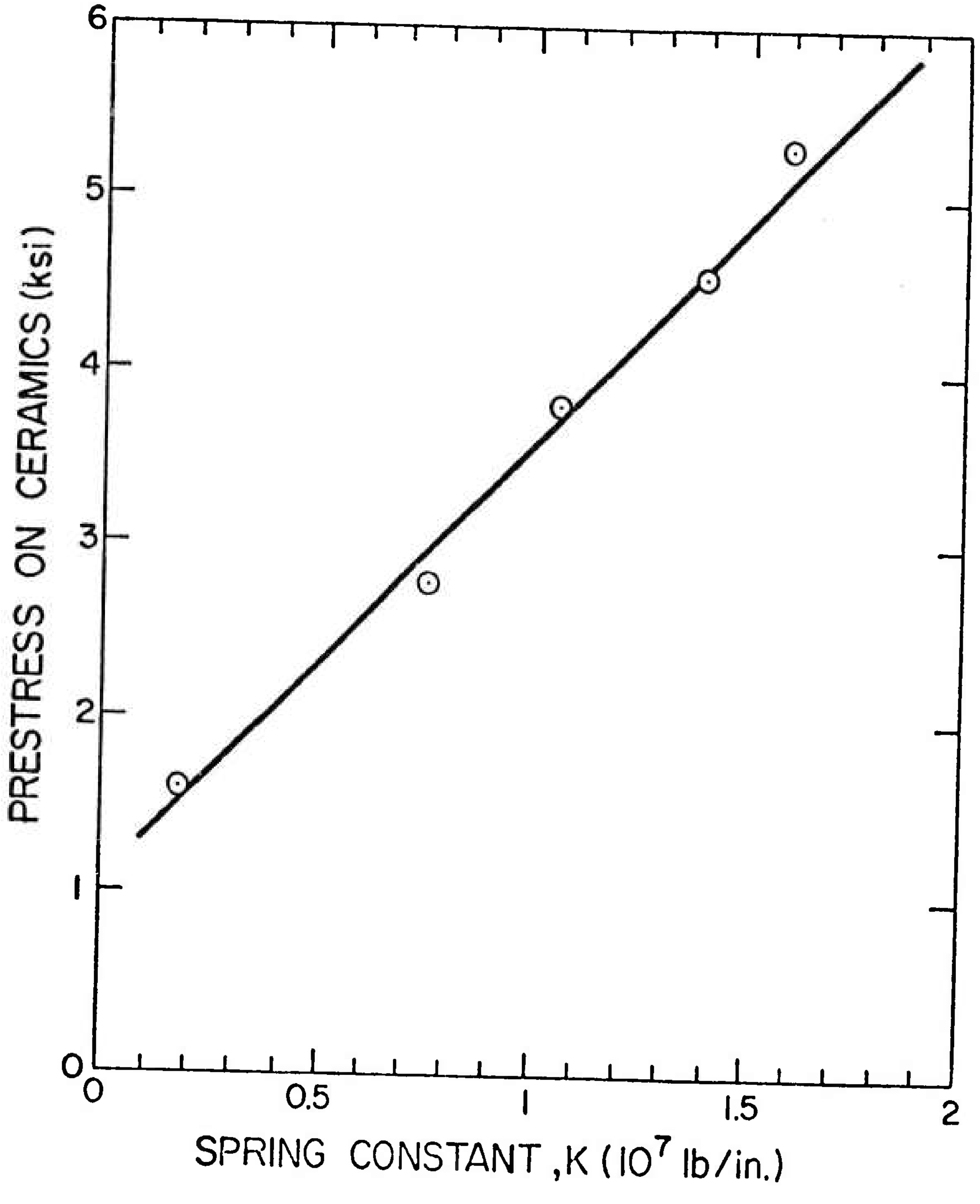

Fig. 5-26 The experimental K versus prestress relation obtained from the symmetric simple resonator

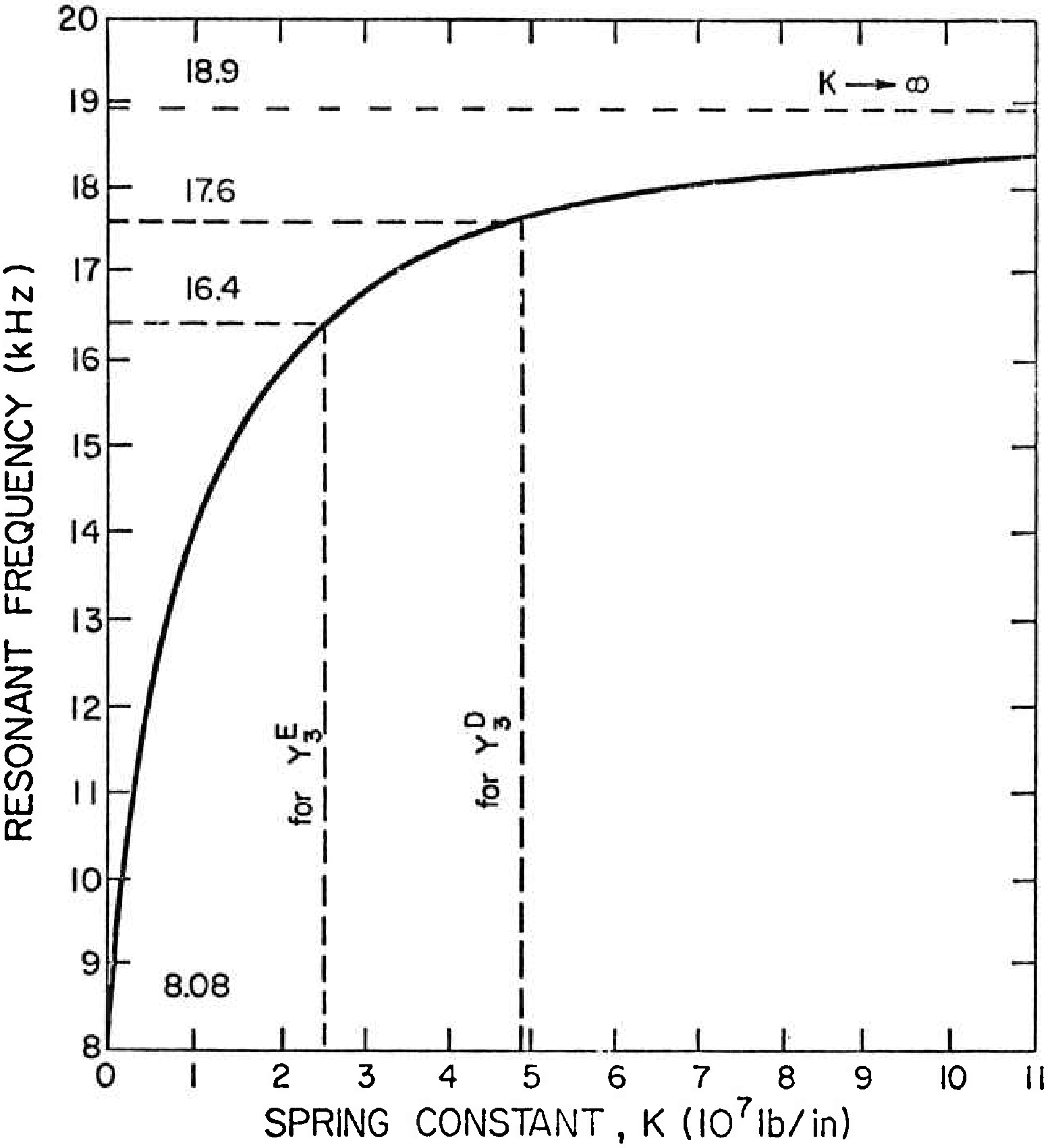

Fig. 5-27 The resonant frequency of the P-7 resonator versus the spring constant K

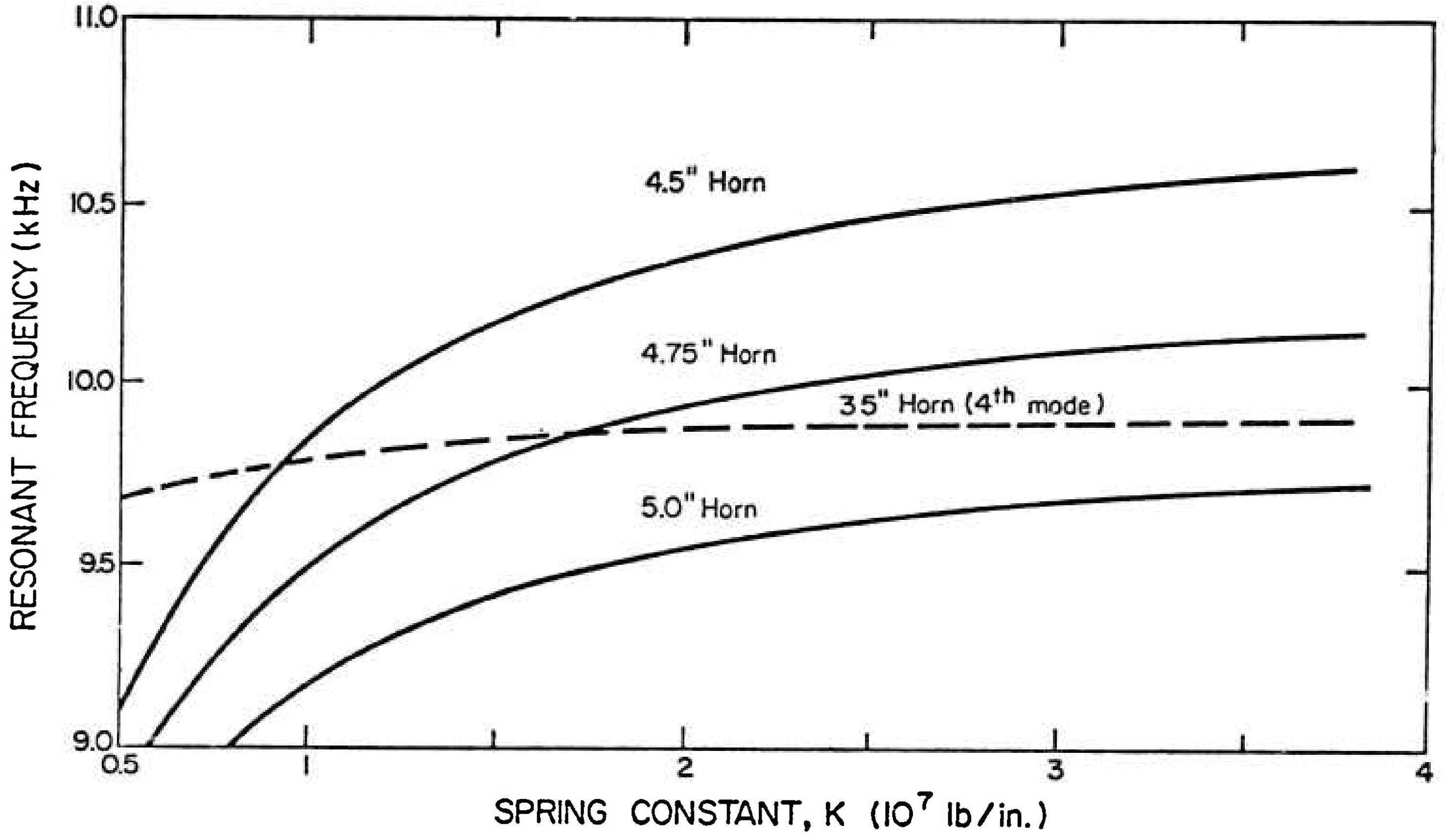

Fig. 5-28 Resonant frequencies of P-7 transducers with horns of different lengths versus K

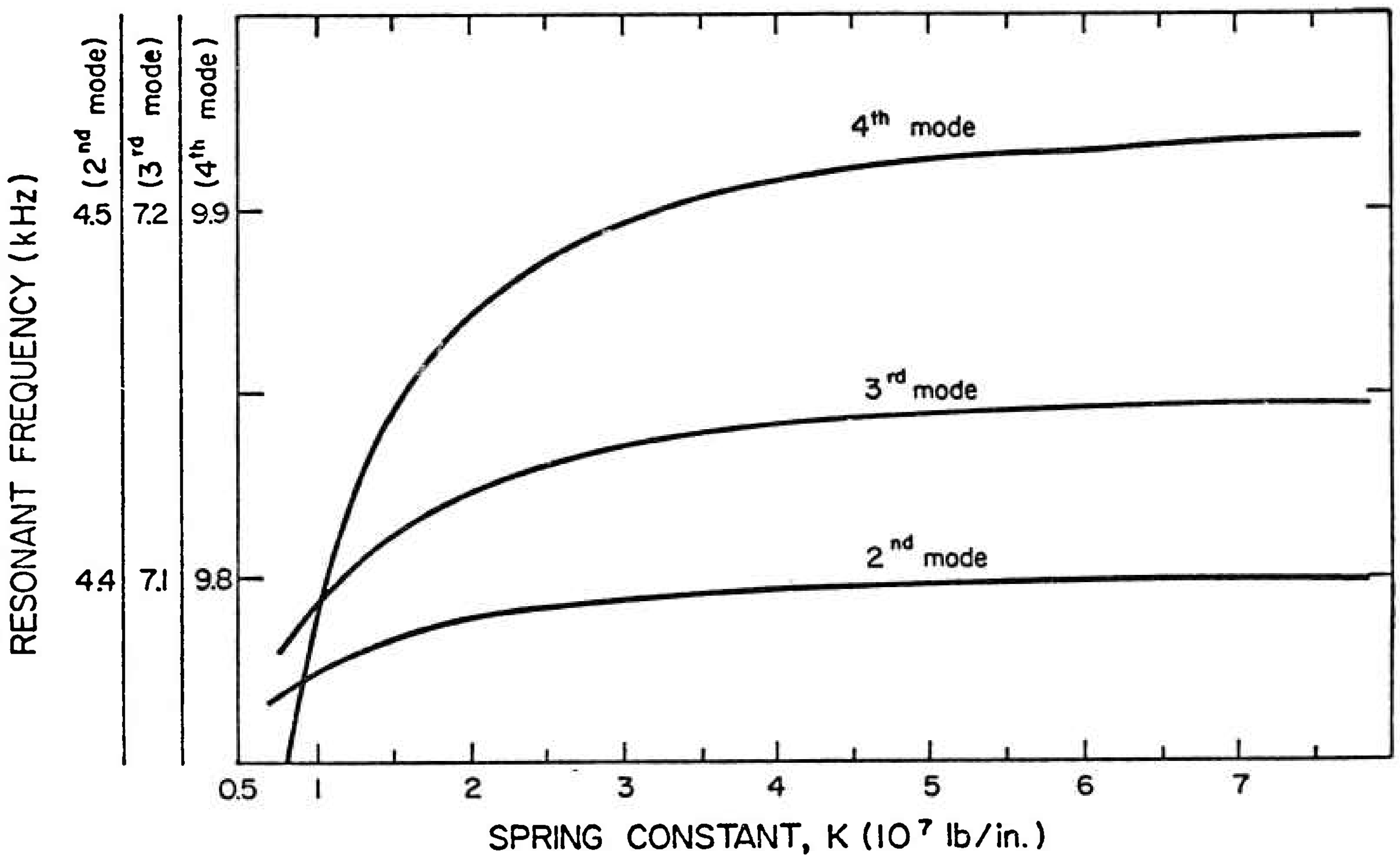

Fig. 5-29 The second, third and fourth modes of a P-7 resonator with a 35-inch horn versus K

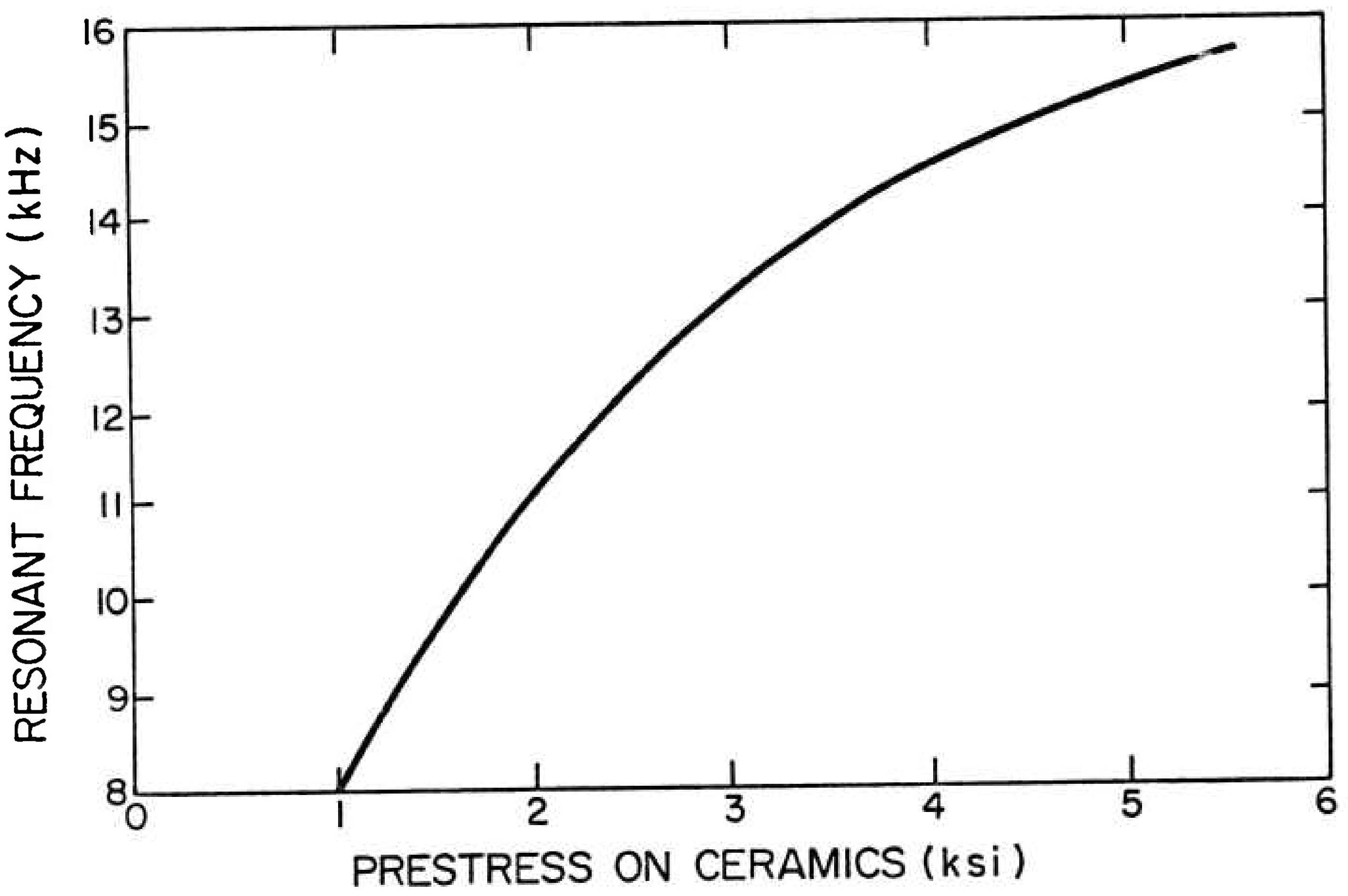

Fig. 5-30 The theoretical prestress effect on resonant frequency of the P-7 resonator, the spring model

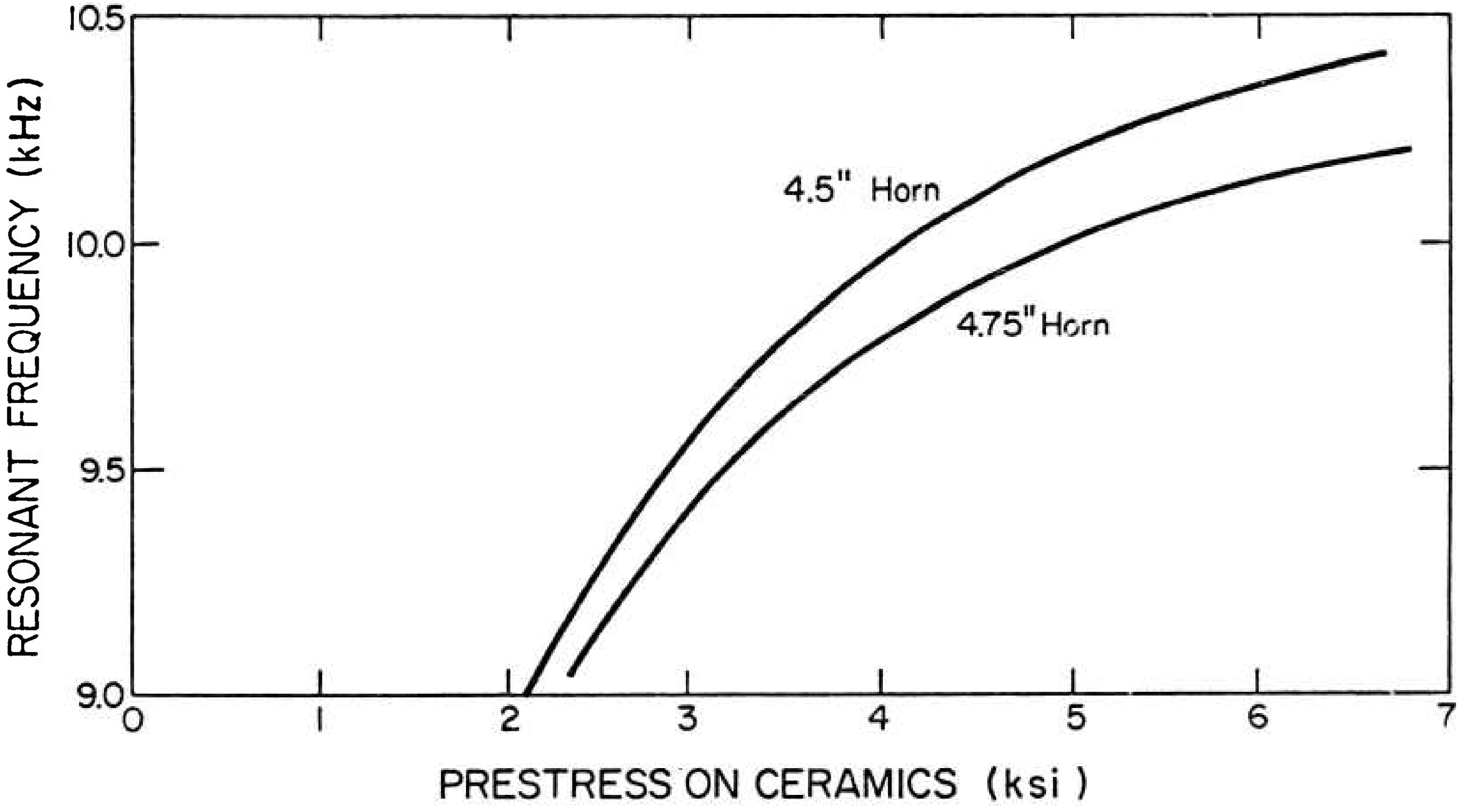

Fig. 5-31 The theoretical prestress effect on the resonant frequency of the P-7 transducer, the spring model

is quite large at the beginning of the prestress and then appears to level off asymptotically at higher prestress to a certain value for each resonator or transducer.

(D) Resonant Frequency Experiments

Some simple experiments have been conducted in the OSU Sonic Power Laboratory to measure the resonant frequencies of various resonators and transducers for different environments. The experimental setup is shown schematically in Fig. 5-32.

The prestress effect on resonant frequency--This experiment has been conducted on the symmetric simple resonator, the P-7 resonator and the P-7 transducer. The prestress was applied by a torque machine on which accurate torques on the end nut were measured. The frequency at every torque reading was then measured on a frequency counter. Although an empirical torque - prestress relation is available, which reads as [16]

Torque = 0.2 x (Prestress on ceramics) x (Area of ceramics) x (Outer diameter of threaded rod)

an actual calibration curve was obtained by placing a strain gage on the steel sleeve of the P-7 transducer. This curve is shown in Fig. 5-33. It is seen that the empirical relationship, which is a straight line, gives a prestress which is slightly too high at large torque values. With a torque at 125 ft-lb (typical for a P-7 transducer), the experimental prestress given by Fig. 5-33 is 5.4 ksi, while the empirical one predicts 7.5 ksi.

The experimental results are shown in Figs. 5-34, 5-35 and 5-36. For comparison, the theoretical results are also included in the above figures, being given as the dashed lines. In the following figures, "theory #1" refers to one-dimensional rod theory; while "theory #2" refers to the spring model. It is seen that the one-dimensional rod theory generally gives a resonant frequency which is too high compared to that given by the experiment. Furthermore, the variation of the resonant frequency with the prestress is much less than the experimental results. On the other hand, the spring model gives very good results for the P-7 transducer, which can be seen from Fig. 5-36. Further, at high prestress in the vicinity of the operation point (5.4 ksi for P-7), the theoretical results and the experimental results are quite close.

From these results, one may conclude that the change of the material properties due to prestress effects could not account for all the frequency shift observed experimentally. However, at high prestress level, material properties appear to account for most of the change. Since a high prestress level tends to increase the interface friction which may, in turn, suppress the vibrational modes other than the longitudinal ones of the ceramic rings, the ceramic may behave more like a longitudinal

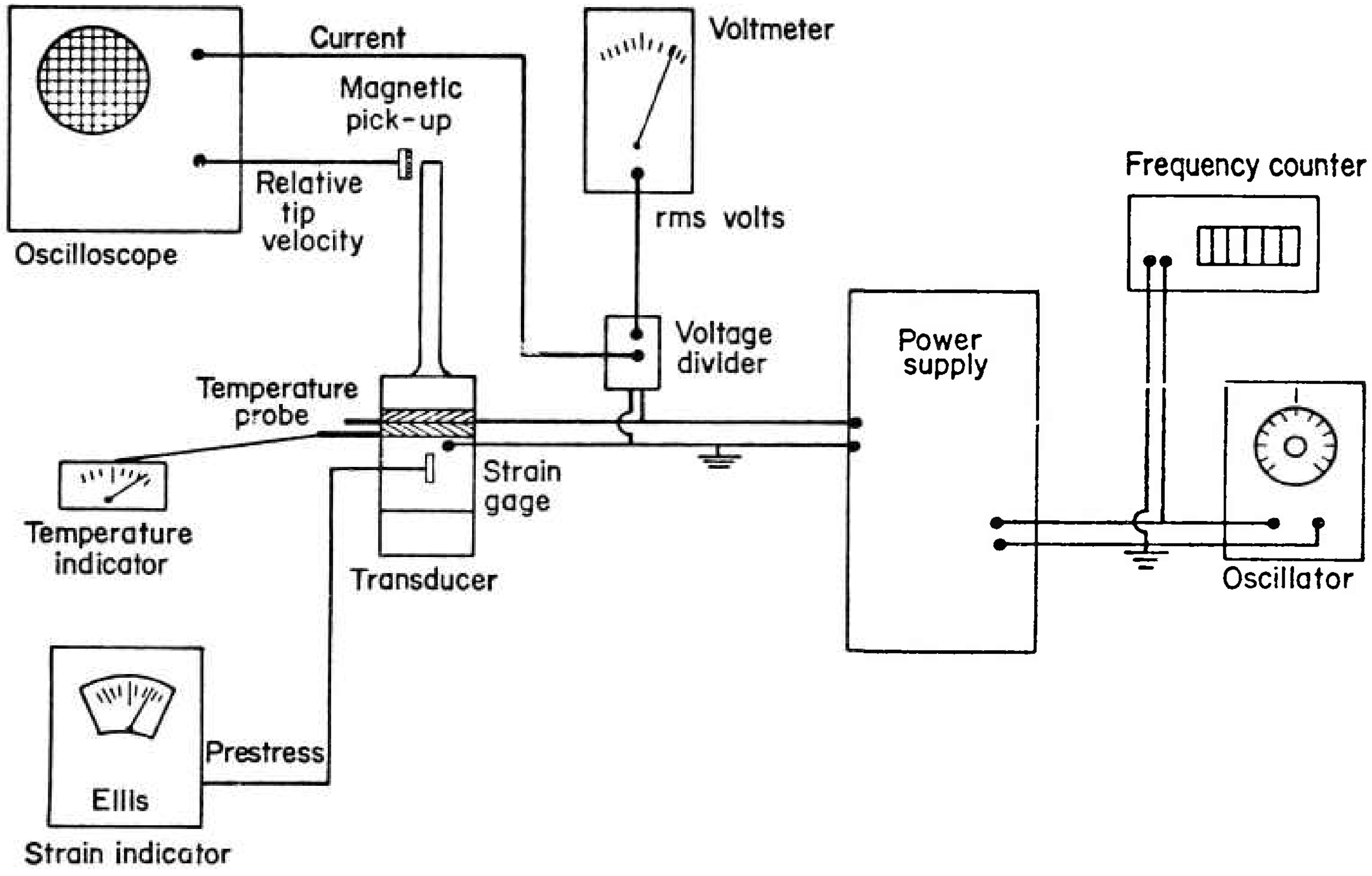
Oscilloscope
Current
Magnetic pick-up
Relative tip velocity
Voltmeter
rms volts
Voltage divider
Frequency counter
Power supply
Oscillator
Temperature probe
Temperature indicator
Strain gage
Transducer
Prestress
Ellis
Strain indicator

Fig. 5-32 Experimental set-up for resonant frequencies of resonators and transducers

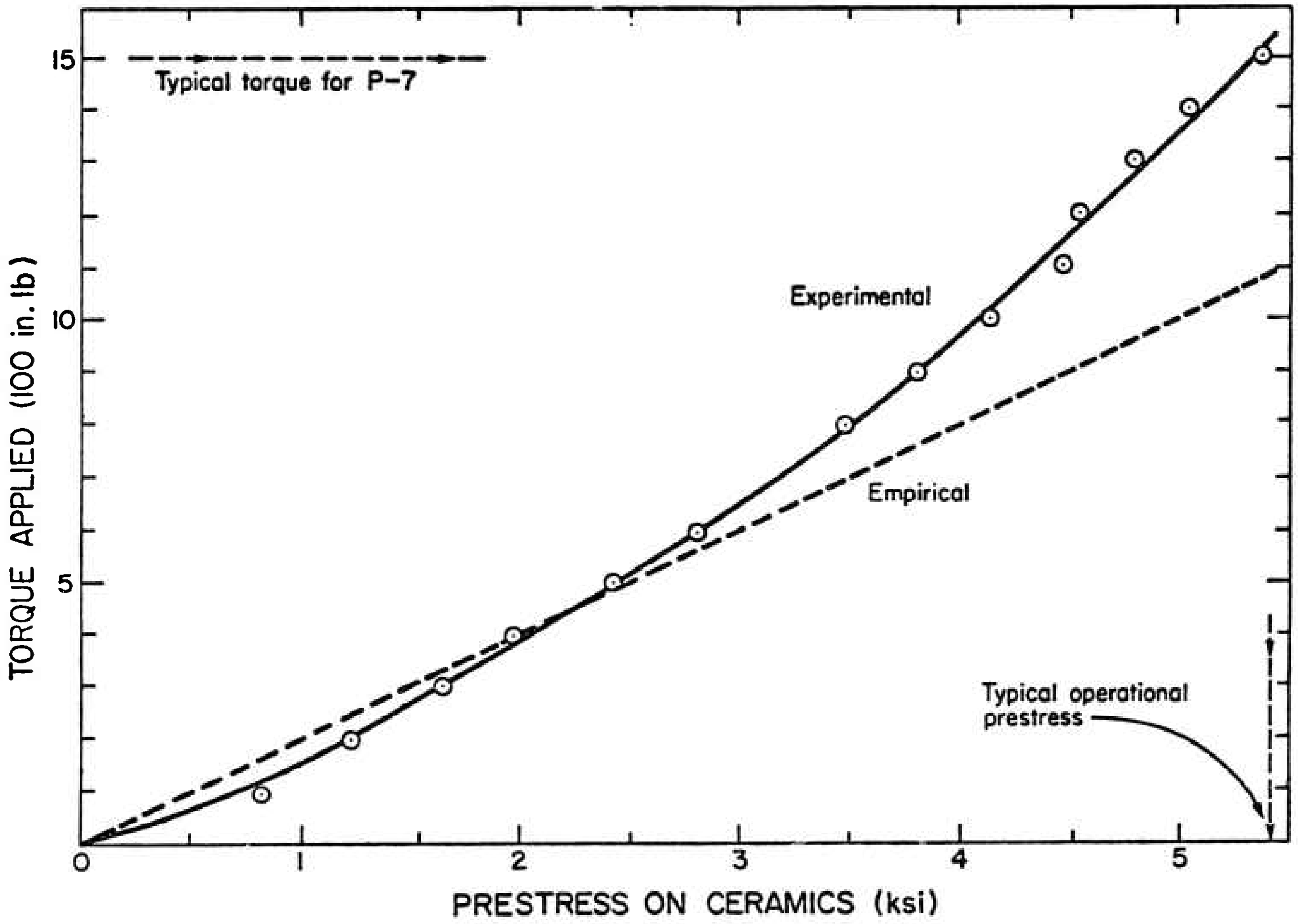

Fig. 5-33 Calibration and empirical curves for the torque versus prestress relation of a P-7 transducer

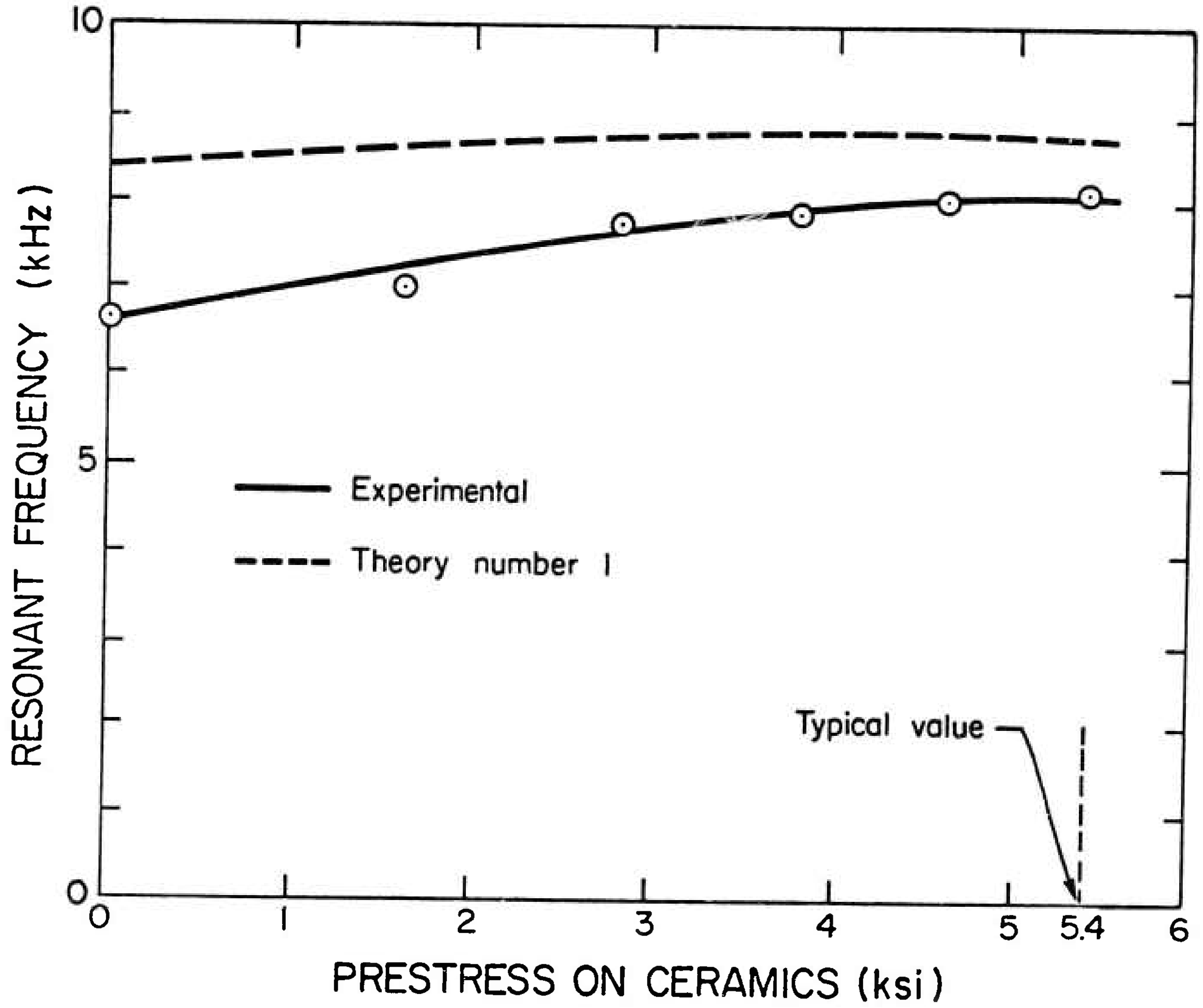

Fig. 5-34 The resonant frequency versus the prestress for a symmetric simple resonator

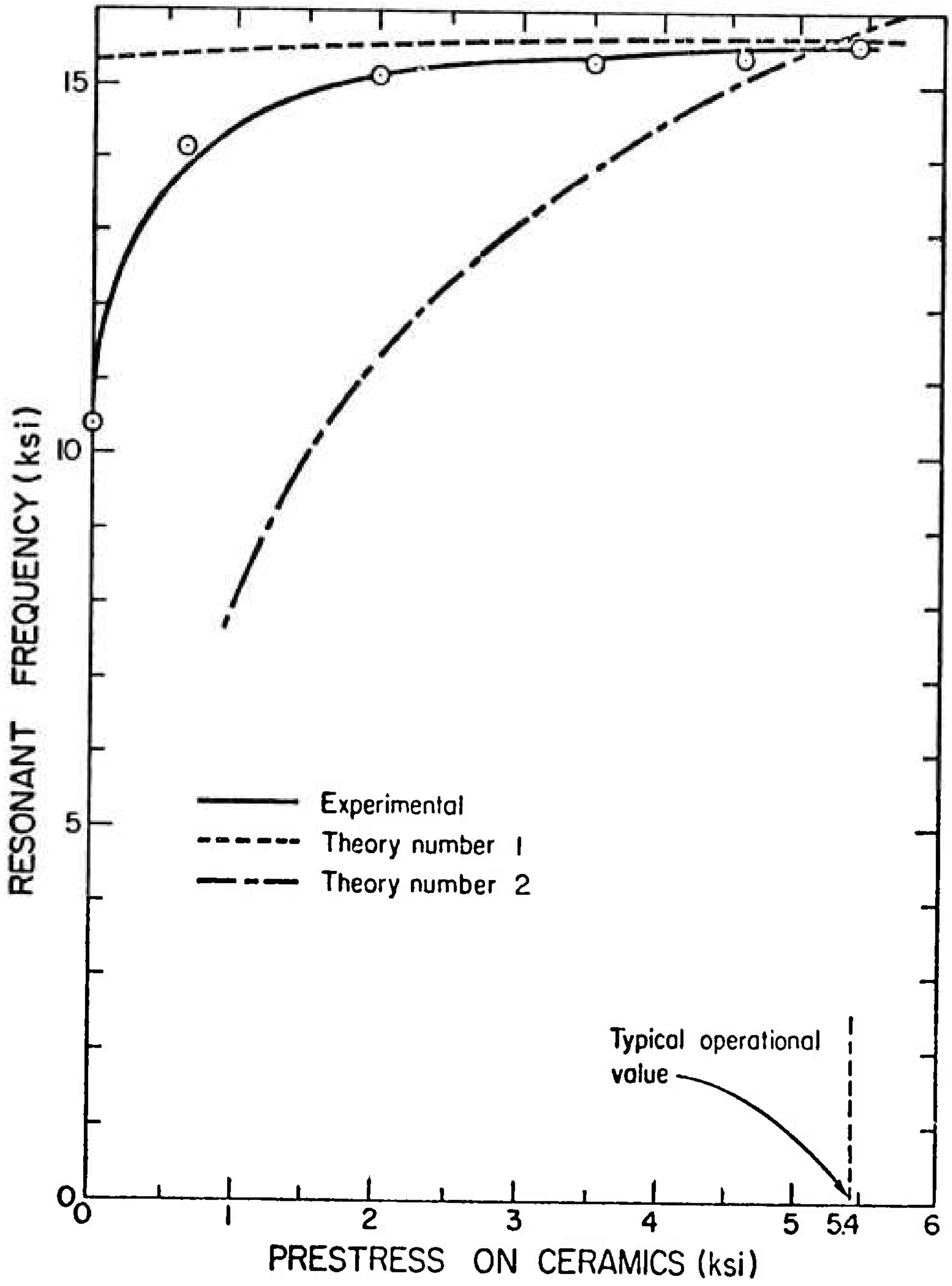

Fig. 5-35 The resonant frequency versus the prestress relations for a P-7 resonator

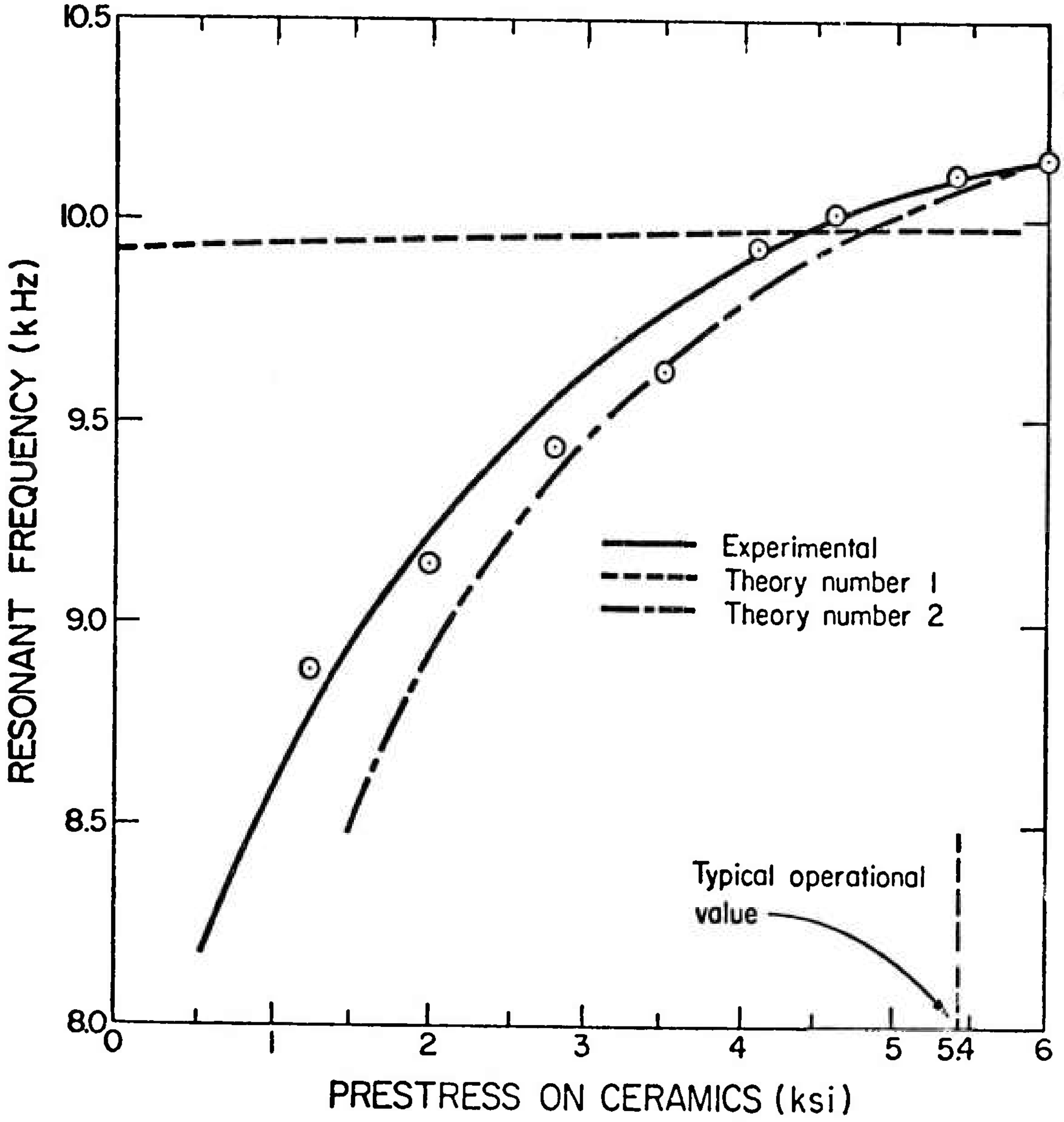

Fig. 5-36 Resonant frequency versus prestress for a P-7 transducer with 4.75 inch horn

rod. At low prestress level, there must be other effects. It could be the friction effect at the interfaces or the two-dimensional effect of the ceramics.

of course, both the theoretical approaches are far from perfect. This is evident from Figs. 5-34, 5-35 and 5-36. In Fig. 5-34, theory #1 is off in both magnitude and shape, though the variation of the resonant frequency with the prestress at high prestress level is comparable to that of the experimental ones. In Fig. 5-35, it is seen that above moderate prestress level theory #1 agrees, better than theory #2, with the experimental values. In Fig. 5-36, theory #2 is in accord with the experimental results, while theory #1 is again off in both magnitude and shape. Unfortunately, there seems to be no consistency in both approaches. However, at ceramic prestress levels of approximately 5 ksi or greater, the discrepancies seem to be less severe for both the theories.

The temperature effect on resonant frequency--Some data were obtained previously in the OSU Sonic Power Laboratory on this effect [17]. Unfortunately, the data are somewhat rough since the temperature was not even along the transducer. Therefore it is difficult to make any meaningful analysis on these data. To overcome this difficulty, the transducer (or resonator) was placed in an oven and slowly heated to a given temperature (130°F), at which time the oven was turned off. While the transducer (or resonator) was gradually cooling down, resonant frequencies were measured at various temperature readings. The results are given in Figs. 5-37, 5-38 and 5-39 as solid lines. On these figures, the theoretical results, as given previously in Figs. 5-22, 5-24 and 5-25, are also plotted as dashed lines for more direct comparisons. Note that the slopes of the theoretical curves are similar to those of the experimental ones which would imply that the decrease in the theoretical resonant frequency due to th thermal prestress release effect is comparable to that of the experimental observation. This may, in turn, imply that the main cause of the decrease in resonant frequency due to temperature increase is the thermal prestress release in the ceramics. However, it was observed that when the temperature of the transducer returned to room temperature after the test, the resonant frequency was higher than the original one (before the test) by a finite amount. Evidently the heat treatment causes some permanent changes in the PZT-4 properties. Krueger [12] noted that this effect can be used to stabilize the ceramic properties. The heat-stabilizing treatment consists simply of immersing the specimens in 200°C oil for one hour according to Krueger.

The voltage effect on the resonant frequency--It has been observed in the OSU Sonic Power Laboratory that a voltage increase will cause a resonant frequency drop for a transducer [18]. The experimental results in this investigation reaffirm the above observation. Figures 5-40, 5-41 and 5-42 give data for the symmetric simple resonator, the P-7 resonator, and the P-7 transducer. They also reveal that the paths of

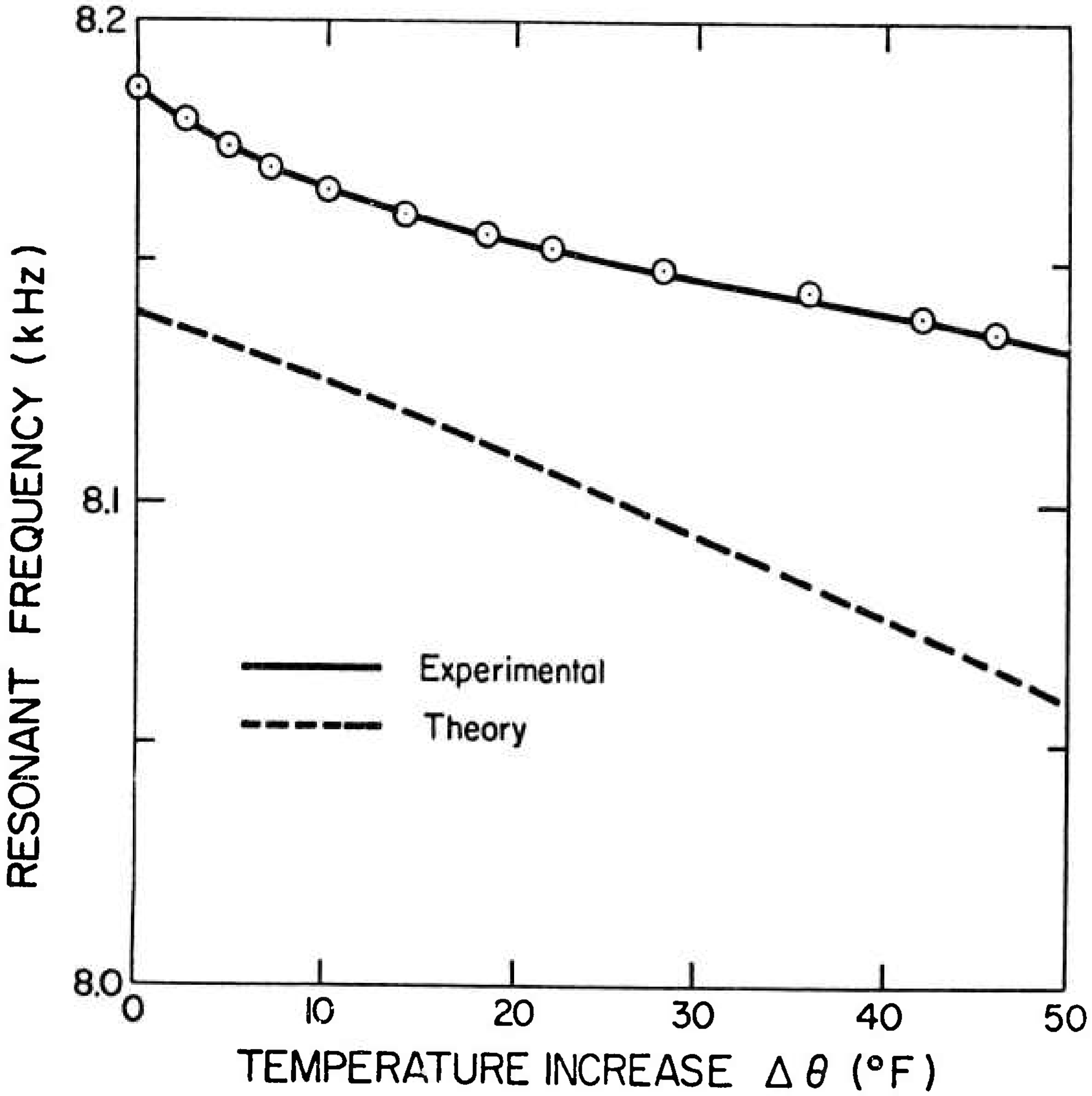

Fig. 5-37 Resonant frequency versus temperature for the symmetric simple resonator

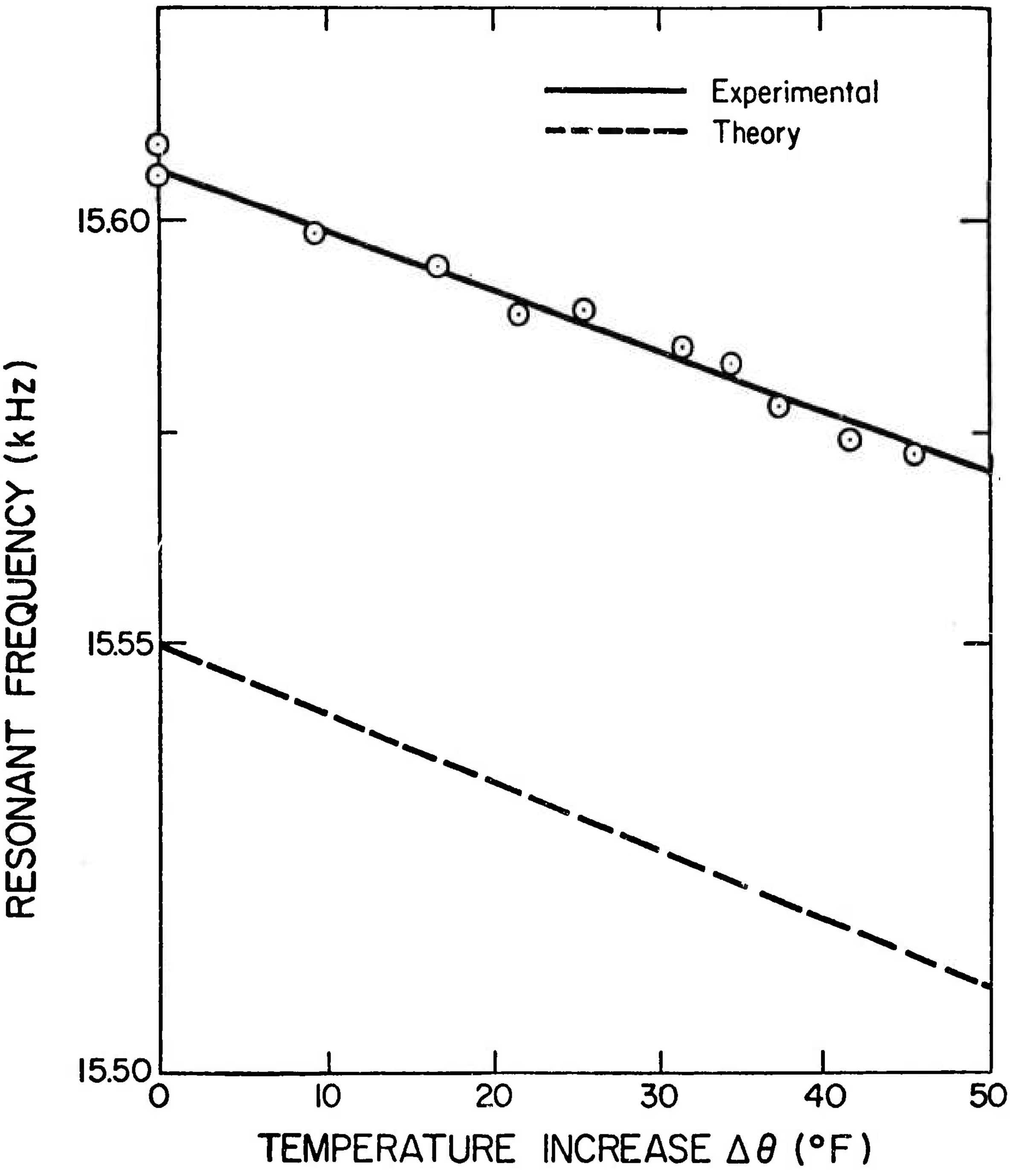

Fig. 5-38 Resonant frequency versus temperature for the P-7 resonator

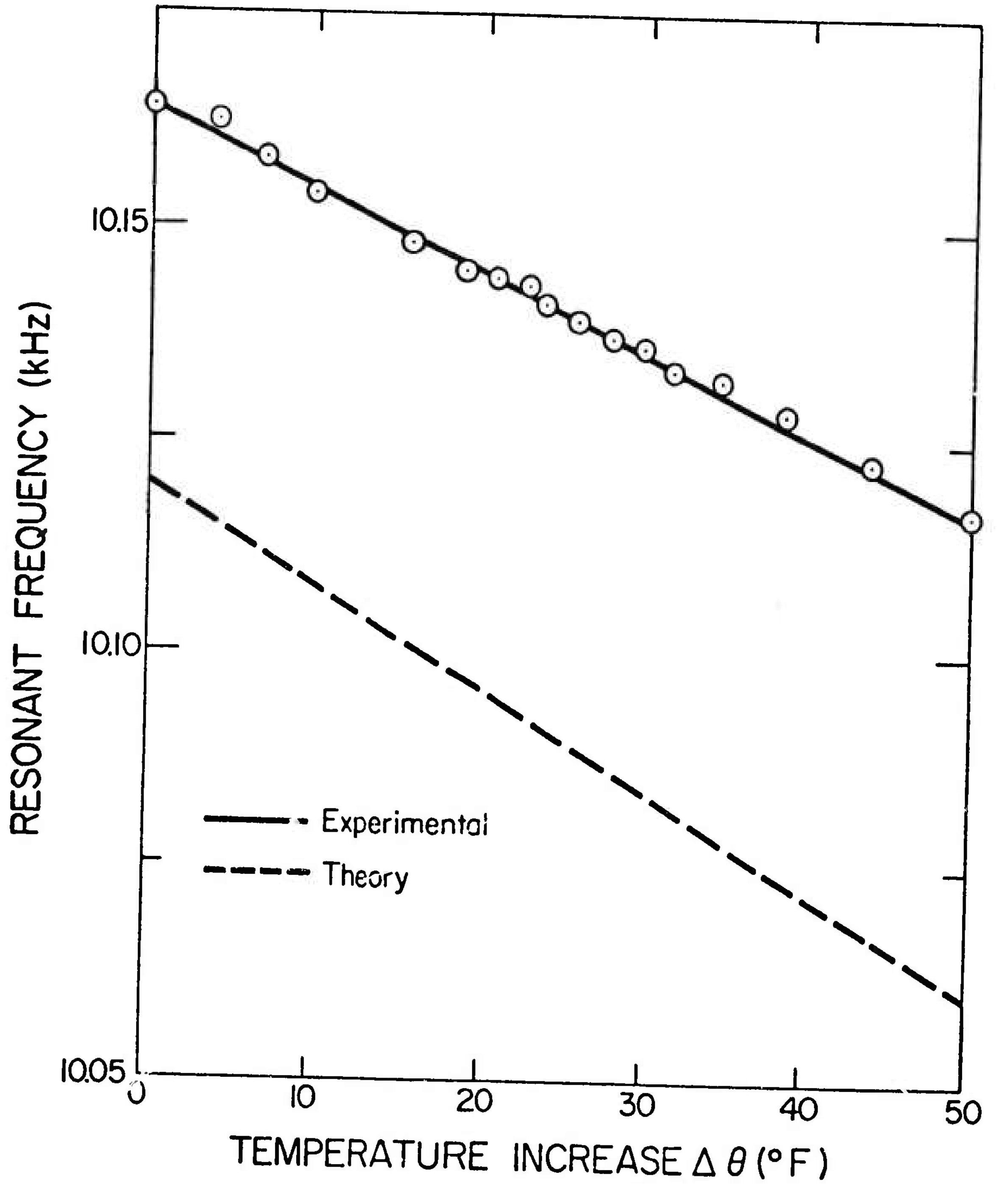

Fig. 5-39 Resonant frequency versus temperature for a P-7 transducer with a 4.75 horn

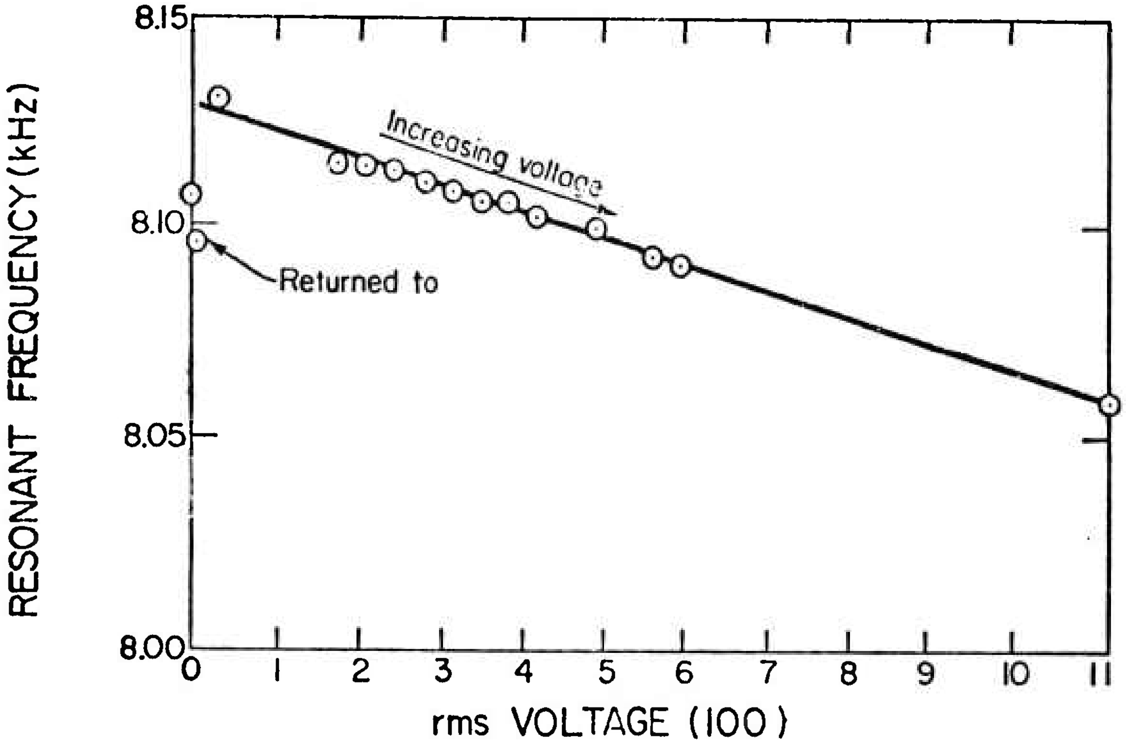

Fig. 5-40 Experimental resonant frequency versus voltage for the symmetric simple resonator

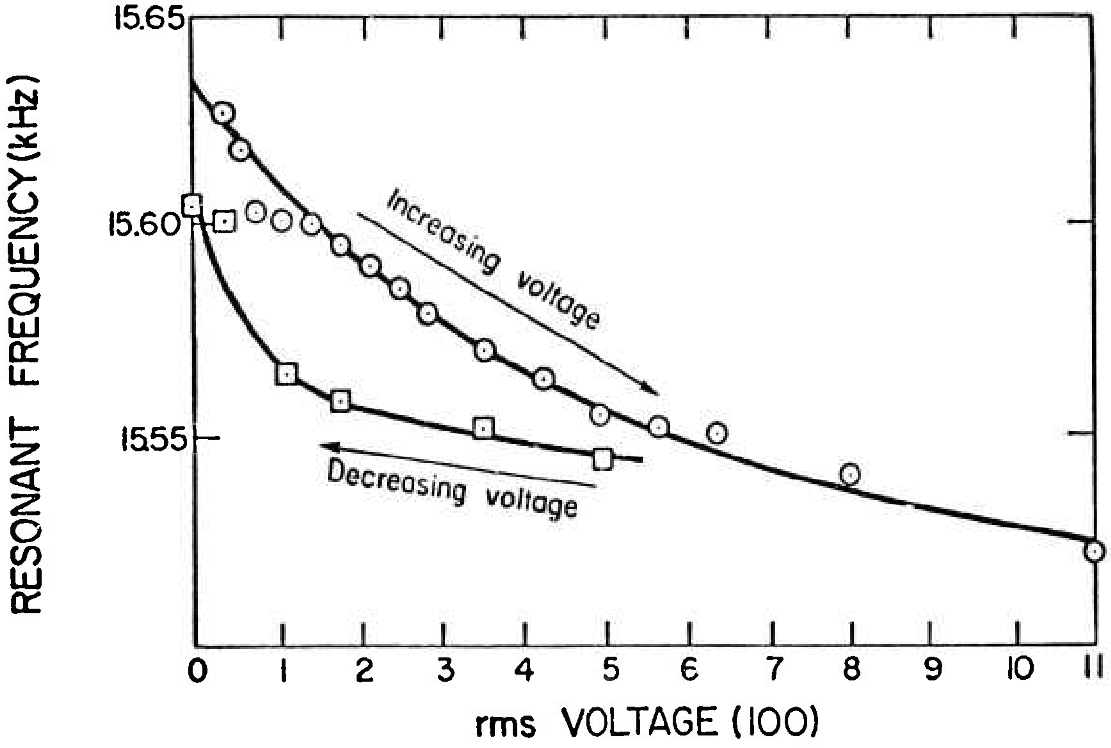

Fig. 5-41 Experimental resonant frequency versus voltage for the P-7 resonator

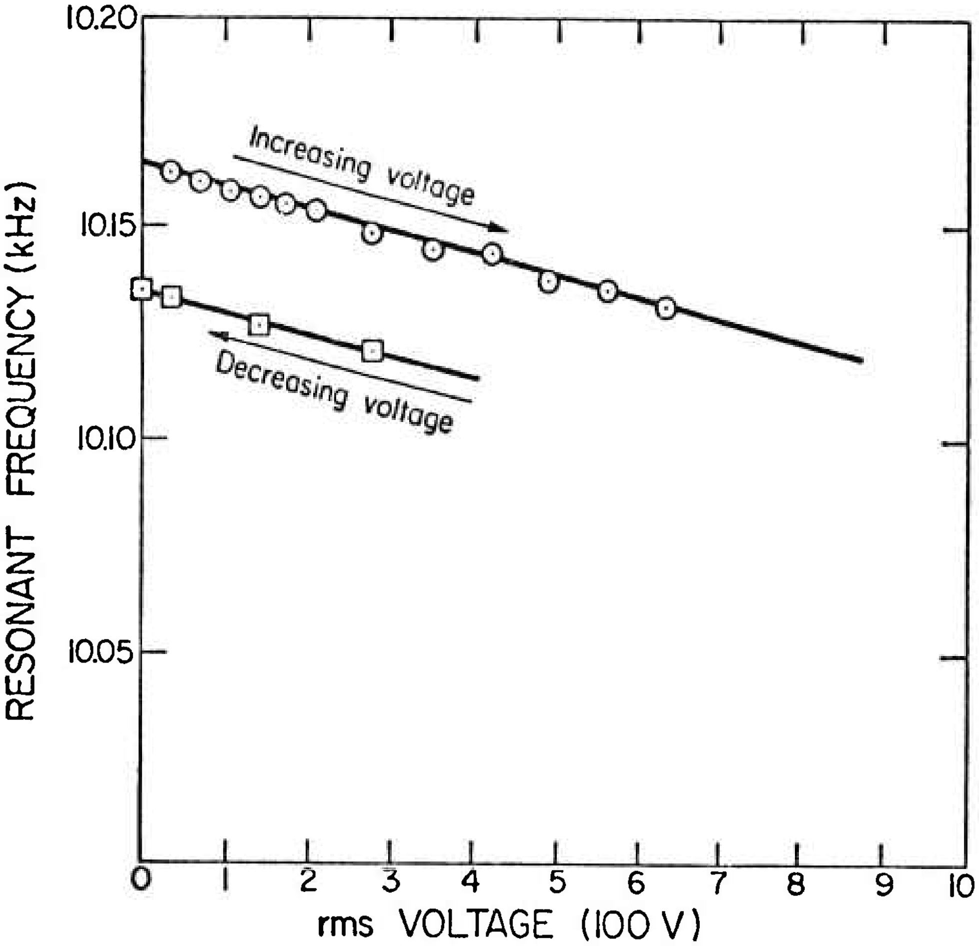

Fig. 5-42 Experimental resonant frequency versus voltage for the P-7 transducer

increasing and decreasing voltages do not coincide. In general, the path for a decreasing voltage is lower than that for an increasing voltage. This is evidence that a high voltage on the ceramic causes some irreversible changes of the ceramic properties as well as certain reversible effects.

5-4 SUMMARY

The ultimate objective of this work has been to model the transducer, predict resonant frequency and to account for frequency shifts due to prestress, temperature and voltage. To accomplish the goal, the symmetric simple resonator, the P-7 resonator and the P-7 transducer have been formulated by one-dimensional wave theory, and the resulting frequency equations were solved numerically on a computer. Prediction of the resonant frequency shifts has been attempted from two standpoints: 1) by utilizing the one-dimensional rod model to consider the effects of piezoelectric material property changes due to environmental changes and 2) by modeling the ceramic as a massless spring and leaving the spring constant to be determined by resonance experiments on the symmetric simple resonator to account for the prestress effects quasi-theoretically. Finally, resonance experiments which included the prestress, the temperature and the voltage effects were conducted. The experimental results were compared to the theoretical ones where they were available.

Comparison between the experimental and the theoretical results shows that at low prestress level on the ceramics, the one-dimensional longitudinal rod model gives resonant frequencies much too high; while the spring model has a better agreement. At high prestress level near the operation point (5.4 ksi on ceramics), both the one-dimensional rod and the spring model give results close to the experimental ones. Although both theoretical models predict an increase of resonant frequency for an increase in prestress level in accord with the experimental observations, neither of the theoretical models accurately predict the rate of increase in resonant frequencies. The temperature and voltage effects on the transducer (resonator) are not thoroughly treated because of the lack of material property change data in the literature. For a more complete assessment of those effects, more experiments must be performed. Nevertheless, the prestress release effect due to the thermal expansion of the transducer elements was found to be in accord with the experimental observations. However, the finite jump of the resonant frequency after heat treatment can only be accounted for after data of the experimental material property changes are available. Recycling information on heat treatment and voltage exposure also needs to be investigated in the future.

Discrepancies between the rates of increase of the resonant frequencies as a result of the prestress may suggest that the one-dimensional rod model is not adequate. A more exact mathematical model may be needed. The numerical result of the one-dimensional rod model reveals that a 30% change of the Young's modulus can only shift the resonant frequency of a simple resonator by about 200-300 Hz (comparing to about 1400 Hz obtained experimentally). Possibly, modeling two-dimensional effects and including the interface friction in the formulation will improve the theoretical results.

Nevertheless, in conclusion, some interesting results should be mentioned. First, it was noted from the symmetric simple resonator analysis that the elastic constants of a piezoelectric material are the dominating factors in resonant frequency calculation. Secondly, the stress release due to thermal expansions does contribute to frequency shift for a temperature rise. This effect can be reduced by using a longer center bolt or soft (with smaller Young's modulus) metals to prestress the ceramics and thus to reduce the spring constant or, this can also be achieved by employing metals with thermal expansion coefficients near that of the ceramic.

5-5 REFERENCES

1. Hoffmann, R. B. and Swartz, J. M., "Analysis of the P-7 Ultrasonic Transducer Using Classical and Transmission Line Theory," OSU Research Project EES 220-B, Quartely Report, 1967.

2. Berlincourt, D. and Krueger, H. H. A., J. Appl. Phys. 30, p. 1804, 1959.

3. Berlincourt, D. and Krueger, H. H. A., Technical Paper TP-228, Clevite Corp., 1964.

4. Mason, P., Physical Acoustics, Vol. I-A, Academic Press, 1964.

5. Mattiat, O. E., Ultrasonic Transducer Materials, Plenum Press, 1971.

6. Brown, R. F., Can. J. Phys. 39, pp. 741-753, 1961.

7. Brown, R. F., and McMahon, G. W., Can. J. Phys. 40, p. 672, 1962.

8. Krueger, H. H. A. and Berlincourt, D., J. Acoust. Soc. Am. 33, pp. 1339-1344, 1961.

9. Berlincourt, D., "High Power and High Voltage Piezoelectric Transducers," Clevite Conference on PZT, 1969.

10. Nishi, R. Y., J. Acoust. Soc. Am. 40, pp. 486-495, 1966.

11. Krueger, H. H. A., J. Acoust. Soc. Am. 42, pp.636-645, 1967.

12. Krueger, H. H. A., J. Acoust. Soc. Am. 43, pp. 576-582, 1968.

13. Krueger, H. H. A., J. Acoust. Soc. Am. 43, pp. 583-591, 1968.

14. Berlincourt, D. A., Curtan, D. R. and Jaffe, H., "Piezoelectric and Piezomagnetic Materials and Their Function in Transducers," in Physical Acoustics, Vol. I-A, edited by Mason, P., Academic Press, 1964.

15. Berlincourt, D. A., "Piezoelectric Crystals and Ceramics," in Ultrasonic Transducer Materials, edited by O. E. Mattiat, Plenum Press, 1971.

16. Spotts, M. F., Design of Machine Elements, 3rd Edition, Prentice-Hall, Inc., 1961.

17. Ma, N. T., "Vibrational Characteristics of a Sonic Transducer," OSU Research Foundation Project RF-3173, Annual Report, Pt. II, Sec. 3., 1971.

18. Yeh, J. J., "Sonic Lap Welding of Aluminum Wires," M. S. Thesis, The Ohio State University, 1971.

6. DEVELOPMENT OF A PULSE REFLECTOR FOR SONIC TRANSDUCERS

The ultrasonic transducer is a device which converts electric input energy into vibratory mechanical energy. It consists of piezoelectric ceramic rings sandwiched in a resonant horn assembly. The horn, which is an energy concentrator, is in turn connected to a transmission line that transmits mechanical energy to the working surface. The piezoelectric ceramic rings, which are the most important elements in the transducer, have two interesting properties: (i) For a given electrical disturbance to the piezoelectric ceramic, mechanical pulses are produced, and (ii) given a mechanical disturbance to the ceramics, an electrical pulse is produced. Due to the first property of the piezoelectric ceramic, the sonic transducer has been widely used for converting electric energy into mechanical energy and thus has found application as a mechanical tool for drilling, cutting, and welding. A technique used for the transmission of energy from the sonic transmission line to the work surface is impact coupling, where a small, bouncing slug of metal is placed between the end of the vibrating sonic transmission line and the work surface. This slug of metal, usually called the "tool" and typically a cylinder one inch in diameter and about an inch long, bounces back and forth between line tip and work piece through repeated impacts with and rebounds from the respective surfaces.

As the tool rebounds from the working surface and consequently impacts on the tip of the transmission line, a stress pulse is generated and propagated along the transmission line into the transducer. As a result of the second property of the piezoelectric ceramic, a high voltage electric pulse is then produced across the face of the ceramic ring. The high voltage electric pulses, especially whenever coupled with the input electric voltage from the electric power supply, may cause an arc-over phenomena across the face of the ceramic. This electric arc may crack the piezoelectric ceramic or eventually cause dielectric breakdown. Therefore, the development of a reflector device to prevent stress pulses from entering the transducer becomes desirable.

The basic concept of designing a pulse reflector originates from understanding that a stress pulse propagating along a transmission line will be completely reflected from a fixed boundary condition and will be largely reflected by a sudden, large increase in cross-section. Therefore, a desirable configuration for a pulse reflector would be a stepped cylinder which closely simulates the fixed edge boundary condition. Early studies in the P-7 transducer by Feng [1]* and Libby [2] observed that P-7 transducers did not fail during the impact-coupling application, but it was noted that this was not the case for the P-11 transducer. This observation suggested that the step at the P-7 transducer may reflect a large amount of the stress pulse and thus prevent the failure of the piezoelectric ceramic.

---

*Numbers in brackets refer to references at the end of this chapter.

In order to design a stress pulse reflector without affecting the function of the transducer-transmission line system, the pulse reflector should have the same resonant frequency as the transducer so that after the reflector is connected to the transducer, the whole system will vibrate at the same resonant frequency.

Based on previous preliminary studies, two basic types of pulse reflectors were developed. Theoretical analyses to investigate the resonance and reflection characteristics of the pulse reflectors were conducted. The theoretical results were later verified by experimental tests. It was found that with the pulse reflector connected to the P-11 transducer, 80% of the incident pulse was reflected. The voltage generated across the face of the piezoelectric ceramic rings by the pulse was also reduced 80%.

6-1 REFLECTOR DESIGN

(A) Theoretical Analysis of Reflection Characteristics

As the first step in the design of a stress pulse reflector, it is necessary to understand the reflection-transmission characteristic of a stress pulse at a discontinuity. A one-dimensional wave theory is used for this purpose. The configuration of the discontinuity is shown in Fig. 6-1.

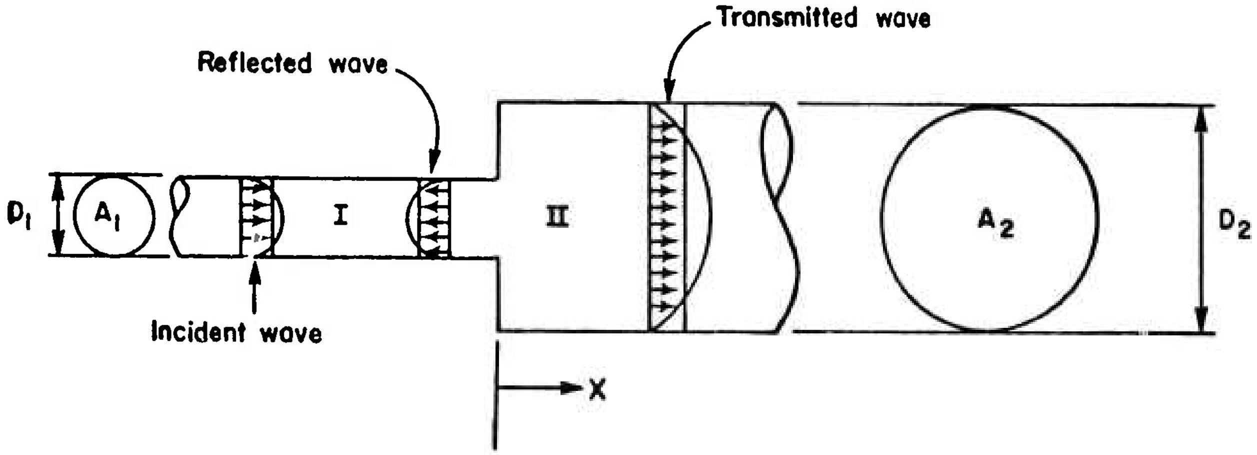

Fig. 6-1 Waves across a discontinuity

Cross-sections and material densities for section I and II are A_1, A_2, and ρ_1, ρ_2, respectively. An arbitrary incident pulse $f_1(x - c_1t)$, may be considered to be made of many frequency components in a Fourier sense. Thus, a superposition of many waves of the type $u_I = A \exp[i\gamma_1(x - c_1t)]$ may be used to obtain a pulse shape $f(x - c_1t)$, where u_I and c_1 are the displacement and wave velocity of the incident wave. Similarly, the reflected wave in section I and the transmitted wave in section II can be expressed as $u_R = g_2(x + c_1t)$, and $u_T = f_2(x - c_2t)$, respectively.

Boundary conditions at the discontinuity are based on continuity of force and of particle velocity and are

$$A_1 \ \sigma_I + \sigma_R) = A_2\sigma_I \quad , \quad x = 0$$

$$v_I + v_R = v_I \quad , \quad x = 0 \qquad (6\text{-}1)$$

where

$$v_I = - c_1f_1', \quad v_R = c_1g_2', \quad v_T = - c_2f_2'$$

$$\sigma_I = E_1 \frac{\partial u_I}{\partial x} = E_1f_1', \quad \sigma_R = E_1 \frac{\partial u_R}{\partial x} = E_1g_2', \quad \sigma_I = E_2 \frac{\partial u_T}{\partial x} = E_2f_2' \qquad (6\text{-}2)$$

and where E_1 and E_2 are the Young's modulus of section I and section II, respectively. The prime indicates differentiation with respect to the argument.

Substituting eq. (6-2) into eq. (6-1) and solving for f_2' and g_2', yields

$$f_2' = \frac{2c_1A_1E_1}{A_1E_1c_2 + A_2E_2c_1} f_1'$$

$$g_2' = \frac{{}_1A_2E_2 - c_2A_1E_1}{A_1E_1c_2 + A_2E_2c_1} f_1' \qquad (6\text{-}3)$$

Since $\sigma_T = E_2f_2'$, $\sigma_R = E_1g_2'$ and $E_1 = c_1^2\zeta_1$, $E_2 = c_2^2\zeta_2$, the results in eq. (6-3) may be put in the form

$$\sigma_T = \frac{2A_1\zeta_2c_2}{A_1\zeta_1c_1 + A_2\zeta_2c_2} \sigma_I$$

$$\sigma_R = \frac{A_2\zeta_2c_2 - A_1\zeta_1c_1}{A_1\zeta_1c_1 + A_2\zeta_2c_2} \sigma_I \qquad (6\text{-}4)$$

Equation (6-4) represents the relationships between transmitted stress σ_T, reflected stress σ_R and incident stress σ_I.

If the materials for both sections are the same, i.e., $E_1 = E_2 = E$, $\zeta_1 = \zeta_2 = \zeta$, and $c_1 = c_2 = c$, eq. (6-4) can be expressed as

$$\sigma_T = \frac{2A_1}{A_1 + A_2} \sigma_I = \frac{2}{1 + \frac{A_2}{A_1}} \sigma_I$$

$$\sigma_R = \frac{A_2 - A_1}{A_1 + A_2} \sigma_I = \frac{\frac{A_2}{A_1} - 1}{1 + \frac{A_2}{A_1}} \sigma_I \qquad (6\text{-}5)$$

Plots of the relations between $2/(1 + A_2/A_1)$, $(A_2/A_1 - 1)/(1 + A_2/A_1)$ ans A_2/A_1 are presented in Fig. 6-2. For $A_2/A_1 = 9$ it is seen that 80% of the incident stress should be reflected at the discontinuity and only 20% of the incident stress should be transmitted to section I.

(B) Analysis of Resonance Characteristics of Reflectors

Two types of pulse reflectors are considered in the present investigation. The "Type A" reflector is shown in Fig. 6-3. Applying one-dimensional analysis for the stepped cylinder, simple strength of materials theory and Hooke's law are assumed to apply. The governing differential equations of motion are

$$\frac{\partial^2 u_1}{\partial x_1^2} = \frac{1}{c^2} \frac{\partial^2 u_1}{\partial t^2}, \qquad \frac{\partial^2 u_2}{\partial x_2^2} = \frac{1}{c^2} \frac{\partial^2 u_2}{\partial t^2} \qquad (6\text{-}6)$$

where u_1 and u_2 are displacements in section I and II, respectively and $c^2 = E/\zeta$. Solutions for eq. (6-6) are:

$$u_1 = (B_1 \sin kx_1 + B_2 \cos kx_1) \cos \omega t$$

$$u_2 = (B_3 \sin kx_2 + B_4 \cos kx_1) \cos \omega t \qquad (6\text{-}7)$$

where $k^2 = \omega^2/c^2$ and ω is the radial frequency.

Boundary conditions for the stepped cylinder are:

$$u_1 = -u_2, \qquad \text{at } x_1 = 0, \quad x_2 = 0$$

$$A_1 \frac{\partial u_1}{\partial x_1} = A_2 \frac{\partial u_2}{\partial x_2}, \qquad \text{at } x_1 = 0, \quad x_2 = 0$$

$$\frac{\partial u_1}{\partial x_1} = 0, \qquad \text{at } x_1 = L_1 = 5 \text{ in.}$$

$$\frac{\partial u_2}{\partial x_2} = 0, \qquad \text{at } x_2 = L_2 = 5 \text{ in.} \qquad (6\text{-}8)$$

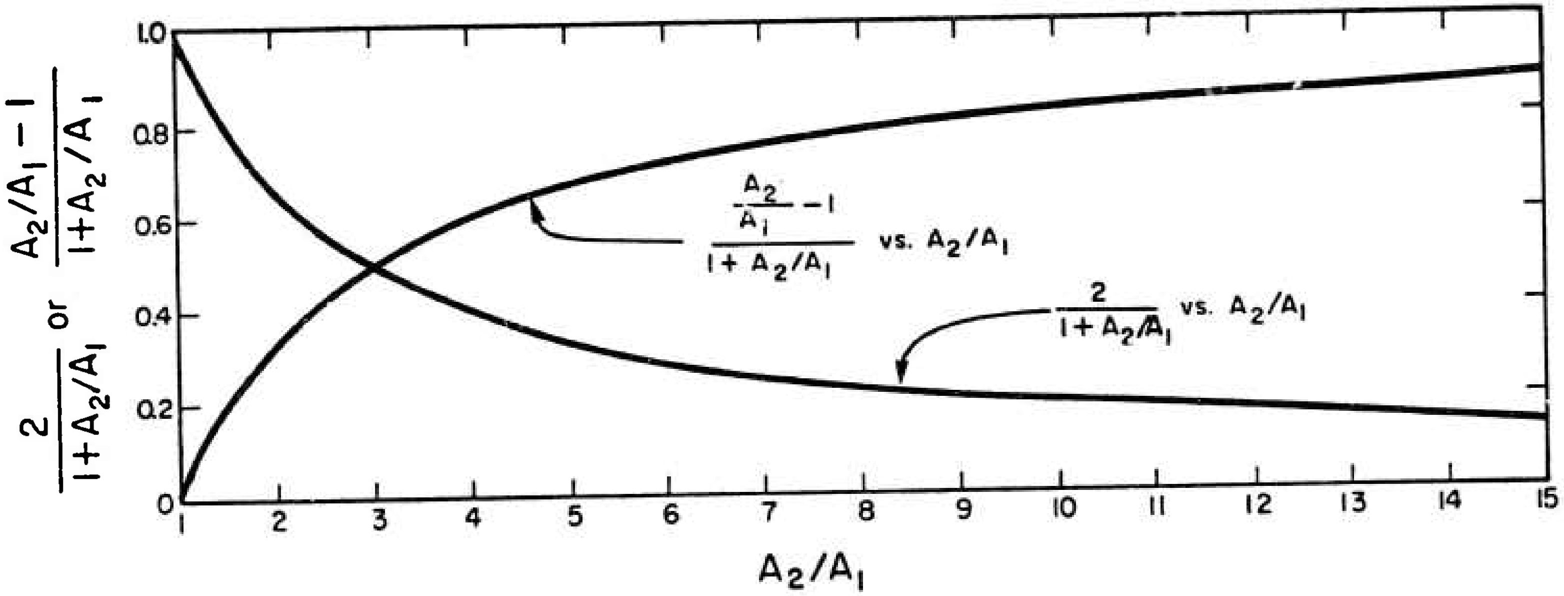

Fig. 6-2 Relations between $2/(1 + A_2/A_1)$, $(A_2/A_1 - 1)/(1 + A_2/A_1)$ versus A_2/A_1

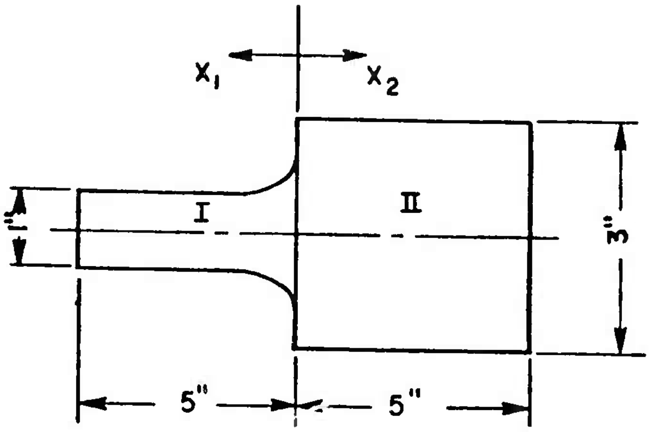

Fig. 6-3 Dimensions and coordinates of Type A pulse reflector

Substituting solutions of eq. (6-7) into the boundary conditions of eq. (6-8), the following set of equations is obtained;

$$B_2 + B_4 = 0, \qquad A_1 B_1 - A_2 B_3 = 0$$

$$B_1 k \cos kL_1 - B_2 k \sin kL_1 = 0$$

$$B_3 k \cos kL_2 - B_4 k \sin kL_2 = 0 \tag{6-9}$$

These can be further reduced to

$$\frac{A_2}{A_1} B_3 \cos kL_1 - B_4 \sin kL_1 = 0$$

$$B_3 \cos kL_1 - B_4 \sin kL_1 = 0 \tag{6-10}$$

The only nontrivial solutions to eq. (6-10) are those for which the determinant of coefficients is equal to zero. This determinant is given by

$$\begin{vmatrix} \frac{A_2}{A_1} \cos kL_1 & \sin kL_1 \\ \cos kL_2 & -\sin kL_2 \end{vmatrix} = 0 \tag{6-11}$$

which expands to the frequency equation

$$\frac{A_2}{A_1} \cos kL_1 \sin kL_2 + \sin kL_1 \cos kL_2 = 0 \qquad (6\text{-}12)$$

For the present case $A_2/A_1 = 9$, and $L_1 = L_2 = 5$ in., the frequency equation becomes

$$10 \cos kL_1 \sin kL_1 = 0 \qquad (6\text{-}13)$$

The solutions for eq. (6-13) are

$$kL_1 = n(\pi/2), \qquad (n = 1,2,3,\ldots)$$

Let n = 1 for the first mode of vibration, to give

$$k = \frac{\pi}{2} \cdot \frac{1}{L_1} = \frac{\pi}{10}$$

so that the first mode resonance is

$$f = \frac{kc}{2\pi} = \frac{\frac{\pi}{10} \cdot c}{2\pi} = \frac{c}{10} = 9989.4 \text{ Hz}$$

A "Type B" reflector configuration, shown in Fig. 6-4, was also considered. The basic idea was to have a half-wavelength device, with the discontinuity in the center. The method of analysis closely followed that used for the Type A reflector. Thus, the governing equations of motion are

$$\frac{\partial^2 u_1}{\partial x_1{}^2} = \frac{1}{c^2}\frac{\partial^2 u_1}{\partial t^2}, \qquad \frac{\partial^2 u}{\partial x_2{}^2} = \frac{1}{c^2}\frac{\partial^2 u_2}{\partial t^2}$$

$$\frac{\partial^2 u_3}{\partial x_3{}^2} = \frac{1}{c^2}\frac{\partial^2 u_3}{\partial t^2} \qquad (6\text{-}14)$$

where u_1, u_2, and u_3 are displacements in sections I, II, and III, respectively and $c^2 = E/\zeta$.

Solutions for eq. (6-14) are

$$u_1 = (A \sin kx_1 + B \cos kx_1) \cos \omega t$$

$$u_2 = (C \sin kx_2 + D \cos kx_2) \cos \omega t$$

$$u_3 = (F \sin kx_3 + G \cos kx_3) \cos \omega t \qquad (6\text{-}15)$$

where $k^2 = \omega^2/c^2$, and ω is the radial frequency. The boundary conditions are

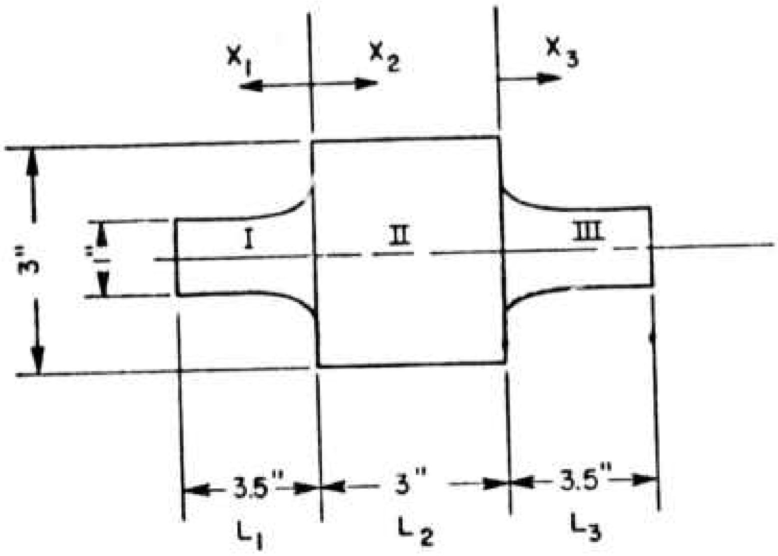

Fig. 6-4 Dimensions and coordinates of the Type B pulse reflector

$$\frac{\partial u_1}{\partial x_1} = 0\,, \qquad \text{at} \quad x_1 = L_1$$

$$u_1 = -u_2\,, \qquad \text{at} \quad x_1 = 0, \quad x_2 = 0$$

$$A_1 \frac{\partial u_1}{\partial x_1} = A_2 \frac{\partial u_2}{\partial x_2}\,, \qquad \text{at} \quad x_1 = 0, \quad x_2 = 0$$

$$u_2 = u_3\,, \qquad \text{at} \quad x_2 = L_2, \quad x_3 = 0$$

$$A_2 \frac{\partial u_2}{\partial x_2} = A_3 \frac{\partial u_3}{\partial x_3}\,, \qquad \text{at} \quad x_2 = L_2, \quad x_3 = 0$$

$$\frac{\partial u_3}{\partial x_3} = 0\,, \qquad \text{at} \quad x_3 = L_3 \qquad (6\text{-}16)$$

Substituting the solutions of eq. (6-15) into the boundary conditions of eq. (6-16), yields the following set of equations;

$$A \cos kL_1 - B \sin kL_1 = 0$$

$$B + D = 0$$

$$A_1 A + A_2 C = 0 \qquad (6\text{-}17)$$

$$C \sin kL_2 + D \cos kL_2 - G = 0$$

$$A_2(C \cos kL_2 - D \sin kL_2) - A_3F = 0$$

$$F \cos kL_3 - G \sin kL_3 = 0 \qquad (6\text{-}17)$$

This reduces to

$$\frac{A_2}{A_1} C \cos kL_1 + D \sin kL_1 = 0$$

$$C \sin kL_2 + D \cos kL_2 - G = 0$$

$$C \cos kL_2 - D \sin kL_2 - \frac{A_3}{A_2} F = 0$$

$$F \cos kL_3 - G \sin kL_3 = 0 \qquad (6\text{-}18$$

This determinant of coefficients is given by

$$\begin{vmatrix} \frac{A_2}{A_1} \cos kL_1 & \sin kL_1 & 0 & 0 \\ \sin kL_2 & \cos kL_2 & 0 & -1 \\ \cos kL_2 & -\sin kL_2 & -A_3/A_2 & 0 \\ 0 & 0 & \cos kL_3 & -\sin kL_3 \end{vmatrix} = 0 \qquad (6\text{-}19)$$

which gives the frequency equation

$$\frac{A_2}{A_1} \cos kL_1\left(\frac{A_3}{A_2} \cos kL_2 \sin kL_3 + \sin kL_1 \cos kL_3\right)$$

$$- \sin kL_1\left(\frac{A_3}{A_2} \sin kL_2 \sin kL_3 - \cos kL_2 \cos kL_3\right) = 0 \qquad (6\text{-}20)$$

For the present case $A_2/A_1 = 9$, $A_3/A_2 = 1/9$, $L_1 = L_3 = 3.5$ in., and $L_2 = 3$ in., so that eq. (6-20) becomes

$$\cos 3k \cos 3.5k \cos 3.5k + 9 \cos 3.5k \sin 3k \cos 3.5k$$

$$- \frac{1}{9} \sin 3.5k \sin 3k \sin 3.5k + \sin 3.5k \cos 3k \cos 3.5k = 0 \qquad (6\text{-}21)$$

The solution for the first mode is k = 0.48433, giving a resonance frequency of

$$f = \frac{kc}{2\pi} \quad \frac{0.48433\,c}{2\pi} = 15{,}323 \text{ Hz}$$

6-2 MEASUREMENT OF RESONANCE AND REFLECTION CHARACTERISTICS

Experimental measurements of the resonance and reflection characteristics is desirable, to verify some of the analysis, particularly since there are some deviations of the configuration used in analysis from the actual pulse reflector. Three types of tests were conducted. The first test was the measurement of the resonance characteristics of the Type A and B pulse reflectors. Also, resonance tests were made on a P-11 as a check of that design. The second test was measurement of the stress reflection from the Type A and B reflectors. Additionally, pulse reflection tests were also done on the P-11 horn. The third test was a comparison of the reflection characteristics of a P-11 transducer with and without the Type A pulse reflector.

(A) Measurement of Resonance Characteristics

The basic set-up for this test consisted of two small magnetic transducers, a Brüel and Kjear 1013 oscillator, an electronic counter and an oscilloscope as shown schematically in Fig. 6-5.

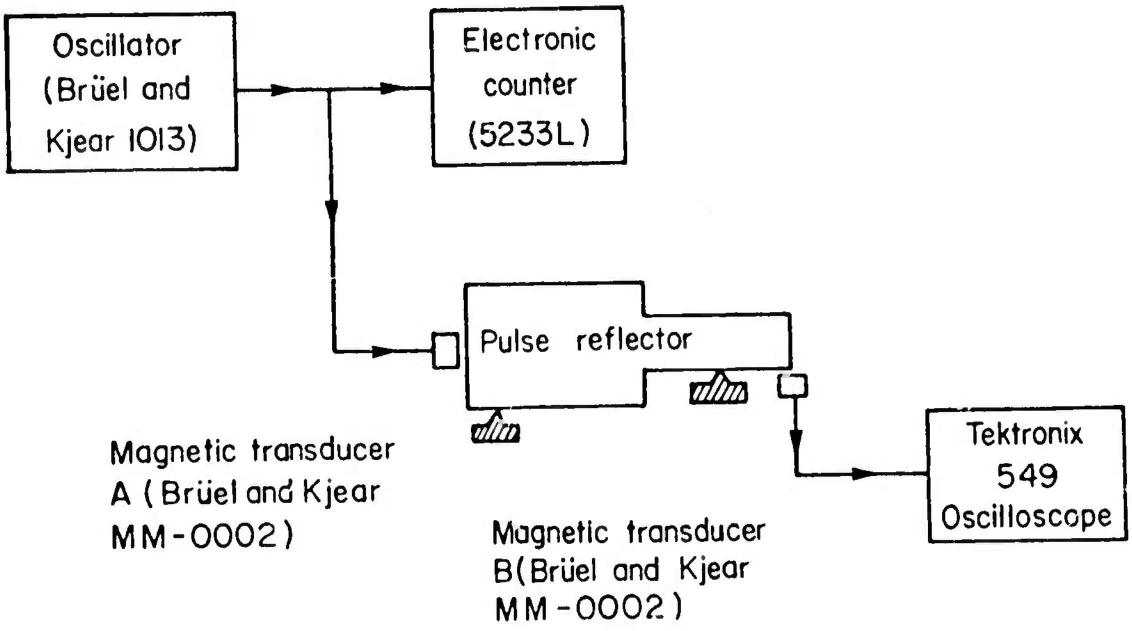
Oscillator (Brüel and Kjear 1013)
Electronic counter (5233L)
Pulse reflector
Tektronix 549 Oscilloscope
Magnetic transducer A (Brüel and Kjear MM-0002)
Magnetic transducer B(Brüel and Kjear MM-0002)

Fig. 6-5 Schematic diagram of apparatus

The B and K oscillator generated a harmonic signal to the magnetic transducer A and it, in turn, vibrated the pulse reflector through magnetic coupling. The magnetic transducer A was placed approximately one-sixteenth of an inch from the end face of the pulse reflector. An identical magnetic transducer was used as a pickup at B, with its output signal displayed on the oscilloscope. By varying the driver frequency from the oscillator, the resonance frequency of the pulse reflector was easily determined from the maximum amplitude of the vibration shown on the oscilloscope. The results of the tests are shown in Table 6-1.

Table 6-1 - Resonance Frequencies of Reflectors and P-11 Horn

Specimen	Resonance Frequency Observed
Type A reflector	f_n = 10,779 kHz
Type B reflector	f_n = 14,309 kHz
P-11 horn	f_n = 10,308 kHz

(B) Measurement of Reflection Characteristics

Incident and reflected stress pulses along a transmission line can be monitored by means of strain gages attached on the transmission line. The incident stress wave is produced by firing a one inch in diameter, one-inch-long steel tool from a spring gun as shown in Fig. 6-6. By comparing the amplitude of the incident stress pulse and the reflected stress pulse, one can determine the percentage of the incident wave being reflected from the pulse reflector. The results can be used directly for comparison with the previous theoretical results.

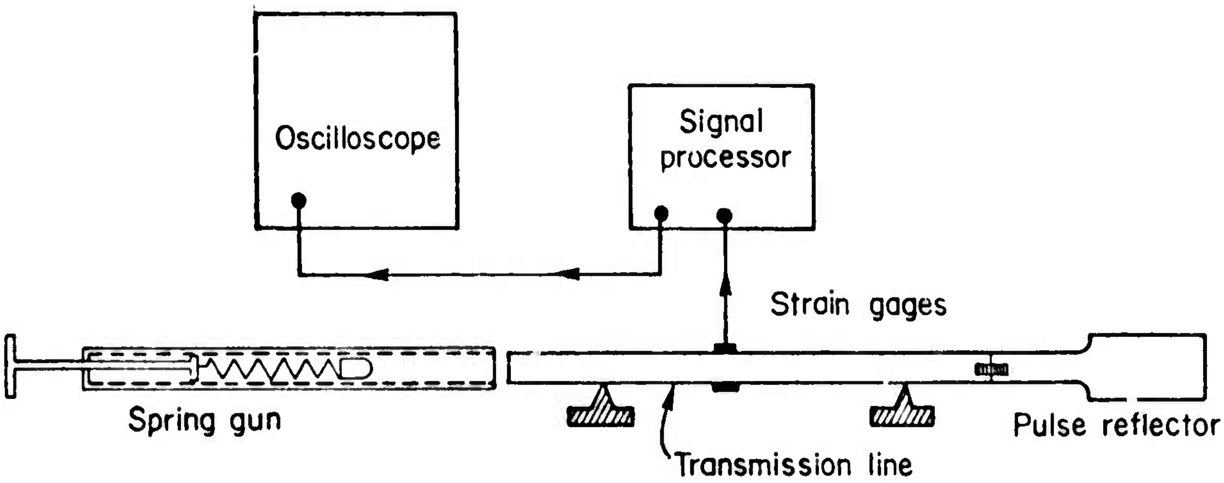

Fig. 6-6 Schematic diagram of experimental set-up

Test of Type A pulse reflector--The results of the Type A pulse reflection are shown in Fig. 6-7. It is seen that the joint at section b_1 where the reflector attaches to the transmission line, and c_1, causes some slight degree of influence in reflection of the stress pulse. It is also observed that the amplitude of the reflected wave is approximately 80% of the incident wave; these results are quite close to theoretical prediction.

Test of Type B pulse reflector--The results for the Type B reflector, shown in Fig. 6-8, are similar to the case of the Type A reflector; an effect due to the connection between the transmission line and pulse reflector is noted. Again, the amplitude of the reflected wave equals to 80% of incident wave, and is in good agreement with the theoretical calculations.

Test of P-11 horn--It is interesting to observe the reflection characteristics of a P-11 horn. As shown in Fig. 6-9, the amplitude of the reflected wave equals approximately 50% of the incident wave amplitude. This means approximately 50% of the energy from the incident pulse will transmit into the transducer.

(C) Measurement of Pulse Reflector Efficiency

Tests were made to determine the difference in electrical pulse amplitude from the ceramic rings of a P-11 transducer with and without the Type A reflectors in place. Figure 6-10 shows the setup and results for the P-11 transducer without the reflector. The top trace of the photograph is the familiar stress wave, while the lower trace is the voltage generated by the stress wave transmitted into the transducer.

Figure 6-11 shows the results with the Type A reflector in place. It is seen that the induced voltage pulse is reduced from 5.4 kV without the reflector to a level of 1.0 kV with the reflector.

6-3 SUMMARY

The theoretical analysis of the reflection characteristics indicated that a pulse reflector design with a stepped cylinder configuration and an A_2/A_1 ratio equal to 9 would provide 80% reflection. Both theoretical calculations and experimental tests verified these findings.

Of the two types of pulse reflectors considered, it was found that the resonance frequency for the Type A pulse reflector was much closer to the natural frequency of the P-11 transducer than the Type B reflector, so that only the Type A reflector was considered in final tests with the P-11. Final comparison tests indicated that the voltage generated at the ceramic rings by the tool impact was reduced more than 80% compared with the results without the pulse reflector.

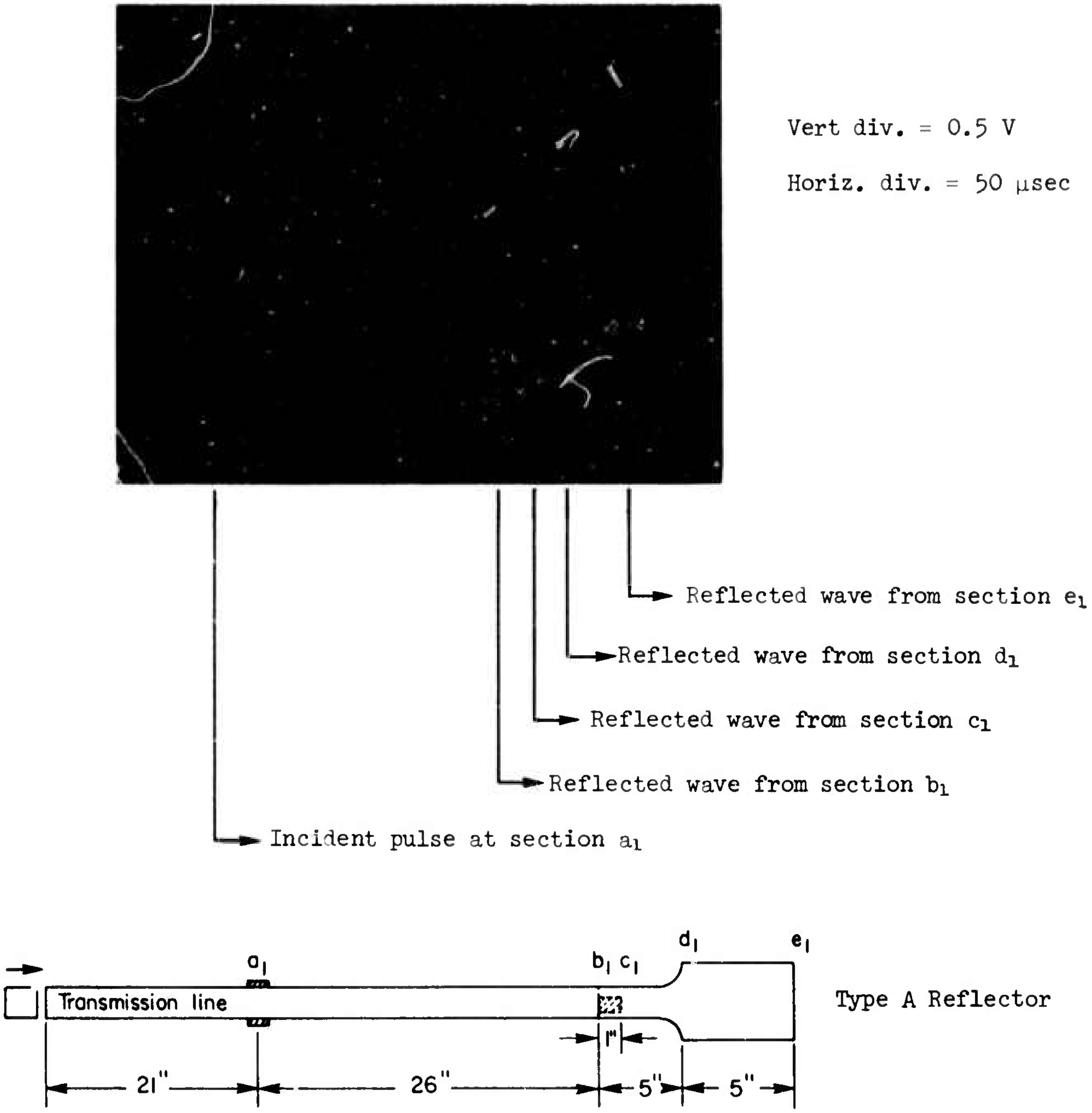
Vert div. = 0.5 V
Horiz. div. = 50 μsec
Reflected wave from section e1
Reflected wave from section d1
Reflected wave from section c1
Reflected wave from section b1
Incident pulse at section a1
a1
b1 c1
d1
e1
Transmission line
1"
21"
26"
5"
5"
Type A Reflector

Fig. 6-7 Typical stress pulse output observed for Type A reflector with interpretation of the wave form

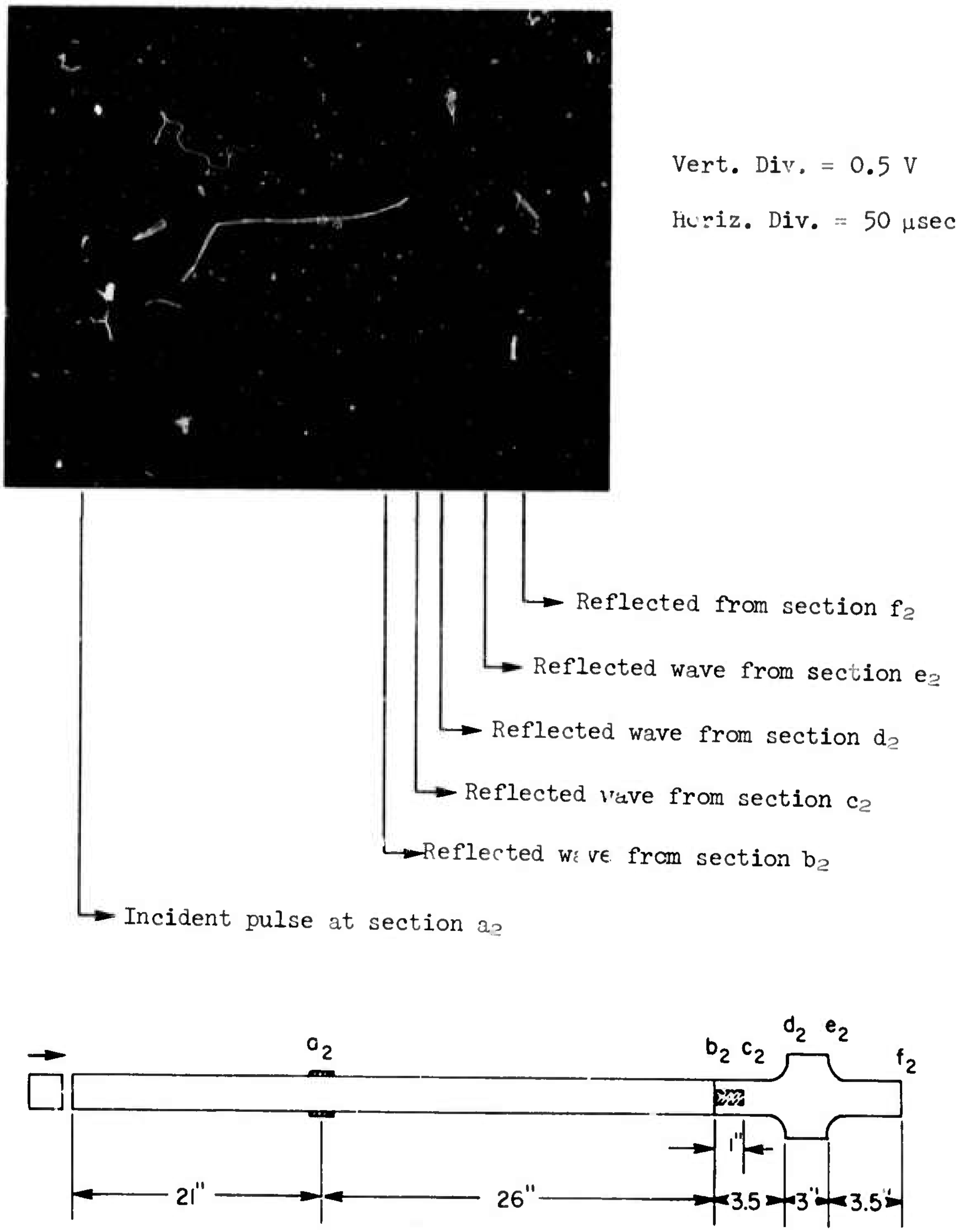

Reflected from section f_2
Reflected wave from section e_2
Reflected wave from section d_2
Reflected wave from section c_2
Reflected wave from section b_2
Incident pulse at section a_2
a_2
b_2 c_2
d_2 e_2
f_2
1"
21"
26"
3.5
3"
3.5"

Vert. Div. = 0.5 V

Horiz. Div. = 50 μsec

Fig. 6-8 Typical stress pulse output for Type B reflector with interpretation of the waveform

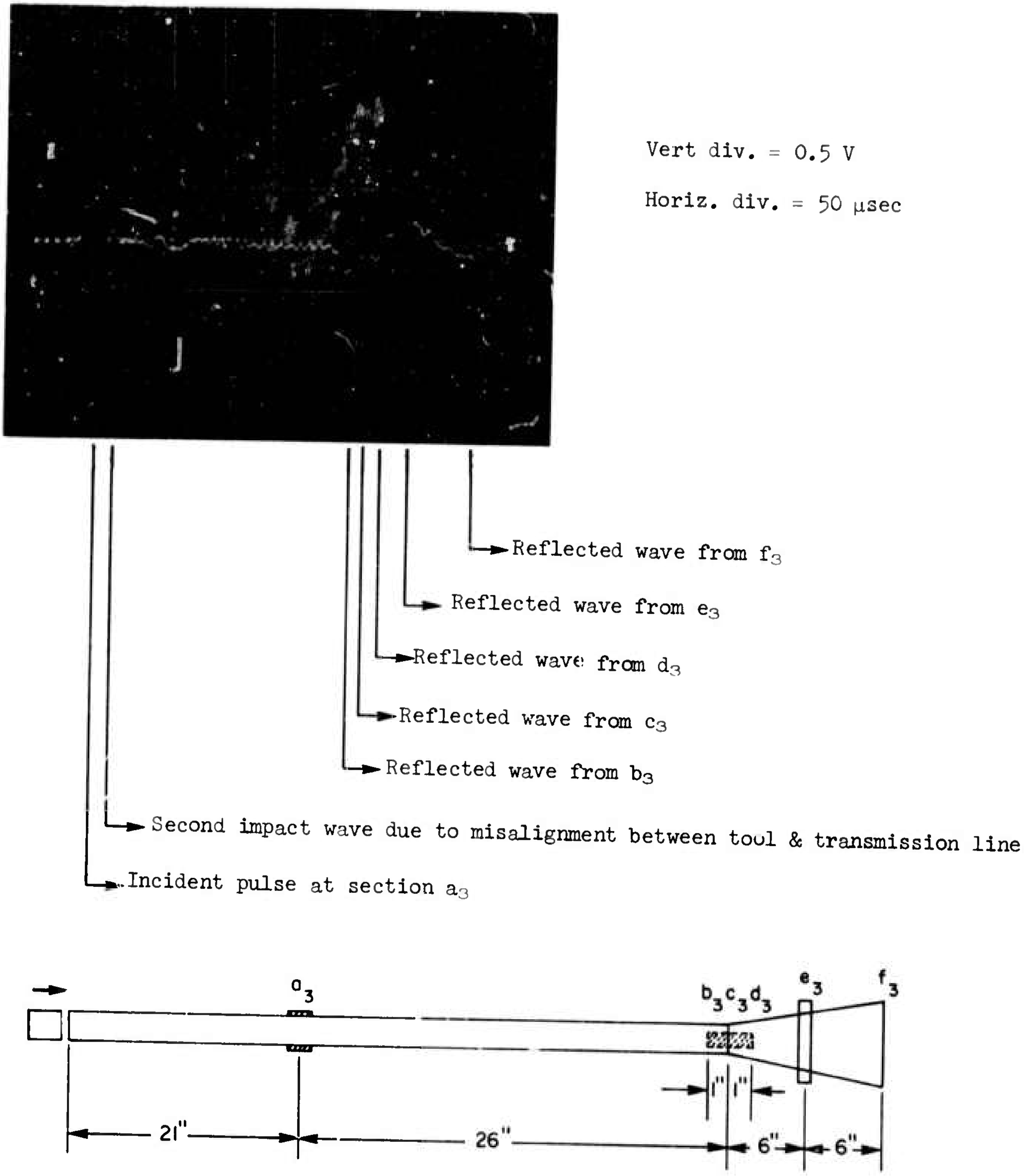

Vert div. = 0.5 V

Horiz. div. = 50 μsec

Reflected wave from f_3

Reflected wave from e_3

Reflected wave from d_3

Reflected wave from c_3

Reflected wave from b_3

Second impact wave due to misalignment between tool & transmission line

Incident pulse at section a_3

Fig. 6-9 Stress pulse output for P-11 horn with interpretation of the waveform

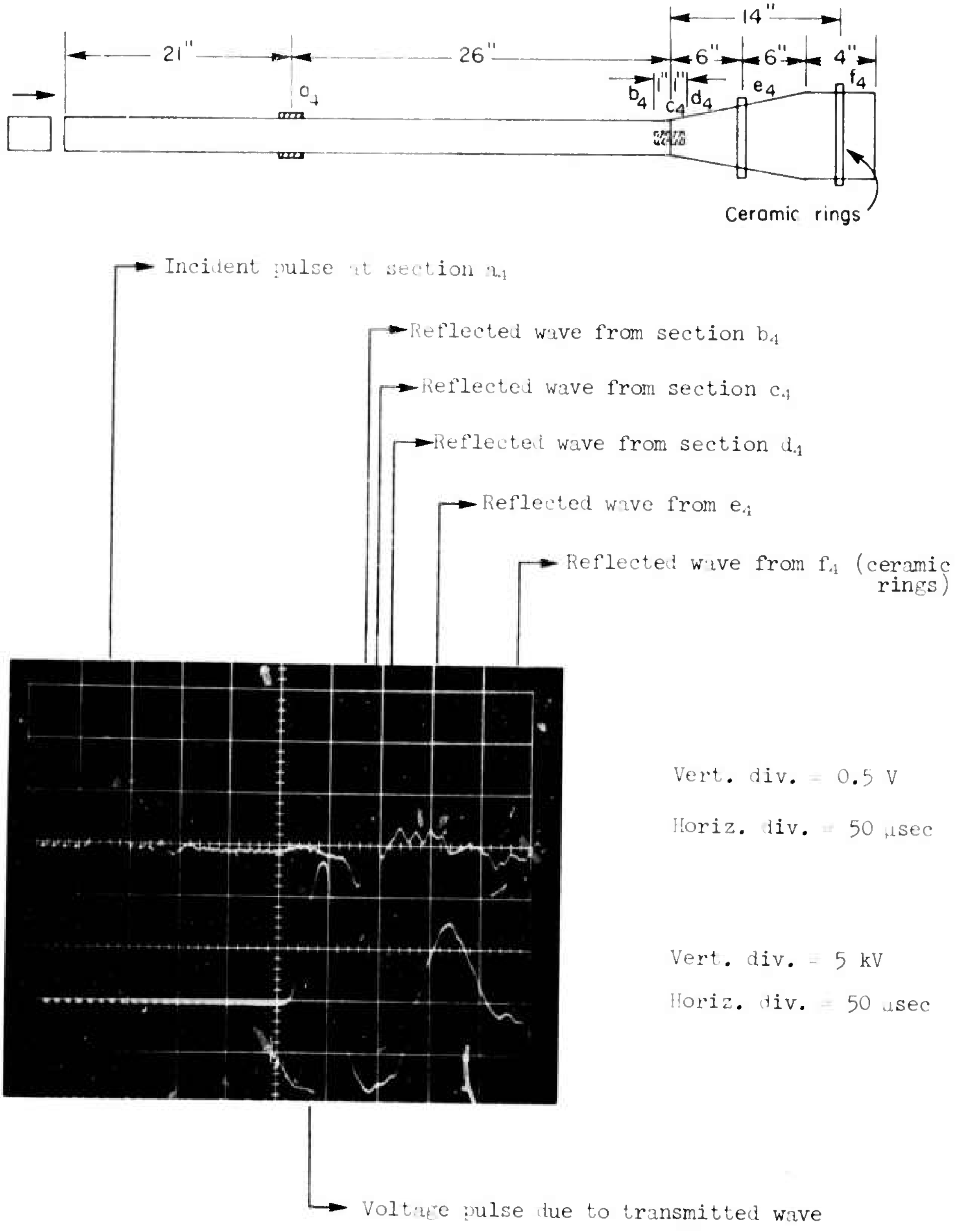
14"
21"
26"
6"
6"
4"
1"
1"
a4
b4
c4
d4
e4
f4
Ceramic rings
Incident pulse at section a4
Reflected wave from section b4
Reflected wave from section c4
Reflected wave from section d4
Reflected wave from e4
Reflected wave from f4 (ceramic rings)
Vert. div. = 0.5 V
Horiz. div. = 50 μsec
Vert. div. = 5 kV
Horiz. div. = 50 μsec
Voltage pulse due to transmitted wave

Fig. 6-10 Typical stress pulse and voltage output for P-11 transducer, without a pulse reflector

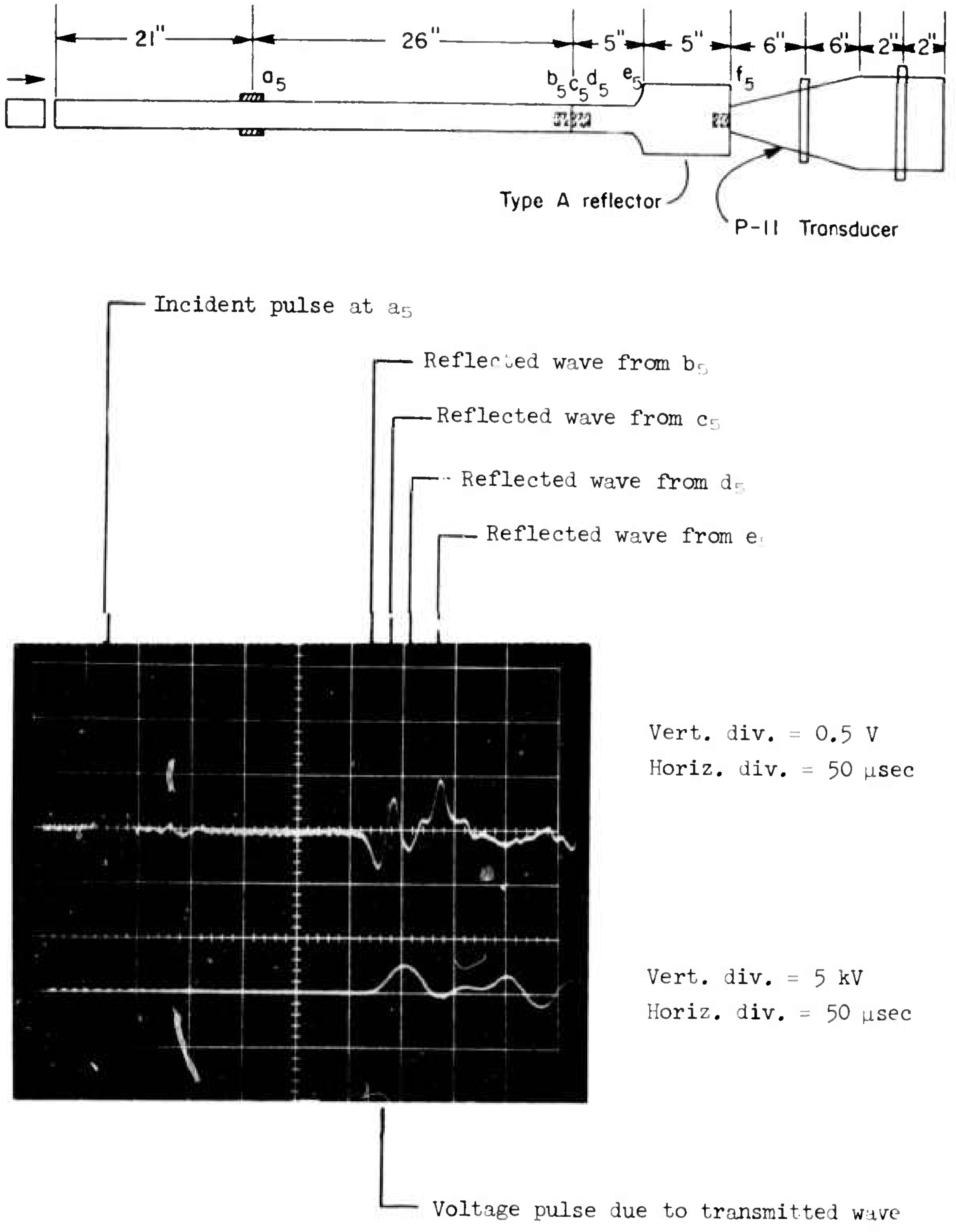
21"
26"
5"
5"
6"
6"
2"
2"
a_5
b_5
c_5
d_5
e_5
f_5
Type A reflector
P-11 Transducer

Incident pulse at a_5

Reflected wave from b_5

Reflected wave from c_5

Reflected wave from d_5

Reflected wave from e

Vert. div. = 0.5 V
Horiz. div. = 50 μsec

Vert. div. = 5 kV
Horiz. div. = 50 μsec

Voltage pulse due to transmitted wave

Fig. 6-11 Typical stress pulse and voltage output for P-11 transducer with the Type A pulse reflector in place

6-4 REFERENCES

1. Feng, C. C. and Graff, K. F., "Impact on a sonic transmission line," Engineering Experiment Station Report 220-Q3-68, The Ohio State University.

2. Libby, C. C., "Impact Coupled Motor Generator Set," Engineering Experiment Station Report 220-Q3-68, The Ohio State University.